

# Control of Wettability of Carbon Nanotube Array by Reversible Dry Oxidation for Superhydrophobic Coating and Supercapacitor Applications

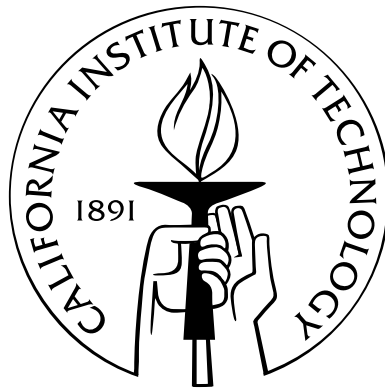
Thesis by

Adrianus Indrat Aria

In Partial Fulfillment of the Requirements

for the Degree of

Doctor of Philosophy



California Institute of Technology

Pasadena, California

2013

(Defended May 3, 2013)

© 2013

Adrianus Indrat Aria

All Rights Reserved

This thesis is dedicated to Maria Christania

# Acknowledgements

First of all, I would like to thank my advisor, Professor Morteza Gharib, for giving me the opportunity to work on exciting and fulfilling research projects. I am deeply grateful for his invaluable support and guidance throughout my PhD work. I also greatly appreciate his trust in me to explore and pursue my scientific interest. I would also like to acknowledge my thesis committee, Professors John Dabiri, Guruswami Ravichandran, and James Heath for giving me helpful comments and suggestions on my research.

I would like to express my gratitude to all my collaborators, without whom this work would not have been possible. I thank Masoud Beizai and Ehsan Jabbarzadeh for the fruitful discussions we had on many topics. I thank Brad Lyon for the great help in the last four years and for being an awesome labmate and comrade. I thank the entire Gharib group, in particular all Charyk lab members, for creating an excellent learning environment where open critical thought is highly appreciated. I am also grateful to all my students for assisting me in conducting time consuming and meticulous experiments: Stephanie Samson, Patrick Arran, and Perren Yang for assisting me with the carbon nanotube chemical modification project, Christina Shu and Anirban Ghosh for assisting me with the superhydrophobic carbon nanotube array project, Adi Gani for assisting me with the graphene project, and Melanie Guittet for assisting me with the carbon nanotube supercapacitor project.

I would like to acknowledge the support from the Kavli Nanoscience Institute (KNI), the Molecular Materials Research Center (MMRC), the Analytical Facility of Geology and Planetary Sciences, and the Environmental Analysis Center (EAC) in giving me a full access to state-of-the-art nanofabrication and analytical instruments.

I gratefully thank Professor George Rossman for allowing me to use several analytical instruments in his laboratory. I would also like to thank Chi Ma, Nathan Dalleska, and Carol Garland for all the help with imaging and chemical analysis.

I would like to thank my good friends for their assistance and friendship: Esperanza Linares, Michio Inoue, Kawai Kwok, Andre Pradhana, and Jeremy Suhardi. I also thank my great roommates during my six years at Caltech: Ian Jacobi and Vikas Trivedi. A special thanks goes to my best buddy and partner in crime, Andrey Gunawan, for the morale support and for keeping me sane these last few years.

Last, but not the least, I would like to express my most sincere and deepest gratitude to my family for their unconditional love and support. Thank you for encouraging me to pursue my dreams and for being the source of my strength this endeavor. Most importantly, I thank Maria Christania, without whom none of this would mean anything.

This research has been supported in part by The Fulbright Fellowship, The Zcube s.r.l., The Office of Naval Research under grant #N00014 – 11 – 1 – 0031, and The Fletcher-Jones Foundation under grant #9900600.

# Abstract

In this thesis, dry chemical modification methods involving UV/ozone, oxygen plasma, and vacuum annealing treatments are explored to precisely control the wettability of CNT arrays. By varying the exposure time of these treatments the surface concentration of oxygenated groups adsorbed on the CNT arrays can be controlled. CNT arrays with very low amount of oxygenated groups exhibit a superhydrophobic behavior. In addition to their extremely high static contact angle, they cannot be dispersed in DI water and their impedance in aqueous electrolytes is extremely high. These arrays have an extreme water repellency capability such that a water droplet will bounce off of their surface upon impact and a thin film of air is formed on their surface as they are immersed in a deep pool of water. In contrast, CNT arrays with very high surface concentration of oxygenated functional groups exhibit an extreme hydrophilic behavior. In addition to their extremely low static contact angle, they can be dispersed easily in DI water and their impedance in aqueous electrolytes is tremendously low. Since the bulk structure of the CNT arrays are preserved during the UV/ozone, oxygen plasma, and vacuum annealing treatments, all CNT arrays can be repeatedly switched between superhydrophilic and superhydrophobic, as long as their O/C ratio is kept below 18%.

The effect of oxidation using UV/ozone and oxygen plasma treatments is highly reversible as long as the O/C ratio of the CNT arrays is kept below 18%. At O/C ratios higher than 18%, the effect of oxidation is no longer reversible. This irreversible oxidation is caused by irreversible changes to the CNT atomic structure during the oxidation process. During the oxidation process, CNT arrays undergo three different processes. For CNT arrays with O/C ratios lower than 40%, the oxidation process

results in the functionalization of CNT outer walls by oxygenated groups. Although this functionalization process introduces defects, vacancies and micropores opening, the graphitic structure of the CNT is still largely intact. For CNT arrays with O/C ratios between 40% and 45%, the oxidation process results in the etching of CNT outer walls. This etching process introduces large scale defects and holes that can be obviously seen under TEM at high magnification. Most of these holes are found to be several layers deep and, in some cases, a large portion of the CNT side walls are cut open. For CNT arrays with O/C ratios higher than 45%, the oxidation process results in the exfoliation of the CNT walls and amorphization of the remaining CNT structure. This amorphization process can be implied from the disappearance of C-C sp<sup>2</sup> peak in the XPS spectra associated with the  $\pi$ -bond network.

The impact behavior of water droplet impinging on superhydrophobic CNT arrays in a low viscosity regime is investigated for the first time. Here, the experimental data are presented in the form of several important impact behavior characteristics including critical Weber number, volume ratio, restitution coefficient, and maximum spreading diameter. As observed experimentally, three different impact regimes are identified while another impact regime is proposed. These regimes are partitioned by three critical Weber numbers, two of which are experimentally observed. The volume ratio between the primary and the secondary droplets is found to decrease with the increase of Weber number in all impact regimes other than the first one. In the first impact regime, this is found to be independent of Weber number since the droplet remains intact during and subsequent to the impingement. Experimental data show that the coefficient of restitution decreases with the increase of Weber number in all impact regimes. The rate of decrease of the coefficient of restitution in the high Weber number regime is found to be higher than that in the low and moderate Weber number. Experimental data also show that the maximum spreading factor increases with the increase of Weber number in all impact regimes. The rate of increase of the maximum spreading factor in the high Weber number regime is found to be higher than that in the low and moderate Weber number. Phenomenological approximations and interpretations of the experimental data, as well as brief comparisons to the

previously proposed scaling laws, are shown here.

Dry oxidation methods are used for the first time to characterize the influence of oxidation on the capacitive behavior of CNT array EDLCs. The capacitive behavior of CNT array EDLCs can be tailored by varying their oxygen content, represented by their O/C ratio. The specific capacitance of these CNT arrays increases with the increase of their oxygen content in both KOH and Et<sub>4</sub>NBF<sub>4</sub>/PC electrolytes. As a result, their gravimetric energy density increases with the increase of their oxygen content. However, their gravimetric power density decreases with the increase of their oxygen content. The optimally oxidized CNT arrays are able to withstand more than 35,000 charge/discharge cycles in Et<sub>4</sub>NBF<sub>4</sub>/PC at a current density of 5 A/g while only losing 10% of their original capacitance.

# Contents

<b>Acknowledgements</b>	<b>iv</b>
<b>Abstract</b>	<b>vi</b>
<b>List of Figures</b>	<b>xiii</b>
<b>List of Tables</b>	<b>xviii</b>
<b>1 Introduction</b>	<b>1</b>
1.1 Motivation . . . . .	1
1.2 Study Objectives . . . . .	4
1.3 Scope of Study . . . . .	6
1.4 Thesis Outline . . . . .	8
<b>2 Materials and Methods</b>	<b>11</b>
2.1 Carbon Nanotubes Fabrication Method . . . . .	11
2.1.1 CVD growth method . . . . .	13
2.1.2 Typical characteristics of CVD growth . . . . .	20
2.2 Dry Oxidation and Reduction Process . . . . .	26
2.2.1 Oxygen Plasma and UV/Ozone Treatment . . . . .	29
2.2.2 Vacuum Annealing . . . . .	32
2.3 Characterization Methods . . . . .	32
2.3.1 Scanning Electron Microscopy . . . . .	32
2.3.2 Transmission Electron Microscopy . . . . .	34
2.3.3 Contact Angle . . . . .	34

2.3.4	Raman Spectroscopy . . . . .	35
2.3.5	Fourier Transform Infra Red Spectroscopy . . . . .	35
2.3.6	X-ray Photoelectron Spectroscopy . . . . .	35
2.3.7	Cyclic Voltammetry, Galvanostatic Charge-Discharge Cycle, and Electrochemical Impedance Spectroscopy . . . . .	36
<b>3</b>	<b>Evolution of Wettability and Surface Chemistry of Carbon Nanotube Arrays</b>	<b>37</b>
3.1	Introduction . . . . .	37
3.2	Materials and Methods . . . . .	38
3.3	Results and Discussion . . . . .	40
3.3.1	Contact angle vs. exposure time . . . . .	40
3.3.2	Oxygen content vs. exposure time . . . . .	46
3.3.3	Contact angle vs oxygen content . . . . .	55
3.3.4	FTIR and XPS analysis . . . . .	56
3.3.5	Micro- and nano-scale surface roughness . . . . .	64
3.3.6	Water immersion and droplet impact behavior on CNT arrays with different wettability . . . . .	66
3.3.7	Dispersibility and zeta potential analysis . . . . .	71
3.3.8	Electrochemical impedance . . . . .	75
3.4	Concluding Remarks . . . . .	81
<b>4</b>	<b>Etching and Amorphization of Carbon Nanotube Arrays by Irreversible Oxidation</b>	<b>83</b>
4.1	Introduction . . . . .	83
4.2	Materials and Methods . . . . .	84
4.3	Results and Discussion . . . . .	86
4.3.1	X-ray photoelectron spectroscopy analysis . . . . .	86
4.3.2	Raman spectroscopy analysis . . . . .	93
4.3.3	Transmission electron microscopy analysis . . . . .	97
4.3.4	BET and Langmuir surface area . . . . .	104

4.3.5	Effect of heavy oxidation on CNT pillars . . . . .	106
4.4	Concluding Remarks . . . . .	110
<b>5</b>	<b>Water Droplet Impact Behavior on Superhydrophobic Carbon Nanotube Arrays</b>	<b>112</b>
5.1	Introduction . . . . .	112
5.2	Materials and Methods . . . . .	117
5.3	Results and Discussion . . . . .	122
5.3.1	Critical Weber number . . . . .	122
5.3.2	Volume ratio . . . . .	126
5.3.3	Coefficient of restitution . . . . .	129
5.3.4	Maximum spreading factor . . . . .	137
5.4	Concluding Remarks . . . . .	143
<b>6</b>	<b>Carbon Nanotube Arrays as Electrodes for Electrochemical Double Layer Capacitor</b>	<b>145</b>
6.1	Introduction . . . . .	145
6.2	Materials and Methods . . . . .	150
6.3	Results and Discussion . . . . .	154
6.3.1	Capacitive behavior of oxidized CNT in KOH . . . . .	154
6.3.2	Capacitive behavior of oxidized CNT in Et <sub>4</sub> NBF <sub>4</sub> / PC . . . . .	159
6.3.3	Effect of oxidation on the specific capacitance . . . . .	164
6.3.4	Lifetime and performance . . . . .	172
6.4	Concluding Remarks . . . . .	178
<b>7</b>	<b>Summary and Future Works</b>	<b>180</b>
7.1	Summary . . . . .	180
7.2	Future Works . . . . .	185
<b>A</b>	<b>Effect of Reversible Oxidation on the Energy Gap and Structure of CVD Graphene</b>	<b>187</b>
A.1	Introduction . . . . .	187

A.2	Materials and Methods . . . . .	190
A.3	Results and Discussion . . . . .	192
A.3.1	Changes in atomic scale morphology probed by scanning tunneling microscopy . . . . .	192
A.3.2	Evolution of local density of states probed by scanning tunneling spectroscopy . . . . .	196
A.3.3	Changes in defects probed by Raman spectroscopy . . . . .	203
A.3.4	Evolution of surface chemistry probed by X-ray photoelectron spectroscopy . . . . .	204
A.4	Concluding Remarks . . . . .	219
	<b>Bibliography</b>	<b>221</b>

# List of Figures

1.1	Control of CNT arrays wettability by UV/ozone, oxygen plasma, and vacuum annealing treatments . . . . .	6
2.1	In house CVD reactor . . . . .	12
2.2	Schematic of CNT growth process using CVD . . . . .	17
2.3	Short and tall CNT arrays . . . . .	21
2.4	TEM image of a carbon nanotube . . . . .	22
2.5	High packing density of CNT arrays . . . . .	23
2.6	Amorphous carbon on CNT arrays . . . . .	24
2.7	Non-uniform growth of CNT arrays . . . . .	25
3.1	Different wettability induced by dry oxidation and vacuum annealing .	38
3.2	Contact angle vs. UV/ozone exposure time . . . . .	41
3.3	Contact angle vs. oxygen plasma exposure time . . . . .	42
3.4	Contact angle vs. vacuum annealing exposure time . . . . .	43
3.5	Contact angle vs. UV/ozone and vacuum annealing cycles . . . . .	44
3.6	Contact angle vs. O <sub>2</sub> plasma and vacuum annealing cycles . . . . .	45
3.7	XPS survey spectra of CNT arrays with different wettability . . . . .	47
3.8	Oxygen/Carbon atomic ratio vs. UV/ozone exposure time . . . . .	48
3.9	Oxygen/Carbon atomic ratio vs. oxygen plasma exposure time . . . . .	49
3.10	Oxygen/Carbon atomic ratio vs. vacuum annealing exposure time . . .	50
3.11	Oxygen/Carbon atomic ratio vs. UV/ozone and vacuum annealing cycles	51
3.12	Oxygen/Carbon atomic ratio vs. O <sub>2</sub> plasma and vacuum annealing cycles	53
3.13	Contact angle vs. Oxygen/Carbon atomic ratio . . . . .	54

3.14	Reversible vs. irreversible oxidation . . . . .	55
3.15	FTIR survey spectra of CNT arrays with different wettability. . . . .	57
3.16	Contact angle vs. C-O integrated absorbance . . . . .	58
3.17	Contact angle vs. C=O integrated absorbance . . . . .	59
3.18	High resolution XPS spectra of hydrophobic carbon nanotube arrays .	60
3.19	High resolution XPS spectra of hydrophilic carbon nanotube arrays . .	62
3.20	High magnification of CNT arrays after dry oxidation and reduction .	65
3.21	High magnification of CNT arrays after dry oxidation and reduction .	67
3.22	As-grown and superhydrophobic carbon nanotube arrays submerged in a shallow pool of water . . . . .	68
3.23	As-grown and superhydrophobic carbon nanotube arrays submerged in a deep pool of water . . . . .	69
3.24	Time-lapse images of the water droplet impacting the surface of as grown CNT arrays . . . . .	70
3.25	Time-lapse images of the water droplet impacting the surface of hy- drophilic CNT arrays . . . . .	71
3.26	Time-lapse images of the water droplet impacting the surface of super- hydrophobic CNT arrays . . . . .	72
3.27	Dispersibility of carbon nanotube arrays with different wettability . . .	73
3.28	Zeta potential of carbon nanotube arrays vs. oxygen/carbon ratio . . .	74
3.29	Bode plot of carbon nanotube arrays with different wettability in DI water	77
3.30	Nyquist plot of carbon nanotube arrays with different wettability in DI water . . . . .	79
3.31	Double layer capacitance and charge transfer resistance of carbon nan- otube arrays with different wettability in DI water . . . . .	80
4.1	XPS of moderately oxidized CNT arrays . . . . .	87
4.2	XPS of highly oxidized CNT arrays . . . . .	88
4.3	C1s peak position vs. oxygen/carbon ratio . . . . .	89
4.4	C-C sp <sup>2</sup> and C-C sp <sup>3</sup> concentration vs. oxygen/carbon ratio . . . . .	90

4.5	C-O and C=O concentration vs. oxygen/carbon ratio . . . . .	92
4.6	Raman spectra of CNT arrays with different oxidation level . . . . .	94
4.7	ID/IG ratio from Raman spectra of CNT arrays with different oxidation level . . . . .	95
4.8	IG'/IG ratio from Raman spectra of CNT arrays with different oxidation level . . . . .	96
4.9	Low magnification TEM images of CNT arrays with different oxidation level . . . . .	98
4.10	High magnification TEM images of CNT arrays with different oxidation level . . . . .	99
4.11	Selected area diffraction patterns of CNT arrays with different oxidation level . . . . .	101
4.12	Spacing obtained from diffraction patterns of CNT arrays with different oxidation level . . . . .	103
4.13	Surface area vs. oxygen/carbon ratio . . . . .	105
4.14	High magnification SEM images of CNT arrays with different oxidation levels . . . . .	107
4.15	Effect of oxidation on hollow CNT pillars . . . . .	109
5.1	Water droplet on a superhydrophobic surface exhibits an almost perfect spherical shape . . . . .	118
5.2	Time-lapse image of water droplet bouncing off of the surface of carbon nanotube arrays . . . . .	119
5.3	Schematic of the droplet impact behavior experiment setup . . . . .	121
5.4	Three different water droplet impact behaviors depending on the Weber number . . . . .	124
5.5	Split and splash probability as a function of Weber number of the water droplet . . . . .	125
5.6	Illustration of different water droplet impact behaviors depending on the Weber number . . . . .	127

5.7	Log-log plot of volume ratio as a function of Weber number of the water droplet . . . . .	129
5.8	Log-log plot of coefficient of restitution as a function of Weber number of the droplet . . . . .	131
5.9	Mass-spring-damper system as a model for restitution coefficient . . . .	136
5.10	Log-log plot of spreading factor as a function of Weber number of the droplet . . . . .	137
5.11	Log-log plot of spreading factor as a function of Reynolds number of the droplet . . . . .	139
6.1	Schematic of electrochemical capacitor . . . . .	147
6.2	Carbon based electrochemical capacitor . . . . .	149
6.3	Effect of wettability to the effective surface area . . . . .	151
6.4	Cyclic voltammogram of hydrophobic CNT arrays in KOH . . . . .	156
6.5	Cyclic voltammogram of hydrophilic CNT arrays in KOH . . . . .	157
6.6	Cyclic voltammogram of hydrophobic CNT arrays in Et <sub>4</sub> NBF <sub>4</sub> . . . . .	160
6.7	Cyclic voltammogram of hydrophilic CNT arrays in Et <sub>4</sub> NBF <sub>4</sub> . . . . .	161
6.8	Galvanostatic charge discharge cycle of CNT arrays in KOH electrolyte	164
6.9	Galvanostatic charge discharge cycle of CNT arrays in Et <sub>4</sub> NBF <sub>4</sub> /PC electrolyte . . . . .	165
6.10	Specific capacitance vs. oxygen/carbon ratio in KOH . . . . .	168
6.11	Specific capacitance vs. oxygen/carbon ratio in Et <sub>4</sub> NBF <sub>4</sub> . . . . .	170
6.12	Specific capacitance vs. number of cycles . . . . .	172
6.13	Effect of oxidation on the energy density and power density of CNT arrays in KOH and Et <sub>4</sub> NBF <sub>4</sub> /PC electrolytes . . . . .	174
6.14	Ragone plot of oxidized CNT arrays in KOH and Et <sub>4</sub> NBF <sub>4</sub> /PC electrolytes	177
A.1	STM image of pristine CVD graphene . . . . .	193
A.2	STM image of lightly oxidized CVD graphene . . . . .	195
A.3	STM image of vacuum annealed CVD graphene . . . . .	197
A.4	STS spectra evolution of UV/ozone treated CVD graphene . . . . .	199

A.5	STS spectra evolution of oxygen plasma treated CVD graphene . . . .	201
A.6	Energy gap and oxygen/carbon ratio evolution of CVD graphene induced by dry oxidation and vacuum annealing cycles . . . . .	202
A.7	Raman spectra of CVD graphene before and after dry oxidation and vacuum annealing cycles . . . . .	204
A.8	Energy gap vs. oxygen/carbon ratio of CVD graphene induced by dry oxidation and vacuum annealing cycles . . . . .	206
A.9	Evolution of XPS C1s spectra of CVD graphene induced by dry oxidation and vacuum annealing cycles . . . . .	208
A.10	Evolution of XPS O1s spectra of CVD graphene induced by dry oxidation and vacuum annealing cycles . . . . .	210
A.11	Evolution of C-C bond concentration of CVD graphene induced by dry oxidation and vacuum annealing cycles . . . . .	211
A.12	Evolution of C-O and C=O bonds concentration of CVD graphene induced by dry oxidation and vacuum annealing cycles . . . . .	213
A.13	Evolution of O-C=O bond concentration of CVD graphene induced by dry oxidation and vacuum annealing cycles . . . . .	215
A.14	Evolution of XPS Ni2p spectra of CVD graphene induced by dry oxidation and vacuum annealing cycles . . . . .	217

## List of Tables

2.1	List of materials and equipment used in the in-house CVD reactor. . . . .	14
2.2	List of materials and equipment used for substrate preparation and catalysts deposition. . . . .	16
2.3	CVD growth parameters. . . . .	19
2.4	Typical CVD growth results. . . . .	22
2.5	Wet chemical modification vs. dry chemical modification. . . . .	27
2.6	Dry oxidation and reduction parameters. . . . .	28
2.7	List of equipment used for dry oxidation and vacuum annealing. . . . .	31
2.8	List of equipment used for characterization. . . . .	33
5.1	Comparison between superhydrophobic surfaces. . . . .	115
5.2	Dimensionless parameters of the experiments. . . . .	122

# Chapter 1

## Introduction

### 1.1 Motivation

In recent years, fabrication of synthetic materials with tunable wettability has been reported (Shirtcliffe et al., 2005; Koch and Barthlott, 2009; Rafiee et al., 2010; Wang et al., 2010; Tao and Tianhong, 2011; Chang and Hunter, 2011). By definition, these materials have the capability to be switched between hydrophilic and hydrophobic under certain conditions. Ideally, these materials have a very wide range of wettability, from superhydrophobic to superhydrophilic, and their wettability can be precisely controlled by external stimuli. Note that a superhydrophobic surface is defined as a surface that is extremely difficult to get wet and has a static contact angle higher than  $150^\circ$  (Bhushan et al., 2009; Wang and Jiang, 2007; Men et al., 2010). In contrast, a superhydrophilic surface is defined as a surface that is extremely easy to get wet and has a static contact angle of less than  $5^\circ$  (Bhushan et al., 2009; Wang and Jiang, 2007; Men et al., 2010). These materials have attracted enormous attention due to their numerous potential applications including self-cleaning surface (Scardino et al., 2009), hydrodynamic skin-friction drag reduction (Rothstein, 2010), drug delivery devices (Bianco et al., 2005), and energy storage devices (Lee et al., 2010).

It has been fully understood that wettability of a material is dictated by its surface chemistry (Emsley, 1980; Wenzel, 1936). Thus, the wettability of a material can be, in principle, tailored by surface chemistry modification (Wang et al., 2010). Surface roughness and topography have a tendency to amplify the magnitude of sur-

face wettability (Bhushan et al., 2009; Gao and McCarthy, 2007, 2006b; Krupenkin et al., 2004). For a wettable material, the surface roughness and topography improve its wettability such that it becomes more hydrophilic. On the other hand, for a non-wettable material, the surface roughness and topography make it more difficult to wet; in other words, it becomes more hydrophobic. Therefore, ideal tunable materials are those with which surface chemistry can be easily modified and have a nanoscale surface roughness and topography.

Among currently available tunable materials, including ZnO (Ebert and Bhushan, 2012; Feng et al., 2003), SiO<sub>2</sub> (Ebert and Bhushan, 2012; Xu et al., 2012), ITO (Ebert and Bhushan, 2012), vertically aligned multi-walled carbon nanotube (CNT) arrays have attracted most of the attention due to their inherent microscale and nanoscale surface roughness and topography and their surfaces are readily functionalized by common methods. In addition, CNT are known to have excellent mechanical, electrical, and thermal properties. For instance, CNT is known to be one of the strongest materials, with an ultimate tensile strength of an order of magnitude higher than that of steel (Yu et al., 2000; Peng et al., 2008). CNT is also known to be a good electrical conductor, with a maximum current density of three orders of magnitude higher than that of copper. Further, the self assembly fabrication process of CNT arrays offers a big advantage compared to other synthetic materials. This assembly process is simple and does not require a patterning process that is often expensive and time consuming.

Previously reported studies suggest that CNT arrays can be made hydrophilic by functionalizing their surfaces with polar functional groups that contain oxygen or nitrogen. Such functional groups, which are introduced by chemisorption of oxygen and nitrogen, allow hydrogen bonds between the surface of CNT and water molecules to form. Compared to surface functionalization by nitrogenated groups, surface functionalization by oxygenated groups offers several advantages. Functionalization process to induce chemisorption of oxygen on carbon structures is typically easier and less complicated than that of nitrogen. In addition, oxygen functionalization on carbon structures has been widely explored, streamlined, and implemented in large-scale

industries.

Although oxygen functionalization of carbon structures is not new, its use to control wettability of CNT arrays still has a virtue for further investigations. Almost all known oxygen functionalization processes rely on wet chemical oxidation methods, which involve the use of highly corrosive acids and oxidizing agents (Hummers and Offeman, 1958; Park and Ruoff, 2009; Li et al., 2008; Sun et al., 2008; Becerril et al., 2008; Marcano et al., 2010). As a result, there are always safety and convenience issues associated with these methods. In addition, these methods do not allow the oxygen uptake process and rate to be fully controlled. Thus, these methods are typically time consuming to perform and often result in an irreversible oxidation. Further, the bulk structural of CNT arrays, especially the vertical alignment of the CNT, is difficult to preserve during the acids or oxidizing agents removal process.

Unlike methods to make CNT arrays more hydrophilic that are mostly known, methods to make CNT arrays more hydrophobic, or even superhydrophobic, are uncommon. Previous studies show that these CNT arrays can be turned superhydrophobic by coating them with non-wettable chemicals such as fluorinated polymers and fluorocarbons, transition metal oxides, fluoroalkylsilanes, and hydrocarbons (Huang et al., 2005; Lau et al., 2003; Feng et al., 2002; Hong and Uhm, 2006; Cho et al., 2007). These non-wetting chemicals prevent hydrogen bond between the chemisorbed oxygen and water molecules from forming, rendering the CNT arrays superhydrophobic. Although the process to coat non-wettable chemicals onto CNT arrays is not too difficult to perform, it is completely irreversible. Once the CNT arrays are exposed to these coating treatments, they can no longer be rendered hydrophilic by common oxidation methods.

Although theoretically CNT arrays are highly hydrophobic due to their non polar nature, in reality they are often found to exhibit a weak hydrophobicity. This behavior is commonly caused by the presence of defects, contaminations, and imperfections on both individual CNT and their bulk structure. One particular problem that occurs naturally to catalytic CVD grown CNT arrays is the presence of oxygen, in the form of oxygenated functional groups, moistures, or molecular oxygen, adsorbed during the

growth. As mentioned earlier, adsorbed oxygen is one of the key elements in rendering a surface hydrophilic. In principle, CNT arrays can be made highly hydrophobic once this adsorbed oxygen is largely removed from their surface. Therefore, chemical reduction methods may be employed to make CNT arrays more hydrophobic, or even superhydrophobic, without the need for non-wettable chemical coating.

This thesis is intended to explore the possibility of using dry chemical modification methods to alter the surface chemistry of CNT arrays in order to control their wettability. These methods offer several advantages over wet chemical modification methods. The lack of highly corrosive chemicals allows them to be used safely and conveniently. In addition, the oxygen adsorption and desorption rate and dosage can be, in principle, controlled precisely such that the process is highly reversible and the bulk structure of CNT arrays is well preserved. CNT arrays treated by these methods are expected to exhibit a wide range of wettability, from superhydrophilic to superhydrophobic, and their wettability can be finely tailored to match particular requirements for specific practical application.

This thesis is also intended to be a foundation for future studies related to chemical modification of CNT arrays and other carbon nanostructures through various types of dry chemical modification methods. The results presented herein can be loosely used as guidelines in understanding the evolution of other physical properties of CNT arrays and other carbon nanostructures, including mechanical, electrical, electrochemical, and thermal properties under the influence of dry chemical modifications. Since CNT arrays can now be used beyond their inherent capabilities, new research areas and applications that take advantage of extreme wettability will be opened up.

## **1.2 Study Objectives**

The overarching goal of this thesis is to prove the hypothesis that the wettability of CNT arrays can be precisely tuned by controlling the amount of oxygenated groups adsorbed on their surfaces. Several specific objectives have been formulated as guid-

ance to achieve this goal and are described as follows:

(a) To show that CNT arrays can be repeatedly switched between hydrophobic and hydrophilic as long as their bulk structures are preserved. It is important to also show that the CNT arrays can be made superhydrophobic and superhydrophilic.

(b) To use well controlled oxidation and reduction processes in order to retain the integrity and preserve the bulk structure of CNT arrays. In this study, the oxidation process is performed using UV/ozone and oxygen plasma treatments, while the reduction process is performed using vacuum annealing treatments.

(c) To elucidate the underlying mechanisms that control the wettability of CNT arrays. To achieve this, the correlation between wettability of CNT arrays and their oxygen content needs to be presented.

(d) To show that the abovementioned oxidation and reduction processes are reversible. It is important to also show the circumstances under which these processes are no longer reversible.

These specific objectives are summarized in Figure 1.1.

The secondary goal of this study is to use the CNT arrays in several high-impact, practical applications. Two applications are selected to demonstrate two opposite extremes of wettability of CNT arrays. The first application is to use vacuum annealed CNT arrays as an ideal Cassie state superhydrophobic surface. This superhydrophobic surface is then employed to study the impact behavior of water droplets under a wide range of Weber numbers. Such study has never been done in the past because of the limitations of the current available superhydrophobic surface. The second application is to use oxidized CNT arrays as electrodes of electrochemical double-layer capacitors. CNT arrays with different degrees of oxidation, which correlate to different degrees of wettability, are used to study the effect of oxidation on their capacitive behavior. Although the use of CNT arrays as electrodes of electrochemical double

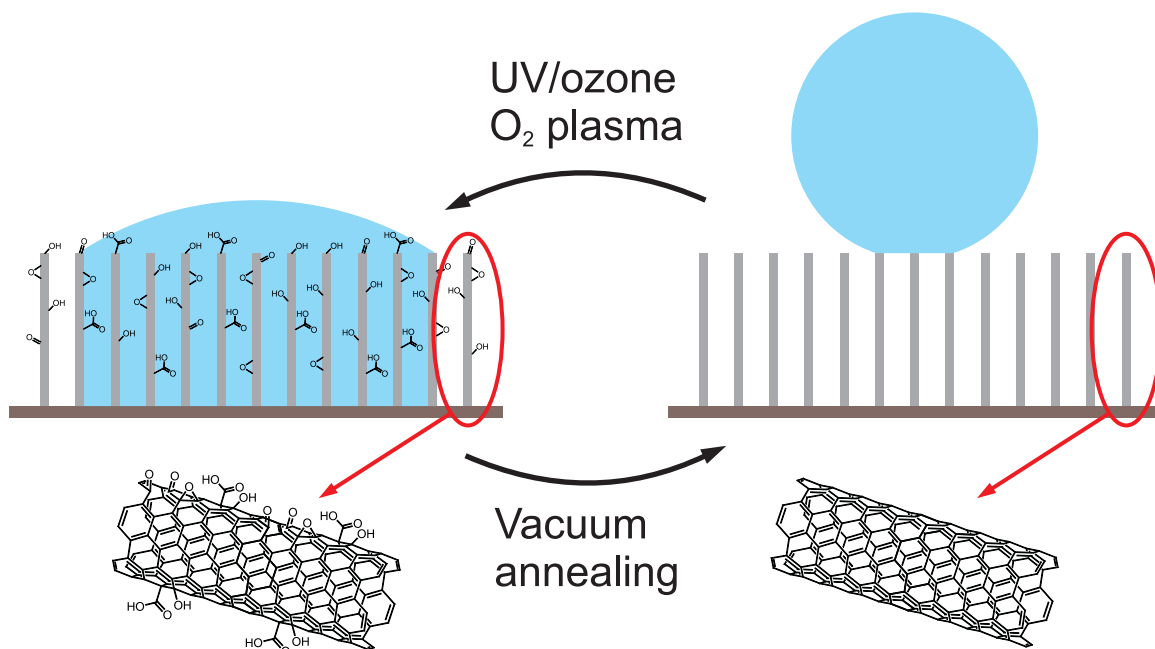


Figure 1.1. Use of UV/ozone, oxygen plasma, and vacuum annealing treatments to modify the surface chemistry of CNT arrays. This surface modification is ultimately used to control the wettability of CNT arrays.

layer capacitors has been previously explored, the study of the effect of oxidation on their capacitive behavior is novel.

### 1.3 Scope of Study

As mentioned earlier, the goal of this thesis is to control the wettability of CNT arrays by tuning the amount of oxygenated groups adsorbed on their surfaces. While the goal seems simple to state, this thesis can be extremely wide if the scope is not limited. The main reason for this is that because there are many different types of CNT arrays, each of them have unique physical characteristics and properties. These physical characteristics are results of permutations of the characteristics of individual CNT and the bulk characteristics of the array. The physical characteristics of individual CNT include the number of walls, inner and outer diameter, chirality, the shape of its graphitic structure, presence of metal catalyst, and presence of amorphous carbon. For example, based on the number of walls, CNT can be classified as single walled

CNT, double walled CNT, triple walled CNT, and multi walled CNT. The bulk physical characteristics of the array include length, inter-tube spacing, packing density, vertical alignment, entanglement, length, and presence of amorphous carbon. For instance, the packing density of CNT arrays may vary over five orders of magnitude between  $10^5 - 10^{11}$  CNTs/cm<sup>2</sup>.

Since, as mentioned above, there are many different types of CNT arrays, it is almost impossible to fully characterize the effect of oxidation on the wettability of each type of CNT arrays. Hence, the scope of this thesis is limited to a very specific type of CNT arrays. These CNT arrays comprise of multi-walled CNT with an outer diameter of 12-30 nm, a number of walls of 6-16, and are free of amorphous carbon. These CNT arrays have a length of 10  $\mu$ m-1 mm, inter-tube spacing of 60-80 nm, packing density of  $10^{10}$  CNT/cm<sup>2</sup>, and are free of amorphous carbon. Details about the physical characteristics of this specific type of carbon nanotube arrays can be read in Chapter 2.1.2.

It has to be noted that the results and findings presented in this thesis are only applicable to this specific type of carbon nanotube arrays. The dry oxidation and reduction processes used in this study may result in a completely different or even opposite behavior to other types of CNT arrays. Therefore, results and findings presented in this thesis should not be applied blindly to all types of CNT arrays without knowing their detailed physical characteristics.

The definition of wettability itself is also limited in this study. Normally, wetting is described as an interaction process when a liquid comes in close contact with a solid surface. The liquid itself can be anything, ranging from polar and non polar solvents, such as water and oil respectively, to molten salts and metals. Here, the liquid is restricted to water. Thus, in this study, wetting is strictly described as an interaction process when water comes in close contact with solid surfaces, which in this case is the surface of CNT arrays.

## 1.4 Thesis Outline

This thesis is divided into seven chapters and one appendix. The first two chapters cover the background of the study as well as all materials and experimental methods used in the study. The following four chapters are the essence of this thesis. Details about the effect of oxidation on the wettability and structure of CNT arrays, as well as the applications of CNT arrays with extreme wetting properties, are discussed in these chapters. The summary of all findings and suggestions for future works are presented in the last chapter. The appendix describes the effect of reversible dry oxidation on graphene. The outline of each chapter is described as follows:

**Chapter 1** In this chapter, the underlying problems that motivate this current study are presented. The background and the importance of this study are also explained. The objectives and scope of this current study are listed in detail in this chapter.

**Chapter 2** In this chapter, all materials and experimental methods used in this study are listed and presented. The first part of this chapter concerns the chemical vapor deposition technique that is used to fabricate CNT arrays. Typical characteristics of the CNT arrays grown using this technique are also explained. The second part of this chapter concerns the dry oxidation and reduction methods. Here, the dry oxidation process is performed using UV/ozone and oxygen plasma treatments, and the dry reduction process is performed using vacuum annealing treatment. The last part of this chapter concerns the characterization techniques that are commonly used in this study. Part of this chapter has been published in *Journal of Visualized Experiments*.<sup>1</sup>

**Chapter 3** In this chapter, the effect of dry oxidation and reduction to the wetting properties of CNT arrays are investigated. The correlation between wettability and the oxygen content of these CNT arrays is presented. The existence of an

---

<sup>1</sup>Aria, A.I. and Gharib, M., *Dry Oxidation and Vacuum Annealing treatments for Tuning the Wetting Properties of Carbon Nanotube Arrays*, *Journal of Visualized Experiments*, 2013, (74), e50378.

oxidation regime, where the effect of oxidation on the wettability of CNT arrays is reversible, is also explained. The wettability of CNT arrays is elucidated not only in terms of their contact angle, but also in terms of droplet impact behavior, dispersibility, and electrochemical characteristics. Part of this chapter has been published in Langmuir.<sup>2</sup>

**Chapter 4** In this chapter, the effect of oxidation on the structure of CNT arrays in the irreversible oxidation regime is explored. The structural evolution of CNT arrays as they undergo a prolonged exposure to dry oxidation process is presented by means of photoelectron spectroscopy and electron microscopy. Such evolution is then highlighted by observing the large scale change of morphology of CNT pillars. Part of this chapter is being prepared for publication in Carbon.<sup>3</sup>

**Chapter 5** In this chapter, the impact behavior of water droplets impinging on the surface of vacuum annealed CNT arrays is studied. These vacuum annealed CNT arrays exhibit superhydrophobic characteristics with an extremely high contact angle and a liquid-vapor-solid interface. The impact behavior of the droplet is presented in the form of four unique characteristics, which include critical Weber number, volume ratio, restitution coefficient, and spreading factor. Empirical approximation and interpretation of the experimental data are also presented. Part of this chapter is currently being reviewed in Experiment in Fluids.<sup>4</sup>

**Chapter 6** In this chapter, the use of oxidized CNT arrays as electrodes for supercapacitors is explored. The effect of oxidation to the capacitance of the CNT supercapacitors is investigated in both aqueous and non-aqueous electrolytes. The lifetime and performance of oxidized CNT supercapacitors in non-aqueous

---

<sup>2</sup>Aria, A.I. and Gharib, M., *Reversible Tuning of Wettability of Carbon Nanotube Arrays: The Effect of UV/Ozone and Vacuum Pyrolysis Treatments*, Langmuir, 2011, 27 (14), pp 9005-9011.

<sup>3</sup>Aria, A.I. and Gharib, M., *Functionalization, Etching, and Amorphization of Hollow CNT Pillars Induced by Oxygen Plasma Treatment*, Carbon, in preparation.

<sup>4</sup>Aria, A.I. and Gharib, M., *Water Droplet Impact Behavior on a Cassie State Nanostructured Superhydrophobic Surface*, Experiments in Fluids, 2013, under review.

electrolyte are also presented. Part of this chapter has been published in the Proceeding of the 11th IEEE Conference on Nanotechnology<sup>5</sup> and in Nanoelectronic Device Applications Handbook.<sup>6</sup>

**Chapter 7** In this chapter, the summary of all findings is reported. The outlook for future directions in this research area is also provided.

**Appendix A** In this appendix, the effect of reversible oxidation to the electronic properties of CVD graphene is investigated. The surface chemistry evolution of CVD graphene induced by cycles of dry oxidation and reduction is also presented. This study is placed in the appendix because it is not directly related to the wetting properties of CNT arrays, although the same exact method of oxidation and reduction is used. The results presented in this appendix can be related, to some extent, with the results presented in Chapter 4. Part of this chapter is currently being reviewed in the Journal of Physical Chemistry C.<sup>7</sup>

---

<sup>5</sup>Aria, A.I., Guittet, M., and Gharib, M., *Use of Vertically-Aligned Carbon Nanotube Array to Enhance the Performance of Electrochemical Capacitors*, Proceeding of the 11th IEEE Conference on Nanotechnology, 2011, 1944-9399, pp 80-85.

<sup>6</sup>Aria, A.I., Guittet, M., and Gharib, M., *Use of Vertically Aligned Carbon Nanotubes for Electrochemical Double Layer Capacitors*, Edited by Morris, J.E. and Iniewski, K., 2013, 9781466565234, CRC Press.

<sup>7</sup>A.I. Aria, A.W. Gani, and M. Gharib, *Effect of Dry Oxidation and Vacuum Annealing Cycles on the Evolution of Energy Gap and Chemistry of CVD Graphene on Nickel*, Journal of Physical Chemistry C, 2013, under review.

## Chapter 2

# Materials and Methods

### 2.1 Carbon Nanotubes Fabrication Method

Carbon nanotubes (CNTs), discovered for the first time by Iijima (1991), are graphite layers rolled into seamless concentric hollow cylinders with typical diameters of several nanometers. Similar to graphite, CNT structures are made of honeycomb-arranged carbon atoms arranged in  $sp^2$  hybridization. One unique feature of CNT, compared to other allotrope of carbon, is its extremely wide range of length. CNTs with lengths ranging from hundreds of nanometers to tens of centimeters have been reported (Li et al., 2006; Wang et al., 2009). In recent years, CNTs have attracted enormous attention due to their exceptional mechanical, electrical, and thermal properties. For instance, CNT is known to be one of the strongest materials, with an ultimate tensile strength of an order of magnitude higher than that of steel and other industrial fibers (Yu et al., 2000; Peng et al., 2008). CNT is also known to be a good electrical conductor, with a maximum current density of three orders of magnitude higher than that of copper (Wei et al., 2001; Hong and Myung, 2007). In addition, CNT is known to be a good thermal conductor, with a thermal conductivity similar to that of diamond (Pop et al., 2005). Because of their exceptional properties, CNTs are envisioned to be used in many future applications (De Volder et al., 2013).

Compared to other synthetic materials, fabrication of CNTs is relatively easy and well-known. There are several widely-known fabrication techniques that can be employed to grow CNTs, including arc discharge, laser ablation, high-pressure

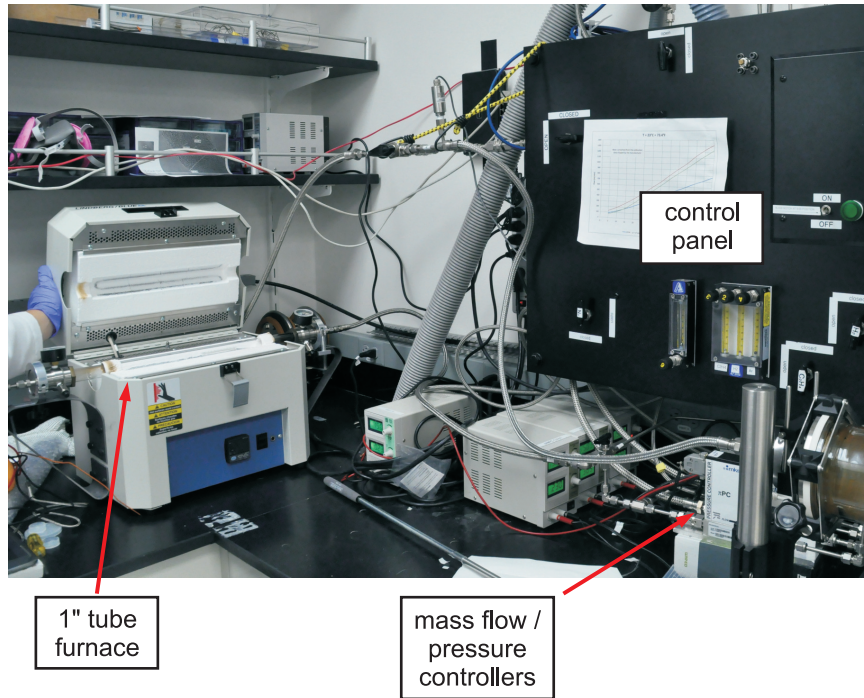


Figure 2.1. In house CVD reactor used for fabrication of CNT arrays.

carbon monoxide conversion (HiPCO), and chemical vapor deposition (CVD). Arc discharge is the most common technique used to fabricate CNTs, due to its simple fabrication method and high quality and purity results. However, it does not have the capability to produce large quantities of CNTs. To address this issue, HiPCO and laser ablation have been widely used for large-volume bulk production of CNTs. These techniques are known for their simplicity and high yields, however, these methods pose a common drawback: the CNT architectures fabricated by these methods are unorganized (De Volder et al., 2013). In other words, these methods can only be used to fabricate CNT powders but cannot be utilized to grow CNT arrays. Note that CNT arrays are densely packed CNTs grown in vertical alignment perpendicular to the growth substrate. Until now, CVD method is the only known method to grow CNT arrays.

### 2.1.1 CVD growth method

Vertically aligned CNT arrays are typically grown using the CVD technique inside a CVD reactor. There are many different variations of CVD reactors, including high pressure or low pressure CVD, hot wall or cold wall CVD, and many more. A high pressure CVD reactor utilizes a near-atmospheric pressure to achieve carbon saturation and CNT nucleation. In contrast, a low pressure CVD reactor allows CNT growth to be performed at a reduced pressure in the range of hundreds of mtorr. In a hot wall CVD reactor, both precursor gas and substrates are heated simultaneously inside a furnace. On the other hand, in a cold wall CVD reactor, the precursor gas is not heated inside the same furnace as the substrates. In fact, this gas may not need to be heated at all since a non-thermal source is used to initiate the gas dissociation. A cold wall CVD reactor is typically associated with plasma-assisted CVD because the dissociation of the precursor gas is not initiated thermally, but instead by plasma generated by RF coils at a frequency of several MHz.

All CNT arrays used in this study are grown in-house using a custom made hot wall thermal CVD reactor. This CVD reactor consists of two main parts: precursor delivery system and reaction chamber (Figure 2.1). Each part consists of several sub-systems that are assembled into one working system. The precursor delivery system for this in-house CVD reactor connects the precursor gas feedstock to the reaction chamber through a series of cleaned stainless steel swagelok tubing. The flow rate and pressure of the precursor gas are maintained by electronic mass flow controllers (MKS  $\pi$  MFC) and a pressure controller (MKS  $\pi$  PC). Here, these controllers are connected to a computer to allow precise and accurate control of the mass flow rate and pressure with a fast response time. The mass flow controllers are located upstream of the reaction chamber, while the pressure controller is located downstream of the reaction chamber. The downstream part of the pressure controller is connected to a vacuum pump (Leybold AMEB 90). CNT arrays are grown inside the reaction chamber of this in-house CVD reactor, which is made of a quartz tube with diameter of 1 inch and length of 24 inches. This quartz tube is housed inside a tube furnace

Table 2.1. List of materials and equipment used in the in-house CVD reactor.

Name	Company	Model number	Key parameter
Tube furnace	Lindberg Blue M - Thermo Scientific	Mini Mite TF- 55030A	D: 1 inch
Electronic mass flow controllers	MKS	PFC-50 MFC	0 - 1000 sccm
Electronic pressure controller	MKS	PC-90 PC	0 - 1000 torr
Vacuum pump	Leybold	AMEB 90	135 L / min
Quartz tube	MTI Corp.	EQ-QZTube- 25GE-610	OD: 1 inch, L: 24 inch
Hydrogen gas	Airgas	HY UHP200	99.999% purity
Ethylene gas	Matheson	G2250101	99.95% purity
Argon gas	Airgas	AR UHP200	99.999% purity

(Lindberg/BlueM Single-Zone Tube Furnace), capable of heating the reaction chamber up to 1100 °C. The temperature of the tube furnace is controlled electronically by the furnace's PID controller. Materials and equipments used in this in-house CVD reactor are listed in Table 2.1.

These CNT arrays are grown using a common CVD method on silicon wafer substrates. Prior to growth, these silicon wafers are coated with layers of support, buffer, and catalyst several nanometers thick. Acting as the support layer is 300nm silicon oxide layer. This layer can be grown thermally as native oxide or deposited using an electron beam evaporator. A 10 nm aluminum oxide layer and a 1 nm iron layer are used as the buffer and catalyst layers, respectively. These buffer and catalyst layers have to be deposited using an electron beam evaporator (Temescal BJD 1800 or CHA Industries Mk40) to ensure the correct thickness and coverage uniformity. Subsequent to the deposition of these layers, the silicon substrates are diced into smaller samples, typically 1x1 cm<sup>2</sup>. Materials and equipment used for substrate preparation and catalysts deposition are listed in Table 2.2.

Up to now, there are countless numbers of growth recipes that have been published for fabrication of CNT arrays, and each of them is different. Because of the uniqueness of each CVD reactor, none of these growth recipes can be used as is without any modification. The growth recipe used in this study is basically a modified version of previously published growth recipes (Bronikowski, 2006; Sansom et al., 2008). The growth recipe used in this study is divided into four periods: heating, sintering, growth, and cooling, and summarized in Table 2.3.

The CNT arrays fabrication process is started by placing several pieces of silicon substrates on a quartz boat inside the quartz reaction chamber. The reaction chamber is then evacuated of ambient air using vacuum until it reaches a pressure lower than 10 torr and purged with argon gas for several minutes. Subsequently, the temperature of the reaction chamber is increased to a temperature of 750°C at a heating rate of about 50°C/minute. During this heating period, argon gas is flowed into the reaction chamber at a flow rate of 500 sccm and a pressure of 600 torr. Once the temperature reaches 750°C, the flow of argon gas is reduced to a flow rate of 200 sccm and hydrogen

Table 2.2. List of materials and equipment used for substrate preparation and catalysts deposition.

Name	Company	Model number	Key parameter
Silicon wafer	El-Cat	2449	300nm polished thermal oxide layer
Iron pellets	Kurt J Lesker	EVMFE35EXEA	99.95% purity
Aluminum oxide pellets	Kurt J Lesker	EVMALO-1220B	99.99% purity
E-beam evaporator	CHA Industries	Mark 40	10 nm Al <sub>2</sub> O <sub>3</sub> and 1 nm Fe
E-beam evaporator	Temescal	BJD 1800	10 nm Al <sub>2</sub> O <sub>3</sub> and 1 nm Fe
Scriber breaker	Dynatex	GST-150	1 x 1 cm <sup>2</sup>

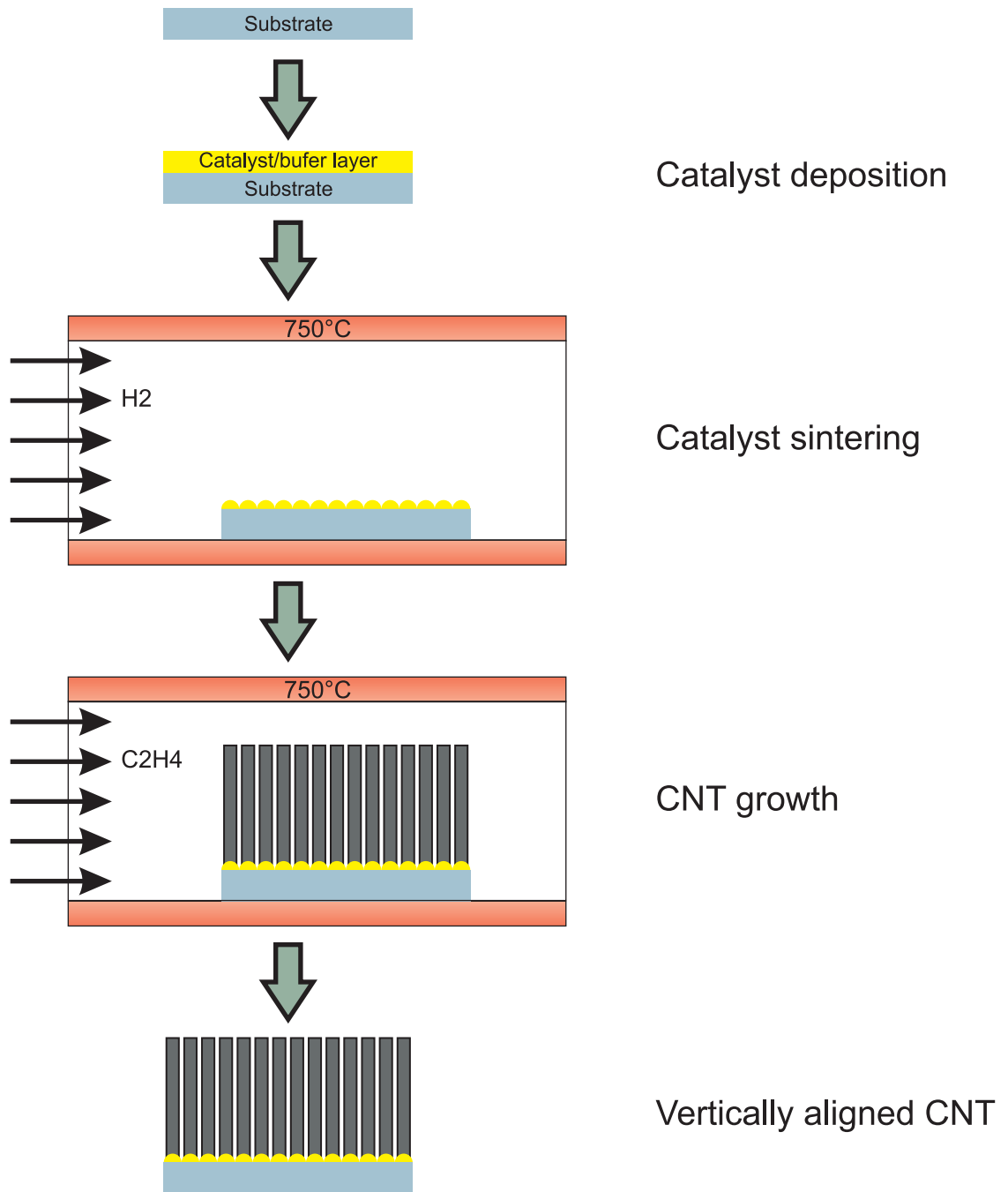


Figure 2.2. Schematic of CNT growth process using a common thermal chemical vapor deposition method.

gas is flowed simultaneously into the reaction chamber at a flow rate of 285 sccm. The pressure of the reaction chamber is maintained at 600 torr. During this period, the buffer and catalyst layers are reduced by the hot hydrogen gas and sintered into catalyst nanoparticles (Figure 2.2). These catalyst nanoparticles will later act as the nucleation sites for CNT growth during the growth period. This sintering period is considered as the most important part of the fabrication process and has to be performed for exactly five minutes to ensure the correct size, roughness, and distribution of these catalyst nanoparticles.

Subsequent to the sintering period, the flow of argon gas is completely shut off and the flow of hydrogen gas is reduced to a flow rate of 210 sccm. Ethylene gas is then flowed into the reaction chamber at a flow rate of 490 sccm. The pressure and temperature of the reaction chamber is maintained at 600 torr and 750 °C respectively. During this period, the catalyst nanoparticles are saturated with carbon, and CNTs start to nucleate and grow on them (Figure 2.2). Because of the tight distribution of the catalysts nanoparticles, CNTs are grown in a densely packed manner. Limitation of lateral space for CNTs to grow means that the growth in vertical direction is more preferable, resulting in vertically aligned, densely packed CNT arrays. The length of CNT arrays grown using this growth recipe can be varied between 10 $\mu$ m and 1 mm by controlling their growth time. Longer growth time results in longer CNT arrays. However, the growth rate is not linear but rather hyperbolic, with a maximum length of 1-1.2 mm. CNT arrays grow very quickly in the first couple of minutes and start to slow down afterwards. The growth process itself seems to be self-terminated after the CNT arrays reach an average length of 1-1.2 mm. Subsequent to the growth period, the flow of both ethylene and hydrogen gasses is shut off completely and the temperature of the reaction chamber is brought back to room temperature by turning off the furnace. This passive cooling allows the reaction chamber temperature to decrease at a rate of about 25°C/minute. During this cooling period, argon gas is flowed into the reaction chamber at a flow rate of 360 sccm. Once the temperature of the reaction chamber reaches room temperature, the flow of argon gas is shut off and ambient air is flowed into the reaction chamber. The vacuum pump is then turned

Table 2.3. CVD growth parameters.

Step	Parameters	Value
Heating	Pressure	600torr
	Temperature	room - 750°C
	Ar	500 sccm
	Heating rate	about 50°C / min
Sintering	Pressure	600torr
	Temperature	750°C
	Ar	200 sccm
	H2	285 sccm
	Pretreatment time	5 min
Growth	Pressure	600torr
	Temperature	750°C
	C2H4	490 sccm
	H2	210 sccm
	Growth time	5 - 60 min
Cooling	Pressure	600torr
	Temperature	750 C - room
	Ar	360 sccm
	Cooling rate	about 25°C / min

off and the pressure regulator is released to allow the pressure inside the reaction chamber to equilibrate with the ambient pressure. The grown CNT arrays can then be taken from the reaction chamber and are ready to be used.

### 2.1.2 Typical characteristics of CVD growth

As mentioned earlier, the abovementioned growth conditions result in vertically aligned CNT arrays. Depending on the growth time, the average length of these CNT arrays can be varied from 10  $\mu\text{m}$  (Figure 2.3.a) to 1 mm (Figure 2.3.b). The average length of the CNT arrays is measured using a scanning electron microscope (SEM). The high packing density of these CNT arrays and the presence of CNT entanglement at the top surface of their bulk structure can be observed at a smaller length scale using an SEM (Figure 2.5). These as-grown CNT arrays have a typical inter-nanotube spacing of 20-80 nm and a packing density of 120-180 CNT/ $\mu\text{m}^2$ . An ultra high magnification characterization using a transmission electron microscope (TEM) reveals the nanoscale feature of the individual CNT. Each CNT in the array is a multiwalled CNT, with a typical number of walls between 8-16 layers and a typical outer diameter of 16-25 nm (Figure 2.4).

In addition to their length, the quality of the growth is also examined using SEM. CNT arrays with excessive amount of amorphous carbon are rejected (Figure 2.6). CNT arrays with non-uniform growth are also rejected (Figure 2.7). These defective CNT arrays are not involved in all experiments performed in this study. A thick amorphous coating is often deposited onto the CNT arrays when the thickness of the catalyst layer is less or more than  $1(\pm)$  nm. On the other hand, a non-uniform CNT growth is typically a result of non-uniform deposition of the catalyst layer. Since the growth quality of CNT arrays is highly sensitive to the change in the catalyst layer, a lot of effort has to be spent to ensure the catalyst layer satisfies the requirement prior to the growth process.

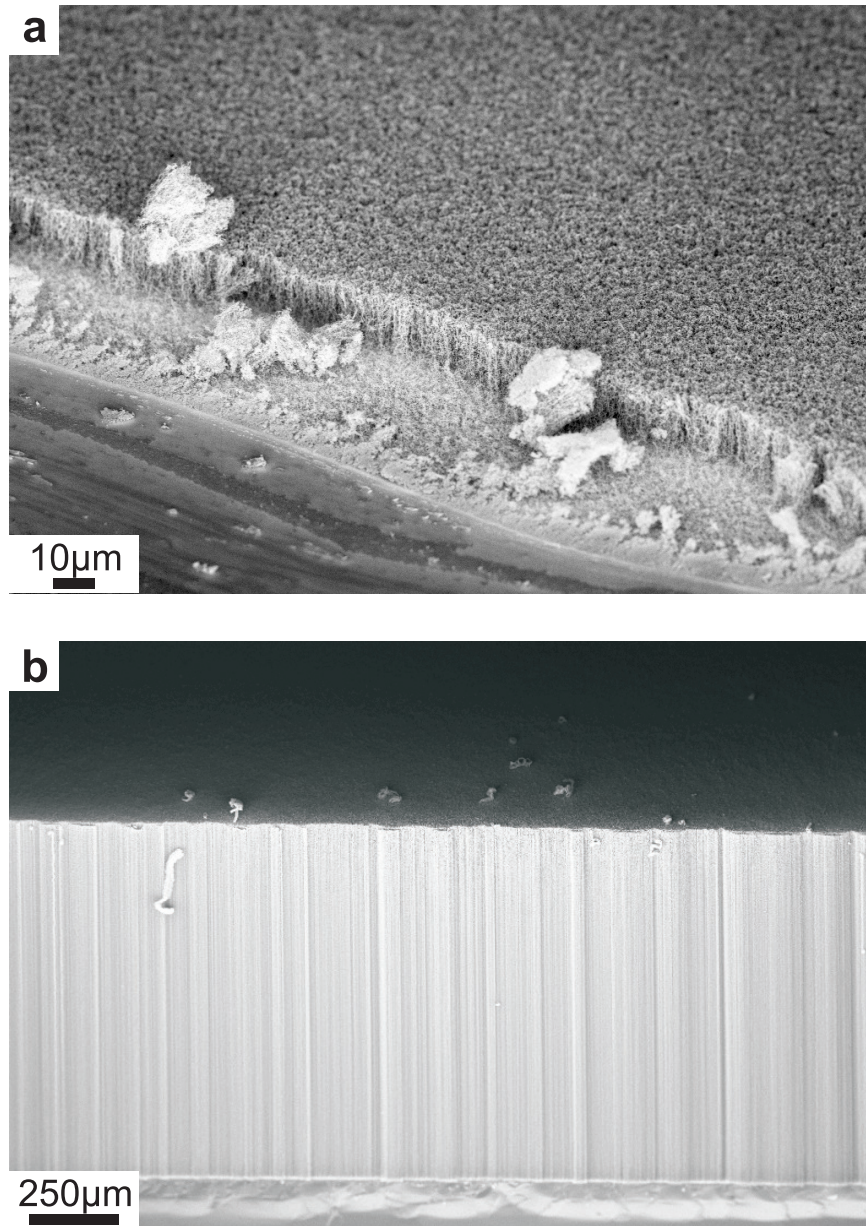


Figure 2.3. SEM images of CNT arrays with different lengths. The average length of CNT arrays can be varied from about 10  $\mu\text{m}$  (a) to about 1 mm (b).

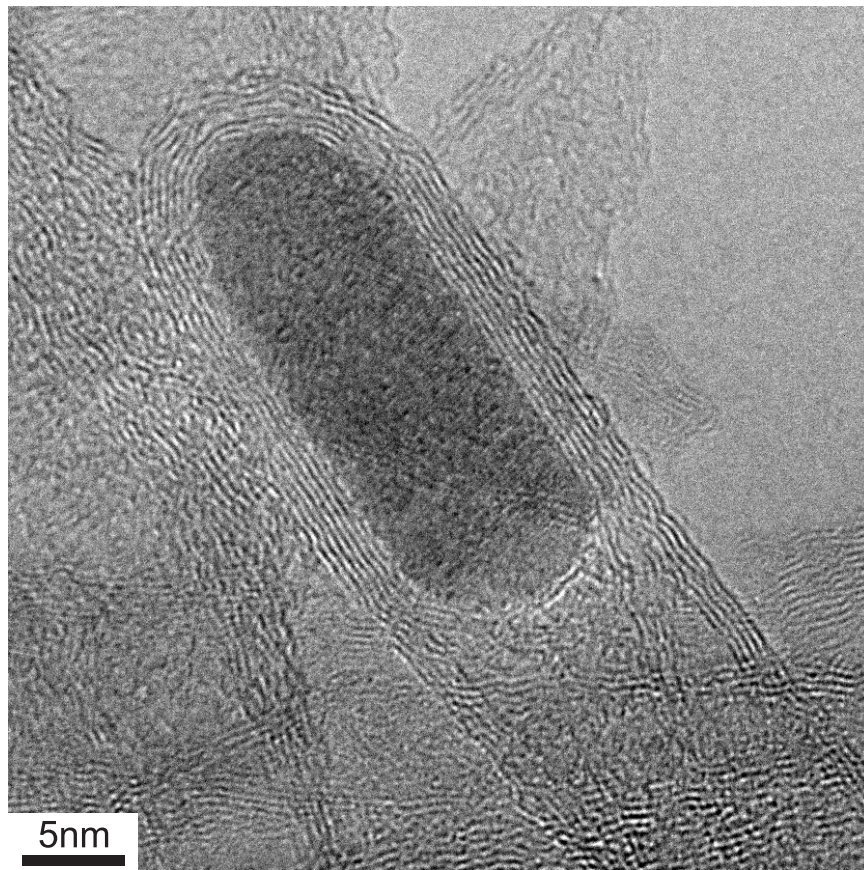


Figure 2.4. An ultra high magnification TEM image of a CNT showing its multi-walled and closed-cap characteristics. The trapped catalyst nanoparticles can be observed at the tip of this CNT.

Table 2.4. Typical CVD growth results.

Parameters	Value
Length	10 $\mu m$ - 1mm
Outer diameter	12 - 30 nm
number of walls	8 - 16
Packing density	120 - 180 CNT / $\mu m^2$

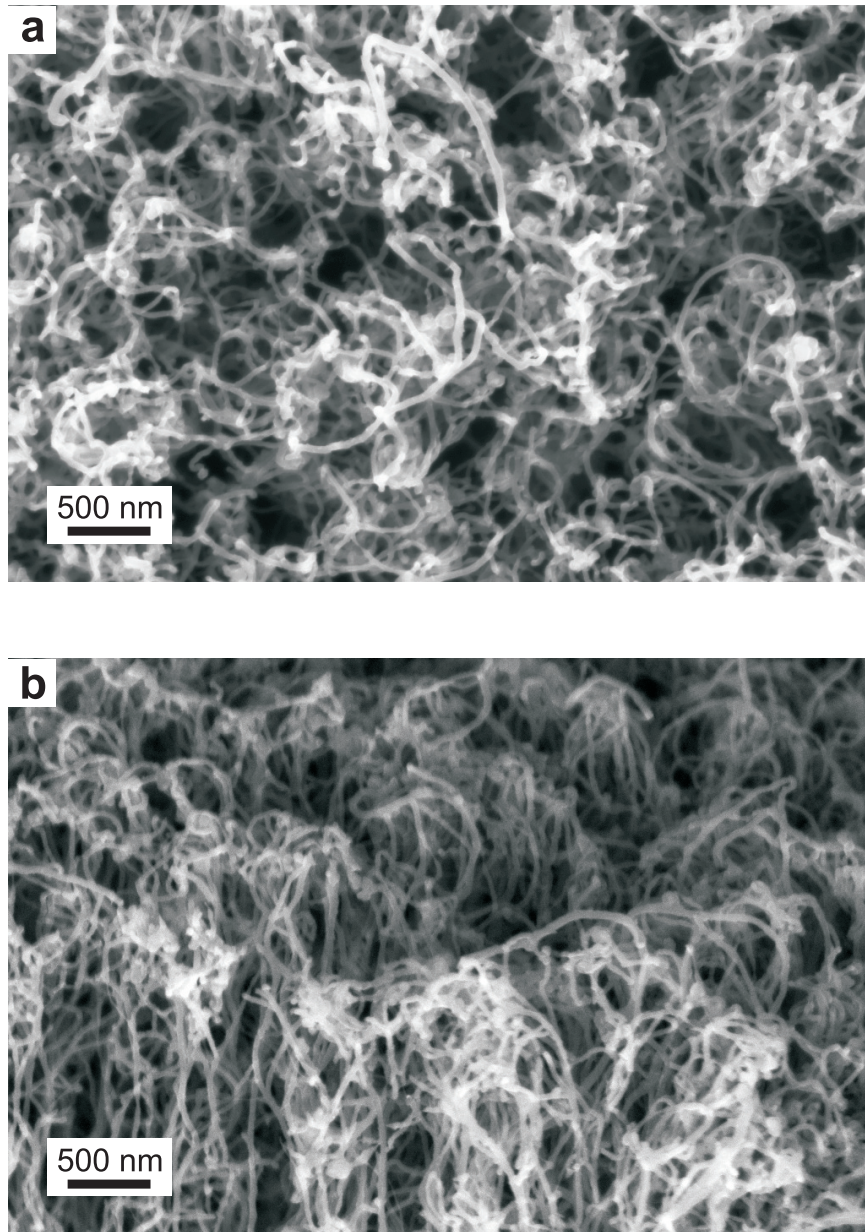


Figure 2.5. High magnification top view (a) and tilted view (b) SEM images of CNT arrays. These images show the high packing density of CNT arrays and presence of CNT entanglement at the top surface of their bulk structure.

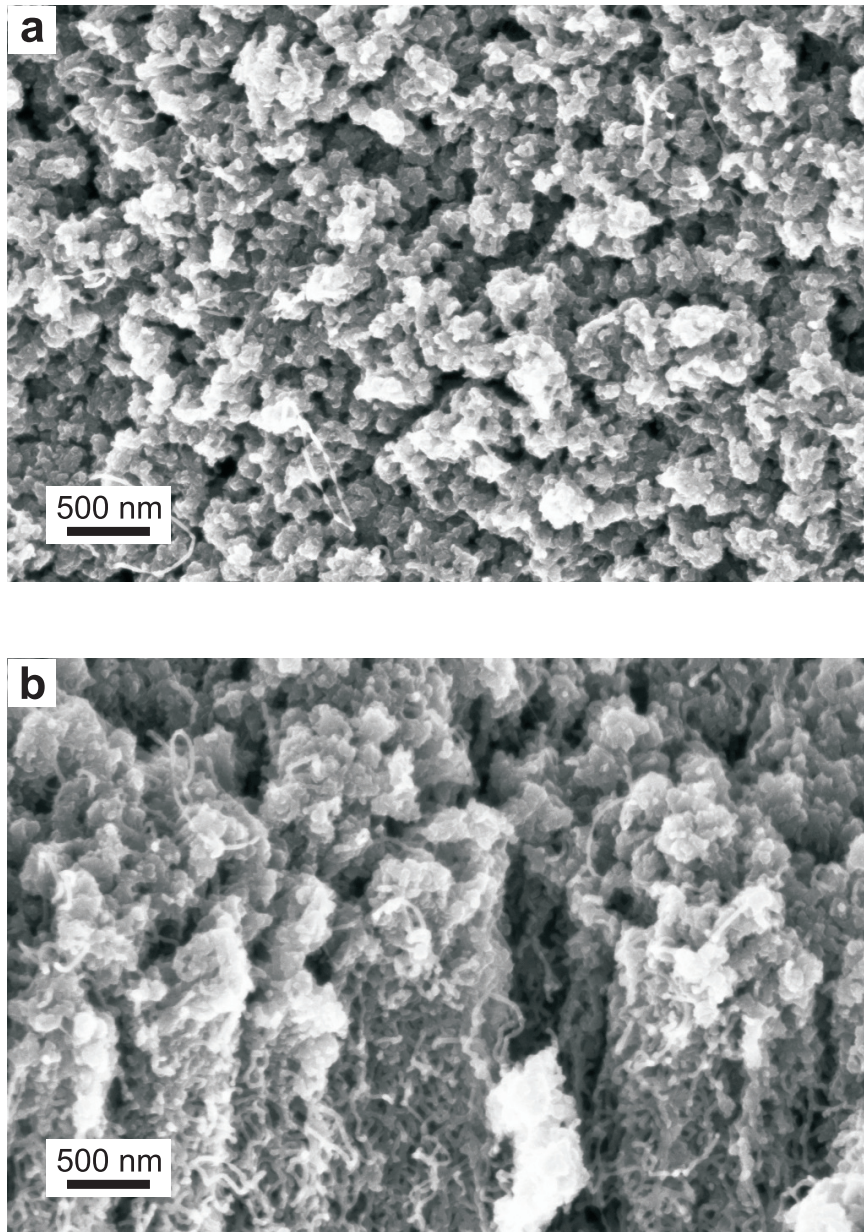


Figure 2.6. High magnification top view (a) and tilted view (b) SEM images of defectively grown CNT arrays. These CNT arrays are coated with a large amount of amorphous carbon.

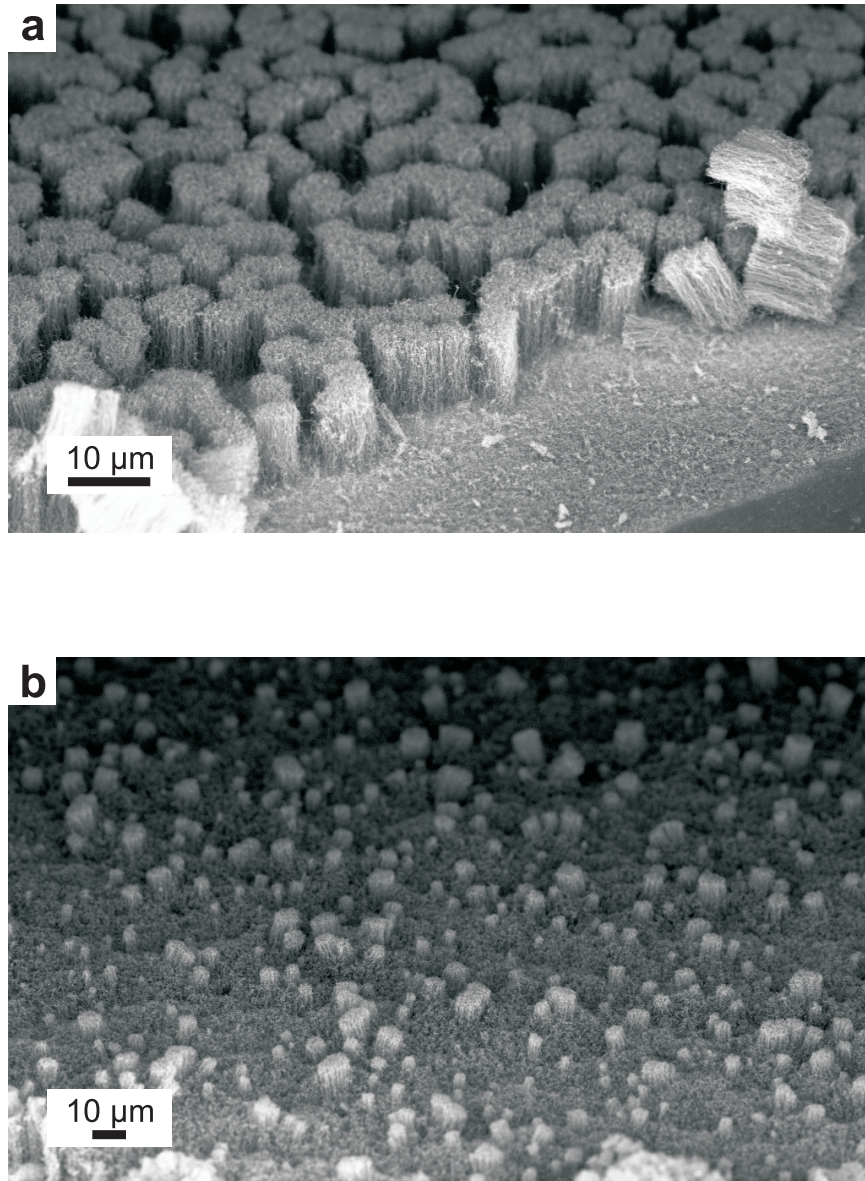


Figure 2.7. Tilted view SEM images of CNT arrays that are grown non-uniformly. Non-uniform growth results in CNT arrays that exhibit large scale voids (a) and macroscopic surface roughness (b).

## 2.2 Dry Oxidation and Reduction Process

The oxidation process of carbon-based bulk and nano structures has been well-studied, and its implementation in large-scale practical applications has been streamlined and engineered. Carbon-based bulk and nano structures are typically oxidized using liquid-phase oxidation methods such as the well-known Hummer's method (Hummers and Offeman, 1958), and its modified versions (Park and Ruoff, 2009; Li et al., 2008; Sun et al., 2008; Becerril et al., 2008; Marcano et al., 2010). Liquid-phase oxidations are carried out by exposing these carbon structures to strong acids and oxidants, including potassium chlorate ( $\text{KClO}_3$ ), potassium permanganate ( $\text{KMnO}_4$ ), sodium nitrate ( $\text{NaNO}_3$ ), phosphoric acid ( $\text{H}_3\text{PO}_4$ ), nitric acid ( $\text{HNO}_3$ ) and sulfuric acid ( $\text{H}_2\text{SO}_4$ ). It is important to note that, in addition to the highly corrosive nature of these chemicals, the oxidation processes usually involve the generation of toxic and explosive gasses (Marcano et al., 2010). Liquid-phase oxidations are also considered impractical for oxidizing carbon-based nano structures, because of the difficulties involved during the acids and oxidants removal and subsequent drying processes. Often, freeze drying or critical point drying methods have to be used to prevent the collapse of nano structures by the capillary forces of these liquid chemicals.

Gas-phase oxidations, also known as dry oxidation, are more favorable as use for oxidizing carbon-based bulk and nano structures. Gas-phase oxidations are typically performed using molecular oxygen ( $\text{O}_2$ ) or carbon dioxide ( $\text{CO}_2$ ) gas, that is dissociated when it is flowed through a hot filament or a coil of RF plasma generator. Gas-phase oxidations can also be performed using ozone ( $\text{O}_3$ ) at room temperature, or water vapor ( $\text{H}_2\text{O}$ ) at an elevated temperature. These oxidation techniques are considered safer, more convenient, and more practical (especially in large industrial-scale production) than the liquid-phase oxidation techniques. In addition, the gas-phase oxidation methods allow site-specific oxidation through the use of sacrificial layer masking, making them compatible with current microfabrication processes.

Similarly, the reduction process of carbon-based bulk and nano structures has been well-studied, and its implementation in large-scale practical applications has been

Table 2.5. Wet chemical modification vs. dry chemical modification.

Methods	Advantage	Disadvantage
<b>Wet oxidation</b>		
H <sub>2</sub> SO <sub>4</sub> + H <sub>2</sub> O <sub>2</sub> , HNO <sub>3</sub> + HCl	well-known process, commonly used in large scale industry	corrosive, slow oxidation rate, oxidation process is difficult to control, bulk structure cannot be preserved, need freeze drying or critical point drying
<b>Wet reduction</b>		
N <sub>2</sub> H <sub>4</sub> , LiAlH <sub>4</sub>	well-known process, commonly used in large scale industry	corrosive, toxic and explosive vapor, reduction process is difficult to control, bulk structure cannot be preserved, need freeze drying or critical point drying
<b>Dry oxidation</b>		
UV/ozone	safe, convenient, gentle, cheap, high degree of control, no risk of overoxidation, bulk structure is preserved	slow oxidation rate
O <sub>2</sub> plasma	safe, convenient, fast oxidation rate, bulk structure is preserved	more expensive, higher risk of overoxidation
<b>Dry reduction</b>		
Vacuum annealing	safe, convenient, gentle, cheap, high degree of control, bulk structure is preserved	slow reduction rate
H <sub>2</sub> plasma	convenient, fast reduction rate, bulk structure is preserved	more expensive, explosive gas, high risk of hydrogenation

Table 2.6. Dry oxidation and reduction parameters.

Process	Parameters	Value
UV/ozone	Pressure	room
	Temperature	room
	UV source	285nm
	UV power density	100mW / cm <sup>2</sup>
	Exposure time	0-120 min
O <sub>2</sub> plasma	Pressure	500 mtorr
	Temperature	room
	O <sub>2</sub> flow rate	150 sccm
	RF power	50 watt
	Exposure time	0-30 min
Vacuum annealing	Pressure	2 - 5 torr
	Temperature	250°C
	Exposure time	0-120 hour

streamlined and engineered. Carbon-based bulk and nano structures are typically reduced using liquid-phase reduction methods by exposing these carbon structures to strong reducers, including hydrazine ( $N_2H_4$ ), hypophosphorous acid ( $H_3PO_2$ ), and solution of lithium aluminum hydride ( $LiAlH_4$ ). Similar to the chemicals involved in liquid-phase oxidation methods, these chemicals are highly corrosive, and the reduction processes often involve the generation of toxic and explosive gasses (Marcano et al., 2010). Liquid-phase reductions are also considered impractical for reducing carbon-based nano structures because of the difficulties involved during the reducing agents removal and subsequent drying processes. Freeze drying or critical point drying methods are often necessary to prevent the collapse of nano structures by the capillary forces of these liquid chemicals.

Gas-phase reduction is more favorable for use in reducing carbon-based bulk and nano structures. Gas-phase reductions are typically performed using molecular hydrogen ( $H_2$ ), carbon monoxide ( $CO$ ), or diborane ( $B_2H_6$ ) gas, that is dissociated when it is flowed through a hot filament or a coil of RF plasma generator. However, these gasses are notoriously known as highly toxic and explosive gasses. One known technique to overcome these problems is the utilization of vacuum annealing treatment for reducing carbon-based bulk and nano structures. Vacuum annealing treatment is typically employed to induce oxygen desorption process without using any harsh reducing agents.

### **2.2.1 Oxygen Plasma and UV/Ozone Treatment**

In this study, the dry oxidation methods are performed using UV/ozone and oxygen plasma treatments. UV/ozone treatment is considered as the most convenient oxidation technique because it can be performed in air at a standard room temperature and pressure for up to several hours, depending on the length of the CNT array and the power of the UV radiation. UV radiation, generated by a high intensity mercury vapor lamp at 185 nm and 254 nm, breaks the molecular bonds on the outer wall of CNT allowing ozone, converted simultaneously from air by UV radiation, to oxidize

their surface (Mawhinney et al., 2000; Sham and Kim, 2006). The oxidation process ceases once the CNT surfaces are fully functionalized, preventing the CNT from being overoxidized. Over-oxidation of CNT ultimately results in the decomposition of CNT into CO and CO<sub>2</sub> molecules.

In contrast, oxygen plasma treatment has to be performed in a special chamber at a reduced pressure and a constant oxygen flow rate. Typically, oxygen plasma is generated remotely under 50 Watts of RF power and delivered at a constant flow rate of 150 SCCM and a chamber pressure of 500 mTorr for several minutes. Although oxygen plasma treatment allows a much faster oxidation process, care has to be taken because it is very capable of completely oxidizing the CNT into CO and CO<sub>2</sub> molecules.

UV/ozone and oxygen plasma treatments have been successfully employed to functionalize the surface of CNT with oxygenated functional groups (Mawhinney et al., 2000; Sham and Kim, 2006; Banerjee and Wong, 2002; Xu et al., 2007; Felten et al., 2005; Chen et al., 2009). However, none of these published methods have been performed previously on CNT arrays. Although the oxidation method described herein is similar to these published methods, it is optimized for CNT arrays, not CNT powders. This current method utilizes low UV lamp irradiation power and plasma generator power to keep the oxygen adsorption rate low. Such low oxygen adsorption rate is essential to ensure that the functionalization process occurs uniformly across the CNT array sample without damaging them. Therefore, the oxidation time for CNT arrays is typically longer than that for CNT powders.

To induce oxygen adsorption by UV/ozone treatment, several samples of CNT arrays are placed under a high-intensity mercury vapor lamp that generates UV radiation at a wavelength of 185 nm and 254 nm. These samples need to be placed at a distance of 5-20 cm from the lamp. A commercial UV/ozone cleaner (Bioforce nanosciences UV/ozone procleaner plus) can be used as an alternative. Expose these CNT arrays to UV radiation in air at standard room temperature and pressure. The total exposure time depends on their physical properties, the power of UV radiation, and the degree of wettability that needs to be achieved. As an approximation, it takes

Table 2.7. List of equipment used for dry oxidation and vacuum annealing.

Name	Company	Model number
UV/ozone	Bioforce nanosciences	UV/Ozone procleaner plus
Oxygen plasma	Tepla	M4L
Vacuum annealing	VWR	Signature vacuum oven

about 30 minutes of UV irradiation using a commercial UV/ozone cleaner to completely switch 15  $\mu\text{m}$  tall CNT arrays from superhydrophobic to superhydrophilic. Re-expose these CNT arrays to another round of UV/ozone treatment to increase their hydrophilicity. Detailed parameters of UV/ozone treatment can be read in Table 2.6.

To induce oxygen adsorption by oxygen plasma treatment, several samples of CNT arrays are placed in the chamber of an oxygen plasma cleaner/asher/etcher. A remote oxygen plasma cleaner/asher/etcher (Tepla M4L) is preferable than the direct one because of its isotropic nature. Set the oxygen flow rate to 150 sccm and the chamber pressure to 500 mTorr. Set the RF power to 50 Watts. Expose these arrays to oxygen plasma for several minutes. The total exposure time depends on their physical properties and the degree of wettability that needs to be achieved. Care has to be taken because oxygen plasma is very capable of completely oxidizing the CNT into CO and CO<sub>2</sub> molecules. As an approximation, it should take less than 10 minutes to completely switch 150  $\mu\text{m}$  tall CNT arrays from superhydrophobic to superhydrophilic. Re-expose these CNT arrays to another round of oxygen plasma treatment to increase their hydrophilicity. Detailed parameters of UV/ozone treatment can be read in Table 2.6.

## 2.2.2 Vacuum Annealing

To induce oxygen desorption by vacuum annealing treatment, several samples of CNT arrays are placed in the chamber of a vacuum oven (VWR Signature vacuum oven). Reduce the chamber pressure to at least 2.5 Torr and increase the chamber temperature to 250°C or higher. Expose these CNT arrays to vacuum annealing treatment for several hours. The total exposure time depends on their physical properties and the degree of wettability that needs to be achieved. As an approximation, it takes at least six hours to switch 15  $\mu\text{m}$  tall CNT arrays from mildly hydrophilic to superhydrophobic, and more than 24 hours to convert 650  $\mu\text{m}$  tall CNT array from mildly hydrophobic to superhydrophobic. Re-expose these CNT arrays to another round of vacuum annealing treatment to increase their hydrophobicity. Detailed parameters of vacuum annealing treatment can be read in Table 2.6.

## 2.3 Characterization Methods

### 2.3.1 Scanning Electron Microscopy

Scanning electron microscopy is performed using a field emission scanning electron microscope (Zeiss 1550 VP). High magnification imaging is performed under backscattered electrons mode with acceleration voltage of 5-10 kV. Low magnification imaging is performed under secondary electrons mode with acceleration voltage of 2-5 kV. Prior to imaging, all CNT array samples are mounted on aluminum stubs using conductive carbon or copper tape. CNT arrays with low oxygen content are conductive enough such that they are imaged without any metal coating. CNT arrays with high oxygen content are imaged after they are coated with a thin layer of metal. Typically a 10 nm layer of palladium or palladium/platinum alloy is coated onto the sample using sputter coater. All wet samples are dried under vacuum for more than 12 hours prior to metal coating.

Table 2.8. List of equipment used for characterization.

Name	Company	Model number	Key parameter
Scanning electron microscope	Zeiss	1550 VP	Backscattered electrons at 5-10 kV, secondary electrons at 2-5 kV
Transmission electron microscope	FEI	TF30UT	Forward scattered electrons at 300 kV
Contact angle goniometer	rame-hart	Model 190	Water droplet volume of 5 - 25 $\mu\text{L}$
Raman spectrometer	Renishaw	M1000	Excitation energy at 2.41 eV
Fourier transform infra red spectrometer	Nicolet	6700	Wavenumber range of 600 - 2000 $\text{cm}^{-1}$
Xray photoelectron spectrometer	Surface science	M-Probe	Binding energy range of 0 - 1000 eV
Electrochemical impedance spectrometer	Biologic	SP-200	Frequency range 10 mHz - 5 MHz

### 2.3.2 Transmission Electron Microscopy

Transmission electron microscopy is performed using a high performance transmission electron microscope (FEI Tecnai F30UT). All images are taken under forward scattered electrons mode with acceleration voltage of 300 kV. Selected area diffraction patterns (SADP) are also collected from each set of CNT to verify their crystalline structure. Prior to imaging, a small amount of sample is collected from the CNT arrays by scraping them physically with tweezers or razor blades. These CNT samples are then dispersed in DI water with the help of ultrasonication for about 5-15 minutes. For CNT samples that are difficult to disperse, 200 proof ethanol is used as the solvent, replacing the DI water. Subsequently, a small amount of the dispersion is pipetted while the dispersion is still homogeneous. This pipetted dispersion is then dropped on a holey carbon TEM grid (EMS CF213) and dried in ambient air. After the solvent is fully evaporated, this TEM grid is mounted into the TEM.

### 2.3.3 Contact Angle

In this thesis, the wettability of CNT arrays is mainly quantified by their static contact angle. All contact angle measurements are conducted using a contact angle goniometer at standard room pressure and temperature. Samples of CNT arrays are placed on the contact angle goniometer sample table. This sample table has to be perfectly level and not tilted toward one direction. A 5 $\mu$ L deionized water droplet was dispensed slowly on the top surface of each CNT array using a 5 $\mu$ L syringe (Hamilton 7105KH) equipped with a 31 gauge flat-tipped needle (Hamilton KF731). Once a water droplet has come to rest on the surface of the CNT array, images of the water droplet are then taken 10 seconds afterwards to ensure the equilibrium condition was achieved and to avoid the excessive evaporation of the droplet. The contact angles are then measured by processing the captured images with LBADSA software (Stalder et al., 2006).

### **2.3.4 Raman Spectroscopy**

Raman spectroscopy characterization is performed using micro Raman spectrometer system (Renishaw M1000) equipped with an Ar ion laser at an excitation wave length of 514.5 nm. Each CNT array sample is characterized as is without prior sample preparation. Each sample is then placed on the sample table of the optical microscope attached to the Raman spectrometer system. Raman spectroscopy characterizations are performed at an optical magnification of 50x or 100x in a non-polarized mode.

### **2.3.5 Fourier Transform Infra Red Spectroscopy**

Fourier Transform Infra Red (FTIR) spectroscopy characterization is performed using an infrared spectrometer (Nicolet 6700) equipped with liquid nitrogen cooled mercury cadmium telluride (MCT) detector. Prior to characterization, a small amount of sample is collected from the CNT arrays by scraping them physically with tweezers or razor blades. These CNT samples are then dispersed in deuterated dichloromethane (Sigma-Aldrich, 99.9 % atom) with the help of ultrasonication for about 5-15 minutes. Subsequently, this dispersion is quickly drop-cast onto an IR transmitting KBr window while the dispersion is still homogeneous. A second KBr window is then placed on top, sandwiching the CNT between two KBr windows. These KBR windows are then turned for a quarter of a rotation and pressed against each other to obtain an even film. This KBr-CNT sandwich is dried overnight under low vacuum (10 Torr) prior to characterization to remove the solvent leftover. A pair of blank KBr windows are used as a baseline correction.

### **2.3.6 X-ray Photoelectron Spectroscopy**

In this study, surface chemistry characterizations are typically assessed using x-ray photoelectron spectroscopy (Surface Science M-Probe XPS). A monochromatic 1486.6eV Al  $K\alpha$  is used as the x-ray source and is directed at an angle of  $35^\circ$  to the sample surface. The emitted photoelectrons are collected by a hemispherical analyzer positioned at an angle of  $35^\circ$  to the sample surface. The oxygen to carbon

atomic ratio (O/C ratio) is calculated from low resolution survey spectra acquired at a binding energy of 1-1000eV, with a resolution of 1eV and a spot size of 800  $\mu\text{m}$ . Higher resolution detailed scans are collected in C 1s region with a resolution of 0.065eV and a spot size of 100  $\mu\text{m}$ . The C 1s spectra are acquired at a binding energy of 280-294 eV. Multiple low resolution survey spectra and high resolution C 1s spectra are collected from different regions of each CNT array sample. During the data collection, the sample chamber is maintained at an ultra high vacuum condition with a base pressure below  $5 \times 10^{-9}$  torr. All photoelectron spectra are obtained using ESCA25 Capture software (Service Physics, V5.01.04), and analyzed using CasaXPS software (Casa Software Ltd, V2.3.15). Deconvolution of the C 1s high resolution spectra are performed using a Gaussian-Lorentzian peak shape fitting with Shirley baseline correction.

### **2.3.7 Cyclic Voltammetry, Galvanostatic Charge-Discharge Cycle, and Electrochemical Impedance Spectroscopy**

Electrochemical impedance spectroscopy characterization is conducted in three-electrode configuration using a potentiostat (Biologic SP-200) at a frequency of 10 mHz - 7 MHz. The CNT arrays are set as the working electrode, a platinum wire is used as the counter electrode, and a saturated calomel electrode is used as the reference electrode. For cyclic voltammetry and galvanostatic charge-discharge cycle characterizations, a two electrodes configuration is used. In a two electrodes configuration, CNT arrays serve as both anode and cathode. A separator film is then sandwiched between the anode and cathode to prevent direct electrical contact between them.

## Chapter 3

# Evolution of Wettability and Surface Chemistry of Carbon Nanotube Arrays

### 3.1 Introduction

For years, vertically aligned carbon nanotube (CNT) arrays have attracted enormous attentions to be used as a hydrophobic or hydrophilic surface due to their promising physical characteristics. Their inherent hydrophobic nature and two-length scale topographic structure make them an ideal hydrophobic surface. On the other hand, their extremely high surface-to-volume ratio make them an ideal hydrophilic surface. Because of these potentials, the ability to switch and tune the wettability of CNT arrays has been considered critical.

The findings presented in this chapter show that the bulk wettability of CNT arrays can be tuned straightforwardly via a combination of UV/ozone and vacuum annealing treatments. UV/ozone treatment is a well known dry-oxidation process to functionalize the surface of CNT with oxygenated functional groups at standard room temperature and pressure (Banerjee and Wong, 2002). Basically, UV radiation attacks the end caps and outer sidewall of the nanotubes, allowing ozone to oxidize their surface defect sites (Mawhinney et al., 2000; Sham and Kim, 2006). Vacuum annealing treatment was used to reverse the effect of oxidation by removing these groups from the surface of nanotubes, while keeping the microscopic structure of the array intact.

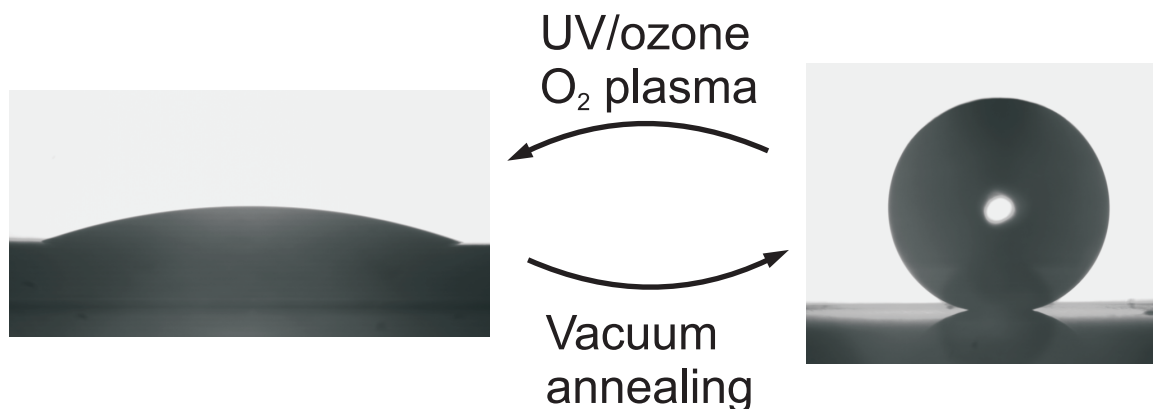


Figure 3.1. Changes in wettability of carbon nanotube arrays induced by dry oxidation and vacuum annealing.

Typically, a vacuum annealing treatment performed at a mild vacuum and a moderate temperature is sufficient to deoxidize the array. Using these treatments, the amount of oxygenated functional groups can be controlled carefully such that the CNT arrays can be repeatedly switched between hydrophilic and hydrophobic (Figure 3.1).

## 3.2 Materials and Methods

In this study, the wettability of multiple sets of CNT arrays with various degrees of oxidation are examined. Four steps of analysis were performed to elucidate the underlying principles that control the wettability of CNT arrays. The oxidation level of the CNT arrays is increased and decreased by exposing them to a longer period of UV/ozone or oxygen plasma treatment and vacuum annealing treatment, respectively. Three sets of as-grown CNT arrays with different heights were oxidized using UV/ozone treatment for up to 20 minutes. These CNT arrays have an average height of  $15\mu$ ,  $100\mu$ , and  $600\mu$ . Three other sets of as-grown CNT arrays with different heights were oxidized using oxygen plasma treatment for up to 120 minutes. These CNT arrays have an average height of  $50\mu$ ,  $150\mu$ , and  $650\mu$ . Additionally, three sets of oxidized CNT arrays with different heights were reduced using vacuum annealing treatment for up to 36 hours. The oxidized CNT arrays used in vacuum annealing studies have been previously oxidized using oxygen plasma or UV/ozone treatment

for five minutes. The detailed methods for UV/ozone and oxygen plasma treatments can be read in Chapter 2.2.1, and those for vacuum annealing treatment can be read in Chapter 2.2.2.

The wettability of the oxidized and reduced CNT arrays is quantified by their static contact angle for water. All static contact angle measurements are measured using DI water with contact angle goniometer at room pressure and temperature. The detailed methods for static contact angle measurements can be read in Chapter 2.3.3. The degree of oxidation of the oxidized and reduced CNT arrays is quantified by their oxygen/carbon atomic ratio (O/C ratio). The oxygen and carbon atomic contents of the CNT arrays are measured using X-ray photoelectron spectroscopy (XPS). The O/C ratio is then calculated from low resolution XPS survey spectra acquired at a binding energy of 1-1000eV with a resolution of 1eV. The detailed methods for O/C ratio measurements can be read in Chapter 2.3.6.

For the first step of analysis, the wettability of the oxidized and reduced CNT arrays is characterized by plotting their contact angle against the exposure time of UV/ozone, oxygen plasma, and vacuum annealing treatments. Similarly, the oxygen content of the CNT arrays is characterized by plotting their O/C ratio of the CNT arrays against the exposure time of UV/ozone, oxygen plasma, and vacuum annealing treatments. A direct correlation between the wettability of the CNT arrays and their oxygen content is then shown by plotting their contact angle against their O/C ratio.

For the second step of analysis, the surface chemistry of the dry oxidized and vacuum annealed CNT arrays is characterized using FTIR and high resolution XPS. Both FTIR and high resolution XPS characterizations are performed to highlight the effect of oxygenated functional groups on the wettability of CNT arrays. The FTIR spectra are obtained at a wavenumber of 600-1900  $\text{cm}^{-1}$ , and the high resolution XPS spectra are obtained at C1s binding energy of 280-298eV. The detailed methods for FTIR and XPS characterization can be read in Chapter 2.3.5 and Chapter 2.3.6, respectively.

For the third step of analysis, the dispersibility of the dry oxidized and vacuum annealed CNT arrays are characterized. The dispersion is characterized qualitatively

and quantitatively by visual observation and zeta potential measurement respectively. For both characterizations, a small portion of dry oxidized or vacuum annealed CNT array is scrapped from its growth substrates and dispersed in DI water for one hour by ultrasonication. A small portion of the dispersion was used for the zeta potential measurement while the rest were then left untouched for more than two months to assess their stability.

For the last step of analysis, the electrochemical properties of the dry oxidized and vacuum annealed CNT arrays are characterized. These electrochemical properties are characterized in terms of impedance and its components by means of electrochemical impedance spectroscopy (EIS) in 1M NaCl. The detailed methods for EIS characterization can be read in chapter 2.3.7.

## 3.3 Results and Discussion

### 3.3.1 Contact angle vs. exposure time

As expected, the as-grown CNT arrays are found to be highly hydrophobic with static contact angle of 140-150°. These CNT arrays become less hydrophobic as the CNT arrays are exposed to UV/ozone treatment. Indeed, after just 15 minutes of UV/ozone exposure, these CNT arrays have turned hydrophilic, which is indicated by their static contact angle of less than 90° (Figure 3.2). Their static contact angle decreases even further as they are exposed to a prolonged UV/ozone treatment. For example, after being exposed to 60 minutes of UV/ozone treatment, the static contact angle of 100 $\mu$ m and 600 $\mu$ m tall as-grown CNT arrays decreases to about 20° and 40°, respectively.

In general, the static contact angle of the UV/ozone treated CNT arrays decreases monotonically as the increase of UV/ozone exposure time, and the decrease rate is dependent on the length of the array. Shorter CNT arrays exhibit a higher static contact angle decrease rate while longer CNT arrays exhibit a lower decrease rate. As-grown CNT arrays with an average height of 15 $\mu$ m can be completely turned

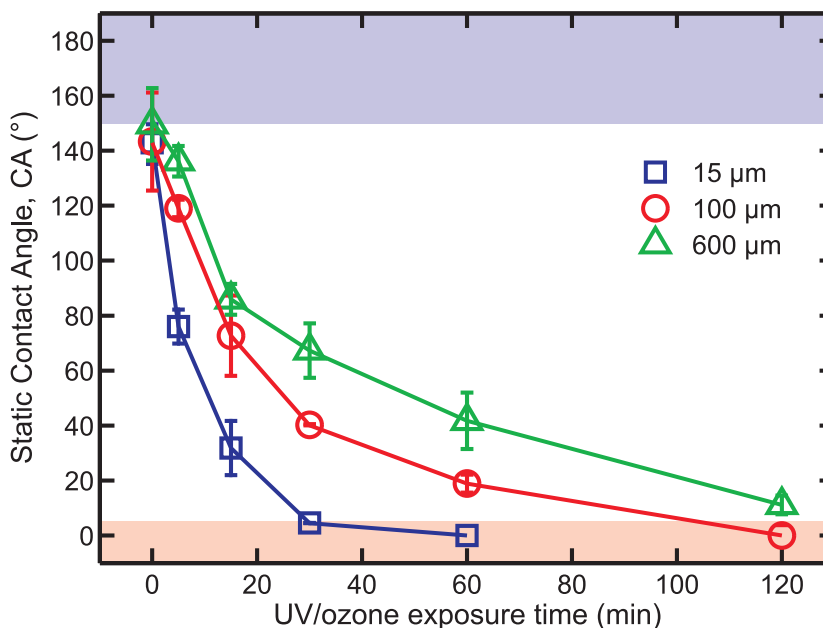


Figure 3.2. Plot of static contact angle of CNT arrays with different lengths as a function of UV/ozone exposure time.

superhydrophilic by just 30 minutes of UV/ozone treatment. On the other hand, 30 minutes of UV/ozone treatment only decrease the static contact angle to about  $40^{\circ}$  and  $70^{\circ}$  for  $100\mu\text{m}$  and  $600\mu\text{m}$  tall as-grown CNT arrays, respectively. In fact, it takes more than 120 minutes to turn CNT arrays with an average height of  $600\mu\text{m}$  superhydrophilic. Note that a superhydrophilic surface is defined as a surface with a static contact angle for water of less than  $5^{\circ}$ .

Similar behavior is also observed when the CNT arrays are exposed to oxygen plasma treatment. These CNT arrays become less hydrophobic as the CNT arrays are exposed to oxygen plasma treatment. The static contact angle of the oxygen plasma treated CNT arrays also decreases monotonically as the increase of oxygen plasma exposure time, and the decrease rate is also influenced by the length of the array (Figure 3.3). Shorter CNT arrays exhibit a higher decrease rate of static contact angle while longer CNT arrays exhibit a lower decrease rate. For example, after being exposed to 10 minutes of UV/ozone treatment, the static contact angle of  $150\mu\text{m}$  tall as-grown CNT arrays decreases by almost  $150^{\circ}$ . On the other hand, for the same exposure time, the static contact angle of  $650\mu\text{m}$  tall as-grown CNT arrays only

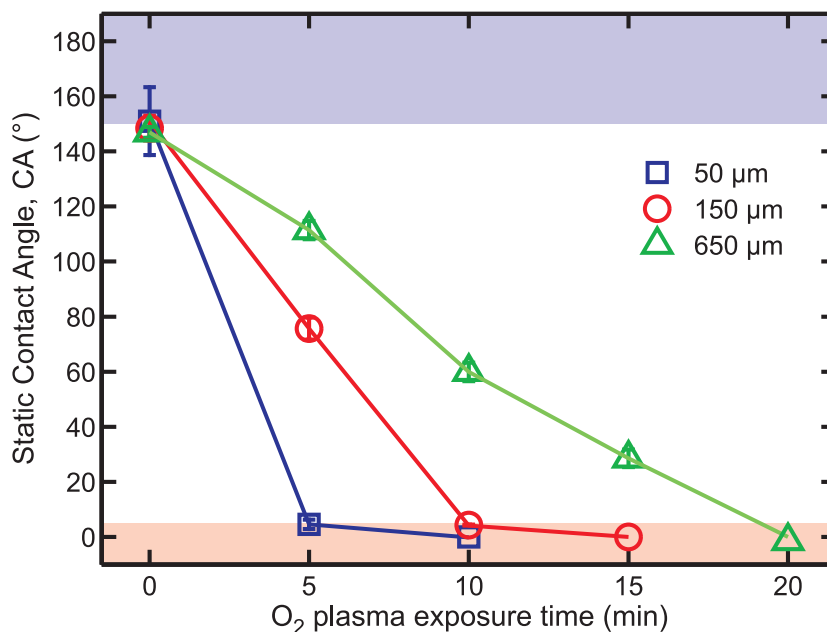


Figure 3.3. Plot of static contact angle of the CNT arrays with different lengths as a function of oxygen plasma exposure time.

decreases by  $90^\circ$ .

Compared to that of UV/ozone treated CNT arrays, the static contact angle of the oxygen plasma treated CNT arrays decreases at a much higher rate. The relation between static contact angle and the exposure time of oxygen plasma treatment is also more linear than that of UV/ozone treatment. This implies that the oxygen plasma treatment is more potent in rendering the CNT array hydrophilic than the UV/ozone treatment. As a result, as-grown CNT arrays with an average height of  $50\mu\text{m}$  can be turned completely superhydrophilic in just less than five minutes of oxygen plasma treatment. It takes about 10 minutes and 20 minutes of oxygen plasma treatment to create superhydrophilic CNT arrays from  $150\mu\text{m}$  and  $650\mu\text{m}$  tall as-grown CNT arrays, respectively.

An opposite behavior is observed when the CNT arrays are exposed to vacuum annealing treatment. The CNT arrays become increasingly hydrophobic as they are exposed to vacuum annealing treatment. After being exposed to a prolonged duration of vacuum annealing treatment, the static contact angle of the CNT arrays may reach as high as  $170^\circ$ . Such a high static contact angle can be reached by all types of

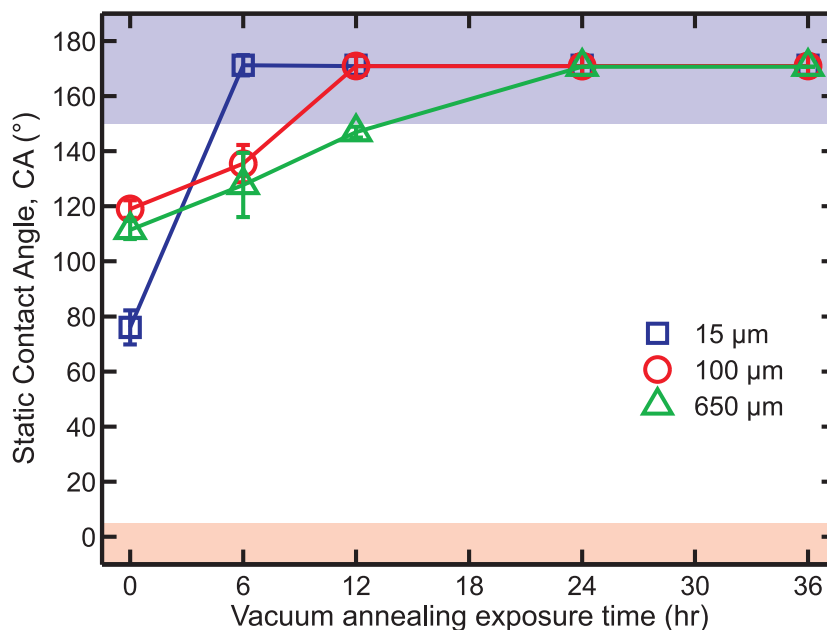


Figure 3.4. Plot of static contact angle of the CNT arrays with different lengths as a function of vacuum annealing exposure time.

CNT arrays, regardless of their height and initial static contact angle. Such behavior confirms the effectiveness of vacuum annealing treatment in rendering the CNT arrays superhydrophobic (Figure 3.4). Note that a superhydrophobic surface is defined as a surface with a static contact angle for water of more than  $150^{\circ}$ .

In general, the static contact angle of the vacuum annealed CNT arrays increases monotonically as the increase of vacuum annealing exposure time, and the increase rate is dependent on the length of the array. Shorter CNT arrays exhibit a higher static contact angle increase rate, while longer CNT arrays exhibit a lower increase rate. CNT arrays with an average height of  $15\mu\text{m}$  and previously exposed to five minutes UV/ozone treatment can be completely turned superhydrophobic, by just six hours of vacuum annealing treatment. On the other hand, CNT arrays with an average height of  $650\mu\text{m}$  and previously exposed to five minutes oxygen plasma treatment can only be turned superhydrophobic after 24 hours of vacuum annealing treatment.

Notice that the static contact angle of CNT arrays does not go higher than  $170^{\circ}$ , even after a prolonged exposure to vacuum annealing treatment. For example, an

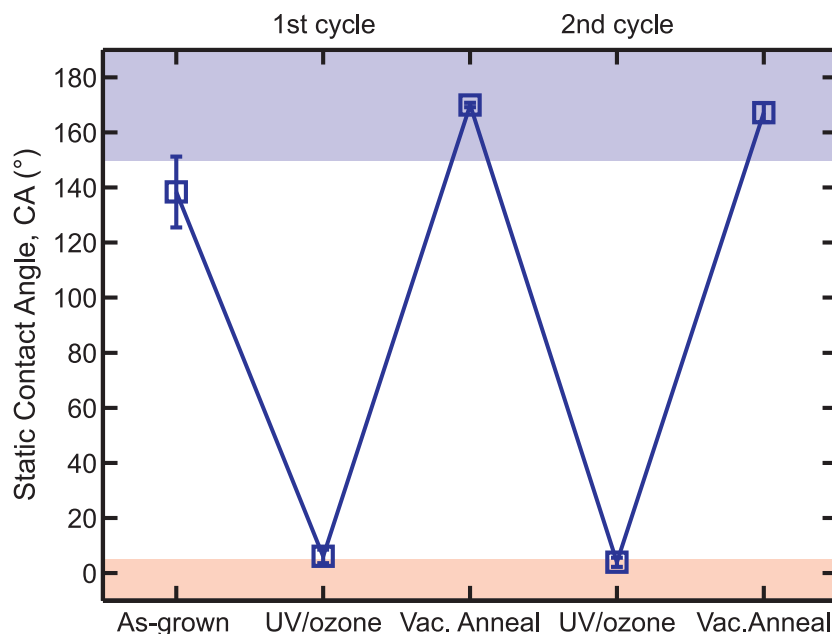


Figure 3.5. Changes in static contact angle of CNT arrays that undergo UV/ozone and vacuum annealing cycles.

extra 30 hours of vacuum annealing treatment does not make the static contact angle of  $15\mu\text{m}$  tall CNT array higher than  $170^\circ$ . Such behavior may indicate the limitation of nanoscale roughness in minimizing the contact point between water and the bulk surface of CNT arrays. Thus, a perfect static contact angle of  $180^\circ$  may only be exhibited by a surface that has hierarchical two-length-scale roughness. This behavior may also be caused by an incomplete removal of the absorbed oxygen by the vacuum annealing treatment. Hence, it is imperative to quantify the amount of oxygen that is adsorbed and desorbed by CNT arrays during the dry oxidation and vacuum annealing treatments, and correlate it with their wettability.

To demonstrate that the CNT arrays can be switched between hydrophobic and hydrophilic by a combination of UV/ozone and vacuum annealing treatments, several as-grown CNT arrays with an average length of about  $120\mu\text{m}$  are exposed to a few cycles of UV/ozone and vacuum annealing treatments. Here, the oxidation and reduction processes are performed by exposing these CNT arrays to UV/ozone treatment for 60 minutes and vacuum annealing treatment for 24 hours, respectively.

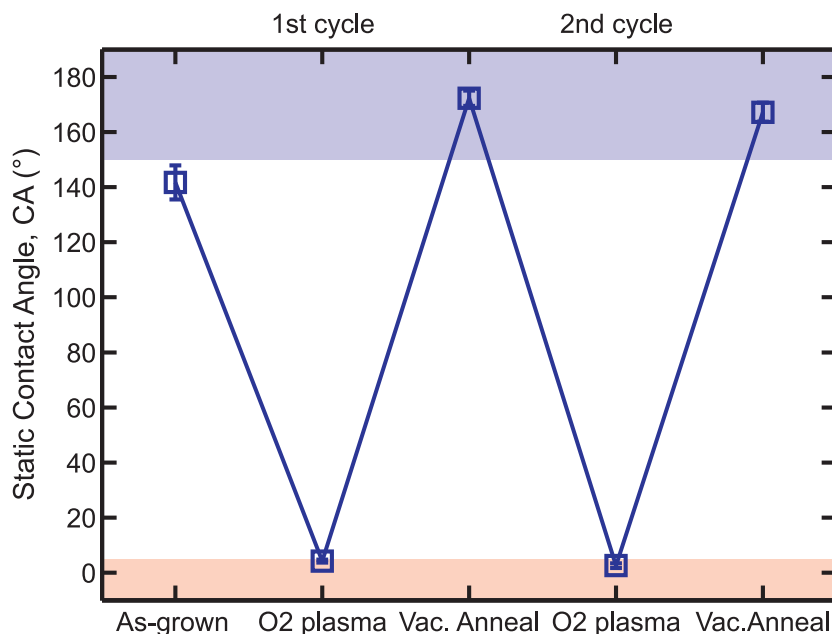


Figure 3.6. Changes in static contact angle of CNT arrays that undergo oxygen plasma and vacuum annealing cycles.

In principle, these CNT arrays should become more hydrophilic after each UV/ozone treatment and more hydrophobic after each vacuum annealing treatment. Indeed, as the CNT arrays undergo cycles of UV/ozone and vacuum annealing, their wettability changes according to these cycles (Figure 3.5). The static contact angle of these CNT arrays decreases from about  $138^\circ$  to about  $6^\circ$  after the first UV/ozone treatment. Their static contact angle increases back to  $170^\circ$  after the first vacuum annealing treatment. As expected, their static contact angle decreases again to about  $4^\circ$  after the second UV/ozone treatment and increases back to  $167^\circ$  after the second vacuum annealing treatment.

Similar behavior is also observed when several as-grown CNT arrays with an average length of about  $340\ \mu\text{m}$  are exposed to a few cycles of oxygen plasma and vacuum annealing treatments. Here, the oxidation and reduction processes are performed by exposing these CNT arrays to oxygen plasma treatment for 15 minutes and vacuum annealing treatment for 24 hours, respectively. In principle, these CNT arrays should become more hydrophilic after each oxygen plasma treatment and more hydrophobic

after each vacuum annealing treatment. Indeed, as the CNT arrays undergo cycles of oxygen plasma and vacuum annealing, their wettability changes according to these cycles (Figure 3.6). The static contact angle of these CNT arrays decreases from about  $142^\circ$  to about  $4^\circ$  after the first oxygen plasma treatment. Their static contact angle increases back to  $172^\circ$  after the first vacuum annealing treatment. Again, their static contact angle decreases to about  $3^\circ$  after the second oxygen plasma treatment and increases back to  $167^\circ$  after the second vacuum annealing treatment.

The cyclic change in wettability, demonstrated by the cyclic change in static contact angle, proves that the wettability of CNT arrays can, indeed, be controlled by a combination of UV/ozone and vacuum annealing treatments or oxygen plasma and vacuum annealing treatments. This cyclic behavior also shows that CNT arrays can, indeed, be switched between superhydrophobic and superhydrophilic repeatedly, as long as their bulk structures are well preserved. The oxidation and reduction process, using a combination of UV/ozone and vacuum annealing treatments or oxygen plasma and vacuum annealing treatments, seems to be fully reversible for more than several cycles. To elucidate the underlying mechanism that controls the wettability of CNT arrays, it is imperative to quantify the amount of oxygen adsorbed and desorbed by CNT arrays during these oxidation and reduction cycles.

### 3.3.2 Oxygen content vs. exposure time

Since it is hypothesized that the adsorption of oxygen dictates the wettability of CNT arrays, it is imperative to quantify the amount of oxygen involved during the dry oxidation and vacuum annealing treatments. Here, the relative concentration of oxygen adsorbates on CNT arrays is represented by their oxygen to carbon atomic ratio (O/C ratio). O/C ratio is a common figure of merit to quickly assess the degree of oxidation of the CNT arrays (Hesse et al., 2005; Peng and Liu, 2006). Therefore, lightly oxidized CNT arrays are expected to have lower O/C ratios and heavily oxidized CNT arrays are expected to have higher O/C ratios. As mentioned earlier, the O/C ratio is calculated from the intensity ratio of O 1s and C 1s peaks

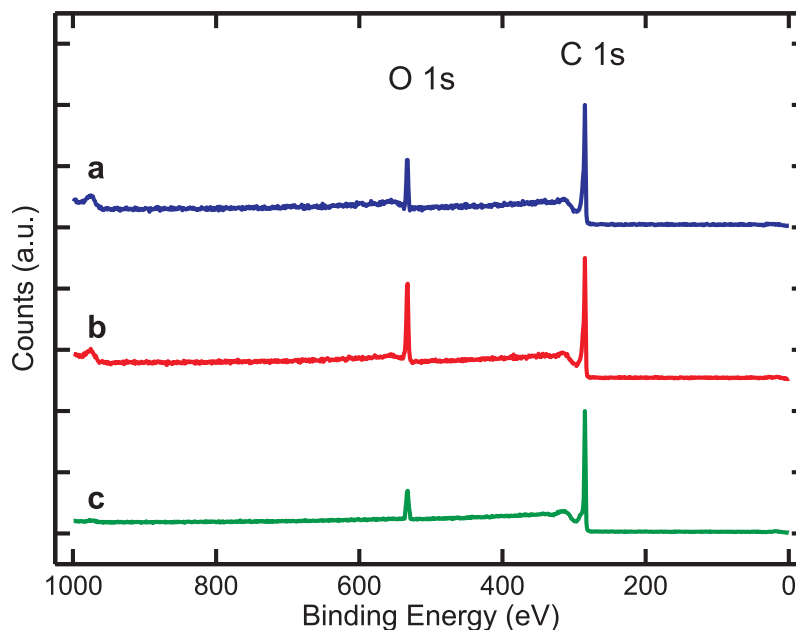


Figure 3.7. XPS survey spectra of as-grown CNT arrays (a), superhydrophilic CNT arrays (b), and superhydrophobic CNT arrays (c).

obtained by low resolution XPS survey scan (Figure 3.7).

As expected, the oxygen content of UV/ozone treated CNT arrays increases monotonically as the increase of exposure time. Indeed, after just 15 minutes of UV/ozone exposure, the O/C ratio of as-grown CNT arrays increases from about 8% to more than 11% (Figure 3.8). Their O/C ratio decreases even further as they are exposed to a prolonged UV/ozone treatment. For example, after being exposed to 60 minutes of UV/ozone treatment, the O/C ratio of  $15\mu\text{m}$  and  $100\mu\text{m}$  tall as-grown CNT arrays increases to about 18% and 16%, respectively.

In general, the rate of increase in O/C ratio of the UV/ozone treated CNT arrays is influenced by the length of the array. Shorter CNT arrays exhibit a higher O/C ratio increase rate, while longer CNT arrays exhibit a lower increase rate. The O/C ratio of as-grown CNT arrays with an average height of  $15\mu\text{m}$  can be doubled from about 8% to about 18% in just 30 minutes of UV/ozone treatment. On the other hand, 30 minutes of UV/ozone treatment only increase the O/C ratio of  $100\mu\text{m}$  and  $600\mu\text{m}$  tall as-grown CNT arrays to about 15% and 11%, respectively. In fact, it takes more than 120 minutes for the CNT arrays with an average height of  $600\mu\text{m}$  to

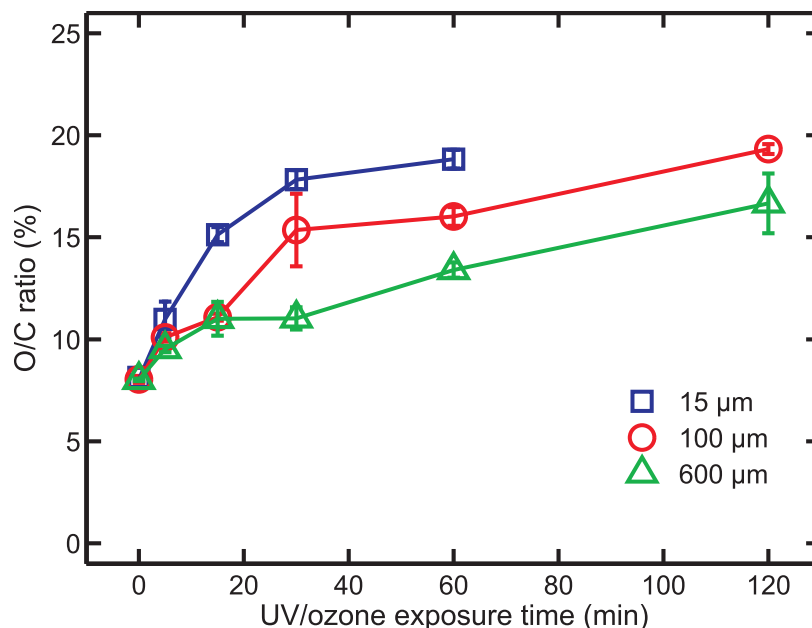


Figure 3.8. Plot of Oxygen/Carbon atomic ratio of the CNT arrays with different lengths as a function of UV/ozone exposure time.

reach an O/C ratio of 17%.

Similar behavior is also observed when the CNT arrays are exposed to oxygen plasma treatment. The O/C ratio of these CNT arrays also increases monotonically as the increase of oxygen plasma exposure time, and the increase rate is also influenced by the length of the array (Figure 3.9). Shorter CNT arrays exhibit a higher O/C ratio increase rate, while longer CNT arrays exhibit a lower increase rate. For example, after being exposed to five minutes of oxygen plasma treatment, the O/C ratio of 150 μm tall as-grown CNT arrays doubled from about 8% to about 17%. On the other hand, for the same exposure time, the O/C ratio of 650 μm tall as-grown CNT arrays only increases by 2%.

Compared to that of UV/ozone treated CNT arrays, the O/C ratio of the oxygen plasma treated CNT arrays increases at a much higher rate. The relation between O/C ratio and the exposure time of oxygen plasma treatment is also different than that of UV/ozone treatment. For the UV/ozone treatment, the rate of increase of O/C ratio is similar to a logarithmic increase with a plateau around 20%. On the other hand, the O/C ratio increases exponentially with the increase of exposure time

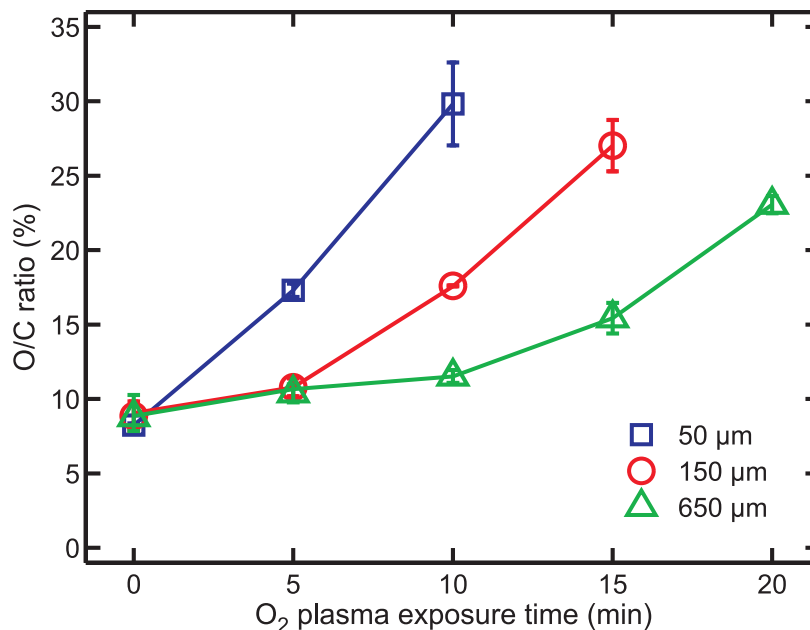


Figure 3.9. Plot of Oxygen/Carbon atomic ratio of the CNT arrays with different lengths as a function of oxygen plasma exposure time.

of oxygen plasma treatment. This implies that the oxygen plasma treatment is a more potent oxidizing method than the UV/ozone treatment. As a result, the O/C ratio of as-grown CNT arrays with an average height of  $650\mu\text{m}$  can reach 23% in just under 20 minutes of oxygen plasma treatment. In contrast, it takes more than 120 minutes of UV/ozone treatment for as-grown CNT arrays with an average height of  $100\mu\text{m}$  to reach an O/C ratio of 19%.

An opposite behavior is observed when the CNT arrays are exposed to vacuum annealing treatment. In general, the O/C ratio of the vacuum annealed CNT arrays decreases monotonically as the increase of vacuum annealing exposure time, and the decrease rate is dependent on the length of the array (Figure 3.10). Shorter CNT arrays exhibit a faster decrease of O/C ratio than the longer CNT arrays. For example, the O/C ratio of  $15\mu\text{m}$  long CNT arrays can be decreased from about 11% to about 5% in just 12 hours. In contrast, the O/C ratio of  $650\mu\text{m}$  long CNT arrays can only be decreased from about 10% to about 6% after 24 hours of vacuum annealing treatment.

Although vacuum annealing treatment is very effective in removing adsorbed oxy-

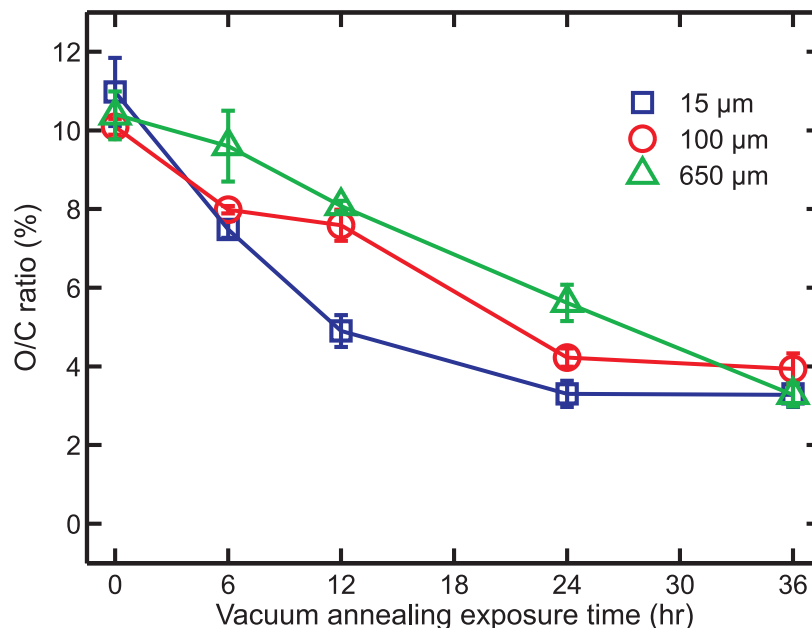


Figure 3.10. Plot of Oxygen/Carbon atomic ratio of the CNT arrays with different lengths as a function of vacuum annealing exposure time.

gen from CNT arrays, it does have a limitation: there exist some forms of adsorbed oxygen that cannot be completely removed by vacuum annealing treatment. These forms of adsorbed oxygen may only be completely removed by vacuum annealing at higher temperature or using chemical reduction technique. Such limitation is highlighted by the fact that the O/C ratio of the vacuum annealed CNT arrays does not go lower than 3%. Even after being exposed to a prolonged duration of vacuum annealing treatment, the O/C ratio of the CNT arrays seems to reach a plateau at around 3%.

As mentioned earlier, the static contact angle for short CNT arrays decreases at a faster rate than the long ones, as they are exposed to either UV/ozone or oxygen plasma treatment and the static contact angle for short CNT arrays increases at a faster rate than the long ones as they are exposed to vacuum annealing treatment. Such difference in rate of change of wettability can be correlated to the difference in rate of change of O/C ratio between short and tall CNT arrays. Indeed, a higher rate of increase and decrease of O/C ratio observed on the short CNT arrays, as they are exposed to dry oxidation and reduction treatments, respectively, leads to a

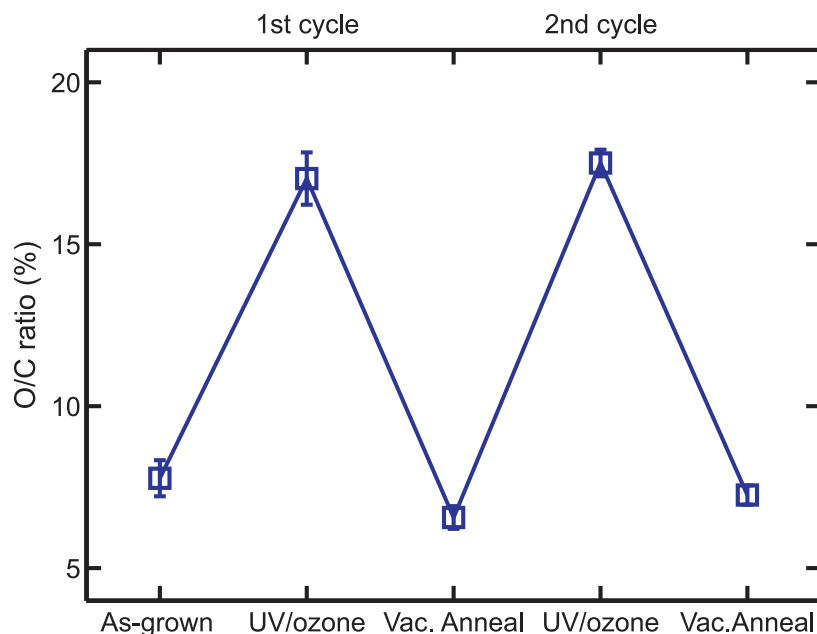


Figure 3.11. Changes in oxygen/carbon atomic ratio of CNT arrays that undergo UV/ozone and vacuum annealing cycles.

higher rate of decrease and increase of their static contact angle. Similarly, a slower change in O/C ratio observed on the long CNT arrays yields a lower rate of change of their static contact angle. This behavior highlights two important aspects of dry oxidation and reduction processes employed to alter the wettability of CNT arrays: the wettability of CNT arrays is not a simple two-dimensional surface phenomenon due to the porous nature of CNT arrays, and the oxidation and reduction processes occurs conformally along the major axis of the CNT.

One may expect that the wettability of CNT arrays is a simple two-dimensional surface phenomenon, similar to that observed on other common materials. The wettability on these common materials is dictated only by the characteristic of their topmost surfaces. Since the only part that is oxidized or reduced during the dry oxidation or reduction treatment is their topmost surfaces, not their bulk structures, the change of wettability of these common materials is not length dependent. On the other hand, the wettability of CNT arrays is dictated by the characteristic of each individual CNT that constitutes their bulk structures. Because of the porous

nature of the bulk structure of CNT arrays, the oxidation and reduction processes occur uniformly in the lateral and axial directions. Since the characteristic of the mid-section and bottom part the CNT arrays is similar to that of their topmost part, the wettability of CNT arrays is determined by the characteristic of their entire bulk structures. As a result, the change of wettability of CNT arrays induced by dry oxidation and reduction is length dependent.

As CNT arrays undergo dry oxidation treatment, their entire structures are oxidized at a similar rate along the lateral and axial directions. Thus, the amount of oxygen adsorbed at the tip of CNT arrays is identical to that adsorbed at the mid-section and bottom of the arrays. As reflected from their O/C ratio, for the same period of UV/ozone or oxygen plasma exposure time, the spatial concentration of adsorbed oxygen on the short CNT arrays is different than that on the long CNT arrays. For the same oxidation dosage, shorter CNT arrays have a higher spatial concentration of adsorbed oxygen than the longer ones. Similarly, when CNT arrays undergo vacuum annealing treatment, their entire structures are reduced at a similar rate along the lateral and axial directions. Thus, the amount of oxygen removed from the tip of CNT arrays is identical to that removed from the mid-section and bottom of the arrays. Therefore, for the same period of vacuum annealing exposure time, shorter CNT arrays lose more adsorbed oxygen than the longer ones, as reflected from their O/C ratio.

By a combination of UV/ozone and vacuum annealing treatments, the wettability of CNT arrays can be switched repeatedly between hydrophobic and hydrophilic (Figure 3.5). In principle, the O/C ratio of these CNT arrays is higher after each UV/ozone treatment, and lower after each vacuum annealing treatment. Indeed, as the CNT arrays undergo cycles of UV/ozone and vacuum annealing, their O/C ratio changes according to these cycles (Figure 3.11). The O/C ratio of these CNT arrays increases from about 7% for the as-grown CNT arrays, to about 17% after the first UV/ozone treatment. Their O/C ratio decreases back to 6% after the first vacuum annealing treatment. As expected, their O/C ratio increases again to about 17% after the second UV/ozone treatment, and decreases back to 7% after the second vacuum

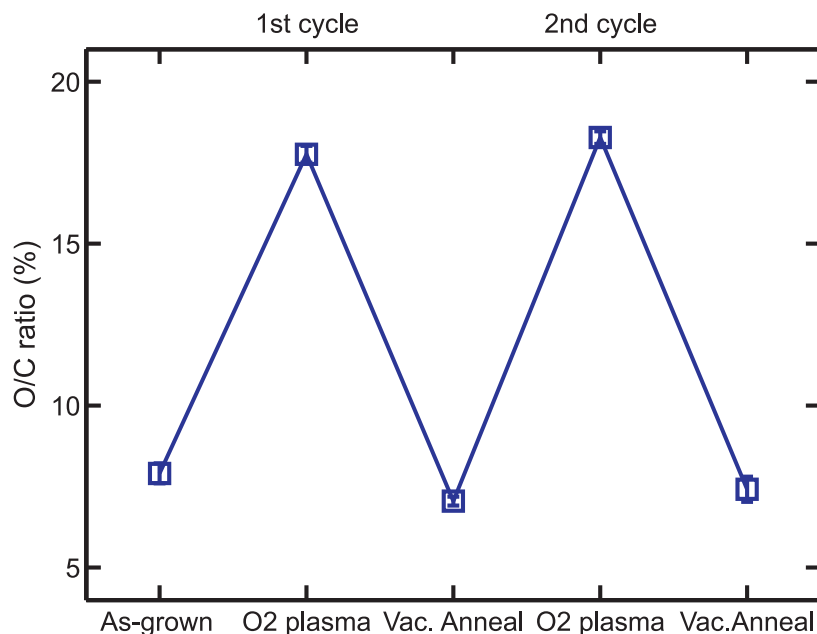


Figure 3.12. Changes in oxygen/carbon atomic ratio of CNT arrays that undergo O<sub>2</sub> plasma and vacuum annealing cycles.

annealing treatment.

Similar behavior is also observed when several as-grown CNT arrays are exposed to a few cycles of oxygen plasma and vacuum annealing treatments. As mentioned earlier, the CNT arrays can also be switched between hydrophobic and hydrophilic by a combination of oxygen plasma and vacuum annealing treatments (Figure 3.6). Just as when they are exposed to cycles of UV/ozone and vacuum annealing treatments, the O/C ratio of these CNT arrays should be higher after each oxygen plasma treatment and lower after each vacuum annealing treatment. Indeed, as the CNT arrays undergo cycles of oxygen plasma and vacuum annealing, their O/C ratio changes according to these cycles (Figure 3.12). The O/C ratio of these CNT arrays increases from about 8% for the as-grown CNT arrays to about 17% after the first oxygen plasma treatment. Their O/C ratio decreases back to about 7% after the first vacuum annealing treatment. Again, their O/C ratio increases to about 18% after the second oxygen plasma treatment and decreases back to 7% after the second vacuum annealing treatment.

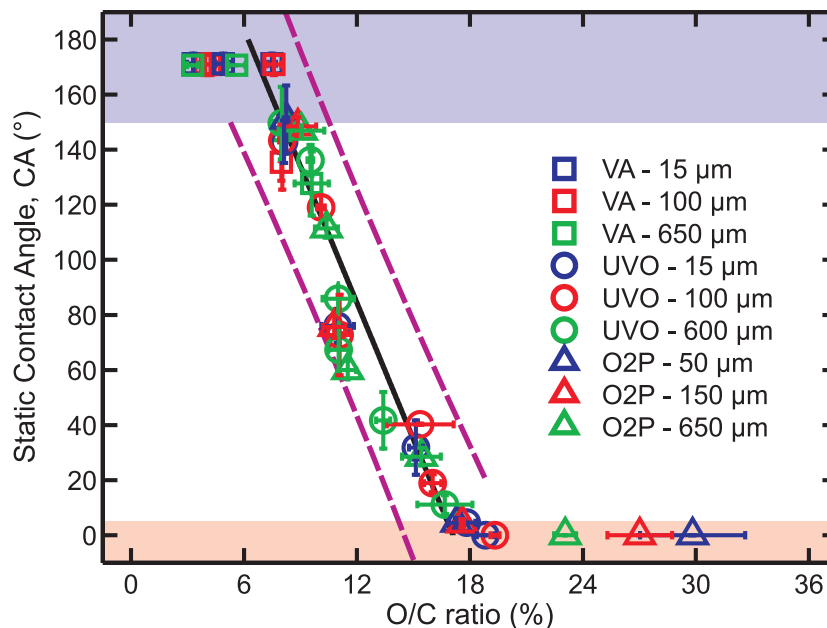


Figure 3.13. Plot of static contact angle of the CNT arrays with different lengths and treatments as a function of their Oxygen/Carbon atomic ratio.

The cyclic evolution of O/C ratio proves that the effect of oxidation induced by UV/ozone and oxygen plasma treatments can be reversed by vacuum annealing treatment. Although these oxidation processes may not be completely reversible, it can be used to safely control the wettability of CNT arrays for more than several cycles. It has to be noted that the cyclic evolution of O/C ratio of CNT arrays perfectly with the cyclic changes in static contact angle, regardless of the oxidation methods used. As CNT arrays undergo the oxidation process, either by exposure to UV/ozone or oxygen plasma treatment, their static contact angle decreases and at the same time their O/C ratio increases. Similarly, as CNT arrays undergo a reduction process by exposure to vacuum annealing treatment, their static contact angle increases and, at the same time, their O/C ratio decreases. This suggests the presence of a linear negative correlation between static contact angle of CNT arrays and their O/C ratio. This correlation may be completely independent to the oxidation methods used.

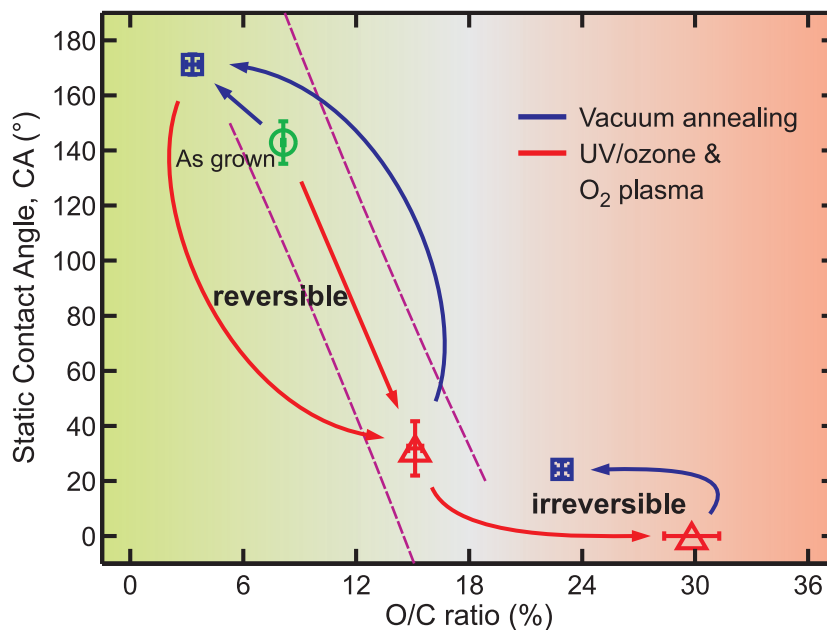


Figure 3.14. Reversible vs. irreversible oxidation.

### 3.3.3 Contact angle vs oxygen content

A direct correlation between the oxygen content of CNT arrays and their wettability can be easily obtained by plotting their static contact angle against their O/C ratio. Although it is expected that this plot is independent of types of oxidation methods and exposure time, it is not expected to be independent of CNT arrays length. Therefore, it is, indeed, fascinating to observe the collapse of the entire evolution of CNT array wettability into one pattern (Figure 3.13). This plot clearly shows that the static contact angle of CNT arrays decreases linearly from about  $170^\circ$  to  $0^\circ$  as the O/C ratio increases from 6% to 18%. Since the static contact angle reaches an upper limit of  $170^\circ$  at an O/C ratio of 6%, the static contact angle remains the same, even if the O/C ratio is decreased to 3%. Similarly, the static contact angle reaches a lower limit of  $0^\circ$  at an O/C ratio of 18%. Obviously, any attempt to further increase the O/C ratio does not result in a decrease of static contact angle.

As the CNT arrays undergo dry oxidation treatment, their O/C ratio increases, while at the same time their static contact angle increases. As the CNT arrays undergo vacuum annealing treatment, their O/C ratio decreases while their static

contact angle increases following the exact same slope. This behavior confirms the effect of oxygen adsorbates on the wettability of CNT arrays, where a higher concentration of oxygen adsorbates leads to a better wettability, and a lower concentration of oxygen adsorbates leads to a lower wettability. It also implies that the dry oxidation and vacuum annealing treatments are highly reversible as long as the O/C ratio is kept under 18%. In this regime, CNT arrays can be reversibly switched between hydrophilic and hydrophobic multiple times without the risk of inducing excessive damage to the graphitic structure of the CNT.

Although the whole oxygen adsorption and desorption cycles in the regime of O/C ratio lower than 18% seem to be completely reversible, it is worth noting that there exists a possibility that a very small amount of carbon atoms is actually etched from the CNT in the form of CO and CO<sub>2</sub> molecules during the desorption process. Hence, the atomic-scale structure of the CNT array is slightly altered each time dry oxidation and vacuum annealing treatments are performed. Nevertheless, the CNT array can still be repeatedly switched between hydrophilic and hydrophobic for numerous numbers of cycles as long as the overall graphitic structure of the CNT arrays is still intact. However, in the regime of O/C ratios higher than 18%, the oxidation process is no longer reversible (Figure 3.14). For instance, excessively oxidized CNT arrays that have an average O/C ratio of 30% can no longer be turned hydrophobic by vacuum annealing. After vacuum annealing, their O/C ratio decreases to about 23% and their static contact angle does not increase higher than 25°. This irreversible behavior is caused by the destruction of the graphitic structure of the CNT arrays. The effect of oxidation in the irreversible regime will be discussed in detail in Chapter 4.

### 3.3.4 FTIR and XPS analysis

Fourier transform infrared (FTIR) spectrometry analysis was performed to evaluate the effect of dry oxidation and vacuum annealing treatments to the surface chemistry of the CNT arrays. Three absorbance peaks at 810–1320 $cm^{-1}$ , 1340–1600 $cm^{-1}$ , and 1650–1740 $cm^{-1}$  can be observed in almost all samples (Figure 3.15). The origin of the

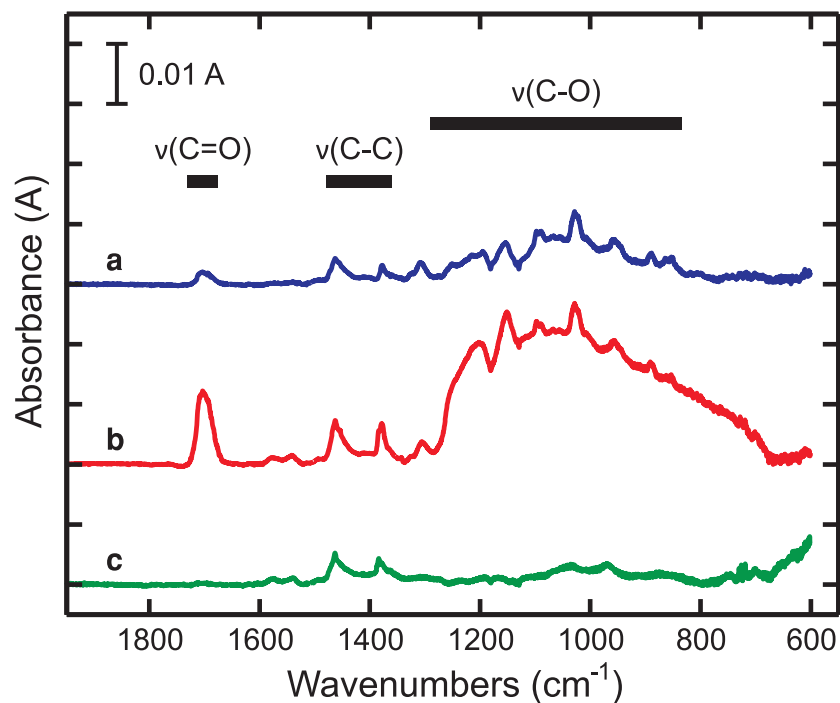


Figure 3.15. FTIR spectra of as-grown CNT arrays (a), superhydrophilic CNT arrays (b), and superhydrophobic CNT arrays (c).

peak at  $718\text{cm}^{-1}$  is still unknown at the moment; hence, it is unassigned at this time. The peaks at  $970$ ,  $1028$ ,  $1154$  and  $1201\text{cm}^{-1}$  correspond to C-O stretching modes (Kuznetsova et al., 2000), and the broad shoulder band at  $810 - 1320\text{cm}^{-1}$  suggests the existence of C-O-C bonds from ester and epoxide functional group (Mawhinney et al., 2000; Sham and Kim, 2006; Socrates, 2001; Kim et al., 2005). The peaks at  $1378$ ,  $1462$ ,  $1541$  and  $1574\text{cm}^{-1}$  indicate the presence of C=C stretching vibration modes of the CNT walls (Mawhinney et al., 2000; Sham and Kim, 2006; Kuznetsova et al., 2000; Socrates, 2001). The narrow band at a peak of  $1703\text{cm}^{-1}$  corresponds to C=O stretching modes of either quinone, carbonyl, or carboxyl groups (Mawhinney et al., 2000; Sham and Kim, 2006; Kuznetsova et al., 2000; Kim et al., 2005).

Qualitatively, all peaks associated to C-O and C=O stretching modes are found to be increasing as the CNT arrays undergo UV/ozone or oxygen plasma treatment. These peaks are found to be very strong in the superhydrophilic CNT arrays, suggesting that oxygen is indeed mainly in the form of C-O and C=O bonds. This finding also implies that the wettability of CNT arrays is indeed dictated by the sur-

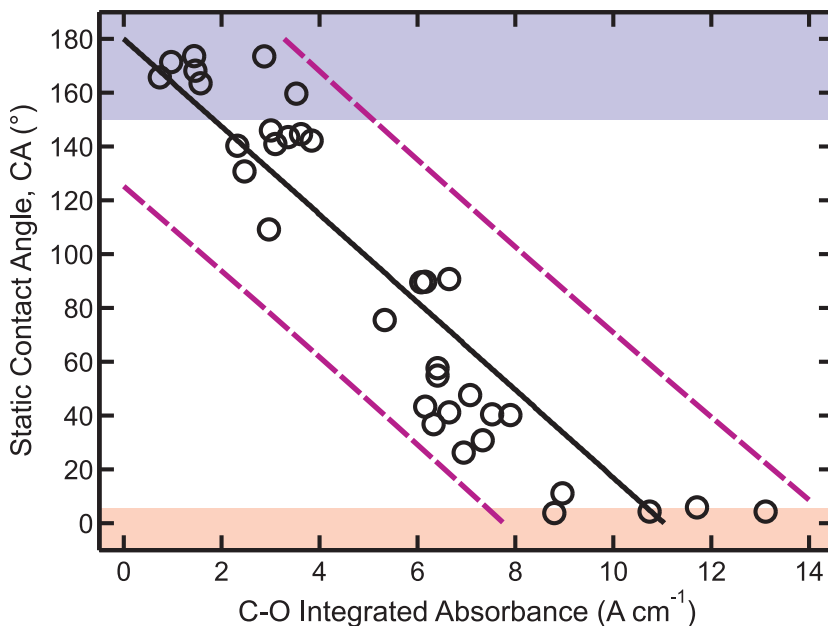


Figure 3.16. Plot of static contact angle of the CNT arrays as a function of their C-O integrated absorbance.

face concentration of C-O and C=O bonds. The intensity of these peaks starts to decrease once the CNT arrays are exposed to vacuum annealing treatment. All peaks corresponding to C-O and C=O stretching modes are found to be very weak in the superhydrophobic CNT arrays, inferring that vacuum annealing treatment is capable of removing the majority of the adsorbed oxygen from the CNT arrays.

Since the CNT arrays wettability is dictated by the surface concentration of C-O and C=O bonds, it is imperative to directly correlate the surface concentration of these bonds to the CNT arrays wettability. Such correlation is obtained by plotting the static contact angle of CNT arrays against the integrated absorbance of C-O and C=O stretching modes. As expected, this plot shows a very strong negative correlation between the integrated absorbance of both C-O and C=O stretching modes, and the static contact angle of CNT arrays, where the static contact angle decreases linearly as the increase of integrated absorbance. The static contact angle of the CNT arrays decreases from  $170^{\circ}$  to  $0^{\circ}$  as their integrated absorbance of C-O stretching mode increases from  $0A\text{cm}^{-1}$  to  $11A\text{cm}^{-1}$  (Figure 3.16). Similarly, the static contact angle of the CNT arrays decreases from  $170^{\circ}$  to  $0^{\circ}$  as their integrated absorbance of

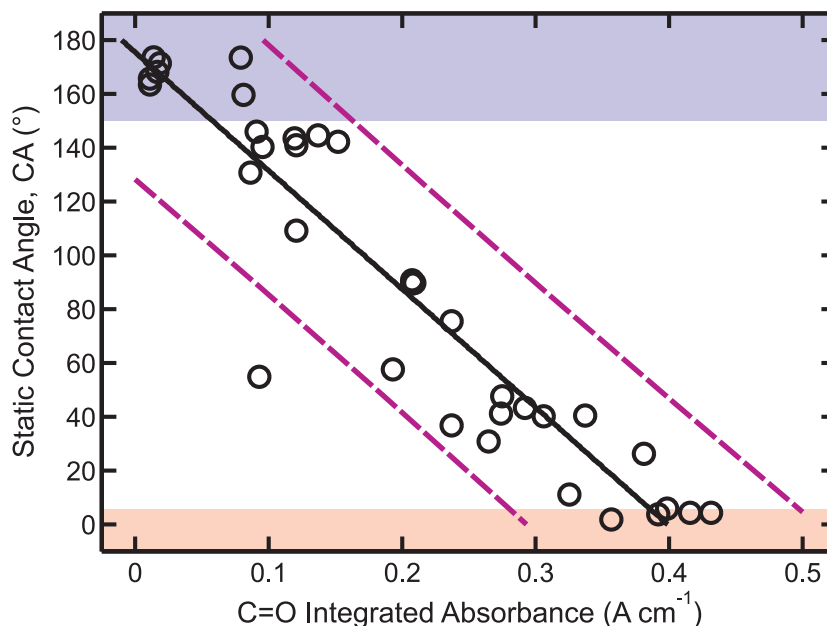


Figure 3.17. Plot of static contact angle of the CNT arrays as a function of their C=O integrated absorbance.

C=O stretching mode increases from  $0.4 \text{ A cm}^{-1}$  to  $0.4 \text{ A cm}^{-1}$  (Figure 3.17). Obviously, CNT arrays with higher surface concentration of C-O and C=O bonds are more hydrophilic, and CNT arrays with a lower concentration of C-O and C=O bonds are more hydrophobic. It is important to note that superhydrophobic CNT arrays have a minute, but nonzero concentration of C-O and C=O bonds.

XPS analysis was conducted to further verify this finding. Deconvolution of the C 1s XPS spectra of CNT arrays shows seven distinct peaks associated with C-C sp<sup>2</sup> ( $284.5 \pm 0.1 \text{ eV}$ , FWHM 0.9 eV), C-C sp<sup>3</sup> ( $285.5 \pm 0.1 \text{ eV}$ , FWHM 1.3 eV), C-O ( $286.5 \pm 0.1 \text{ eV}$ , FWHM 1.4 eV), C=O ( $287.4 \pm 0.2 \text{ eV}$ , FWHM 1.4 eV), O-C=O ( $289.1 \pm 0.4 \text{ eV}$ , FWHM 1.7 eV), O-C(O)=O ( $290.3 \pm 0.4 \text{ eV}$ , FWHM 1.7 eV), and  $\pi - \pi^*$  ( $292.1 \pm 0.4 \text{ eV}$ , FWHM 1.6 eV) peaks (Peng and Liu, 2006; Naseh et al., 2010; Yang et al., 2009; Aria and Gharib, 2011). The C-C sp<sup>2</sup> peak is the signature of the graphitic structure of CNT, and C-C sp<sup>3</sup> peak is typically associated with the presence of defects and functional groups. The C-O peak is typically associated with the presence of hydroxyl and epoxide groups on the CNT outer wall, and cyclic ether at the edges of CNT defect sites (Hossain et al., 2012; Acik et al., 2011, 2010). The

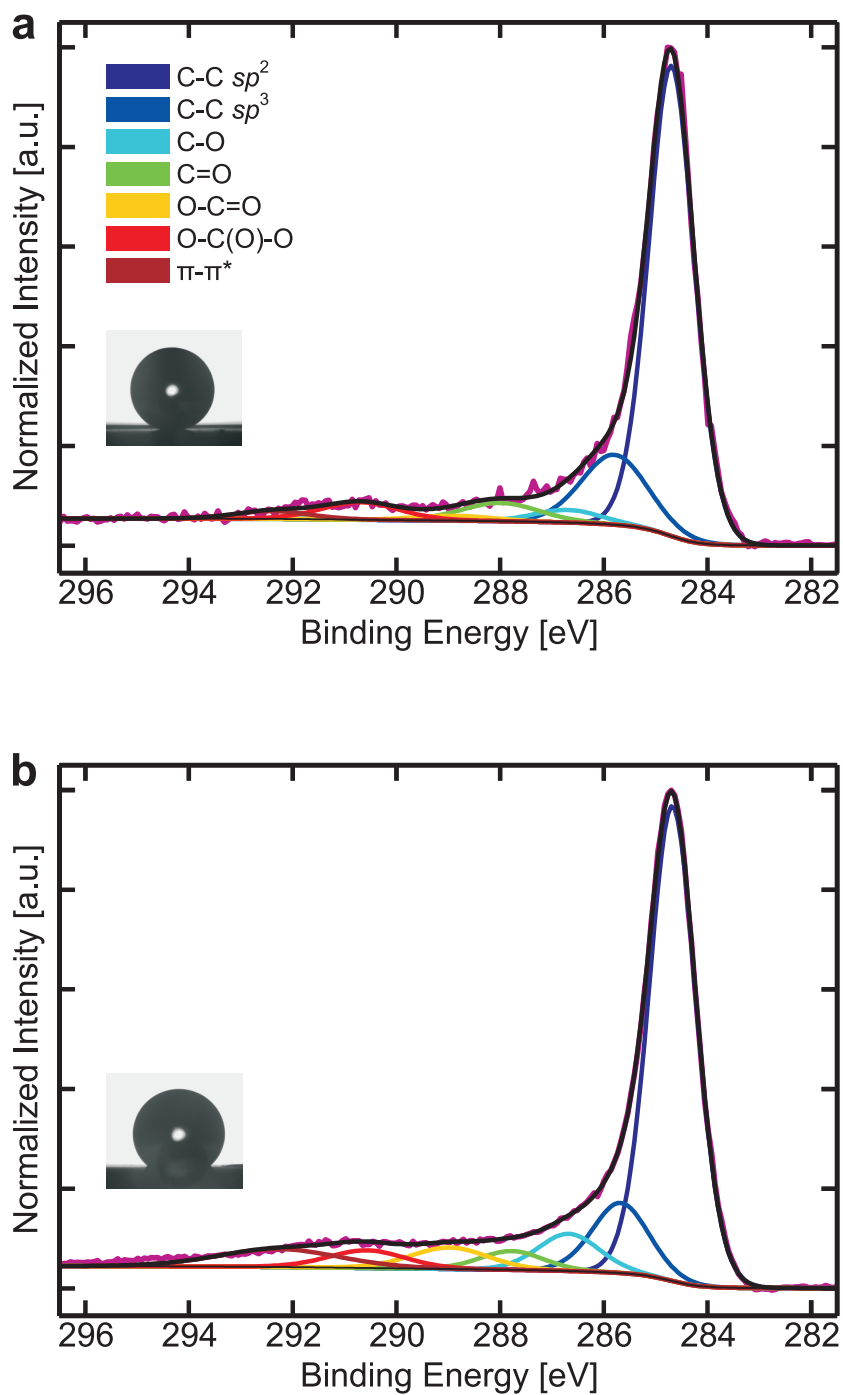


Figure 3.18. High resolution C 1s XPS spectra of superhydrophobic (a) and highly hydrophobic (b) CNT arrays. Deconvolution of the C 1s XPS spectra of CNT arrays shows seven distinct peaks associated with C-C  $sp^2$  ( $284.5 \pm 0.1$  eV, FWHM 0.9 eV), C-C  $sp^3$  ( $285.5 \pm 0.1$  eV, FWHM 1.3 eV), C-O ( $286.6 \pm 0.1$  eV, FWHM 1.4 eV), C=O ( $287.4 \pm 0.2$  eV, FWHM 1.4 eV), O-C=O ( $289.1 \pm 0.4$  eV, FWHM 1.7 eV), O-C(O)=O ( $290.3 \pm 0.4$  eV, FWHM 1.7 eV), and  $\pi - \pi^*$  ( $292.1 \pm 0.4$  eV, FWHM 1.6 eV) peaks.

C=O peak indicates the presence of quinone and carbonyl groups at the edges of CNT defect sites (Acik et al., 2011). The O-C=O and O-C(O)-O peaks indicate the presence of carboxyl and carbonate terminating groups, respectively. The  $\pi - \pi^*$  peak is associated with the graphite stacking between layers of the CNT wall and between neighboring CNT.

The C 1s XPS spectra of the as-grown CNT arrays exhibit an extremely strong C-C sp<sup>2</sup> peak and a mild C-C sp<sup>3</sup> peak. In addition, peaks associated with C-O, C=O, O-C=O, O-C(O)-O groups are considerably weak (Figure 3.18.b). The implication of the presence of a mild C-C sp<sup>3</sup> peak and weak oxygenated group peaks are twofold: a small amount of oxygen is adsorbed by CNT during the growth period and the resulting CNT is not defect-free. Unlike hydroxyl and epoxide groups that are most likely to form out-of-plane on the CNT outer wall due to their lowest energy configuration (Leconte et al., 2010; Nourbakhsh et al., 2010; Vinogradov et al., 2011; Samarakoon and Wang, 2011), cyclic ether and carbonyl group is more likely to form in-plane at the edges of CNT defect sites (Acik et al., 2011). In addition, carboxyl and carbonate terminating groups are also more likely to form in-plane at the edges of CNT defect sites.

Although epoxide, carbonyl, and carboxyl groups are relatively stable at room temperature and pressure, they can be, in principle, removed at an elevated temperature (Leconte et al., 2010; Vinogradov et al., 2011; Acik et al., 2011). Thermal reduction treatment, i.e. vacuum annealing, has been demonstrated to be an effective means of removing the majority of the adsorbed oxygen from the basal plane of graphitic structures (Vinogradov et al., 2011; Hossain et al., 2012). A moderate temperature of 250°C is known to be adequate in initiating the removal of adsorbed hydroxyl, epoxide, carbonyl, and carboxyl groups (Acik et al., 2010). Similar to those of as-grown CNT arrays, the C 1s XPS spectra of superhydrophobic CNT arrays show an extremely strong C-C sp<sup>2</sup> peak. However, a decrease in intensity of almost all oxygenated group peaks, as well as the C-C sp<sup>3</sup> bonds, is observable (Figure 3.18.a). This confirms the removal of the majority of the adsorbed oxygen from the CNT arrays by vacuum annealing treatment. Although these oxygenated groups

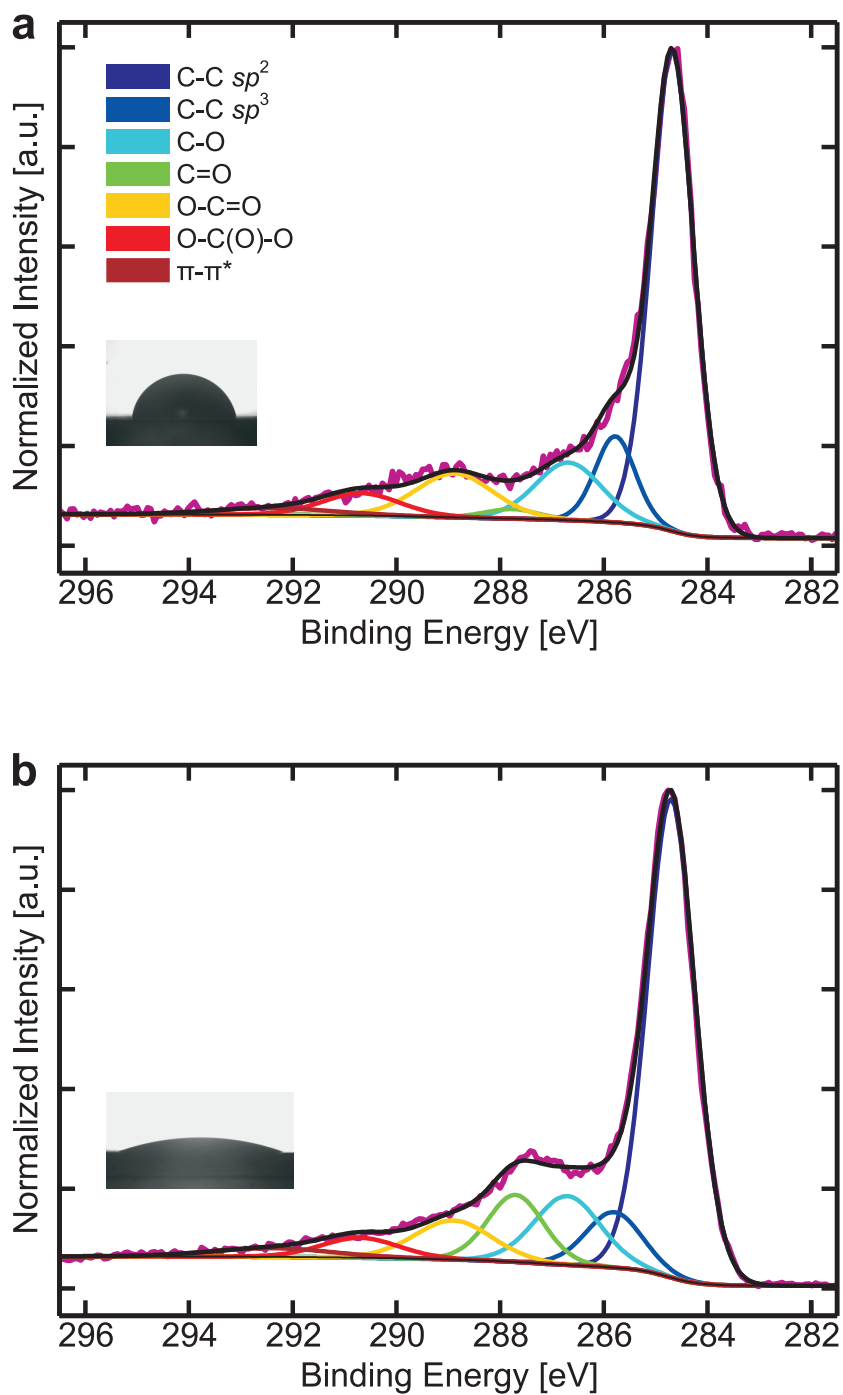


Figure 3.19. High resolution C 1s XPS spectra of mildly hydrophilic (a) and highly hydrophilic (b) CNT arrays. Deconvolution of the C 1s XPS spectra of CNT arrays shows seven distinct peaks associated with C-C  $sp^2$  ( $284.5 \pm 0.1$  eV, FWHM 0.9 eV), C-C  $sp^3$  ( $285.5 \pm 0.1$  eV, FWHM 1.3 eV), C-O ( $286.6 \pm 0.1$  eV, FWHM 1.4 eV), C=O ( $287.4 \pm 0.2$  eV, FWHM 1.4 eV), O-C=O ( $289.1 \pm 0.4$  eV, FWHM 1.7 eV), O-C(O)=O ( $290.3 \pm 0.4$  eV, FWHM 1.7 eV), and  $\pi - \pi^*$  ( $292.1 \pm 0.4$  eV, FWHM 1.6 eV) peaks.

are not removed completely by vacuum annealing treatment, their surface concentration is found to be extremely low. This finding does agree with the FTIR analysis, which shows that CNT arrays can be rendered superhydrophobic even though there are still some traces of C-O and C=O bonds on the CNT arrays. One may expect that the pristine CNT arrays that are free from these oxygenated groups will exhibit a perfect superhydrophobic behavior with contact angle of  $180^\circ$ .

It has to be noted that the intensity of the C=O peak associated with carbonyl or quinone groups remains constant, even after a prolonged exposure to vacuum annealing treatment. This suggests that new carbonyl groups are formed during the vacuum annealing treatment, offsetting the decomposition of carbonyl groups on vacuum annealed CNT array (Acik et al., 2011). Simultaneous desorption of adjacent hydroxyl groups are often followed by the formation of water molecules and in-plane ether groups or out-of-plane carbonyl groups (Acik et al., 2011; Bagri et al., 2010). Further, at an elevated temperature, the transformation of carboxyl groups to carbonyl groups is highly favorable due to the more stable configuration of carbonyl groups (Acik et al., 2011; Bagri et al., 2010).

As the CNT arrays undergo UV/ozone or oxygen plasma treatment, all peaks associated with oxygenated groups become more pronounced. Notice that after mild exposure of dry oxidation treatment the intensity of C-O and O-C=O peaks is higher than that of the C=O peak (Figure 3.19.a). A stronger C-O peak suggests that the concentration of hydroxyl and epoxide groups on the outer wall of dry oxidized CNT is significantly higher than that on as-grown CNT. A more pronounced O-C=O peak suggests that both UV/ozone and oxygen plasma treatments induce the formation of carboxyl terminating groups at the edges of CNT defect sites. These carboxyl groups are often stabilized by electrostatic repulsive forces among themselves (Acik et al., 2011). An epoxide group can be formed when an atomic oxygen radical produced by plasma or ozone is bonded above the middle of a C-C bond (Samarakoon and Wang, 2011). It can also be formed when ozone is adsorbed as ozonide that subsequently lost its molecular oxygen (Suggs et al., 2011). The presence of hydroxyl and carboxyl groups on dry oxidized CNT suggests that substantial amounts of reactive hydroxyl

radicals are generated by the UV/ozone and oxygen plasma treatments. These hydroxyl radicals may be generated from moisture in the ambient air or physisorbed water molecules. Reaction between these water molecules and atomic oxygen radicals produced by plasma or ozone gives rise to peroxides, which, upon homolysis, yields free hydroxyl radicals (Gunes et al., 2011; Acik et al., 2011). In contrast, the presence of hydroxyl and carboxyl groups can be excluded when an oxidation process using hot atomic oxygen at an ultra-high-vacuum is used (Vinogradov et al., 2011).

However, at a longer exposure time, the intensity of the C=O peak increases at a much faster rate than that of C-O and O-C=O peaks (Figure 3.19.b). The apparent increase of intensity of the C=O peak can be associated with an increase of concentration in carbonyl groups on the CNT outer wall, or at edges of CNT defect sites. There is a possibility that some of the epoxide groups are converted to carbonyl during a prolonged exposure of UV/ozone and oxygen plasma treatments. It has been known that epoxide groups have the tendency to create pair structures which readily form two neighboring carbonyl groups in a quinone-like configuration (Samarakoon and Wang, 2011; Acik et al., 2011). In addition, formation of a carbonyl group is often caused by a hydrogen atom migration induced by a weak hydrogen bond between two adjacent hydroxyl groups (Acik et al., 2011). Since carbonyl groups arranged in pairs are relatively stable, further reaction with atomic oxygen or hydroxyl radical is quite unlikely. Therefore, a rapid reaction between paired carbonyl groups and hydroxyl radicals may not occur during the prolonged exposure of UV/ozone and oxygen plasma treatments (Acik et al., 2011).

### 3.3.5 Micro- and nano-scale surface roughness

As explained by the XPS analysis above, the molecular structure of CNT arrays undergoes a transformation during the dry oxidation and reduction treatments. However, such transformation is not obvious in the larger length scale. There is no apparent change in the micro- and nano-scale surface roughness of CNT arrays, even after they are exposed to dry oxidation and reduction cycles. The nanoscale surface roughness

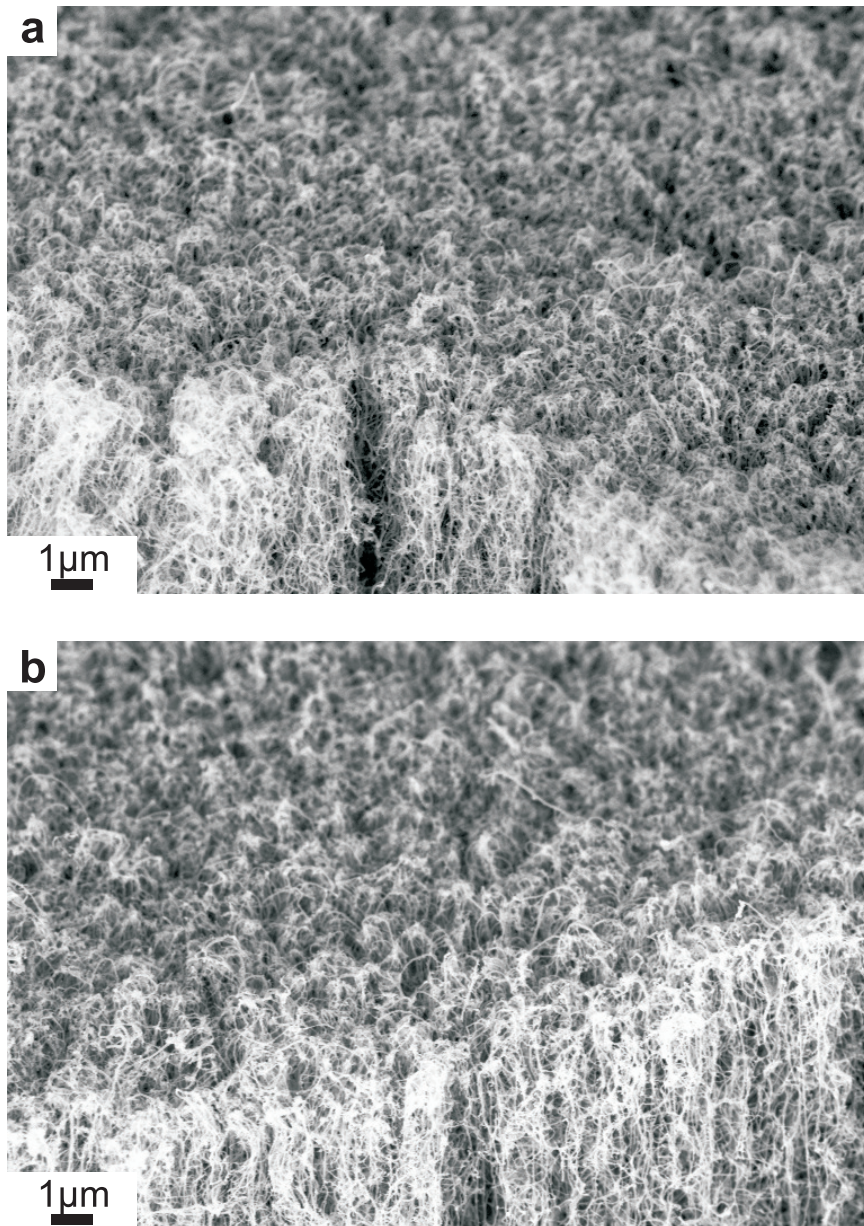


Figure 3.20. High magnification SEM images of CNT arrays after vacuum annealing treatment (a), and oxygen plasma treatment (b). Both CNT arrays exhibit similar nanoscale surface roughness and morphology with no apparent effect of oxidation and reduction.

after vacuum annealing treatment (Figure 3.20.a) is basically similar to that after dry oxidation process either by UV/ozone or oxygen plasma treatment (Figure 3.20.b). Similarly, the microscale surface roughness after vacuum annealing treatment (Figure 3.21.a) is basically similar to that after dry oxidation process either by UV/ozone or oxygen plasma treatment (Figure 3.21.b).

In contrast, previously reported studies show that dry oxidation processes have a tendency to alter the surface roughness of CNT arrays (Liu et al., 2004; Hou et al., 2008). Changes in surface roughness and morphology of CNT arrays are commonly induced by a long exposure of plasma treatment using oxygen or other gasses. This transformation can actually be seen in the oxidized CNT arrays with O/C ratios higher than 18%. In the regime of O/C ratios lower than 18%, such large scale transformation does not occur. Structural transformation of CNT arrays in the regime of O/C ratios higher than 18% can be read in Chapter 4.

### **3.3.6 Water immersion and droplet impact behavior on CNT arrays with different wettability**

As mentioned earlier, CNT arrays can be turned superhydrophobic by exposing them to vacuum annealing treatments. Not only do these CNT arrays exhibit a very high static contact angle, their capability of repelling water is unparalleled. Such capability can be seen clearly when these CNT arrays are submerged in water. In a shallow pool of water, the water-free surface is deformed near the surface such that walls of water are formed around it, leaving the surface dry. This phenomenon indicates that water is being repelled strongly by the bulk surface of superhydrophobic CNT arrays (Figure 3.22). In a deep pool of water, it exhibits a silvery mirror-like surface, indicating the presence of liquid-vapor-solid interface between water and the bulk surface of superhydrophobic CNT arrays (Figure 3.23). Interestingly, this liquid-vapor-solid interface only exists between water and the bulk surface of superhydrophobic CNT arrays, and does not exist between water and the bulk surface of hydrophobic as-grown CNT arrays. Instead of silvery mirror-like color, the as-grown CNT arrays, which

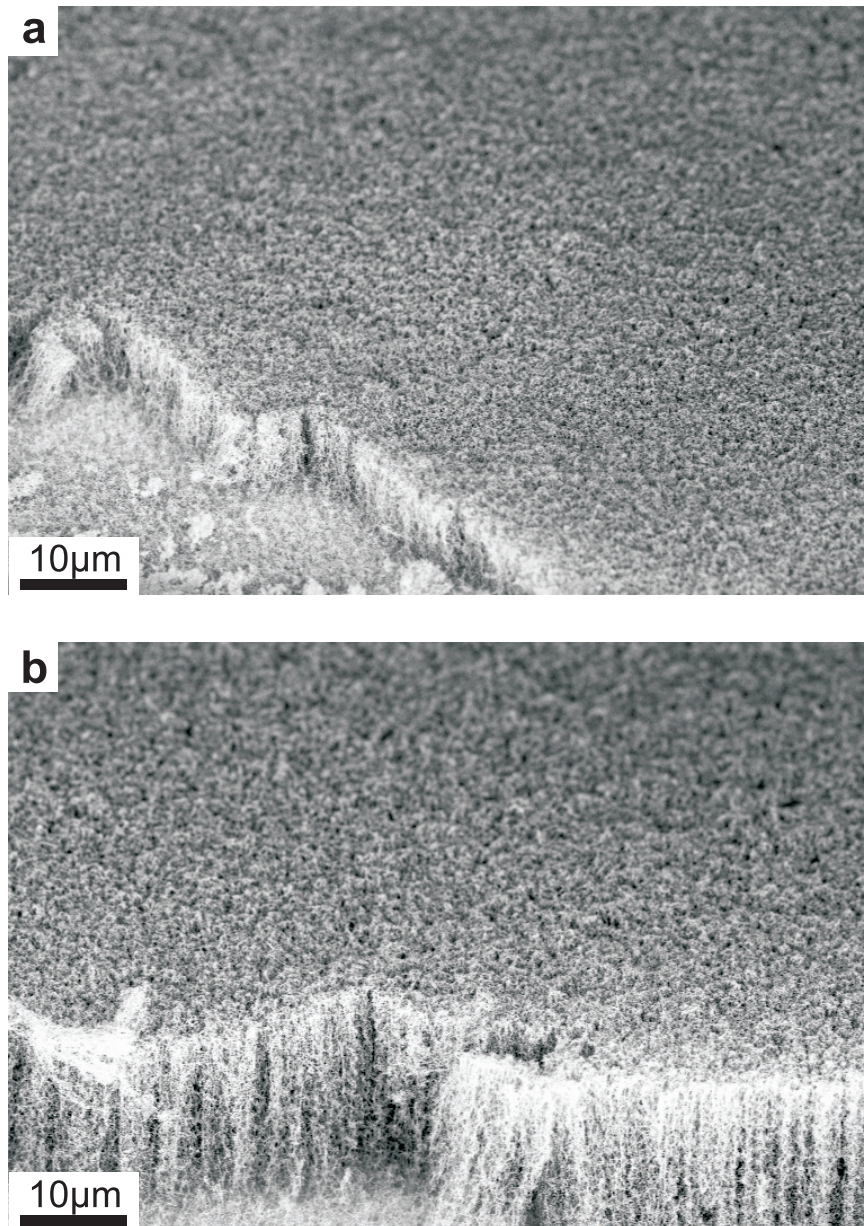


Figure 3.21. Low magnification SEM images of CNT arrays after vacuum annealing treatment (a) and oxygen plasma treatment (b). Both CNT arrays exhibit similar microscale surface roughness and morphology, with no apparent effect of oxidation and reduction.

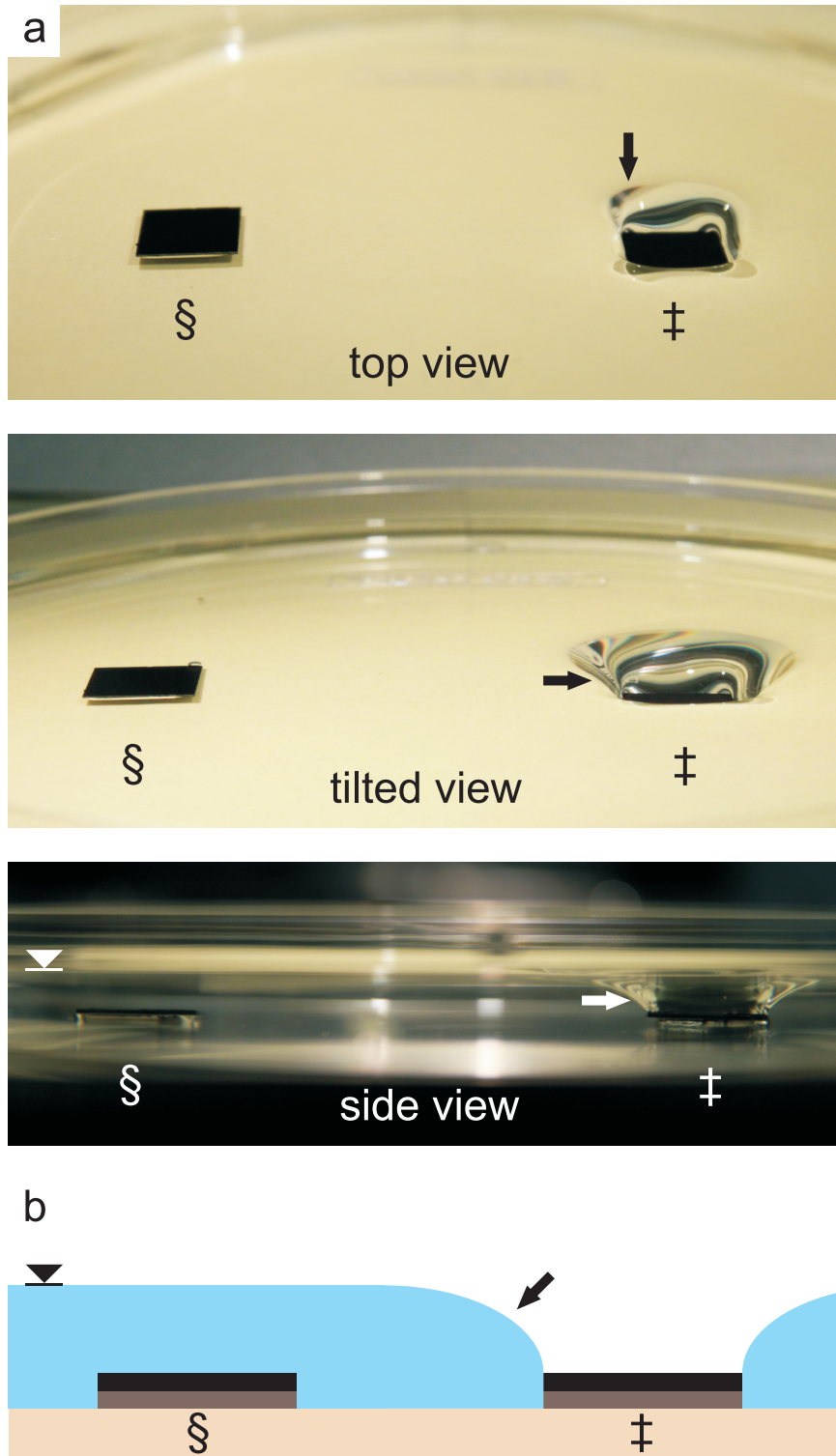


Figure 3.22. (a) Top view, tilted view, and side view of an as-grown CNT array (denoted by §) and a superhydrophobic CNT array (denoted by ‡). (b) Schematic of (a) that highlights the deformation of water free surface (indicated by an arrow) near the surface of superhydrophobic carbon nanotube array.

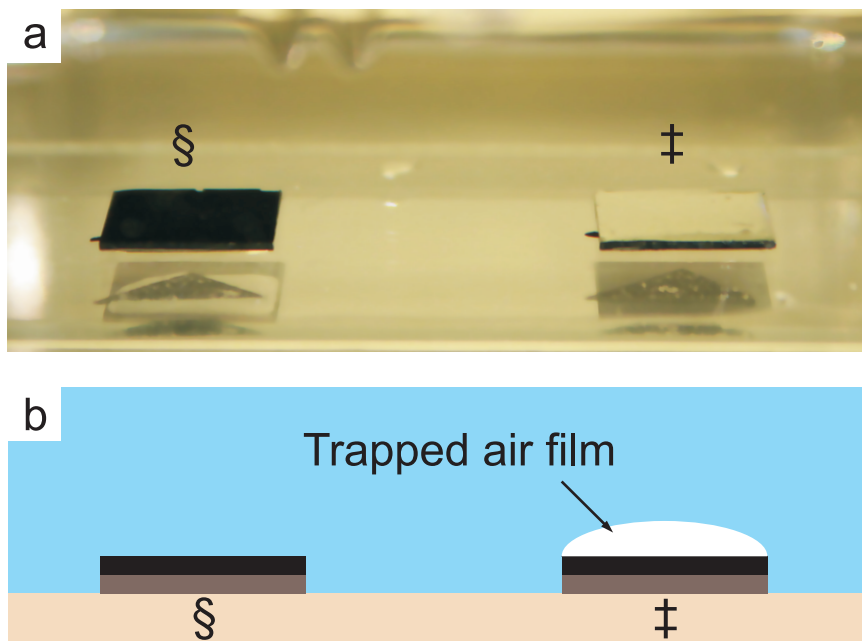


Figure 3.23. (a) Tilted view of an as-grown CNT array (denoted by §) and a superhydrophobic CNT array (denoted by ‡). (b) Schematic of (a) that highlights the presence of a film of trapped air at the interface between water and the surface of superhydrophobic carbon nanotube array.

hydrophobicity is slightly less than that of superhydrophobic CNT arrays, show their original black color.

According to Luo et al. (2010) and McHale et al. (2010), a bright region on the surface of CNT arrays corresponds to a strong light reflection, due to the presence of a thin air cushion trapped between water and the surface. Judging from the size of the reflective area, it can be confirmed that the entire surface of the arrays is covered by a continuous layer of air. This trapped air cushion keeps the entire surface completely dry and prevents a direct contact between water and the surface to be made anywhere on the surface. Indeed, this air film is the signature interface of an ideal Cassie state superhydrophobic surface.

It is widely known that superhydrophobicity of a surface can be explained by Cassie state, Wenzel state, or a transition between these two states (Lafuma and Quere, 2003; Wang and Jiang, 2007). For both states, the static contact angle for water is very high, typically higher than  $150^\circ$  (Wang and Jiang, 2007; Bhushan et al., 2009). In the case of a Cassie state, there exists a liquid-vapor-solid interface between

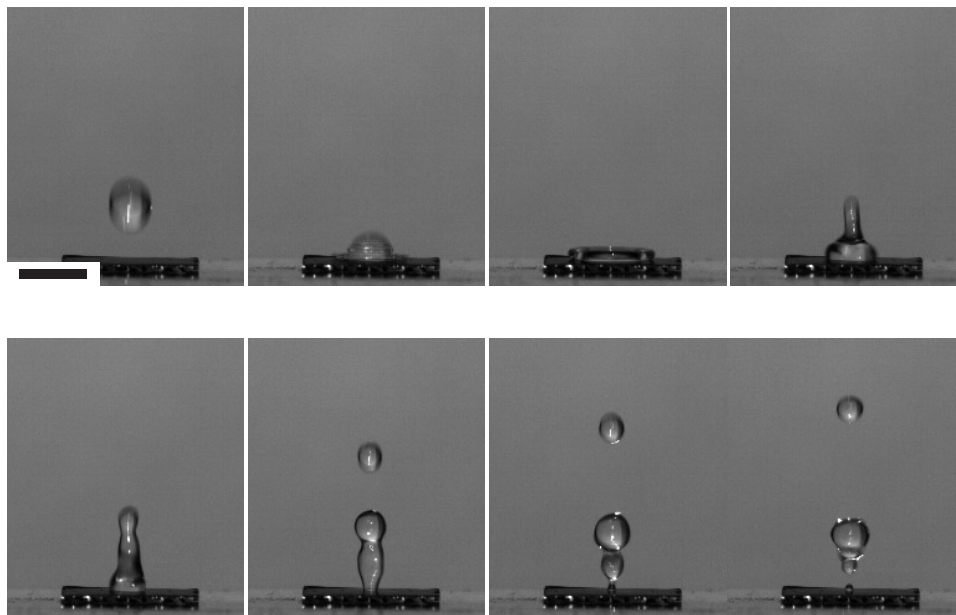


Figure 3.24. (a) Time-lapse images of the water droplet impacting the surface of as grown CNT arrays. Scale bar indicates 5 mm.

water and the surface, such that only a tiny fraction of water is in a direct contact with the surface asperities. Because of such interface, the adhesion between water and the surface is negligible. Hence, both contact angle hysteresis and roll-off angles for water are very low, typically lower than  $10^\circ$ . In the case of a Wenzel state, the interface between water and the surface is dominated by a liquid-solid interface, such that water is always in intimate contact with the surface asperities. This results in a high adhesion between water and the surface such that both contact angle hysteresis and roll-off angles for water are high.

To demonstrate that the dry oxidized and vacuum annealed treated CNT arrays are, indeed, hydrophilic and hydrophobic respectively, the dynamic effect of a free-falling water droplet on the surface of these CNT arrays was qualitatively compared. As a free-falling water droplet hits the surface of the hydrophobic as-grown arrays, it deforms heavily and then bounces off the surface (Figure 3.24). However, because the as-grown arrays are just hydrophobic, there is always a small portion of the droplet pinned to the surface, preventing the droplet from bouncing off completely from the surface. This pinning phenomenon was more pronounced when the water droplet hit

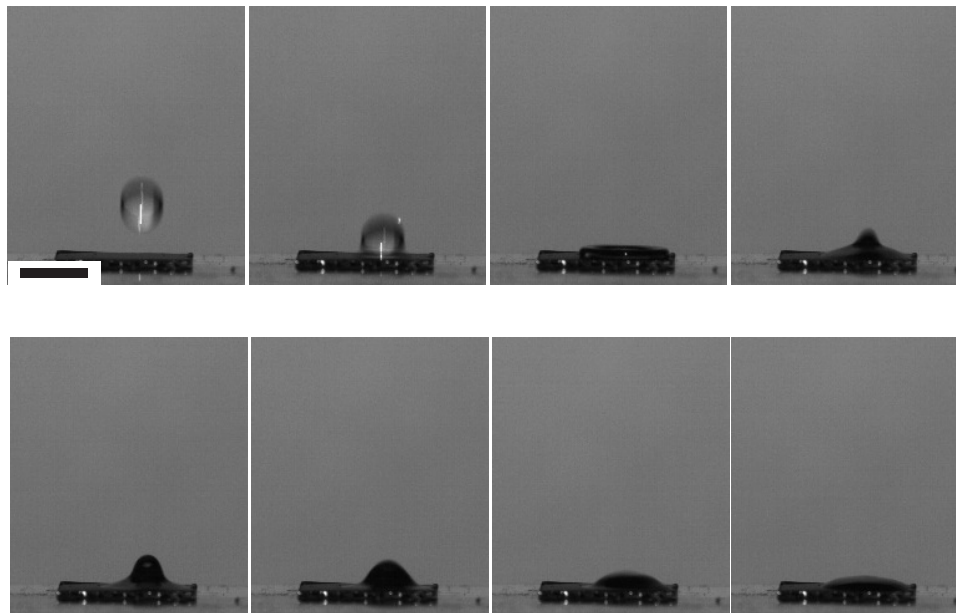


Figure 3.25. (a) Time-lapse images of the water droplet impacting the surface of hydrophilic CNT arrays. Scale bar indicates 5 mm.

the surface of the more hydrophilic CNT arrays. For example, on the CNT arrays with an average static contact angle of  $30^\circ$ , the droplet is always pinned to the surface and comes to rest shortly after the impact (figure 3.25). A totally different behavior is observed on superhydrophobic CNT arrays, where the free-falling water droplet bounces completely off the surface (Figure 3.26). In contrast to another published study (Jung and Bhushan, 2008), the droplet pinning does not occur on the superhydrophobic CNT arrays, even at a considerably high impact velocity of  $2.22\text{m.s}^{-1}$ . Detailed investigation of water droplet impact behavior on superhydrophobic CNT arrays can be read in Chapter 5.

### 3.3.7 Dispersibility and zeta potential analysis

The dispersions of the dry oxidized and vacuum annealed CNT arrays in DI water were investigated to further verify their wetting properties. Dispersion of CNT in DI water from CNT arrays with different wettability is qualitatively compared. As expected, the floating clump of CNT on the surface of the water column indicated that the CNT taken from the superhydrophobic vacuum annealed CNT arrays are

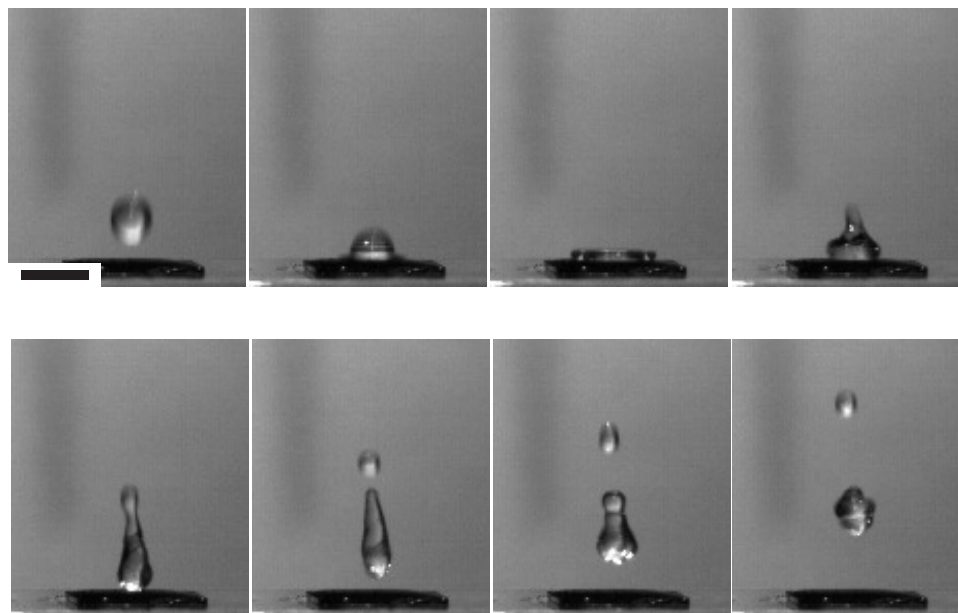


Figure 3.26. (a) Time-lapse images of the water droplet impacting the surface of superhydrophobic CNT arrays. Scale bar indicates 5 mm.

indeed extremely hydrophobic (Figure 3.27.a). Just like any other highly hydrophobic substances, the extremely hydrophobic CNT clump up together to minimize the interface area between the CNT and water. Similar to the phenomenon observed when these superhydrophobic CNT arrays are immersed in a deep pool of water, there exist large scale air pockets encapsulating them such that their effective density becomes extremely low. Consequently, they are always found to float on the surface of water, even after being subjected to ultrasonication. Interestingly, by floating, the interface area between the CNT and water is decreased even further.

Similarly, the hydrophobic CNT from the as-grown CNT arrays could not be dispersed easily in DI water, although a different behavior can be observed. Instead of floating, these hydrophobic CNT are completely submerged in the water column (Figure 3.27.b). The dispersibility of these hydrophobic CNT in DI water was unquestionably higher than that of superhydrophobic CNT. Since these CNT have a higher concentration of oxygenated groups than that of superhydrophobic CNT, they are more polar and are not encapsulated inside large scale air pockets. However, they are still clumping up together to minimize the interface area between the CNT and

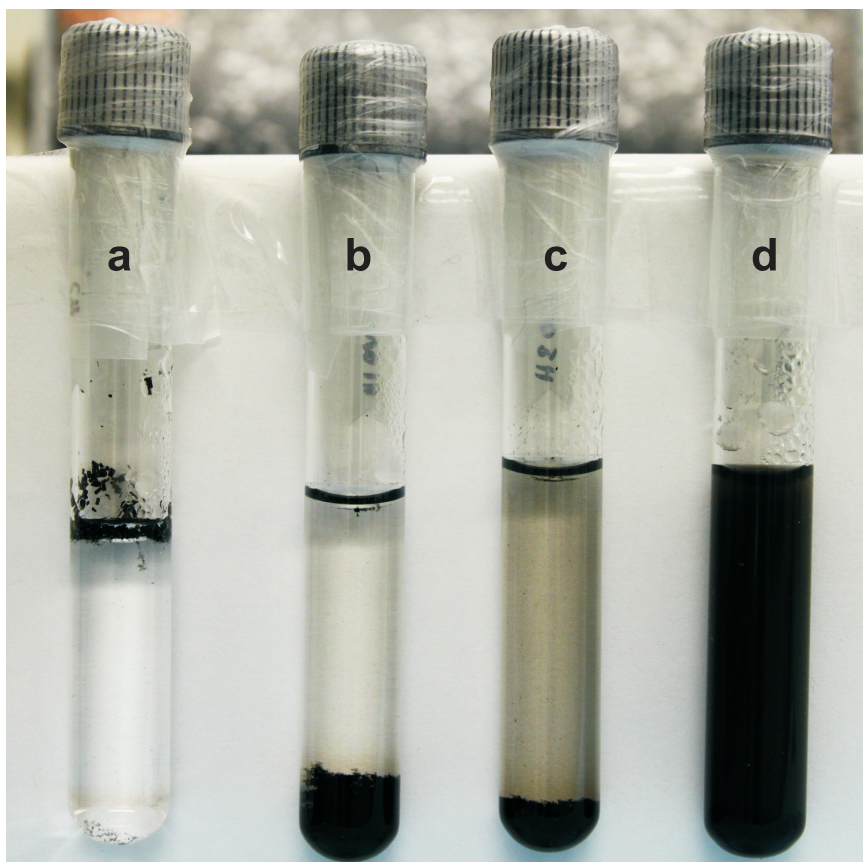


Figure 3.27. Dispersion of CNTs with various wetting properties in DI water. The wettability of the CNT increases from left to right. The nanotubes from (a) cannot be dispersed in DI water. The nanotubes from (b) and (c) arrays precipitated in several hours and days, respectively, after the dispersions were performed. The dispersion of nanotubes from (d) arrays was found stable even after more than two months.

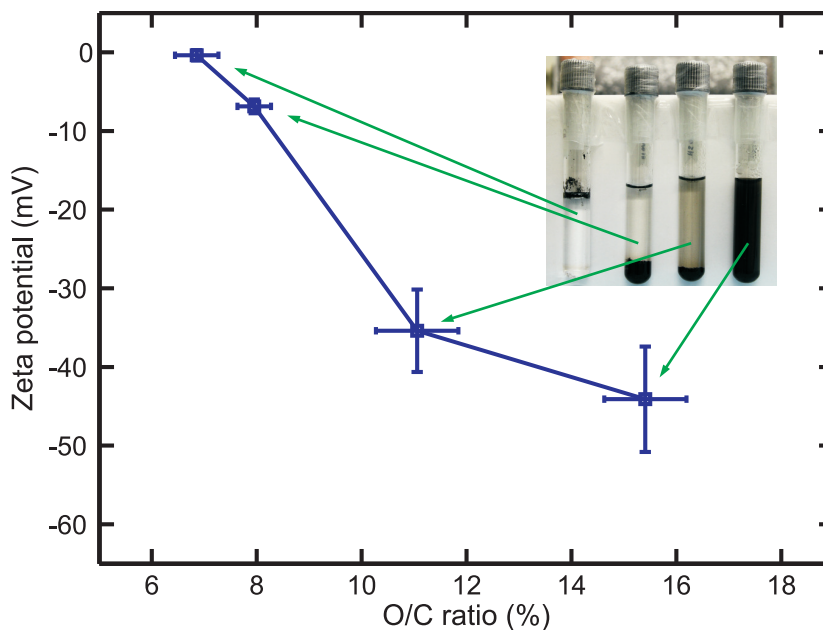


Figure 3.28. Plot of zeta potential of CNTs with various wetting properties in DI water as a function of their oxygen/carbon atomic ratio.

water. Consequently, their effective density becomes higher than water and, instead of floating, they are sinking into the bottom of the water column and immediately forming sedimentation.

A better dispersibility is shown by hydrophilic CNT from the CNT arrays, with an average static contact angle of  $75^\circ$ . Although sedimentation of CNT is still observable, a small fraction of the CNT is already well dispersed. This behavior can be observed from the color of the dispersion, which has turned dark and is no longer clear (Figure 3.27.c). Obviously, the CNT dispersibility can be improved by exposing them to a longer UV/ozone or oxygen plasma treatment. For example, the CNT from the highly hydrophilic CNT arrays with an average static contact angle of  $30^\circ$  can be dispersed quite easily in DI water. In agreement with works by Naseh et al. (2010) and Chen et al. (2010), dispersion of hydrophilic CNT from the highly hydrophilic CNT arrays is very stable and does not form sedimentation even after two months of settling time (Figure 3.27.d).

The dispersibility of CNT arrays in DI water can be quantified by their zeta potential measurement. Zeta potential is a measure of electric potential that is exhibited

by any particle in suspension and is measured by the difference of potential at the slipping plane and the bulk suspension medium. Particles with higher magnitude of zeta potential, either positive or negative, have the tendency to repel each other such that they do not coagulate or flocculate. On the other hand, the closer the magnitude of zeta potential to zero, the less dominant the repulsive force is. Hence, they have a higher tendency to coagulate or flocculate. Since the magnitude of the zeta potential gives an indication of the stability of the dispersion, it is expected that the zeta potential of a dispersion of hydrophilic dry oxidized CNT in DI water will be quite high. In contrast, a dispersion of superhydrophobic vacuum annealed CNT in DI water is expected to exhibit a near zero zeta potential.

As expected, the zeta potential of a dispersion of superhydrophobic CNT with an average O/C ratio of 7% in DI water is almost zero. In agreement with the qualitative observation of the dispersion, a near zero zeta potential means that the dispersion is highly unstable and the superhydrophobic CNT coagulate rapidly in DI water. The value of zeta potential of CNT dispersion decreases monotonically as the increase of O/C ratio (Figure 3.28.c). An increase of O/C ratio by 1% results in an decrease of zeta potential by 10mV. For the dispersion of hydrophilic CNT with an average O/C ratio of 11%, its zeta potential is measured to be -36mV, which in theory should exhibit a moderate stability. Indeed, as observed qualitatively, these hydrophilic CNT exhibit a better dispersibility, although sedimentation of CNT is still observable on the bottom of the dispersion. Dispersion of highly oxidized CNT with an average O/C ratio of 15.5% exhibits a zeta potential of -45mV, which in theory indicates a good dispersion stability. Indeed, qualitative observation confirms that the dispersion of highly oxidized CNT is stable even for more than two months of settling time.

### 3.3.8 Electrochemical impedance

The electrochemical characterization was conducted to provide additional insight on the effect of dry oxidation and vacuum annealing treatments to the physiochemical properties of CNT arrays. It has been known that hydrophobic CNT exhibit a very

low electrochemical capacitance in aqueous solution and the presence of carboxyl groups may increase such capacitance by a factor of three (Kim et al., 2005). In agreement with that study, the impedance of CNT arrays was found to be highly dependent on their wettability. In other words, the impedance of the CNT arrays in aqueous electrolytes can be varied by manipulating the surface concentration of oxygenated functional groups via dry oxidation and vacuum annealing treatments.

The Bode impedance plot of the electrochemical impedance spectroscopy (EIS) data in 1M NaCl aqueous electrolyte shows that the superhydrophobic CNT arrays yield much higher impedance than the hydrophilic counterpart. The difference in impedance can be observed clearly at considerably low frequency of  $f < 1$  kHz, where the effect of double layer capacitance becomes increasingly dominant. In fact, the frequency at which the transition from pure resistive behavior to a capacitive-resistive behavior decreases with the increase of wettability of the array. Such a transition can be observed from the absolute impedance of the CNT arrays, where a pure resistive behavior is indicated by a constant absolute impedance over a large frequency range, and a capacitive-resistive behavior is indicated by an exponential increase of absolute impedance with the exponential decrease of frequency (Figure 3.29.a). This transition can also be seen from the change in phase angle of the impedance (Figure 3.29.b), where a pure resistive behavior is indicated by a constant phase angle over a large frequency range, and a capacitive-resistive behavior is indicated by an exponential decrease of phase angle with the exponential decrease of frequency. Based on these two plots, it is obvious that the transition for the superhydrophobic CNT arrays occurs at a frequency of about 1.5 kHz, while the transition for the highly hydrophilic CNT arrays occurs at a much lower frequency of about 45 Hz.

The change in transition frequency as the change in wettability of CNT arrays can also be observed from the Nyquist impedance plot of the EIS data in the high frequency regime (Figure 3.30.c). The Nyquist plot of the superhydrophobic CNT arrays shows a transition from pure resistive behavior to a capacitive-resistive behavior at a frequency of 108.6 kHz. This transition frequency is shifted down as the wettability of CNT arrays improves. In fact, the Nyquist plot of the as-grown CNT arrays

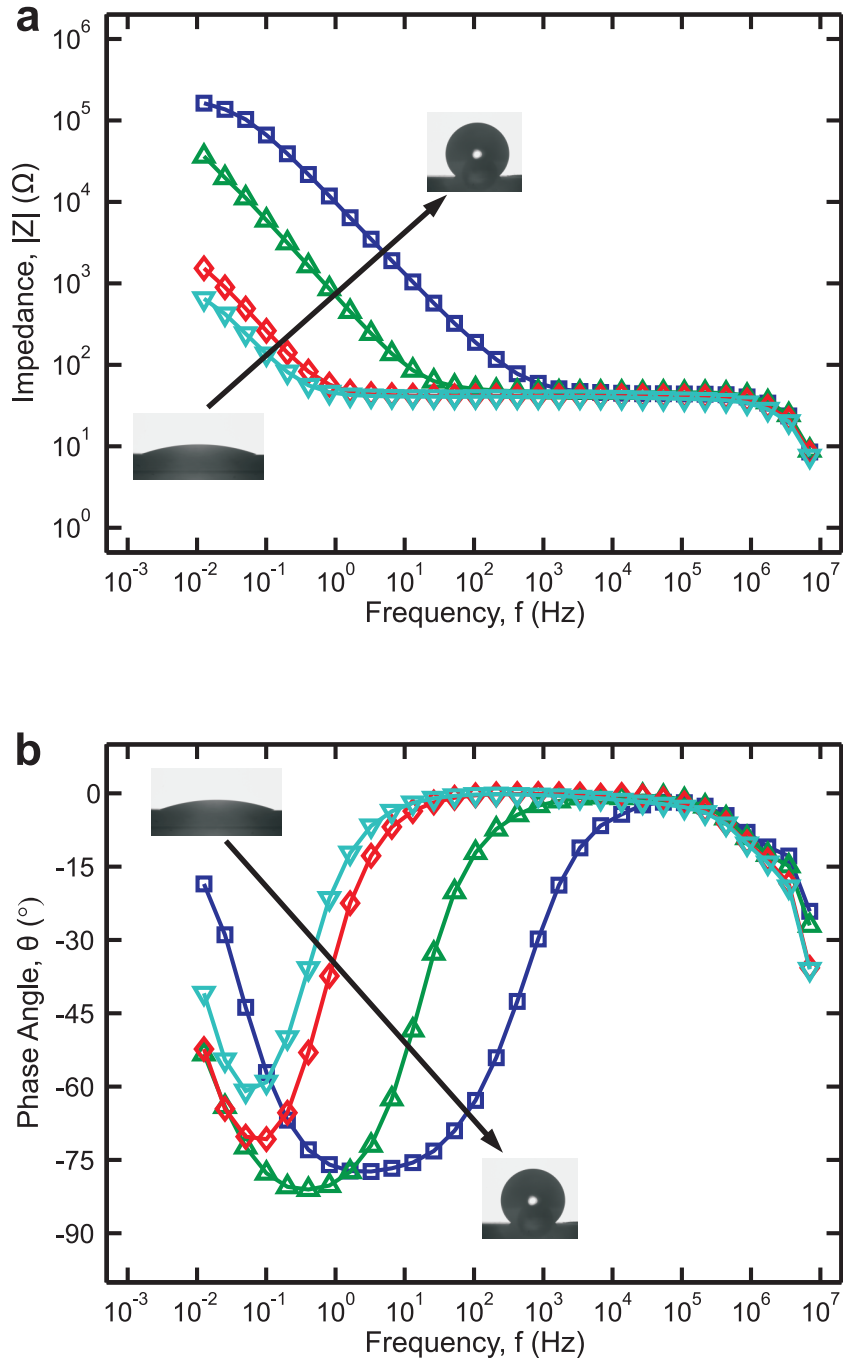


Figure 3.29. Bode plot of CNT arrays with various wettability in DI water. Plot of magnitude of impedance (a) and phase angle (b) as a function of the applied alternating electric field frequency.

shows a transition at a frequency of 27 kHz. Similarly, the Nyquist plot of the mildly hydrophilic and highly hydrophilic CNT arrays shows a transition at a frequency of 841.4 Hz and 209.8 Hz respectively. This behavior suggests that the transition frequency decreases rapidly with the decrease of static contact angle of CNT arrays in the high static contact angle regime, and it decreases slowly in the low static contact angle regime.

The absolute impedance of the superhydrophobic CNT arrays at a very low frequency is measured to be about three orders of magnitude higher than that of the hydrophilic CNT arrays at the same frequency. Indeed, at a frequency of about 13 mHz, the absolute impedance of the superhydrophobic CNT arrays is about  $160\Omega$ , while that of the highly hydrophilic CNT arrays is about  $650\Omega$ . The extremely large discrepancy of absolute impedance at lower frequency suggests that the double layer capacitance of superhydrophobic CNT arrays is much smaller than that of hydrophilic CNT arrays. The double layer capacitance can be approximated by fitting the Nyquist diagram with the Randles equivalent electrical circuit for both low-frequency regime (Figure 3.30.a and Figure 3.30.b), and high frequency regime (Figure 3.30.c). The Randles equivalent electrical circuit consist of an electrolyte resistance ( $R_s$ ) in series with the parallel combination of the double-layer capacitance ( $C_{dl}$ ) and an impedance of a faradaic reaction. The impedance of a faradaic reaction itself consist of a charge transfer resistance ( $R_{ct}$ ) and a specific electrochemical element of diffusion ( $W$ ). In short, Randles equivalent electrical circuit can be represented as  $((R_{ct}+W)/C_{dl})+R_s$  circuit. Since  $R_s$  and  $W$  are a function of the electrolyte, their values are constant for exactly the same electrolyte.

The fit of  $((R_{ct}+W)/C_{dl})+R_s$  circuit to the Nyquist diagram of CNT arrays with different wettability reveals a monotonic increase of double layer capacitance and monotonic decrease of charge transfer resistance as the increase of O/C ratio of the CNT arrays. For superhydrophobic CNT arrays with an average O/C ratio of 6.5%, the double layer capacitance is found to be extremely low at  $2 \times 10^{-5}$  F (Figure 3.31.a), while the charge transfer resistance is extremely high at  $2 \times 10^5\Omega$  (Figure 3.31.b). For highly hydrophobic CNT arrays with an average O/C ratio of

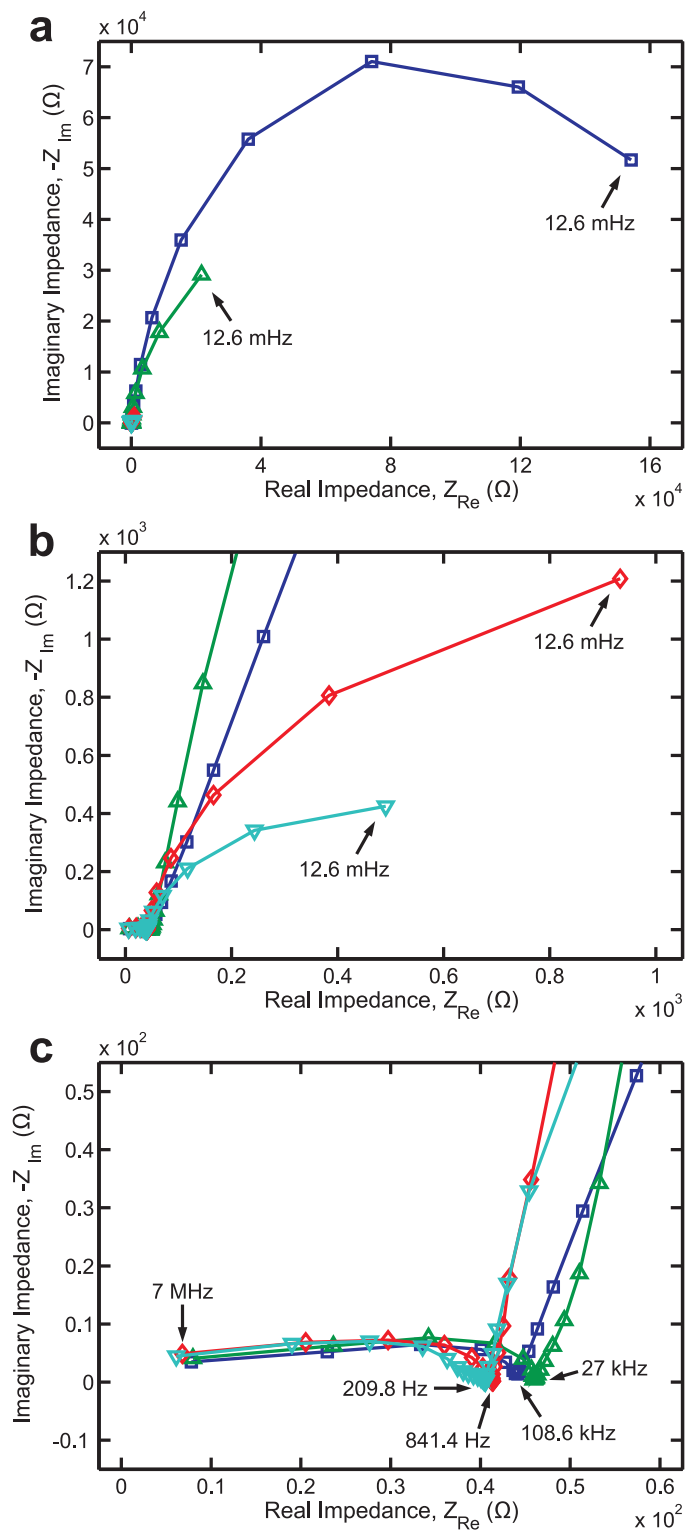


Figure 3.30. Nyquist plot of CNT arrays with various wettability in DI water. Plot of imaginary part versus real part of impedance for hydrophobic CNT arrays (a) and hydrophilic CNT arrays (b) at low-frequency range. Plot of the same at high-frequency range (c).

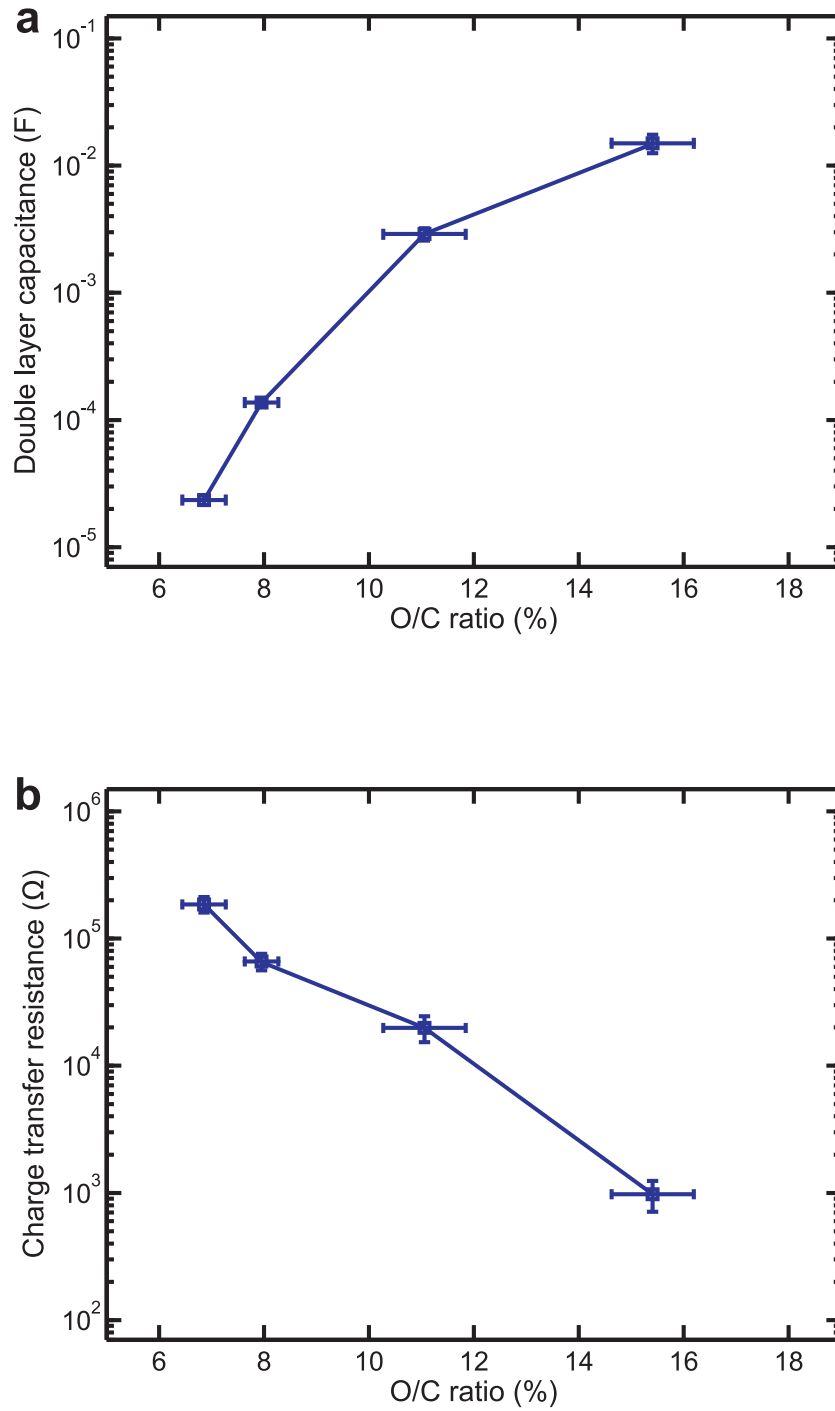


Figure 3.31. Double layer capacitance (a) and charge transfer resistance (b) of CNTs with various wetting properties in DI water as a function of their oxygen/carbon atomic ratio.

8%, the double layer capacitance is found to be an order of magnitude higher at  $1.5 \times 10^{-4}$  F, while the charge transfer resistance decreases to  $6 \times 10^4 \Omega$ . Further increase in O/C ratios improves both double layer capacitance and charge transfer resistance by several orders of magnitude. For highly hydrophilic CNT arrays with an average O/C ratio of 15.5%, the double layer capacitance is found at  $1.5 \times 10^{-2}$  F, while the charge transfer resistance is found at  $1 \times 10^3 \Omega$ . The effect of oxygenated groups on the double layer capacitance of CNT arrays will be discussed in detail in Chapter 6.

This finding is expected because of the presence of a thin film of air on the interface between the bulk surface of the superhydrophobic CNT array and the aqueous electrolyte, which inhibits electrons transfer from the arrays and blocks protons in the electrolyte to approach the surface of the array (Kim et al., 2005). In addition, this thin air film significantly reduces the effective contact area between the surface of the CNT and the electrolyte molecules, which results in a much smaller effective area of Helmholtz layer and a dramatic decrease of double layer capacitance. Thus, the double layer capacitance of the superhydrophobic CNT arrays is measured more than two orders of magnitude smaller than that of the hydrophilic CNT arrays. Similarly, the charge transfer resistance of the superhydrophobic CNT arrays is measured more than two orders of magnitude larger than that of the hydrophilic CNT arrays.

### 3.4 Concluding Remarks

In conclusion, the findings reported herein show that the wetting properties of CNT arrays can be tuned easily and precisely using a combination of dry oxidation and vacuum annealing treatments. By varying the exposure time of these treatments, the surface concentration of oxygenated functional groups adsorbed on the CNT arrays can be controlled. CNT arrays with very low amount of oxygenated functional groups exhibit a superhydrophobic behavior. In addition to their extremely high static contact angle, they cannot be dispersed in DI water, and their impedance in aqueous electrolytes is extremely high. These arrays have an extreme water repellency capabil-

ity, such that a water droplet will bounce off of their surface upon impact and a thin film of air is formed on their surface as they are immersed in a deep pool of water. In contrast, CNT arrays with very high surface concentration of oxygenated functional groups exhibit an extreme hydrophilic behavior. In addition to their extremely low static contact angle, they can be dispersed easily in DI water, and their impedance in aqueous electrolytes is tremendously low. Since the graphitic structures and vertical alignment of the CNT arrays are maintained during the dry oxidation and vacuum annealing treatments, all CNT arrays can be switched repeatedly between hydrophilic and hydrophobic, as long as their O/C ratio is kept below 18%.

## Chapter 4

# Etching and Amorphization of Carbon Nanotube Arrays by Irreversible Oxidation

### 4.1 Introduction

As described in detail in Chapter 3, the bulk wettability of CNT arrays can be tuned straightforwardly via a combination of dry oxidation and vacuum annealing treatments. A combination of dry oxidation and vacuum annealing treatments is capable of switching repeatedly the wettability of CNT arrays between hydrophilic and hydrophobic, as long as their O/C ratio is kept below 18%. The findings presented in this chapter show the effect of oxidation to the CNT structure when its O/C ratio goes higher than 18%. Basically the CNT side walls are heavily functionalized with stable oxygenated groups that are difficult to remove at an O/C ratio higher than 18%. At an even higher O/C ratio, etching processes start to occur such that large-scale holes are formed on the CNT walls, and the CNT walls are eventually transformed from graphitic to amorphous structure. The evolution of the CNT structure at a wide range of O/C ratio is elucidated by means of XPS, Raman spectroscopy, TEM, and BET and Langmuir surface area.

## 4.2 Materials and Methods

In this study, the effect of oxidation on the structure of CNT arrays at a wide range of oxidation level is examined. As explained in Chapter 3, the oxidation level of CNT arrays is quantified by their oxygen/carbon atomic ratio (O/C ratio). Here, the O/C ratio of CNT arrays is varied between 8% and 55%. Such a wide range of oxidation level is achieved by exposing the as-grown CNT arrays to a prolonged period of oxygen plasma treatment. An O/C ratio of 8% is obtained from the as-grown CNT arrays, while an O/C ratio of 55% is obtained from the heavily oxidized CNT arrays. The detailed methods for oxidizing CNT arrays using oxygen plasma treatment can be read in Chapter 2.2.1. The O/C ratio is calculated from a low resolution XPS survey spectra acquired at a binding energy of 1-1000eV. The detailed methods for O/C ratio measurements can be read in Chapter 2.3.6.

Four steps of analysis were performed to elucidate the structural evolution of CNT arrays as they underwent a prolonged oxidation process. For the first step of analysis, the surface chemistry of the dry oxidized CNT arrays is characterized using high resolution XPS at C 1s binding energy of 280-298 eV. Deconvolution of the C 1s high resolution spectra is performed using a Gaussian-Lorentzian peak shape fitting with Shirley baseline correction. This XPS characterization is performed to highlight the change in concentration of different types of C-C bonds and oxygenated groups chemisorbed by the CNT array as they undergo a prolonged exposure to oxygen plasma treatment. Such change in concentration is visualized by plotting the peak position of C 1s binding energy against the O/C ratio. The relative surface concentration of C-C sp<sup>2</sup>, C-C sp<sup>3</sup>, C-O, and C=O bonds is also plotted against the O/C ratio. This relative surface concentration is measured by integrating the area under the curve of each bond. The detailed methods for XPS characterization can be read in Chapter 2.3.6.

For the second step of analysis, Raman spectroscopy analysis is performed on the oxidized CNT arrays. Each set of CNT arrays with different oxidation levels is excited using Ar ion laser at 514.5 nm through optical microscope under a non-

polarized mode. Three distinct peaks of D band ( 1350cm<sup>-1</sup>), G band ( 1585cm<sup>-1</sup>), and G' band ( 2695 cm<sup>-1</sup>) can be seen in the Raman spectra of CVD graphene before and after oxidation. The effect of oxidation to the increase of defect site density is quantified by normalizing the integrated area of D band and G' band with that of G band. The detailed methods for Raman spectroscopy characterization can be read in Chapter 2.3.4.

For the third step of the analysis, transmission electron microscopy (TEM) analysis is performed to give an insight into the atomic structure of CNT with different oxidation levels. High magnification imaging was performed under bright field forward scattered electrons mode with acceleration voltage of 300kV. Prior to imaging, a small amount of CNT is collected from each set of oxidized CNT arrays by scraping them physically with tweezers. These CNT samples are then dispersed in 200 proof ethanol with the help of ultrasonication for about five minutes. Selected area diffraction patterns are also collected from each set of oxidized CNT to probe its crystalline structure. The detailed methods for TEM characterization can be read in Chapter 2.3.2. Selected area diffraction patterns (SADP) are also collected from each set of CNT, with different oxidation levels to verify their crystalline structure.

For the last step of analysis, the surface area of the dry oxidized CNT arrays is characterized by means of BET and Langmuir surface area. The surface area is calculated from the adsorption and desorption isotherm of nitrogen gas at a temperature of 77 K. Langmuir surface area is measured based on the assumption that the adsorbed nitrogen forms a single layer that conformally coats the available surface of the CNT. BET surface area is measured based on the assumption that the adsorbed nitrogen may form multi layers that conformally coat the available surface of the CNT. Therefore, the surface area measured using Langmuir method is typically larger than that measured using BET method.

## 4.3 Results and Discussion

### 4.3.1 X-ray photoelectron spectroscopy analysis

XPS analysis was conducted to elucidate the chemical composition of the oxidized CNT arrays. Deconvolution of the C 1s XPS spectra of CNT arrays shows seven distinct peaks associated with C-C sp<sup>2</sup> ( $284.5 \pm 0.1$  eV, FWHM 0.9 eV), C-C sp<sup>3</sup> ( $285.5 \pm 0.1$  eV, FWHM 1.3 eV), C-O ( $286.6 \pm 0.1$  eV, FWHM 1.4 eV), C=O ( $287.4 \pm 0.2$  eV, FWHM 1.4 eV), O-C=O ( $289.1 \pm 0.4$  eV, FWHM 1.7 eV), O-C(O)=O ( $290.3 \pm 0.4$  eV, FWHM 1.7 eV), and  $\pi - \pi^*$  ( $292.1 \pm 0.4$  eV, FWHM 1.6 eV) peaks (Peng and Liu, 2006; Naseh et al., 2010; Yang et al., 2009; Aria and Gharib, 2011). The C-C sp<sup>2</sup> peak is the signature of the graphitic structure of CNT, and the C-C sp<sup>3</sup> peak is typically associated with the presence of defects and functional groups. The C-O peak is typically associated with the presence of hydroxyl and epoxide groups on the CNT outer wall and cyclic ether at the edges of CNT defect sites (Hossain et al., 2012; Acik et al., 2011, 2010). The C=O peak indicates the presence of quinone and carbonyl groups at the edges of CNT defect sites (Acik et al., 2011). The O-C=O and O-C(O)-O peaks indicate the presence of carboxyl and carbonate terminating groups respectively. The  $\pi - \pi^*$  transition peak is associated with the graphite stacking between layers of the CNT wall and between neighboring CNT.

As explained in Chapter 3.3.4, the C 1s XPS spectra of CNT arrays with an average O/C ratio of lower than 16% exhibits an extremely strong C-C sp<sup>2</sup> peak and a mild C-C sp<sup>3</sup> peak (Figure 3.18 and Figure 3.19). In addition, peaks associated with C-O, C=O, O-C=O, and O-C(O)-O groups, as well as  $\pi - \pi^*$  transition, are considerably weak. Although the intensity of all peaks associated with oxygenated groups and C-C sp<sup>3</sup> peak increases as the increase of O/C ratio of CNT arrays, their intensity is, in general, weaker than that of the C-C sp<sup>2</sup> peak. Even at an O/C ratio of 16%, the C 1s XPS spectra of CNT arrays are still dominated by the strong C-C sp<sup>2</sup> peak.

In contrast, the C 1s XPS spectra of CNT arrays at higher O/C ratios are no longer dominated by the strong C-C sp<sup>2</sup> peak. The intensity of the C-C sp<sup>3</sup> peak

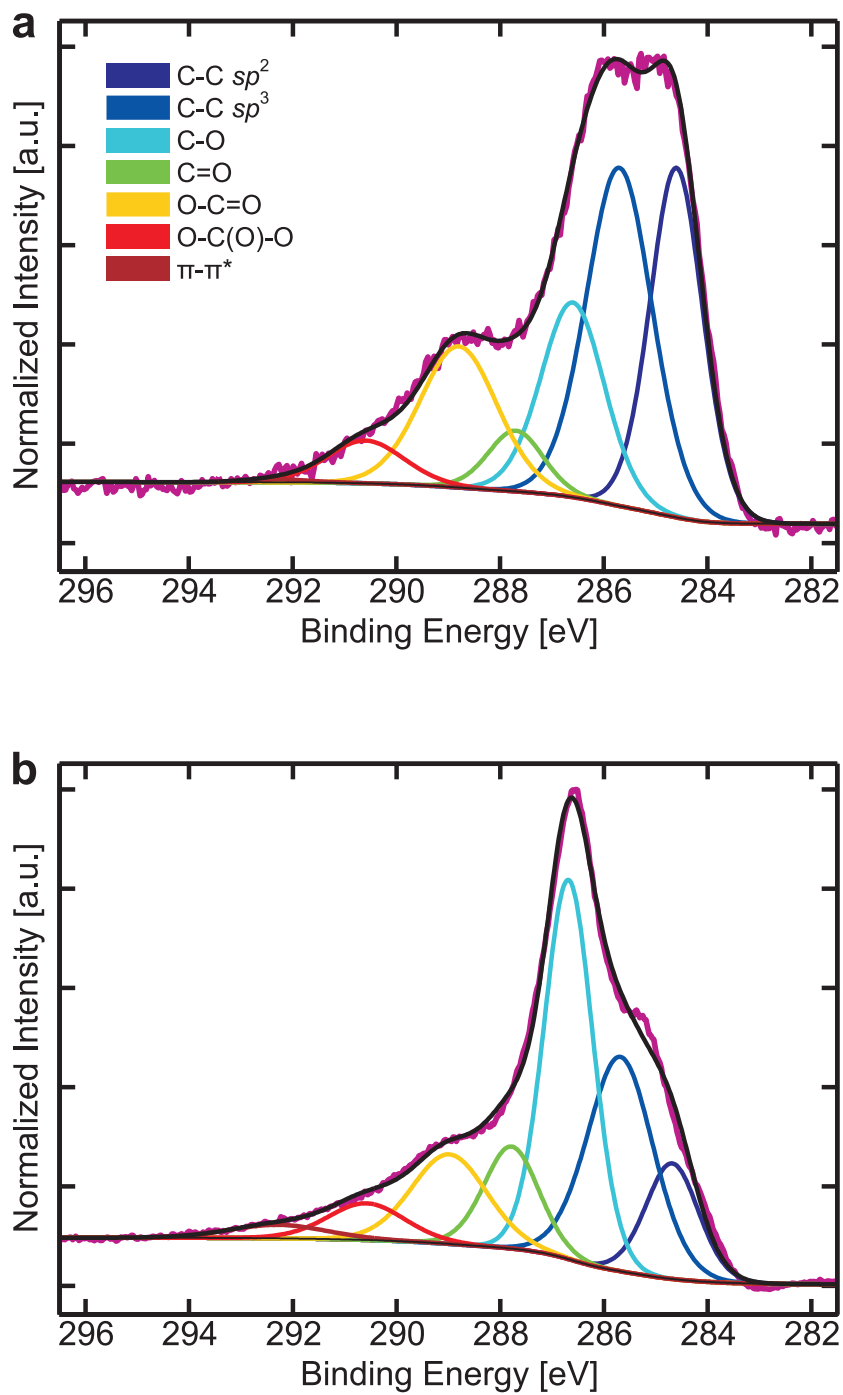


Figure 4.1. XPS spectra of oxidized CNT arrays with an average O/C ratio of 25% (a) and 38% (b).

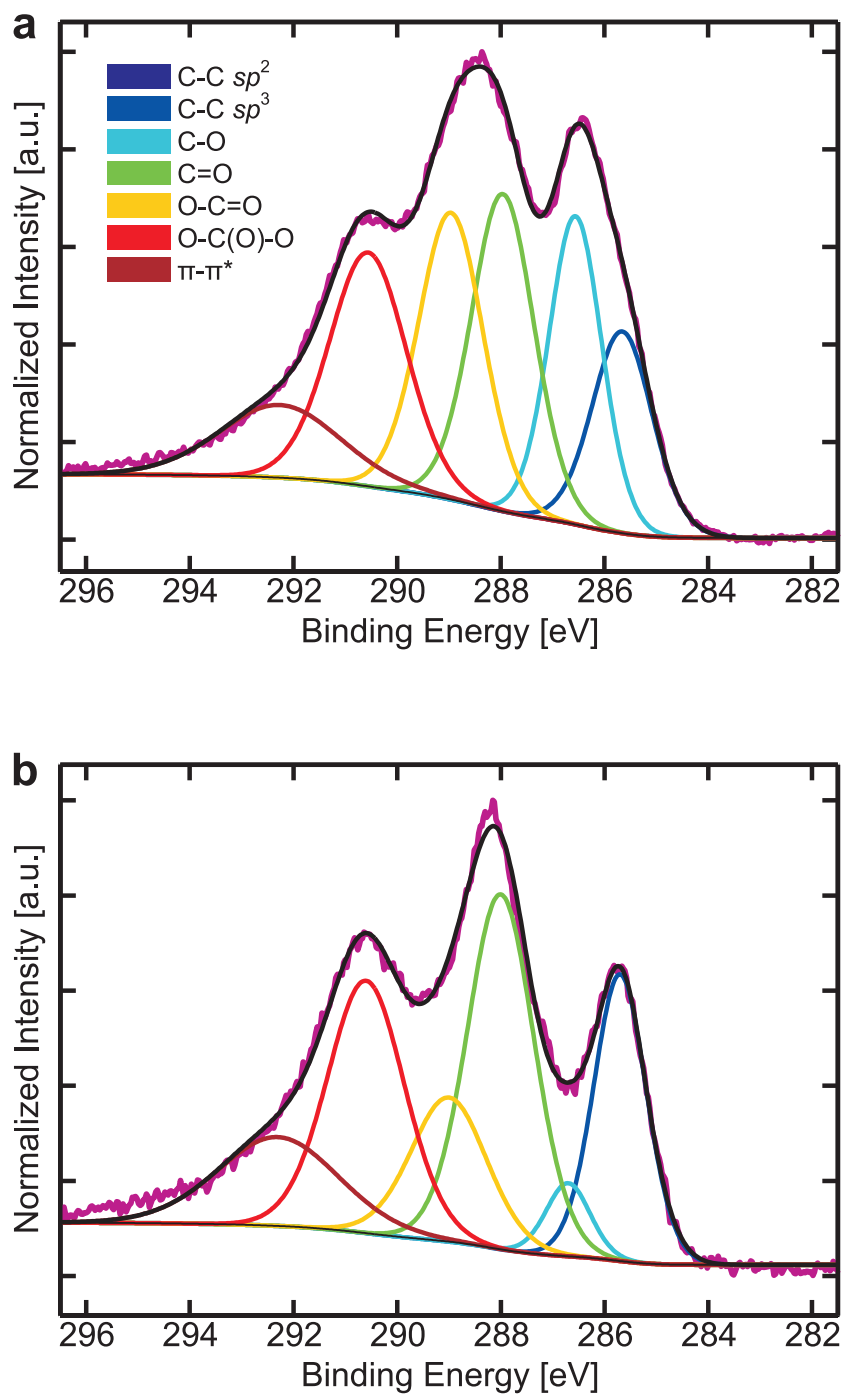


Figure 4.2. XPS spectra of oxidized CNT arrays with an average O/C ratio of 42% (a) and 55% (b).

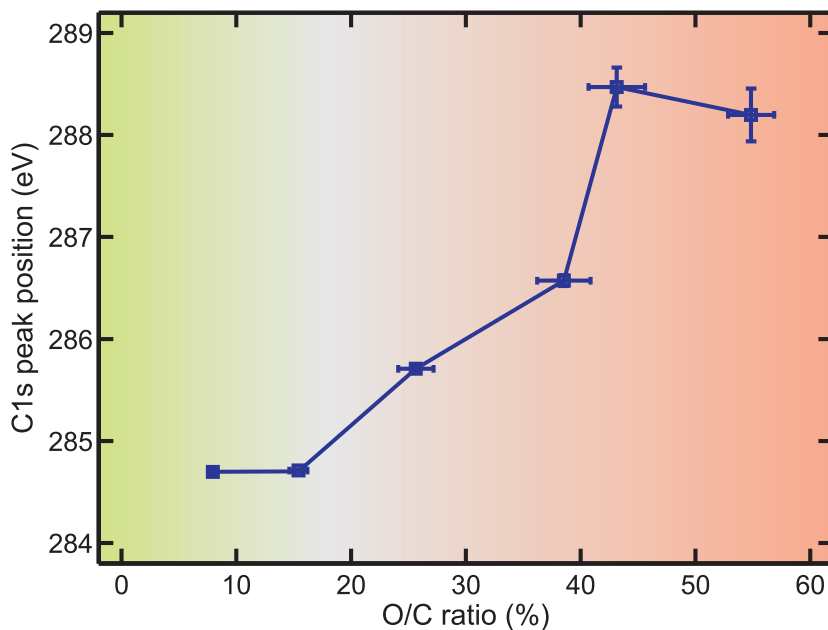


Figure 4.3. Plot of C1s peak position as a function of oxygen/carbon ratio.

and all oxygenated group peaks increases very rapidly, while the intensity of the C-C sp<sup>2</sup> peak decreases exponentially with the increase of O/C ratios. At an O/C ratio of 25%, the intensity of the C-C sp<sup>3</sup> peak is already about the same as that of the C-C sp<sup>2</sup> peak (Figure 4.1.a). In fact, the surface concentration of C-C sp<sup>3</sup> bonds is measured to be about 30%, which is about 5% higher than that of C-C sp<sup>2</sup> bonds (Figure 4.4). This phenomenon leads to a shift in the peak of C 1s XPS spectra to a higher binding energy. At this O/C ratio, the maximum for C 1s XPS spectra is shifted by 1eV from 284.7 eV to 285.7 eV (Figure 4.3). Such rapid increase in the intensity of the C-C sp<sup>3</sup> peak suggests a major transformation in the atomic structure of the CNT arrays. At this O/C ratio, their atomic structure is no longer dominated by the sp<sup>2</sup>  $\pi$ -bond network, but instead by the sp<sup>3</sup> hybridization.

The dramatic increase in concentration of sp<sup>3</sup> bonds can be attributed to the significant increase in concentration of chemisorbed oxygenated groups. For each epoxide group formed on the CNT outer wall, a transformation of one C-C bond from sp<sup>2</sup> carbon hybridization to sp<sup>3</sup> carbon hybridization occurs. An exact same transformation is also true for each formation of hydroxyl group. Such transformation

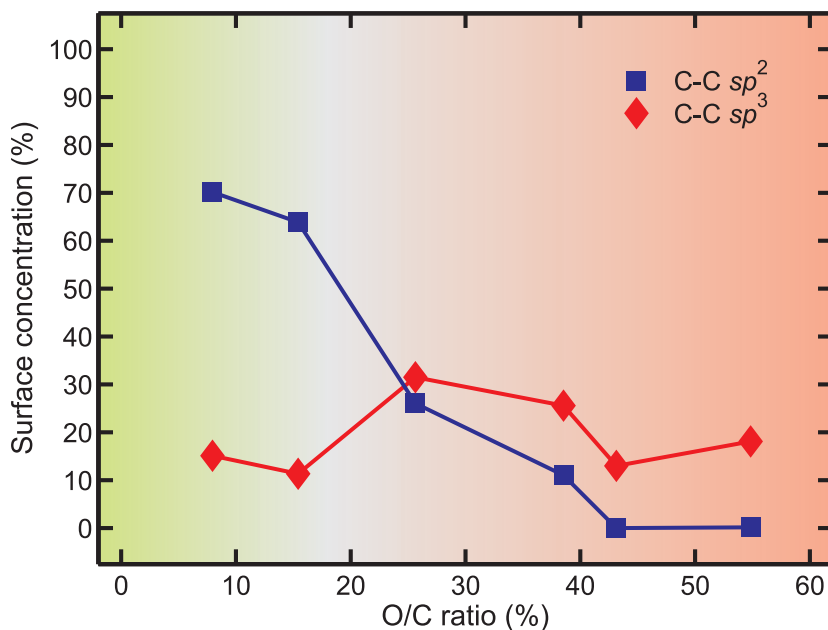


Figure 4.4. Plot of C-C  $sp^2$  and C-C  $sp^3$  concentration as a function of oxygen/carbon ratio.

can be, in principle, reversed by removing the chemisorbed epoxide or hydroxyl groups using vacuum annealing treatment. This transformation may induce excessive strain to the structure of the CNT because of the change in length of C-C bonds from the trigonal planar  $sp^2$  carbon hybridization to the tetragonal  $sp^3$  carbon hybridization (Vinogradov et al., 2011; Samarakoon and Wang, 2011; Suggs et al., 2011; Muniz and Maroudas, 2010).

Notice that the increase of intensity of the C-O and O-C=O bonds is considerably faster than that of the C=O and O-C(O)-O bonds. At an O/C ratio of 25%, the surface concentration of C-O bonds is found to be around 17%, which is about three times that of C=O bonds (Figure 4.5). This fact suggests that significant amounts of epoxide and hydroxyl groups are formed on the outer wall of the CNT, while a small amount of carbonyl groups are formed at the edges of CNT defect sites. Therefore, it is expected that at this O/C ratio, the defect density of CNT remains low.

It has been previously reported that the adsorbed oxygen atoms prefer to form epoxide groups on the CNT outer wall due to their stability at room temperature and pressure (Leconte et al., 2010; Vinogradov et al., 2011; Samarakoon and Wang, 2011).

Similarly, a strong O-C=O peak suggests a rapid formation of carboxyl terminating groups at the edges of CNT defect sites. These carboxyl groups are formed by a rapid reaction between carbonyl groups that already present at the edges of CNT defect sites, and hydroxyl radicals generated by the oxygen plasma treatment (Acik et al., 2011). As described in Chapter 3.3.4, a substantial amount of reactive hydroxyl radicals are generated by the UV/ozone and oxygen plasma treatments.

A dramatic transformation can be observed at a higher O/C ratio. At an O/C ratio of 38%, the intensity of the C-C sp<sup>2</sup> peak is considerably weaker than that of C-C sp<sup>3</sup> peak (Figure 4.1.b). In fact, the surface concentration of C-C sp<sup>2</sup> bonds is measured to be just around 10%, which is about one third that of C-C sp<sup>3</sup> bonds (Figure 4.4). This suggests that at this O/C ratio, the CNT  $\pi$ -bond network is no longer intact. The destruction of the  $\pi$ -bond network indicates a transition in the oxygen uptake process during the oxygen plasma treatment. At such high O/C ratios, etching or amorphization process occurs simultaneously as the functionalization process.

Notice that the C 1s XPS spectra is now dominated by the C-O bonds. The surface concentration of C-O bonds is measured as high as 35%, which is about three times higher than that of C=O and C-C sp<sup>2</sup> bonds (Figure 4.5). As a result, the maximum for C 1s XPS spectra is now shifted by another 0.9 eV from 285.7 eV to 286.6 eV (Figure 4.3). In addition to the formation of epoxide and carboxyl groups on the outer wall of CNT, such a high concentration of C-O bonds may also be attributed to the formation of cyclic ether groups that terminate the edges of CNT defect sites. The relative concentration of cyclic ether groups is expected to increase as the increase of defect sites density caused by the etching or amorphization process that takes place during the oxygen plasma treatment.

As the CNT arrays undergo an even longer oxygen plasma treatment to reach an even higher O/C ratio, the C-C sp<sup>2</sup> bonds start to disappear. At an O/C ratio of 42%, the surface concentration of C-C sp<sup>2</sup> bonds completely disappears and the remaining C-C bonds are in the form of sp<sup>3</sup> hybridization (Figure 4.4). The disappearance of C-C sp<sup>2</sup> bonds is also followed by the disappearance of C-O bonds. In fact, the surface concentration of C-O bonds at an O/C ratio of 42% is measured to be about

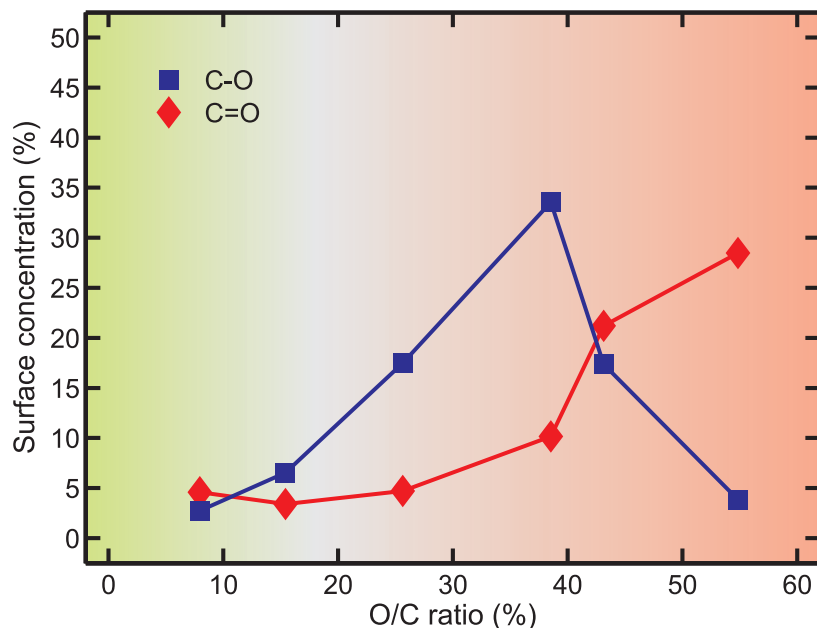


Figure 4.5. Plot of C-O and C=O concentration as a function of oxygen/carbon ratio.

17% (Figure 4.5). On the other hand, the surface concentration of C=O bonds jumps to about 17%. Since now the C 1s XPS spectra is dominated by the C=O and O-C(O)=O bonds (Figure 4.2.a), the maximum for C 1s XPS spectra is shifted to 288.6 eV (Figure 4.3).

Similarly, at an O/C ratio of 55%, no sign of C-C sp<sup>2</sup> bonds can be detected (Figure 4.4). The C-C bonds of the CNT is now completely in the form of sp<sup>3</sup> hybridization. This trend is also followed by the disappearance of C-O bonds. In fact, the surface concentration of C-O bonds at an O/C ratio of 55% is measured to be less than 4% (Figure 4.5). On the other hand, the surface concentration of C=O bonds continues to increase to about 30%. Similar to the C 1s XPS spectra of CNT with an O/C ratio of 42%, those of CNT with an O/C ratio of 55% is dominated by the C=O and O-C(O)-O bonds (Figure 4.2.b), and has a maximum at 288.2 eV (Figure 4.3). This implies that the CNT surface is now dominated by carbonyl and carbonate groups that are most likely to form at the edges of CNT defect sites.

The rapid increase of concentration of carbonyl groups at an O/C ratio higher than 40% indicates a transition in the oxygen uptake process during the oxygen plasma

treatment. At such high O/C ratios, the oxygen uptake process is dominated by etching and amorphization processes, not by the functionalization process of the CNT outer wall. Etching and amorphization processes introduce a significant amount of holes and defect sites on the CNT wall, which results in the formation of considerable amounts of carbonyl and carbonate groups. There is also a possibility that some of the epoxide groups are converted to carbonyl during a prolonged exposure of oxygen plasma treatment. It has been known that epoxide groups have the tendency to create pair structures which readily form two neighboring carbonyl groups in a quinone-like configuration (Samarakoon and Wang, 2011; Acik et al., 2011). Since carbonyl groups arranged in pairs are relatively stable, further reaction with atomic oxygen or hydroxyl radical is very unlikely.

### 4.3.2 Raman spectroscopy analysis

The increase in defect site density induced by oxygen plasma treatments can be verified by Raman spectroscopy. Four distinct peaks of D band (1350 $\text{cm}^{-1}$ ), G band (1585 $\text{cm}^{-1}$ ), G' band (2695  $\text{cm}^{-1}$ ), and D+D' band (2695  $\text{cm}^{-1}$ ) can be seen in the Raman spectra of CNT arrays with different oxidation levels (Figure 4.6). These peaks are the signature of graphitic structure of CNT. The G band is the Raman scattering due to strain in the  $\pi$ -bond network of CNT. The D band is the Raman scattering associated with disorder and non-sp<sup>2</sup> bonds of CNT. The G' band is the resonance of the G band (Ferrari et al., 2006; Reina et al., 2009; Dresselhaus et al., 2010; Nourbakhsh et al., 2010; Dresselhaus et al., 2010).

The quality of the CNT is commonly quantified by the ratio between the integrated area under the D band and the G band ( $I_D/I_G$ ). High quality CNT arrays typically exhibit  $I_D/I_G$  of less than unity. CNT arrays with lower  $I_D/I_G$  are in general better in terms of quality than those with higher  $I_D/I_G$ . Here, the quality of CNT arrays is defined as the defect density and degree of disorder of the CNT arrays. The strain acting on the  $\pi$ -bond network of the CNT can also be quantified by the ratio between the integrated area under the G' band and the G band ( $I_{G'}/I_G$ ). A higher ( $I_{G'}/I_G$ )

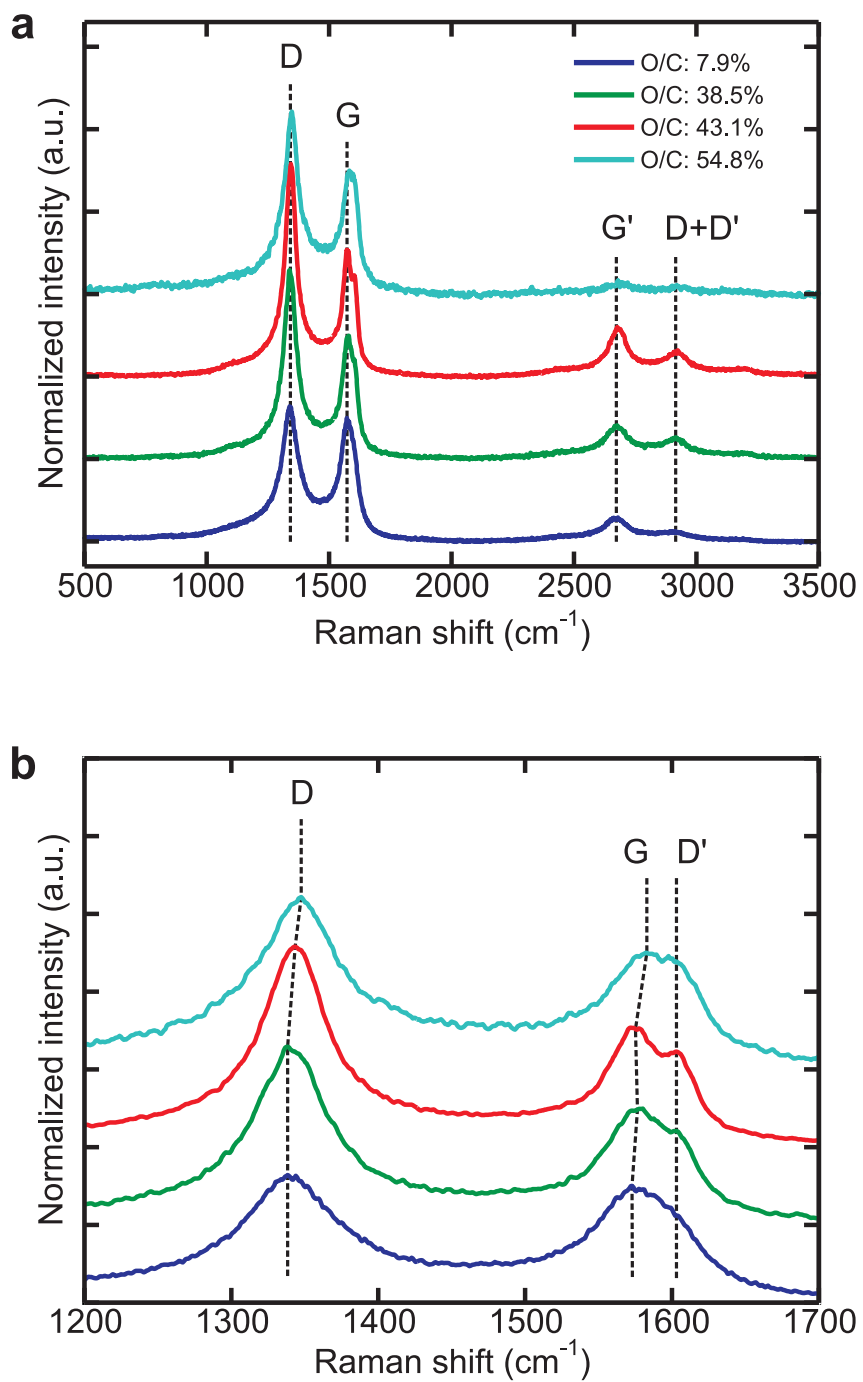


Figure 4.6. Raman spectra of CNT arrays with different oxidation level.

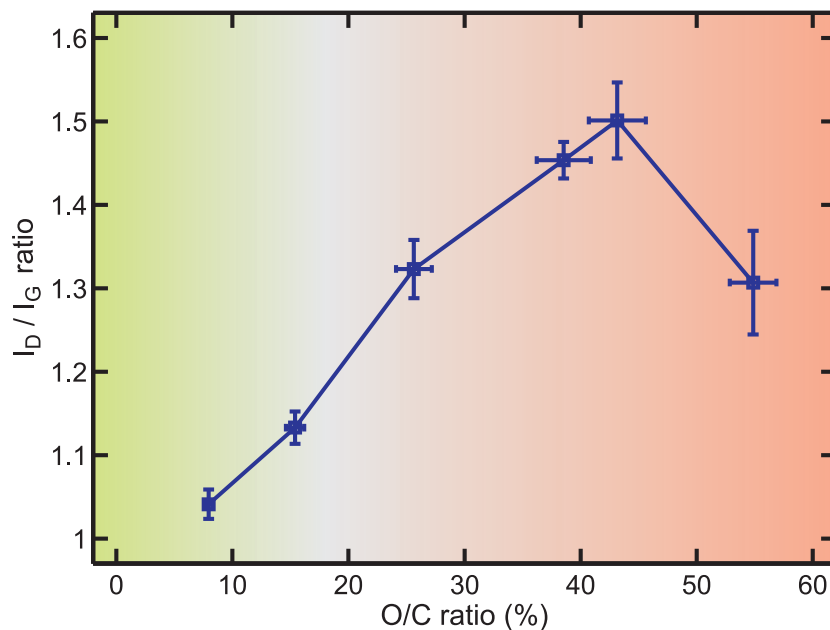


Figure 4.7.  $I_D/I_G$  ratio from Raman spectra of CNT arrays with different oxidation level.

indicates a higher strain acting on the CNT arrays, which may be caused by higher curvature or lattice mismatch.

In general CNT arrays exhibit strong D band and G band, with relatively weak G' band and D+D' band (Figure 4.6.a). The  $I_D/I_G$  for the as-grown CNT arrays with an O/C ratio of 8% is measured to be about 1.05, and their  $I_{G'}/I_G$  is measured to be about 0.25. The  $I_D/I_G$  and  $I_{G'}/I_G$  of CNT arrays start to increase once they are being exposed to oxygen plasmas treatment. An increase of O/C ratio from 8% to 42% results in an increase of  $I_D/I_G$  from 1.05 to 1.5 (Figure 4.7). Interestingly, the increase of  $I_D/I_G$  is almost linear compared to the increase of O/C ratio. Similarly, an increase of O/C ratio from 8% to 38% results in an increase of  $I_{G'}/I_G$  from 0.25 to 0.35. In general, the increase of  $I_{G'}/I_G$  is also almost linear compared to the increase of O/C ratio. However, The  $I_{G'}/I_G$  jumps to about 0.5 as the O/C ratio increases even further to 42% (Figure 4.8). The  $I_D/I_G$  and  $I_{G'}/I_G$  of CNT arrays start to decrease drastically as CNT arrays undergo a further exposure to oxygen plasma treatment. Both  $I_D/I_G$  and  $I_{G'}/I_G$  drop to 1.3 and 0.1 respectively as the O/C ratio reaches 55%.

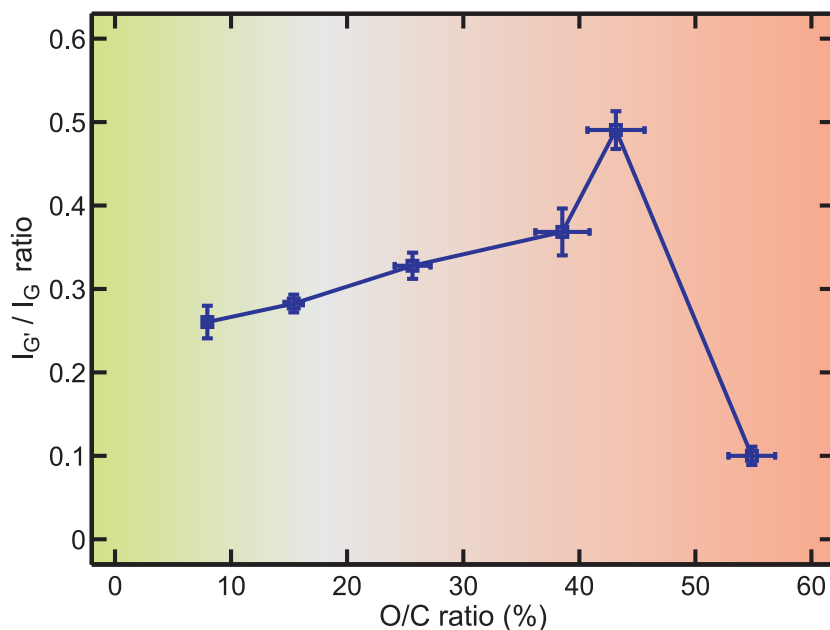


Figure 4.8.  $I_{G'}/I_G$  ratio from Raman spectra of CNT arrays with different oxidation level.

For CNT arrays with an average O/C ratio of higher than 20%, a shoulder D' peak (1620 $\text{cm}^{-1}$ ) becomes visible in their Raman spectra (Figure 4.6.b). This D' band is associated with disorder-induced intravalley resonance Raman scattering (Nourbakhsh et al., 2010; Samarakoon and Wang, 2011). Similarly, a blue shift in both D and G band becomes visible once the average O/C ratio of the CNT arrays is higher than 20%. This blue shift may be caused by an increase of n-doping level and electron-electron scattering rate as the defect site density increases Nourbakhsh et al. (2010); Kim et al. (2009); Childres et al. (2011).

An increase in  $I_D/I_G$  with the increase of O/C ratio, as well as the appearance of D' band, can be interpreted as an increase of disorder-induced Raman scattering as the concentration of oxygen adsorbates increases. Therefore, it can be implied that higher disorder to the  $\pi$ -bond network and the formation of non-sp<sup>2</sup> bonds is, indeed, caused by chemisorption of oxygen during the oxygen plasma treatment. As mentioned earlier, the transition from C-C sp<sup>2</sup> hybridization dominated structure to C-C sp<sup>3</sup> hybridization dominated structure takes place at an average O/C ratio of about 20%. An increase in  $I_{G'}/I_G$  with the increase of O/C ratio can be interpreted as

an increase of strain in the CNT structure as the concentration of oxygen adsorbates increases. An increase in strain of CNT may be caused by an increase of interaction with other CNT or by the presence of out-of-plane oxygenated groups that intercalate between layers of the CNT side wall. The observed blue shift in both D and G bands are most likely caused by in-phase and out-of-phase stretching of epoxide and carbonyl bonded on the CNT side wall (Samarakoon and Wang, 2011).

A sharp decrease in  $I_D/I_G$  as the O/C ratio of the CNT goes higher than 45%, and a sharp decrease in  $I_{G'}/I_G$  at the same O/C ratio, may be caused by a sudden exfoliation of the CNT side wall. Such exfoliation may happen completely or locally. A local exfoliation of the CNT side wall results in the formation of holes that can be several layers deep. A complete exfoliation of the CNT side wall results in a decreased number of walls of the CNT, along with the emergence of amorphous carbon coating between the neighboring CNT. Therefore, it can be suggested that the O/C ratio of 45% is a threshold where etching or amorphization processes become more dominant than the functionalization process during the oxygen plasma treatment. This finding agrees with the results obtained from the XPS analysis, where the surface concentration of C-C sp<sup>2</sup> bonds decreases to zero at an O/C ratio of about 45%.

### 4.3.3 Transmission electron microscopy analysis

As mentioned earlier, three different processes may occur during the oxygen plasma treatment: functionalization, etching, and amorphization. Based on the result of XPS and Raman spectroscopy analyses, it is hypothesized that the oxygen uptake is dominated by functionalization process in the low O/C ratio regime, while etching and amorphization processes are the dominant mechanism in the high O/C ratio regime. Here, low and high magnification TEM images of CNT with different degrees of oxidation are used to verify this hypothesis. High magnification TEM image of as-grown CNT with an O/C ratio of 8% shows the presence of a thin layer of amorphous carbon coating on the outer wall of the CNT (Figure 4.10.a). This amorphous carbon coating can be related to the presence of C-C sp<sup>3</sup> bonds observed in the XPS spectra of

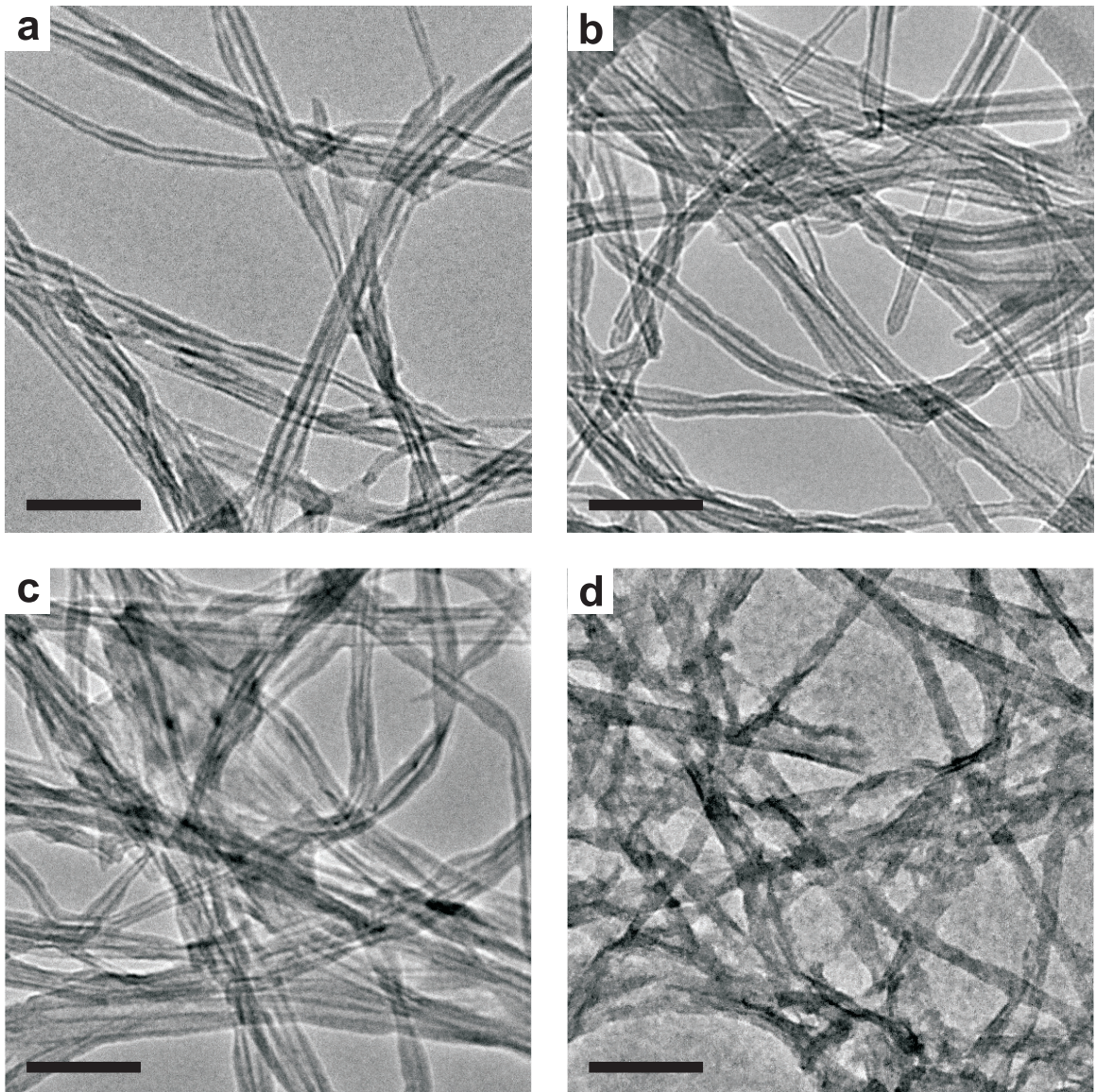


Figure 4.9. Low magnification TEM images of CNT with O/C ratio of 8% (a), 25% (b), 45% (c), 55% (d). Scale bars indicate 100 nm.

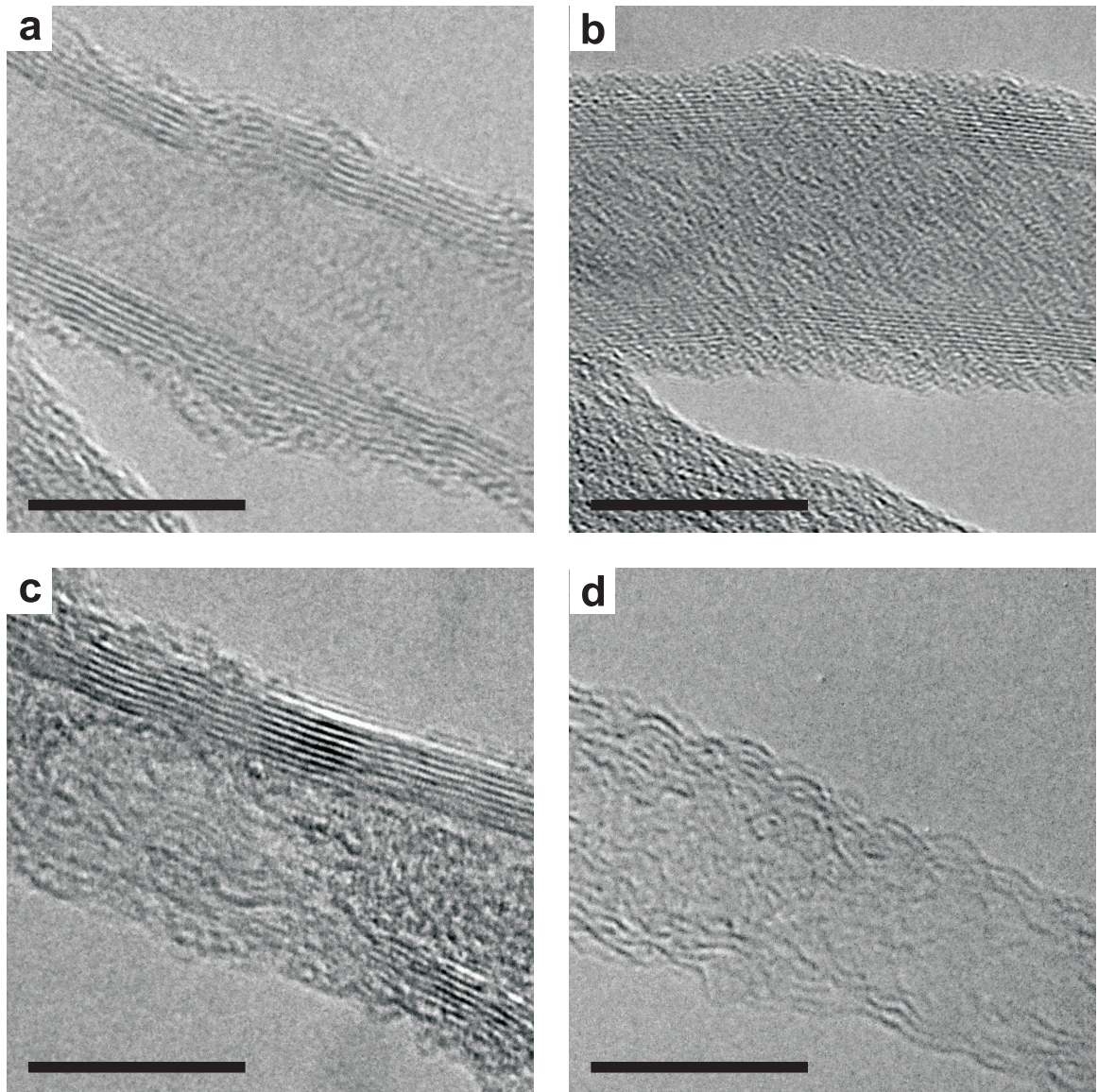


Figure 4.10. High magnification TEM images of CNT with O/C ratio of 8% (a), 25% (b), 45% (c), 55% (d). Scale bars indicate 10 nm.

the as-grown CNT (Figure 3.18.b). The thickness of such amorphous carbon coating is less than 1 nm, such that it cannot be observed in the low magnification TEM image of the as-grown CNT (Figure 4.9.a).

As the O/C ratio of the CNT increases, the thickness of such amorphous carbon coating increases significantly. The thickness of this amorphous carbon coating is about the same as that of the CNT side wall (Figure 4.10.b). This amorphous carbon coating is quite thick, such that it can be observed in the low magnification TEM image (Figure 4.9.b). Since the number of side walls and the diameter of the graphitic structure of the CNT do not change, this amorphous carbon coating can be associated with the increase of oxygenated groups that are chemisorbed during the oxygen plasma treatment. It is possible that a small amount of organics is also adsorbed during the oxygen plasma treatment, during the subsequent storage and handling period. In agreement with the XPS spectra of CNT with an O/C ratio of 25% (Figure 4.1.b), the graphitic structure of the CNT is still largely intact.

As the O/C ratio of the CNT increases even further, the thickness of such amorphous carbon coating decreases significantly, while holes start to form on the CNT side wall. In contrast to the findings from XPS analysis of CNT with an O/C ratio of 45% where the C-C sp<sup>2</sup> is completely disappeared, the graphitic structure of the CNT is still partially intact (Figure 4.10.c). However, a formation of holes that are several layers deep is very obvious. Since the graphitic structures at the edge of these holes are typically terminated by carbonyl, carboxyl, and carbonate groups, an increase of concentration of these groups is expected, which agrees with the finding from XPS analysis (Figure 4.2.a). Notice from the low magnification TEM image that the CNT are bundled together by the amorphous carbon coating (Figure 4.9.c).

In the very high O/C ratio regime, the graphitic structure of the CNT is rather amorphous. In agreement with the findings from XPS analysis of CNT with an O/C ratio of 55% where the C-C sp<sup>2</sup> is completely disappeared (Figure 4.2.b), the graphitic structure of the CNT is no longer intact (Figure 4.10.d). The remaining structure of the CNT is rather amorphous and only has a few layers left. Notice from the low magnification TEM image that the CNT are bundled together by substantial amounts

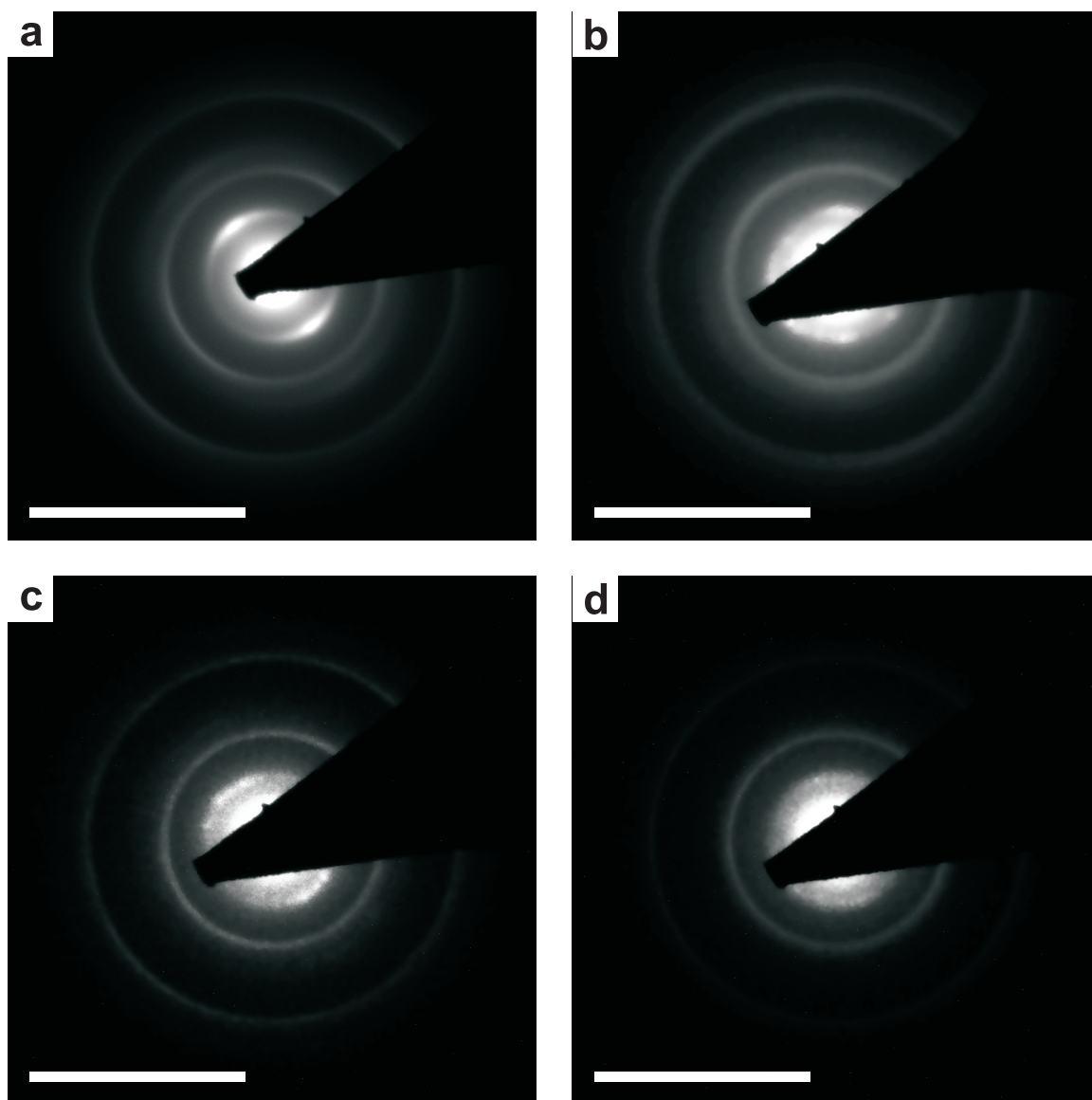


Figure 4.11. Selected area diffraction patterns of CNT with O/C ratio of 8% (a), 25% (b), 45% (c), 55% (d). Scale bars indicate  $10 \text{ nm}^{-1}$ .

of amorphous carbon coating (Figure 4.9.d). This amorphous carbon coating may be generated by the exfoliation of CNT during oxygen plasma treatment. As more and more side walls of the CNT are exfoliated, surface charge between the exfoliated carbon layer and the remaining CNT increases and brings the CNT closer together. As a result, more CNT are bundled in a smaller inter-tube spacing.

SADP of the as-grown CNT with an O/C ratio of about 8% show that its structure is highly polycrystalline (Figure 4.11.a). The continuous circular concentric patterns observed on its SADP, which are a signature of a polycrystalline structure, are originated from the multiple orientation of the CNT walls. In addition, each circular pattern consist of a sharp line, confirming the negligible amount of the thin amorphous carbon coating present on the outer wall of the CNT. The SADP of the as-grown CNT also exhibit four distinct lines (Figure 4.12). The first line (I) and the third line (III) at spacing of  $2.9 \text{ nm}^{-1}$  and  $5.9 \text{ nm}^{-1}$ , respectively, indicate the  $\langle 0002 \rangle$  and  $\langle 0004 \rangle$  orientations which are associated with the graphitic stacking of the CNT wall. The second line (II) and the fourth line (IV) at spacing of  $4.9 \text{ nm}^{-1}$  and  $8.4 \text{ nm}^{-1}$ , respectively, indicate the  $\langle 10\bar{1}0 \rangle$  and  $\langle 11\bar{2}0 \rangle$  orientations which are associated with the hexagonal lattice of the C-C sp<sup>2</sup> hybridized carbon structure.

Similarly, the SADP of the mildly oxidized CNT with an O/C ratio of about 38% show that its structure is also polycrystalline (Figure 4.11.b). However, each circular pattern now consists of a dispersed blurry line, confirming the significant amount of the amorphous carbon coating present on the outer wall of the CNT. Although they are not sharp, four distinct lines can still be observed from its SADP (Figure 4.12). Such blurry, yet distinguishable, lines imply that both polycrystalline and amorphous configuration exist on the structure of this CNT.

The SADP of the heavily oxidized CNT with an O/C ratio of about 43% shows that its structure is still polycrystalline (Figure 4.11.c). However, the SADP of this CNT is somewhat different than that of CNT with a lower O/C ratio. Both line II and IV are sharp and distinguishable, while line I is very dispersed. Moreover, line III has now disappeared and can no longer be observed (Figure 4.12). These patterns indicate an exfoliation of the graphitic stacking of the CNT side wall. However, the

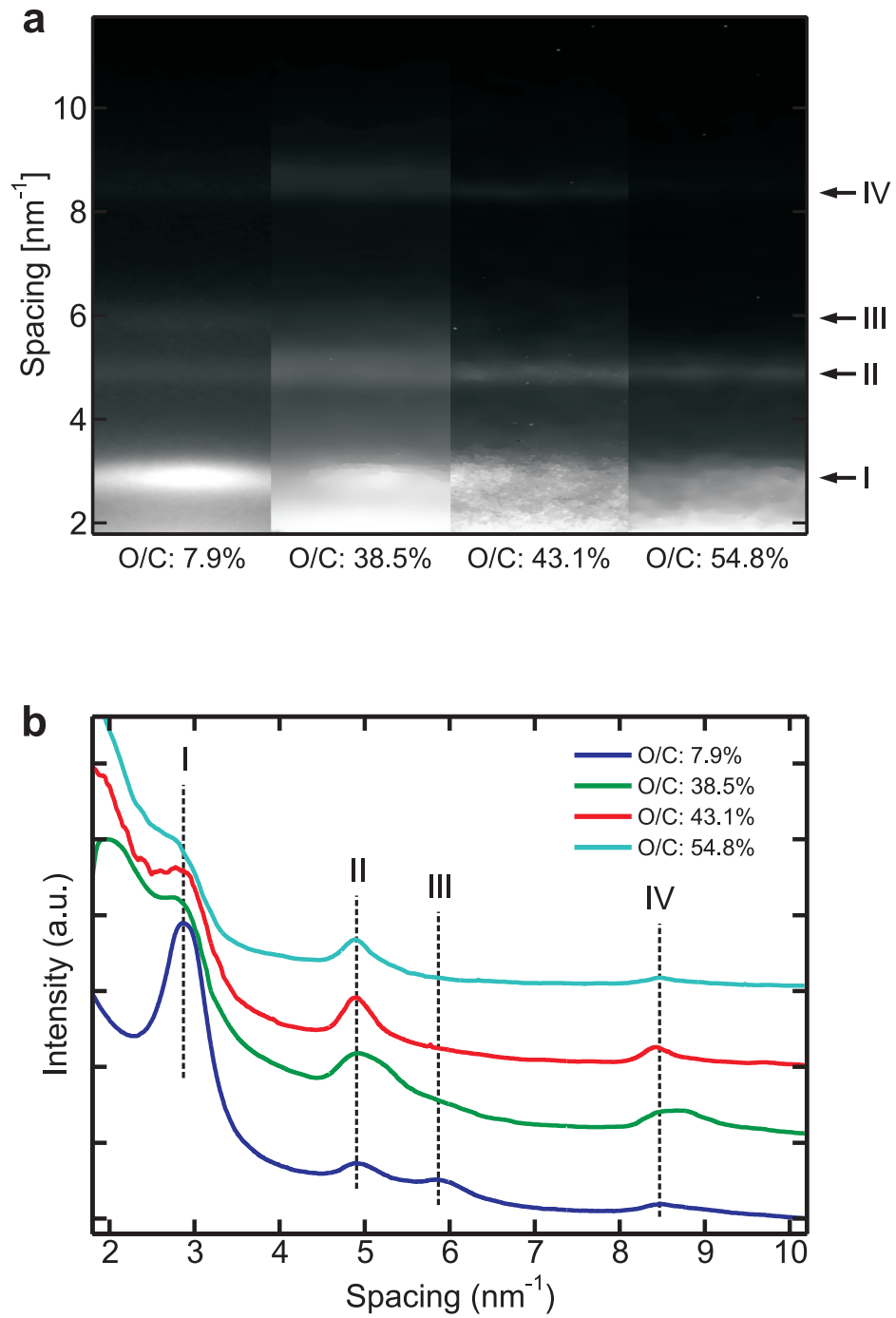


Figure 4.12. Spacing obtained from diffraction patterns of CNT arrays with different oxidation level.

hexagonal lattice of the C-C sp<sup>2</sup> hybridized carbon structure of the remaining CNT wall is still intact.

For the CNT with an even higher O/C ratio of about 55%, a polycrystalline pattern can still be observed from its SADP (Figure 4.11.d). However, the SADP of this CNT is very different than that of CNT with a lower O/C ratio. Only line II is still sharp and distinguishable, while line III and IV have disappeared. Moreover, line I is now similar to the pattern of amorphous structure and no longer distinguishable (Figure 4.12). These patterns indicate a large scale exfoliation of the graphitic stacking of the CNT side wall and a destruction of the hexagonal lattice of the C-C sp<sup>2</sup> hybridized carbon structure. The sharp line II indicates the presence of C-C bonds which are now in the form of sp<sup>3</sup> hybridization.

This SADP analysis indeed confirms the occurrence of three different processes during the oxygen plasma treatment. In the low O/C ratio regime, the oxygen chemisorption process results in the functionalization of CNT outer walls by oxygenated groups. In the moderate O/C ratio regime, the oxygen chemisorption process results in the hole etching of CNT walls, and the remaining functionalization process largely occurs at the edges of the CNT defect sites. In the high O/C ratio regime, the oxygen chemisorption process results in the exfoliation of the CNT walls and amorphization of the remaining CNT structure. Based on this study, it seems that the transition from the first to the second regimes occurs at an O/C ratio of around 38%, while the transition from the second to the third regimes occurs at an O/C ratio of around 43%. Further studies need to be conducted to verify this finding.

#### **4.3.4 BET and Langmuir surface area**

The presence of three different processes during the oxygen plasma treatment also affect the change in surface area of the CNT arrays. Here, the surface area of CNT arrays is measured by means of BET and Langmuir surface area based on adsorption and desorption isotherm of nitrogen at 77 K. Using both methods, the surface area of CNT arrays is found to be increasing with the increase of their O/C ratio. The BET

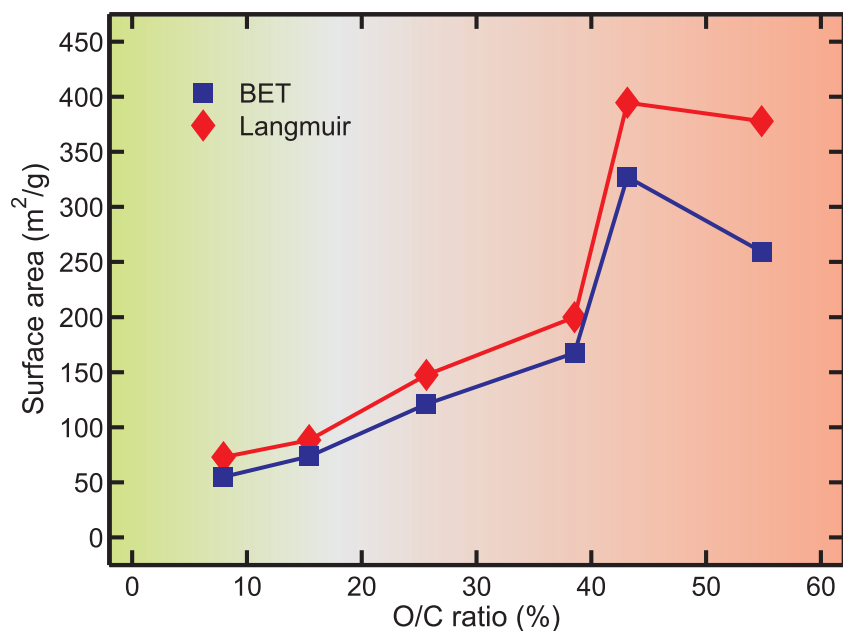


Figure 4.13. Plot of surface area as a function of oxygen/carbon ratio.

and Langmuir surface area of as-grown CNT arrays with an O/C ratio of 8% is found to be about 50 m<sup>2</sup>/g and 80 m<sup>2</sup>/g, respectively. The BET and Langmuir surface area increases almost linearly to about 160 m<sup>2</sup>/g and 200 m<sup>2</sup>/g, respectively, as the O/C ratio of the CNT arrays increases to about 38% (Figure 4.13). Such linear increase indicates a mild micropores opening process, due to surface functionalization during the oxygen plasma treatment.

As mentioned earlier, some of the oxygenated functional groups chemisorbed during the oxygen plasma treatment are in the form of ether, carbonyl, carboxyl, and carbonate. The formation of these groups often results in the formation of small scale vacancies and holes on the CNT side walls. As the surface concentration of these oxygenated groups increases, the micropores density is expected to increase, due to the formation of vacancies and holes. Therefore, the surface area of CNT arrays increases with the increase of O/C ratio in the low O/C ratio regime, due to the increase in the micropores density.

A sharp increase in the BET and Langmuir surface area can be observed as the

O/C ratio of the CNT arrays increases to about 42% (Figure 4.13). In this regime, an increase of an O/C ratio by 4% results in an increase of BET and Langmuir surface area by more than 100%, from about 160 m<sup>2</sup>/g and 200 m<sup>2</sup>/g to about 325 m<sup>2</sup>/g and 400 m<sup>2</sup>/g, respectively. This sudden jump in surface area can be related to the destruction of the CNT side wall due to the etching process that takes place during the oxygen plasma treatment in the moderate O/C ratio. Such an etching process results in the formation of the large scale holes such that most of the CNT lose a large portion of their side walls, allowing their inner cavity to be accessed by nitrogen. Since the nitrogen is now adsorbed on both inner and outer wall of the CNT, the measured surface area of CNT in this O/C ratio is doubled.

Interestingly, a further increase in O/C ratio results in a decrease in BET and Langmuir surface area. Indeed, an increase of O/C ratio to 55% results in a decrease in BET and Langmuir surface area to 250 m<sup>2</sup>/g and 380 m<sup>2</sup>/g. Since micropores and large scale holes cannot be closed or mended by a further adsorption of oxygen, the decrease in surface area has to be related to a drastic transformation in the structure of the CNT. In fact, this phenomenon may be related to the closing of micropores by the presence of amorphous carbon or a destruction of the CNT side walls. As mentioned earlier, amorphous carbon coating can be formed from the exfoliated CNT wall during oxygen plasma treatment in the high O/C ratio regime. During the exfoliation process, the side walls of the CNT are often transformed into amorphous structures.

#### **4.3.5 Effect of heavy oxidation on CNT pillars**

As mentioned above and in Chapter 3.3.7, an increase in concentration of oxygenated groups leads to an increase in magnitude of the CNT surface charge. In addition, the presence of oxygenated groups allows multiple hydrogen bonds to form between these groups. Further, it has been observed under TEM that amorphous carbon generated by etching and destruction of CNT side walls brings the remaining CNT closer together. A combination of an increase of surface charge and an increase of the

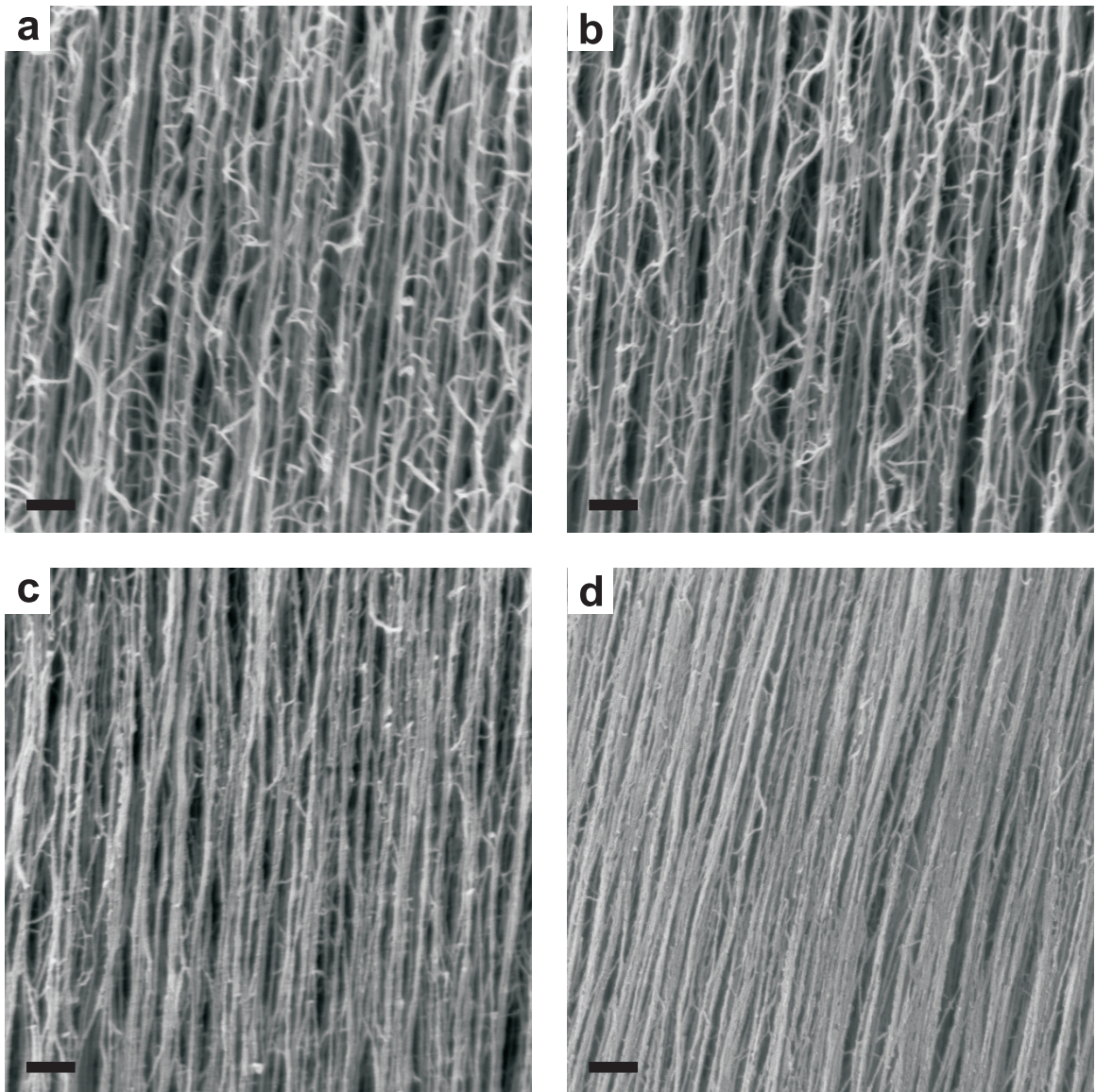


Figure 4.14. High magnification SEM images of CNT arrays with O/C ratio of 8% (a), 25% (b), 42% (c), 55% (d). Scale bars indicate 300 nm.

number of hydrogen bonds should increase the attraction between individual CNT in the array, and ultimately decrease their inter-tube spacing.

Typically, as-grown CNT arrays with an O/C ratio of 8% have an average inter-tube spacing of about 60-80 nm, which is about two to three times the diameter of individual CNT. Thus, as-grown CNT arrays appear to be very porous and the empty space between each CNT can obviously be seen from their SEM image (Figure 4.14.a). Although, based on the abovementioned argument, the inter-tube spacing of CNT arrays should decrease with the increase of O/C ratio, this behavior is not obvious at an O/C ratio of 25%. The inter-tube spacing of these CNT arrays is about 60-80 nm, similar to that of as-grown CNT arrays (Figure 4.14.b). The decrease in inter-tube spacing is more pronounced at higher O/C ratios. For CNT arrays with an O/C ratio of 45%, their inter-tube spacing is found to be about 20-60 nm. In fact, the CNT in these arrays are closely packed such that their entanglement starts to disappear (Figure 4.14.c). An even lower inter-tube spacing is observed for CNT arrays with higher O/C ratios. For CNT arrays with an O/C ratio of 55%, almost each CNT is in close contact with its neighboring CNT. Thus, these CNT arrays are densified such that the empty space between each CNT can no longer be observed (Figure 4.14.d).

The large scale implication of this phenomenon can be observed clearly from the change in morphology of hollow CNT pillars as their O/C ratio is varied. Here, the hollow CNT pillars have an inner and outer diameter of 25  $\mu\text{m}$  and 75  $\mu\text{m}$ , respectively. Hollow CNT pillars are utilized to elucidate two processes that occur simultaneously during the oxygen plasma treatment in the high O/C ratio regime. As mentioned earlier, in the high O/C ratio regime, the etching and amorphization of CNT structures dominate the oxidation process. At the same time, the densification process of CNT arrays takes place due to the increase of magnitude of surface charge, and perhaps hydrogen bond as well.

Since the etching and densification process takes place in the high O/C ratio regime, the change in morphology of hollow CNT pillars should not be apparent in the low and moderate O/C ratio regime. Indeed, the morphology of hollow CNT pillars with an O/C ratio of 25% is similar to that of the as-grown hollow CNT

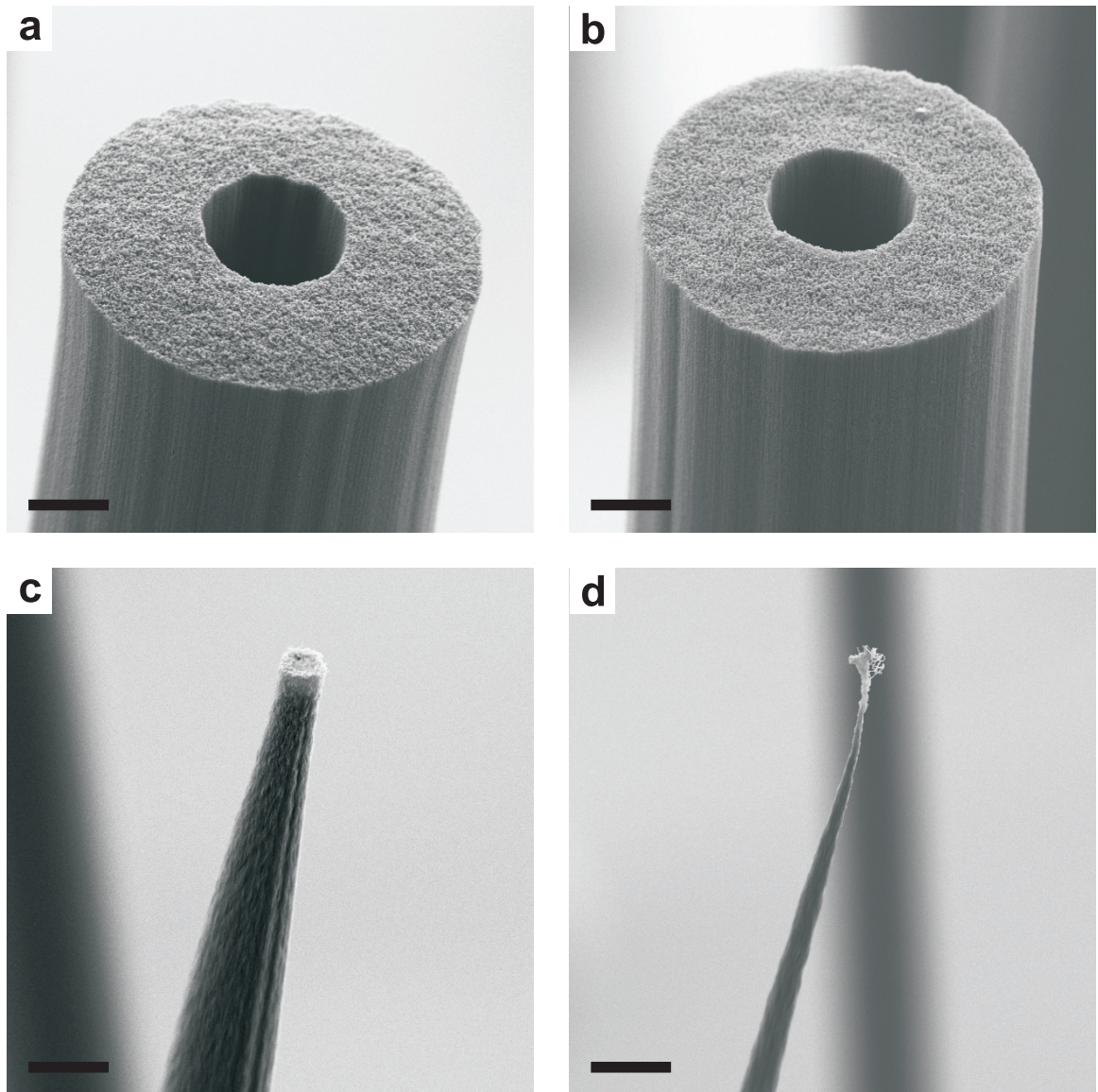


Figure 4.15. High magnification SEM images of hollow CNT pillars with O/C ratio of 8% (a), 25% (b), 42% (c), 55% (d). Scale bars indicate 10  $\mu\text{m}$ .

pillars with an O/C ratio of 8% (Figure 4.15.a and Figure 4.15.b). The change in morphology becomes apparent once the O/C ratio of the hollow CNT pillars goes higher than 40%. At an O/C ratio of 42%, the shape of hollow CNT pillars changes into a frusto-conical shape (Figure 4.15.c). Their inner and outer tip diameter also decreases significantly to about 2  $\mu\text{m}$  and 6  $\mu\text{m}$ , respectively. At an O/C ratio of 55%, the shape of hollow CNT pillars is further transformed into a needle-like shape, and their outer tip diameter decreases even further to less than 1  $\mu\text{m}$  (Figure 4.15.d). This phenomenon clearly shows that the CNT arrays undergo etching and densification processes as they are subjected to a prolonged exposure of dry oxidation in the high O/C ratio regime. However, judging from the fast decrease of the overall diameter of the CNT pillars, the etching process takes place at a much higher rate than the densification process.

## 4.4 Concluding Remarks

In conclusion, the findings reported herein show the effect of oxidation to the evolution of CNT arrays atomic structure. There are at least three different processes which occur during the oxidation process. For CNT arrays with an O/C ratio lower than 40%, the oxidation process results in the functionalization of CNT outer walls by oxygenated groups. Although this functionalization process introduces defects, vacancies, and micropores openings, the graphitic structure of the CNT is still largely intact. In this regime, most of the chemisorbed oxygenated groups are in the form of epoxide, hydroxide, or cyclic ether groups. As discussed in Chapter 3, a low concentration of these oxygenated groups can be removed by vacuum annealing treatment, such that the effect of oxidation is reversible for O/C ratios lower than 18%. For O/C ratios between 18% and 40%, the concentration of these oxygenated groups becomes extremely high, such that they form pair structures that cannot be easily removed by vacuum annealing treatment.

For CNT arrays with O/C ratios between 40% and 45%, the oxidation process results in the etching of CNT outer walls. This etching process introduces large scale

defects and holes that can obviously be seen under TEM at high magnification. Most of these holes are found to be several layers deep, and in some cases a large portion of the CNT side walls are cut open. Such large-scale holes make the inner cavity of CNT accessible from outside. Access to both inner and outer walls of CNT results in a dramatic increase of surface area, such that the surface area of the etched CNT is about twice as large as the heavily functionalized but not etched CNT. In this O/C ratio range, densification process of CNT arrays also starts to occur.

For CNT arrays with an O/C ratio higher than 45%, the oxidation process results in the exfoliation of the CNT walls and amorphization of the remaining CNT structure. This amorphization process can be implied from the disappearance of the C-C sp<sup>2</sup> peak in the XPS spectra associated with the  $\pi$ -bond network. Such a process results in the disintegration of graphitic structure of the CNT side walls, which can obviously be seen under TEM at high magnification. SADP of the amorphous CNT walls shows an extremely weak line associated with  $\langle 11\bar{2}0 \rangle$  plane and the lack of lines associated with  $\langle 0002 \rangle$  and  $\langle 0004 \rangle$  planes. In this O/C ratio range, the densification process of CNT arrays continues to occur, although the etching process takes place at a much higher rate than the densification process. Further increase of O/C ratio will most likely result in the complete decomposition of the CNT walls.

## Chapter 5

# Water Droplet Impact Behavior on Superhydrophobic Carbon Nanotube Arrays

### 5.1 Introduction

The liquid droplet impact behavior on a dry surface has been studied intensively in the last few decades, due to its numerous practical applications such as ink jet printing, direct injection for internal combustion engines, microelectronic fabrication, and rain drops (Yarin, 2006; Vadillo et al., 2009). It has been known that such behavior is dictated by several parameters including the physical properties of the liquid, e.g., viscosity and surface tension, the kinematic properties of the droplet, e.g., volume and impact velocity, and the wettability of the surface itself, e.g., contact angle and roll-off angle (Rioboo et al., 2001; Lee and Lee, 2011). Depending on the value of these parameters, there are at least six possible outcomes when a liquid droplet impinges on a dry but wettable surface: deposition, prompt splash, corona splash, receding break-up, partial rebound, and complete rebound (Rioboo et al., 2001). In contrast to the liquid droplet impact behavior on a wettable surface, the impact behavior on a non-wettable surface is still not completely understood.

Many published studies have shown that in the case of a water droplet impinging on a non-wettable surface (e.g., a superhydrophobic surface), it deforms and flattens into a pancake shape, then spreads on the surface, subsequently recedes after it

reaches its maximum spreading diameter, and finally rebounds off the surface completely. Although those studies do agree on the overall impact behavior, there remain some significant discrepancies that still need to be resolved. The biggest obstacle that hinders investigators from drawing a unified conclusion is the use of a non-ideal superhydrophobic surface where the impinging water droplet is pinned onto the surface at a certain condition (Rioboo et al., 2002; Biance et al., 2006; Jung and Bhushan, 2009; Lee and Lee, 2011). Such surface properties transition from Cassie state to Wenzel state in a higher Weber number regime and has continued to prevent investigators from obtaining valid experimental data, which in turn complicates the process of interpreting and modeling the impact behavior correctly. Further, the use of thermodynamically modified surfaces (e.g., superheated plates), as superhydrophobic surfaces add to the confusion, mainly because of the underestimated effects of water evaporation and convection (Chandra and Avedisian, 1991). Therefore, the objective of this work is to fully characterize the water droplet impact behavior on an ideal Cassie state superhydrophobic surface via carefully controlled experimental procedures at standard room temperature and pressure. This ideal superhydrophobic surface has the capability to remain in a Cassie state in any experimental conditions, such that water droplets will never get pinned onto this surface even in a very high Weber number regime and at a non-elevated temperature. Comparison between commonly used superhydrophobic surfaces is summarized in Table 5.1.

One widely known example of the above mentioned discrepancies is whether or not the impact behavior on a non-wettable surface satisfies the energy conservation principle. It was long thought that the impact behavior at a low viscosity regime on a non-wettable surface would satisfy the conservation of energy. Based on this energy conservation approach, Chandra and Avedisian (1991) suggested a model where the maximum spreading factor would scale as the square root of the Weber number of the droplet. However, there was a considerable difference between this proposed model and the experimental data observed by Biance et al. (2006), which might have been caused by the underestimated effect of water evaporation and upward flow of air, due to convection from the superheated Leidenfrost surface. Works done by Pasandideh-

Fard et al. (1996), Kim and Chun (2001), Ukiwe and Kwok (2004), Vadillo et al. (2009), and Li et al. (2010) on various surfaces show that the conservation of energy indeed holds, as long as the effect of viscous dissipation and wettability are taken into account.

On the contrary, works by Clanet et al. (2004), Bartolo et al. (2005), and Biance et al. (2006) show that a straightforward energy conservation approach cannot be used due to the existence of internal flows induced by an “effective gravity” during the impingement. According to this effective gravity theory, the maximum spreading factor does not scale as the square root of the Weber number, but instead scales as the Weber number to the one-fourth power. However, the conclusion of these studies has been refuted by Eggers et al. (2010), mainly because they only investigated a small regime where both energy conservation and effective gravity approaches could not be reliably discriminated. Work by Eggers et al. (2010) suggests that in the low viscosity regime, the maximum spreading radius is, indeed, dictated by a balance between kinetic energy and capillary forces, not by the effective gravity. More recently, Lee and Lee (2011) suggest that a more accurate model for the maximum spreading factor could indeed be made by incorporating a geometrical modification induced by surface textures into the energy conservation principle. Note that different materials, ranging from superheated Leidenfrost surfaces (Chandra and Avedisian, 1991; Biance et al., 2006), to hydrophobic metal and polymeric surfaces (Pasandideh-Fard et al., 1996; Ukiwe and Kwok, 2004; Bartolo et al., 2005; Vadillo et al., 2009), as well as micro-textured hydrophobic surfaces (Clanet et al., 2004; Biance et al., 2006; Tsai et al., 2009; Lee and Lee, 2011), were used in these published works.

The complication introduced by surface properties’ transition to the otherwise simple problem has led many studies to revolve around it, leaving several other important impact behavior characteristics unexplored. Despite their importance, these impact behavior characteristics, which include critical Weber number, volume ratio, and restitution coefficient, have received the least amount of attention due to the excessive amount of effort spent drawing a unified conclusion about the maximum spreading factor. Until now, only Range and Feuillebois (1998) and Rioboo et al.

Table 5.1. Comparison between superhydrophobic surfaces.

Surface	Static contact angle	Roll-off angle	Contact angle hysteresis	Droplet pinning condition	Liquid-vapor-solid interface
Micropatterned Si pillars (Jung and Bhushan, 2008)	173	3	1	$We > 78$	no
Microtextured wax (Biance et al., 2006)	160	N/A	N/A	$We < 1$ and $We > 85$	no
Superheated plate (Chandra and Avedisian, 1991)	180	N/A	0	no pinning	yes
Lotus leaf (Koch and Barthlott, 2009)	162	4	4	N/A	yes
CNT arrays (this study)	173	3	3	no pinning	yes

(2001) have mentioned the existence of critical Weber numbers. A critical Weber number is basically a threshold that separates two different outcomes when a drop impinges the surface and is a unique property of a surface that depends heavily on its wettability. Hence, a critical Weber number of an ideal superhydrophobic surface should be different than that of any other wettable surfaces. Although they discussed the role of critical Weber numbers on the morphology of an impinging droplet, their discussions were based on phenomena observed on conventional materials, not on non-wettable surfaces.

Another example of an important characteristic that has also been neglected is the restitution coefficient, which is defined as a ratio between the droplet's velocity before and after the impact. So far, the restitution coefficient has only been briefly mentioned by Richard and Quere (2000) and Bianco et al. (2006). Although both of them claimed that superhydrophobic surfaces were used in their experiment, their experimental data did not agree with each other. Richard and Quere (2000) show that the restitution coefficient is approximately constant over a large range of Weber numbers, while Bianco et al. (2006) suggest restitution coefficient scales as the inverse of a square root of the Weber number. Such a discrepancy might have been caused by the use of different types of non-wettable surface, where Richard and Quere (2000) used a proprietary micro-textured hydrophobic surface, while Bianco et al. (2006) used a superheated Leidenfrost surface. This clearly shows that the droplet impact behavior is heavily influenced by the types of surface used in the experiment, and highlights the importance of using an ideal Cassie state superhydrophobic surface to provide valid experimental data.

This work presents for the first time a complete characterization of water droplet impact behavior on a Cassie state nanostructured superhydrophobic surface. Experimental data are gathered comprehensively via carefully controlled experimental procedures at standard room temperature and pressure over a wide range of Weber number. These experimental data are presented in the form of several important impact behavior characteristics, which include critical Weber number, volume ratio, restitution coefficient, as well as maximum spreading diameter. Empirical approxima-

tions and interpretations of the data, as well as brief comparisons to the previously proposed scaling laws, are also shown here. This work will ultimately provide the basis for future study to develop a logical mathematical model that describes the droplet impact behavior on a non-wettable surface by eliminating any complications induced by surface properties transition.

## 5.2 Materials and Methods

The ideal Cassie state superhydrophobic surface used in this study was made of CNT arrays. These CNT arrays have inherent hierarchical structures needed to minimize the adhesion between a water droplet and its surface. According to Gao and McCarthy (2006a) and Bhushan et al. (2009), an ideal Cassie state superhydrophobic surface can only be fabricated from a material with hierarchical structures, which provide two length scales topography. In the case of CNT arrays, their two length scales topography is provided by a combination of micro-scale height variation of the arrays and nano-scale entanglement of the nanotubes. Carbon nanotube arrays used in this study have an average length of about  $15 \mu m$  and an average height variation of about  $1 \mu m$ . At a smaller scale, the presence of entanglements on the top surface of the CNT arrays is apparent. A detailed discussion on the CNT array fabrication technique and their physical properties can be read in Chapter 2.1.1 and Chapter 2.1.2, respectively.

Further, to ensure that surface properties transition from Cassie state to Wenzel state did not occur during the entire study, the surface chemistry of these CNT arrays was carefully controlled and maintained. The detailed methods for surface chemistry modification and characterization can be read in Chapter 3. The combination of inherent two length scales topography and the carefully controlled surface chemistry of the carbon nanotube arrays results in a surface with an extreme water repellent capability. Such capability is shown by its extremely high static contact angle of about  $173^\circ$  (Figure 5.1) and its very low contact angle hysteresis of about  $3^\circ$ . These superhydrophobic CNT arrays also exhibit a very low roll-off angle of less than  $3^\circ$  (Figure 5.2), which means that no millimeter-size water droplet can maintain

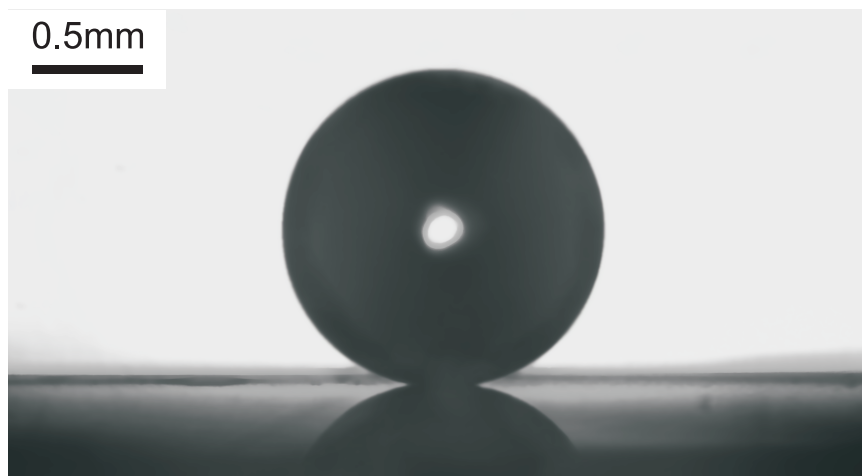


Figure 5.1. Water droplet on an ideal superhydrophobic surface exhibits an almost perfect spherical shape, with static contact angle of higher than  $170^\circ$ .

a stable position on its surface when it is tilted more than  $3^\circ$ . Further, the surface of superhydrophobic CNT arrays is always covered by air film cushion that it cannot be wetted by water. This liquid-vapor-solid interface is the signature interface of an ideal Cassie state superhydrophobic surface. A detailed discussion on the liquid-vapor-solid interface on the surface of superhydrophobic CNT arrays can be read in Chapter 3.3.6.

In this study, all droplets were generated by a flat-tipped stainless steel needle connected to a syringe pump (Harvard Apparatus PHD 22/2000). The flat-tipped needle used here was varied from 24-gauge to 33-gauge, depending on the volume of the droplet. This combination allows the volume of the droplet to be carefully controlled with less than 10% variability. Each droplet was formed using the pendant drop method, where water with a specific volume was slowly pushed by the syringe pump through the needle until it detached under its own weight. Using this method, the shape of the free-falling droplet may not be perfectly spherical, which may increase the uncertainty of the experimental results. However, according to Vadillo et al. (2009) and Lee and Lee (2011), this phenomenon should not drastically change the observed impact behavior.

The evolution of the droplet before, during, and after the impingement was captured using a backlight technique, where the impacting droplet and the surface were

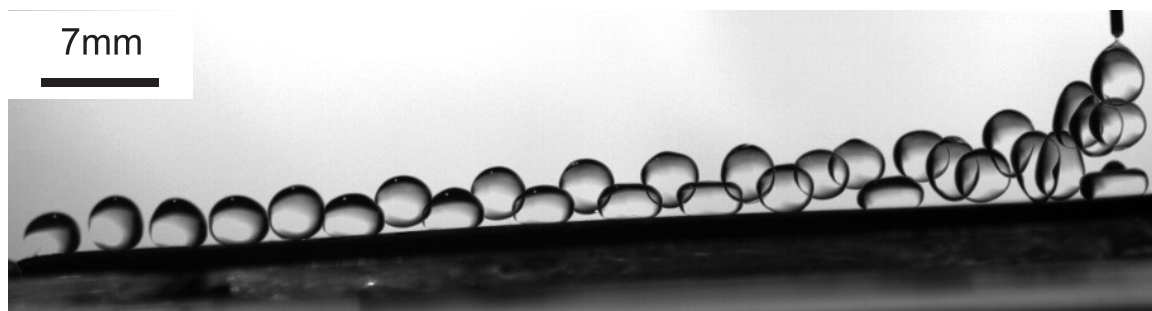


Figure 5.2. Time-lapse image of water droplet bounce off of the surface of carbon nanotube arrays. This surface was tilted by  $2.5^\circ$  to clearly show the bouncing behavior of the droplet. Each frame was recorded with  $17ms$  interval.

placed in between the high speed camera and the illumination source (Figure 5.3). The impact behavior was recorded with an image resolution of  $600 \times 400$  pixels using a high speed camera (Dantec Dynamics NanoSense MkIII), running at a frame rate of 2000 frames per second. The droplet and the surface were illuminated from behind by arrays of white LED (Bridgelux BXRA-C800) running at a color temperature of 5600K. A smooth PET light diffuser was placed between the objects of study and the LED arrays to distribute the light evenly. All measurements regarding droplet size and height were done manually using an open-source image processing software (NIH ImageJ).

To minimize variability of the experimental results, the entire experiment was performed using deionized (DI) water with a resistivity of  $18.2 \text{ M}\Omega\text{-cm}$ , in a controlled environmental condition at an ambient temperature and humidity of  $20^\circ\text{C}$  and 50%, respectively. Since the influence of external air pressure to the impact behavior was considered insignificant (Tsai et al., 2009), the ambient pressure was left uncontrolled at a standard atmospheric pressure. The interference from the ambient environment was further minimized by placing the needle, from which the droplet fell freely, inside transparent acrylic windscreens. The drop impact velocity itself was controlled by varying the distance between the tip of the needle and the surface. The relation between the impact velocity and the fall height is described elsewhere (Bartolo et al., 2005; Biance et al., 2006). Measurements for each data point were repeated at least twelve times to ascertain their reproducibility and to ensure that the obtained data

are normally distributed. Outlier removal algorithm was employed, such that the experimental data presented herein are free from outliers. Outliers were defined as data points that fall more than 1.5 times the interquartile range below the first quartile or above the third quartile.

There are several important parameters governing the nature of impinging droplets that have to be taken into account. Those parameters are the droplet diameter ( $d_i$ ), density ( $\rho$ ), dynamic viscosity ( $\mu$ ) and surface tension ( $\sigma$ ) of the liquid, impact velocity ( $v_i$ ) of the droplet and the external air pressure. To make the analysis simpler, these parameters are represented by several important dimensionless numbers: Weber number ( $We$ ), Reynolds number ( $Re$ ), Ohnesorge number ( $Oh$ ), Froude number ( $Fr$ ), Bond number ( $Bo$ ), and Capillary number ( $Ca$ ). Weber number is defined as  $We = \rho v_i^2 d_i / \sigma$ . Reynolds number is defined as  $Re = \rho v_i d_i / \mu$ . Ohnesorge number is defined as  $Oh = \mu / \sqrt{\rho \sigma d_i} = \sqrt{We} / Re$ . Froude number is defined as  $Fr = v_i^2 / g d_i$ . Bond number is defined as  $Bo = \rho g d_i^2 / \sigma$ . Capillary number is defined as  $Ca = \mu v_i / \sigma$ . In this work, Weber number was varied from  $We = 1.79$  to  $We = 335.32$ , which proportional to Reynolds number from  $Re = 529.64$  to  $Re = 10701.23$ . This broad range of Weber number was achieved by varying the initial droplet size from  $d_i = 2.2$  mm to  $d_i = 3.8$  mm, and impact velocity from  $v_i = 0.24$  m/s to  $v_i = 2.51$  m/s, using DI water with a density of  $\rho \approx 0.997$  g/cm<sup>3</sup> and a surface tension of  $\sigma \approx 71.89$  dyne/cm.

The effect of viscosity to the droplet can be considered minimal since the Ohnesorge number of experiment was found to be  $1.71 \times 10^{-3} \leq Oh \leq 2.52 \times 10^{-3}$ . In addition, the Froude, Bond, and Capillary number were set to be  $2.24 \leq Fr \leq 229.22$ ,  $0.65 \leq Bo \leq 2.02$ , and  $3.37 \times 10^{-3} \leq Ca \leq 3.13 \times 10^{-2}$ , which imply the following: the effect of inertia is stronger than that of gravity, the effect of gravity is comparable to that of surface tension, and the effect viscosity is much less than that of surface tension. Further, the ratio between Bond and capillary numbers was found to be much larger than unity in each experiment. This ratio, which is defined as  $Bo/Ca = \rho g d_i^2 / \mu v_i$ , compares the effect of gravity and viscosity to the water droplet. Consequently, the effect of viscosity is also insignificant compared to the effect of

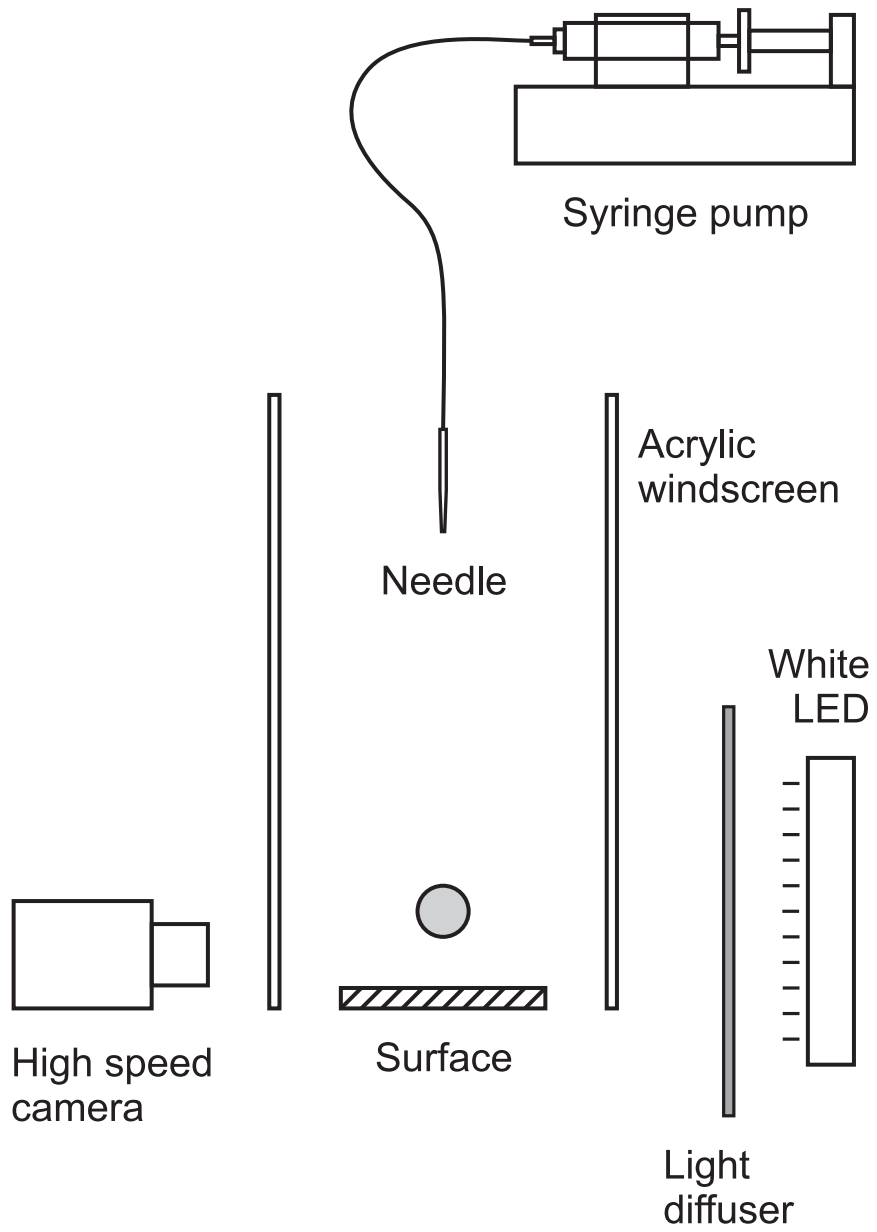


Figure 5.3. Schematic of the experimental setup.

Table 5.2. Dimensionless parameters of the experiments.

	We	Re	Oh	Fr	Bo	Ca	Bo/Ca
Min	1.79	529.64	$1.71 \times 10^{-3}$	2.24	0.65	$3.37 \times 10^{-3}$	21.14
Max	335.32	10701.23	$2.52 \times 10^{-3}$	229.22	2.02	$3.13 \times 10^{-2}$	287.99

gravity. Therefore, the impact behavior can be conveniently expressed just by Weber number. Weber number is considered as the most important parameter mainly because of its appearance in the energy balance of the droplet, which has been discussed in detail elsewhere (Chandra and Avedisian, 1991; Pasandideh-Fard et al., 1996; Kim and Chun, 2001; Ukiwe and Kwok, 2004; Vadillo et al., 2009; Li et al., 2010; Lee and Lee, 2011), and to avoid competition between two main components of kinetic energy, i.e.,  $v_i$  and  $d_i$ . These dimensionless parameters are summarized in Table 5.2.

## 5.3 Results and Discussion

### 5.3.1 Critical Weber number

As a free-falling water droplet hits the superhydrophobic surface, it deforms and flattens into a pancake shape and then spreads on the surface. Depending on the Weber number, there are at least three apparent outcomes after the droplet reaches its maximum spreading diameter. At a low Weber number, the droplet starts to recede right after it reaches its maximum spreading diameter and finally rebounds off of the surface completely while creating some sort of an upward flow, which elongates the droplet vertically. The droplet remains intact during, and subsequent to, the impact (Figure 5.4.a). At a moderate Weber number, the droplet also starts to recede once it reaches its maximum spreading diameter. However, when this droplet rebounds off of the surface, it creates a stronger upward flow, known as a Worthington jet, and forms several smaller secondary droplets (Figure 5.4.b). At a high Weber number,

the surface tension of water is no longer able to keep the droplet intact. Hence, it breaks into many smaller secondary droplets once it reaches its maximum spreading diameter and the remaining primary droplet rebounds off of the surface (Figure 5.4.c).

The existence of three distinguishable impact regimes implies that there are two critical Weber numbers separating them (Range and Feuillebois, 1998; Rioboo et al., 2001). The first critical Weber number,  $We_1$ , indicates the condition when the upward flow created during the rebound phase starts to split into several smaller secondary droplets. The second critical Weber number,  $We_2$ , indicates the threshold when the impinging droplet splashes into many smaller secondary droplets during the impact right after it reaches its maximum spreading diameter. Although the existence of  $We_2$  on conventional materials has been previously observed by Range and Feuillebois (1998) and Rioboo et al. (2001), the existence of  $We_1$  and  $We_2$  on superhydrophobic surfaces has never been observed.

As observed experimentally, the first critical Weber number was found at  $We_1 = 11(\pm 3)$ , while the second critical Weber number was found at  $We_2 = 106(\pm 17)$  (Figure 5.5). This result infers that at  $We < 8$ , an impinging water droplet always bounces off of the surface completely without forming any secondary droplets. At  $14 < We < 89$ , all impinging water droplets always bounce off of the surface while forming Worthington jets and secondary droplets. At  $We > 123$ , every impinging water droplet always splashes upon impact and forms a myriad of secondary droplets. Interestingly, the  $We_2$  observed in this study is in the same order of magnitude as that observed on conventional materials with similar surface roughness (Range and Feuillebois, 1998). Since critical Weber numbers are unique properties of a surface (Range and Feuillebois, 1998; Rioboo et al., 2001), the transition of impact behavior at  $We_1 = 11(\pm 3)$  and  $We_2 = 106(\pm 17)$  may only be observed on an ideal superhydrophobic surface.

Notice that the variation of  $We_2$  is larger than that of  $We_1$ . Such large variation in  $We_2$  is expected, considering the imperfect spherical shape of the free-falling droplet due to the nature of a pendant drop. Further, droplets with higher kinetic energy have more pronounced oscillation due to additional internal waves and motions compared

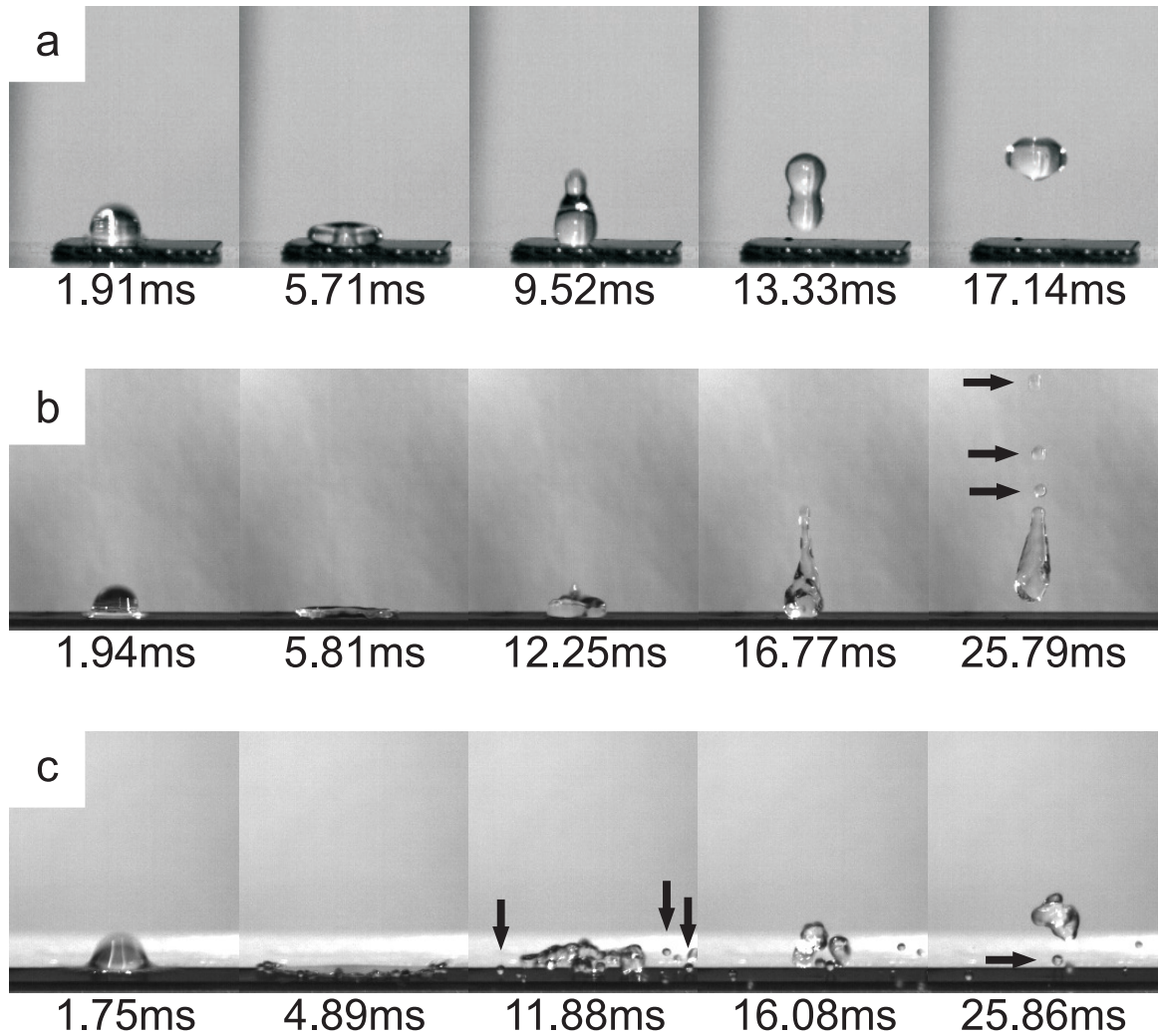


Figure 5.4. (a) At  $We = 9.1$ , the water droplet bounces off of the surface of the array. (b) At  $We = 57.5$ , the primary rebounded droplet starts to elongate and eventually splits into several smaller secondary droplets as indicated by the black arrows. (c) At  $We = 150$ , the water droplet splashes upon impact and breaks into many smaller secondary droplets. The primary rebounded droplet is noticeably larger than the secondary droplets.

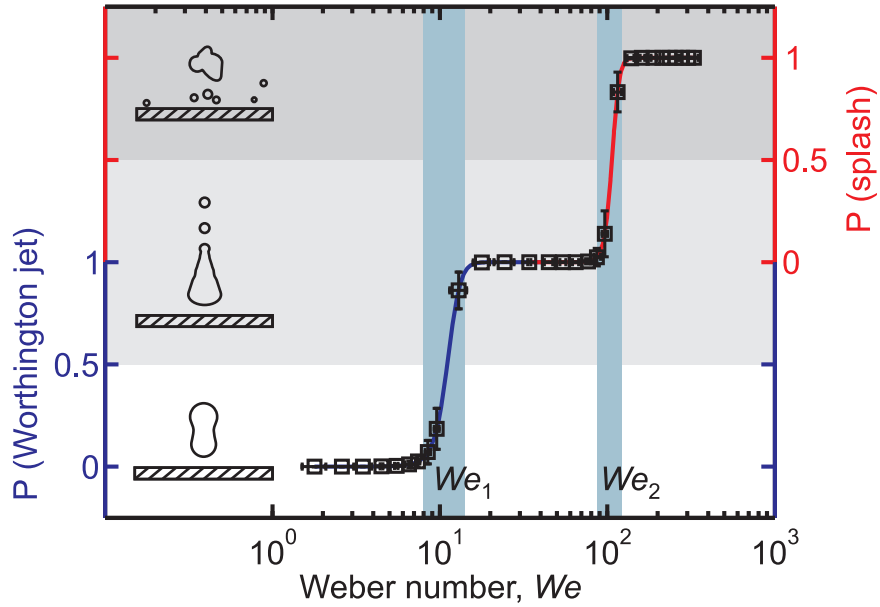


Figure 5.5. Probability of a water droplet to create a Worthington jet or a splash upon impact. Transition from a full rebound to a rebound with a Worthington jet occurs at  $We_1 = 11(\pm 3)$ , while transition from a rebound with a Worthington jet to a splash takes place at  $We_2 = 106(\pm 17)$ .

to ones with lower kinetic energy (Biance et al., 2006). The shape uncertainty of the droplet at the time of impact may also contribute to the widening of the  $We_2$  range. Although the surface roughness may influence the widening of  $We_2$  (Range and Feuillebois, 1998; Rioboo et al., 2001), there is no obvious evidence that such large variation is caused by the micro- and nano-scale surface roughness of the carbon nanotube arrays.

It is worth mentioning that there may exist a third critical Weber number,  $We_3$ , at which the ratio between the primary and the secondary droplets is zero. In other words, at  $We > We_3$  the impinging droplet completely breaks and scatters upon impact into a myriad of smaller droplets and the primary droplet can no longer be distinguished from the secondary ones (Rioboo et al., 2001; Yarin, 2006). Since no recorded observations of  $We_3$  have been made in this study, mainly due to the limitation of the high speed camera, it is hypothesized that  $We_3$  has to be much higher than  $We_2$ . However, the existence  $We_3$  could not be proven in this study.

It would be interesting to see if the third critical Weber number follows the order of magnitude trend of the first and the second critical Weber numbers, such that  $We_1 \sim 10^1$ ,  $We_2 \sim 10^2$ , and  $We_3 \sim 10^3$ . Further studies to confirm this hypothesis and to understand the underlying mechanism of droplet segmentation still need to be done in the future. Various scenarios mentioned above are summarized in Figure 5.6.

### 5.3.2 Volume ratio

As mentioned earlier, in the  $We > We_1$  regime, secondary droplets are always formed upon impact, either by a Worthington jet or by a splash. Experimental observations indicate that the ratio between the primary and the secondary droplets is dictated by the Weber number, such that this ratio decreases as the increase of Weber number. The ratio between the volume of the primary rebounded droplet and its initial volume is known as the volume ratio,  $\xi$ , and is defined by the following formula:  $\xi = (d_r/d_i)^3$ , where  $d_i$  is the initial diameter of the droplet before impact, and  $d_r$  is the diameter or its equivalent spherical diameter of the primary rebounded droplet (Figure 5.6). At a low and moderate Weber number, the total volume of the smaller secondary droplets should be considerably smaller compared to the volume of the primary droplet. At a high Weber number, the total volume of the smaller secondary droplets should be comparable to or even higher than the volume of the primary droplet.

In the  $We < We_1$  impact regime,  $\xi$  is always unity because the droplet remains intact during and subsequent to the impingement. In the  $We_1 \leq We < We_2$  impact regime,  $\xi$  starts to decrease as the rebounded droplet starts to split into one big primary droplet and a few smaller secondary droplets due to the formation of a Worthington jet. In the  $We \geq We_2$  impact regime,  $\xi$  continues to decrease as the droplet starts to break into many smaller secondary droplets upon impact. Based on this observation, the number of secondary droplets tends to increase exponentially with the increase of Weber number. Although the number of secondary droplets formed upon impact has not been quantified in this study, it shows that for all impact regimes other than the first one, the volume ratio tends to decrease exponentially

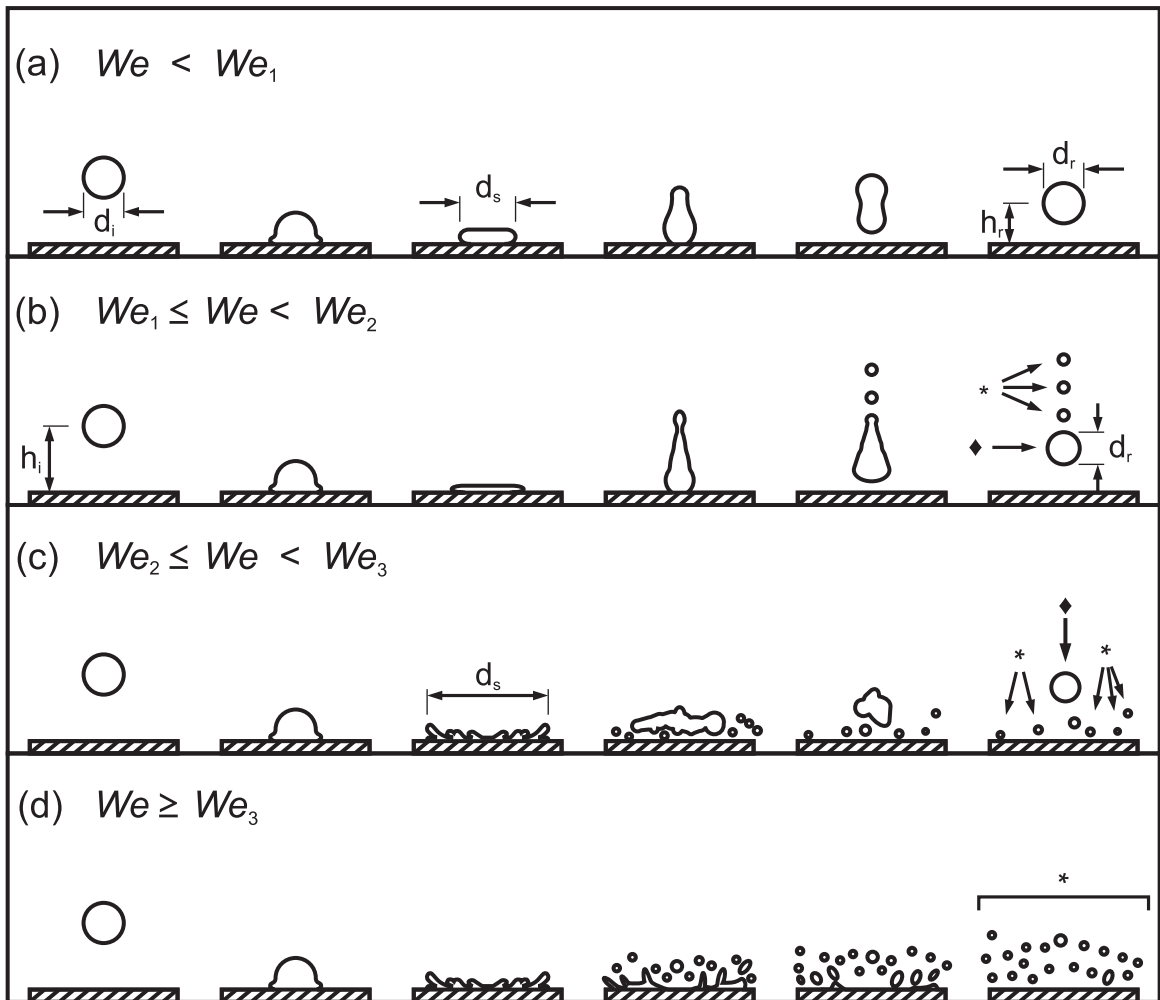


Figure 5.6. Illustration of the evolution of a droplet before, during, and after the impact with a superhydrophobic surface at (a)  $We < We_1$ , (b)  $We_1 \leq We < We_2$ , (c)  $We_2 \leq We < We_3$ , and (d)  $We \geq We_3$ .  $d_i$  is the initial diameter of the droplet before impact and  $d_r$  is the diameter of the primary rebounded droplet or the equivalent spherical diameter if its shape is not spherical.  $d_s$  is the maximum spreading diameter of the droplet during impact. At  $We \geq We_2$ ,  $d_s$  is measured right before the droplet breaks into many smaller secondary droplets. At  $We \geq We_3$  the primary droplet is no longer distinguishable from the secondary ones. Note that the existence of  $We \geq We_3$  regime is still hypothetical.  $h_i$  is the initial drop height of the droplet and  $h_r$  is the maximum bounce height of the primary rebounded droplet. Primary droplet and secondary droplets are indicated by diamond and asterisk markers respectively. This figure is adapted from Rioboo et al. (2008).

with the increase of Weber number. The volume ratio in the second and third impact regimes can be approximated by a scaling of  $\xi \sim We^{-1/8}$  and  $\xi \sim We^{-1}$ , respectively. These relations show that in the  $We_1 \leq We < We_2$  impact regime,  $\xi$  decreases slowly with the increase of  $We$ , while in the  $We \geq We_2$  impact regime,  $\xi$  decreases at a higher rate with the increase of  $We$ .

This approximation fits the experimental data quite well in all impact regimes. The numerical coefficient of the approximation can be obtained by curve fitting the experimental data. Hence, the volume ratio in all ranges of Weber number follows the following relation:

$$\xi = \begin{cases} 1 & , We < We_1 \\ 1.35We^{-1/8} & , We_1 \leq We < We_2 \\ 85We^{-1} & , We \geq We_2 \end{cases} \quad (5.1)$$

Equation (5.1) satisfies the condition of the droplet impact behavior, where  $\xi = 1$  at  $We \leq We_1$  and  $\xi \approx 0$  at  $\lim_{We \rightarrow +\infty}$ . This relation also shows that the droplet volume ratio can be generalized into one expression for each impact regime. A more rigorous study still needs to be conducted to correlate the number of secondary droplets formed by the splashing phenomenon to the Weber number, and to quantify the volume of each secondary droplet.

If the relations described above are extrapolated to an even higher Weber number, one will find the third critical Weber number,  $We_3$ , where the volume of the primary rebounded droplet is almost zero. Although such extrapolation is tenuous, for the sake of argument it is assumed for now that  $\xi \sim We^{-1}$  remains valid for  $We \gg 300$ . Based on this extrapolation,  $\xi \approx 0.01$  at  $We = 1000$ , and since in the  $We \geq We_3$  impact regime the volume ratio should be zero or close to zero, it implies that  $We_3 \approx 1000$ . If such extrapolation is valid, it suggests that the critical Weber number may indeed follow the order of magnitude trend, such that  $We_1 \sim 10^1$ ,  $We_2 \sim 10^2$ , and  $We_3 \sim 10^3$ . Experiments at an even higher Weber number regime have to be conducted in the future to validate this assumption.

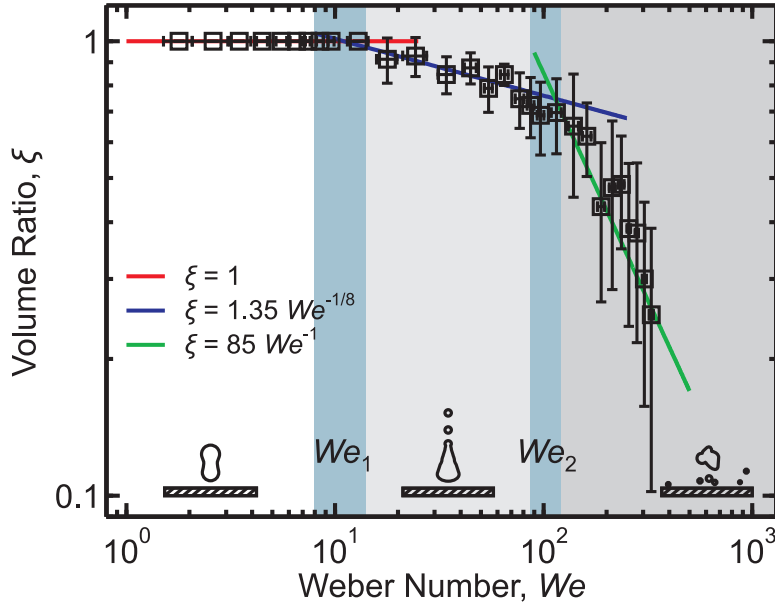


Figure 5.7. Log-log plot of  $\xi$  as a function of  $We$  of the droplet.  $\xi$  is always unity in the first impact regime, while  $\xi$  decreases as  $We$  increases in the second and third impact regimes.

Notice from Figure 5.7 that variations in  $\xi$  start to occur at  $We \geq We_1$  and become more prominent at  $We \geq We_2$ . Such variations are mainly caused by the uncertainties in measuring the diameter of the primary rebounded droplet. As droplets with higher Weber numbers splash off of the surface, the primary rebounded droplets oscillate vigorously, creating non-spherical shapes. At  $We \geq We_2$ , the shape of the rebounded droplets becomes highly non-spherical, which makes it even more difficult to determine their equivalent spherical diameter. Hence, droplets with higher Weber numbers are expected to have higher uncertainties in the measurement of  $d_r$ , which lead to larger variations in calculating  $\xi$ .

### 5.3.3 Coefficient of restitution

Coefficient of restitution,  $\varepsilon$ , represents the loss of energy of an object upon impact on a hard surface and can be quantified by simply taking a ratio between the velocity of such an object after and before the impact. Assuming that the aerodynamic drag during the free-fall and rebound phases can be neglected (Bartolo et al., 2005; Bianco

et al., 2006),  $\varepsilon$  can be measured by taking a ratio between the rebound height and the initial height according the following formula:  $\varepsilon = v_r/v_i = \sqrt{h_r/h_i}$ , where  $h_i$  is the initial drop height of the droplet and  $h_r$  is the maximum bounce height of the primary rebounded droplet (figure 5.6). Under normal circumstances, all objects have  $\varepsilon < 1$ , which means that those objects lose a fraction of their energy upon impact. Just like any other objects, a free-falling water droplet deforms and loses a fraction of its energy as it hits a surface. As the droplet deformation becomes more pronounced with the increase of Weber number, the energy loss of the droplet becomes more significant. Therefore, a water droplet with a higher Weber number is expected to have a lower coefficient of restitution.

As suggested by Biance et al. (2006), a bouncing droplet, and consequently  $\varepsilon$ , can be approximated by a spring-mass model. Using such approximation, the coefficient of restitution scales as  $\varepsilon \sim We^{-1/2}$ . Although this model fits their experimental data for the Leidenfrost drops, it does not agree with their experimental data for droplets impinging on a micro-textured surface, which was claimed to be superhydrophobic. In the case of drops on a micro-textured surface,  $\varepsilon$  reaches a maximum value for some intermediate  $We$ . This maximum value was found to be  $\varepsilon = 0.85$ , which is significantly lower than that of Leidenfrost drops. There are at least two root causes that may lead to such discrepancy: the water loss due to evaporation in the case of Leidenfrost drop might be underestimated, and the fact that a non-ideal superhydrophobic surface was used.

For the Leidenfrost drops, all rebounded droplets are arguably smaller than their original size prior to impact. Given that the contact time of a water droplet to bounce on a superheated plate is in the order of tens of a milliseconds, and the droplet lifetime based on the evaporation rate in such condition is in the order of seconds (Biance et al., 2003), droplets smaller than their capillary length may lose about 3% of their volume during the impact. In addition, the temperature difference between the superheated plate and the ambient air may induce an upward flow of hot air from the surface of the plate that has to be taken into account in the measurement of the impact and rebound velocity of the droplet. Such convection flow may also

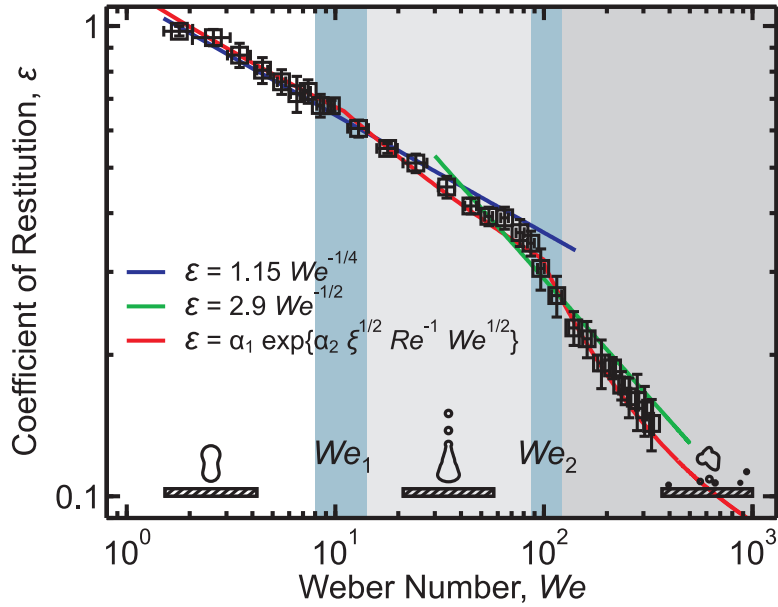


Figure 5.8. Log-log plot of  $\varepsilon$  as a function of  $We$  of the droplet.  $\varepsilon$  decreases as  $We$  increases in all impact regimes. Here  $\alpha_1 = 0.05$  and  $\alpha_2 = 1155$ .

increase the evaporation rate of the droplet before, during, and after the impact. For larger droplets, where the surface to volume ratio is smaller, such loss in volume due to evaporation may not be as severe as that for smaller droplets, and hence it could be neglected.

In the case of drops on a micro-textured surface, there exists a non-negligible adhesion force between the droplet and the surface, such that if the kinetic energy of the droplet is too low or the size of the droplet is too large such a droplet will be pinned to the surface and lose its ability to bounce (Richard and Quere, 2000; Bianco et al., 2006). Such adhesion force only exists when the water droplet is in intimate contact with the surface asperities. The presence of a large-scale liquid-solid interface infers the use of a non-ideal Wenzel state superhydrophobic surface in those studies. Since their experimental data does not represent the actual impact behavior on an ideal superhydrophobic surface, any further studies on an ideal superhydrophobic surface should only be compared to the Leidenfrost drops.

According to Bianco et al. (2006), the rate of decrease of  $\varepsilon$  in the  $We < We_2$  impact regime should be as high as that in the third impact regime. However, as

observed experimentally,  $\varepsilon$  decreases at a much smaller rate in the low and moderate Weber number regime compared to that in the high Weber number regime. This suggests that the loss of energy upon impact on an ideal superhydrophobic surface is much lower than that on a superheated surface, i.e., Leidenfrost drop. In other words, there are some non-negligible factors, e.g., water evaporation and convective flow of hot air, that are responsible for this additional loss of energy. These non-negligible factors should be taken into account in any future studies on the impact behavior of a Leidenfrost drop.

As expected,  $\varepsilon$  decreases as the increase of  $We$ , even in the  $We < We_1$  impact regime. In the  $We_1 \leq We < We_2$  impact regime, the rate of decrease of  $\varepsilon$  is actually similar to that in the  $We < We_1$  impact regime. In fact, the coefficient of restitution decreases from  $\varepsilon \approx 1$  to  $\varepsilon \approx 0.4$  as Weber number increases from  $We \approx 1$  to  $We \approx 70$ . A significant transition occurs at  $We_2$ , such that  $\varepsilon$  plummets at an even faster rate in the  $We \geq We_2$  impact regime. Such transition, which is shown by an elbow right before  $We_2$  in Figure 5.8, indicates a change in the recoverability of droplet deformation. In the  $We < We_2$  impact regime, the droplet undergoes a recoverable deformation upon impact, and the fragmentation only occurs after the droplet rebounds off of the surface. On the other hand, in the  $We \geq We_2$  impact regime, the droplet undergoes an irrecoverable deformation upon impact, which is demonstrated by the splashing phenomenon.

Phenomenologically, the coefficient of restitution in the first and second impact regimes can be described by a scaling of  $\varepsilon \sim We^{-1/4}$ , and in the third impact regime by a scaling of  $\varepsilon \sim We^{-1/2}$ . These relations shows that the energy loss upon impact is proportional to the deformation of the droplet and the loss of energy due to irrecoverable deformation, i.e., droplet fragmentation due to splashing, is enormous compared to that due to recoverable deformation. Although the  $\varepsilon$  approximation in the first and second impact regime does not agree with the scaling law suggested by Bianco et al. (2006), such scaling is indeed observed in the  $We \geq We_2$  impact regime.

As suggested by Bianco et al. (2006), a bouncing water droplet on a non-wettable surface has a similar behavior as an elastic ball, thus  $\varepsilon$  can be approximated by a

spring-mass model. Using this approximation, Bianco et al. (2006) obtained a scaling of  $\varepsilon \sim We^{-1/2}$  as the model for the coefficient of restitution. Although this model seems to fit their experimental data for Leidenfrost case, it does not agree with their experimental data for droplets impinging a non-wetted micro-textured surface. Such discrepancy may be caused by the underestimation of water loss due to evaporation in the case of Leidenfrost drop. Given the contact time of a water droplet to bounce on a superheated plate is in the order of tens of a milliseconds, and the droplet lifetime based on the evaporation rate in such condition is in the order of seconds (Bianco et al., 2003), all small droplets with sizes smaller than the capillary length will lose about 3% of their volume during the impact. In addition, the temperature difference between the superheated plate and the ambient air may induce an upward flow of hot air from the surface of the plate that has to be taken into account in the measurement of the impact and rebound velocity of the droplet. Such convection flow may also increase the evaporation rate of the droplet before, during and after the impact.

Because of this discrepancy, a better model to approximate the coefficient of restitution for a superhydrophobic surface that fits to our experimental data needs to be proposed. It does make sense to develop a model for a bouncing water droplet based on a spring-mass model. However, as suggested by Pasandideh-Fard et al. (1996), Kim and Chun (2001), Ukiwe and Kwok (2004), and Vadillo et al. (2009), the effect of viscous dissipation has to be included in the model, even though all experiments are done at a low viscosity regime. Here we propose a model for  $\varepsilon$  that is developed from a linear mass-spring-damper model. Using this model, the effect of viscous dissipation is not completely neglected, although it is small compared to the effect of surface tension and inertia. Such a linear mass-spring-damper model has been successfully implemented in the past to explain the bouncing behavior of free-falling linear solid elastic balls (Falcon et al., 1998; Nagurka and Huang, 2006).

Based on a linear mass-spring-damper model, the equation of motion of the droplet during the impact phase can be expressed as:

$$m\ddot{x} + c\dot{x} + kx = -mg \quad (5.2)$$

where  $x$  represents the position of the droplet's center of mass over time with respect to the initial droplet's center of mass right when the droplet touches the surface (Figure 5.9). It also means that the position of the surface is always at  $x = -d_i/2$ . The velocity and the acceleration of the droplet during the impact are represented by  $\dot{x}$  and  $\ddot{x}$ , respectively. The mass, viscous damping, and linear elastic stiffness of the droplet are denoted by  $m$ ,  $c$ , and  $k$ , respectively. The linear elastic stiffness  $k$  scales as the droplet's surface tension  $\sigma$ . However, the circumstances with the viscous damping  $c$  are more ambiguous since it may include viscous dissipation of the droplet in the air, viscous boundary layer during the impact, and viscous dissipation due to the interaction with the surface. In this study, the viscous damping  $c$  represents the global viscosity of the system, which includes all the viscous terms mentioned above. Thus,  $c$  can be scaled as the droplet's bulk viscosity  $\mu$  times the length scale of the droplet  $d_i$ . Equation (5.2) is subjected to initial conditions  $x(0) = 0$  and  $\dot{x}(0) = -v_i$ , where  $v_i$  is the impact velocity of the droplet.

Since in this case  $c/\sqrt{km} \ll 1$ , the solution of Equation (5.2), after the imaginary parts are removed, is given by:

$$x(t) = \left[ \frac{cg}{2k\omega} - \frac{v_i}{\omega} \right] \exp\left\{-\frac{c}{2m}t\right\} \sin \omega t + \frac{mg}{k} \exp\left\{-\frac{c}{2m}t\right\} \cos \omega t - \frac{mg}{k} \quad (5.3)$$

where  $\omega$  is the natural frequency of the droplet described as following:

$$\omega = \frac{1}{2m} \sqrt{4km - c^2} \approx \sqrt{\frac{k}{m}} \quad (5.4)$$

By order of magnitude approximation  $mg/k < cg/k\omega \ll v_i/\omega$ . Therefore, equation (5.3) can be simplified as following:

$$x(t) \approx -\frac{v_i}{\omega} \exp\left\{-\frac{c}{2m}t\right\} \sin \omega t \quad (5.5)$$

Contact time ( $t_r$ ) is defined as the time when the droplet start to rebound from the surface, but still in contact with the surface, and can be estimated from the nontrivial

solution of Equation (5.5) by setting  $x(t_r) = 0$ . Such estimation is valid for all range of  $We$ , even though the deformation of the rebounded droplet is considerably large at  $We \geq We_1$ , due to the formation of Worthington jet or the occurrence of splashing phenomena. Since  $x(t)$  indicates the position of the droplet's center of mass, not its centroid,  $x(t_r)$  will be close to zero regardless of the shape of the rebounded droplet, as long as the droplet is still in contact with the surface. Therefore,  $t_r$  is given by:

$$t_r = \frac{\pi}{\omega} \quad (5.6)$$

The velocity of the droplet upon impact can be obtained by differentiating equation (5.5) as following:

$$\begin{aligned} \dot{x}(t) \approx & \frac{cv_i}{2m\omega} \exp\left\{-\frac{c}{2m}t\right\} \sin \omega t \\ & - v_i \exp\left\{-\frac{c}{2m}t\right\} \cos \omega t \end{aligned} \quad (5.7)$$

The velocity of the droplet at  $t = t_r$ , right before the droplet lifts off from the surface, is then given by:

$$v_r \approx \dot{x}(t_r) = v_i \exp\left\{-\frac{c}{2m}t_r\right\} \quad (5.8)$$

As mentioned earlier, coefficient of restitution is defined as  $\varepsilon = v_r/v_i$ . Accordingly, Equation (5.8) can be written as:

$$\varepsilon \approx \exp\left\{-\frac{c}{2m}t_r\right\} \quad (5.9)$$

Hence,  $t_r$  is obtained by substituting Equation (5.4) into Equation (5.6), which yields  $t_r = \pi\sqrt{m/k}$ . Since  $t_r$  represents the typical inertial oscillation response time of the droplet with mass  $m \sim \rho d_r^3$  and linear elastic stiffness  $k \sim \sigma$  (Reyssat et al., 2010; Clanet et al., 2004; Schiaffino, 1997), the contact time can be approximated as:

$$t_r \sim \sqrt{\frac{\rho d_r^3}{\sigma}} \quad (5.10)$$

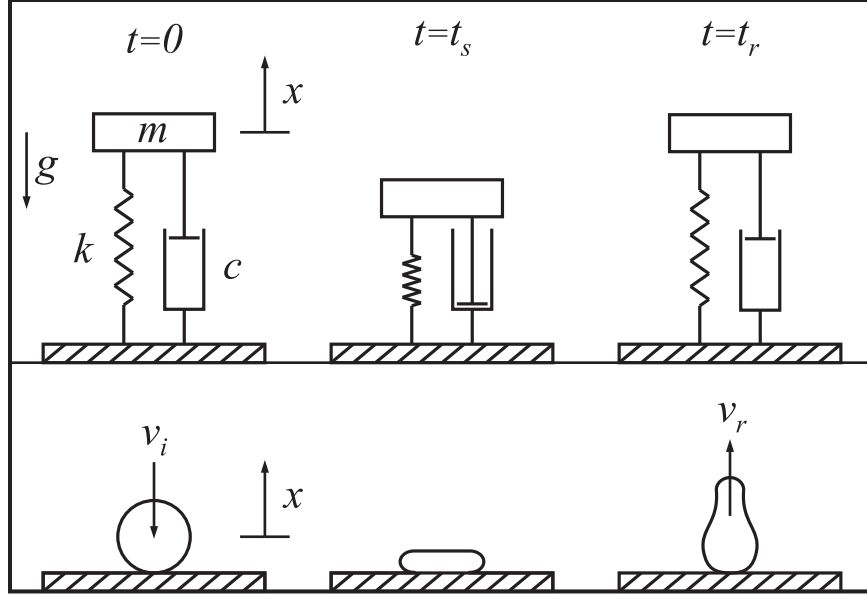


Figure 5.9. A model for coefficient of restitution,  $\varepsilon$ , can be obtained by representing the droplet as a linear mass-spring-damper system during the impact phase. The initial condition at  $t = 0$  is defined as the condition right when the free falling droplet touches the surface, where the position of the droplet's center of mass is equal to zero and the impact velocity is  $-v_i$ . At time  $t = t_s$ , the droplet reaches its maximum spreading diameter during the impact phase. At time  $t = t_r$ , the droplet starts to lift off from the surface and begin the rebound phase.

The ratio between the viscosity and mass of the droplet is given by:

$$\frac{c}{m} \sim \frac{\mu}{\rho d_i^2} \quad (5.11)$$

By substituting Equation (5.10) and Equation (5.11) into Equation (5.9), and by taking into account the droplet's volume ratio  $\xi = (d_r/d_i)^3$ , the coefficient of restitution can be approximated as  $\varepsilon \sim \exp\{-\sqrt{\xi\mu^2/\rho\sigma d_i}\}$ . In general, it can be written in term of Reynolds and Weber numbers as:

$$\varepsilon = \alpha_1 \exp\{\alpha_2 \xi^{1/2} Re^{-1} We^{1/2}\} \quad (5.12)$$

By fitting Equation (5.12) to the experimental data using least square method, the coefficients  $\alpha_1$  and  $\alpha_2$  were found to be  $\alpha_1 = 0.05$  and  $\alpha_2 = 1155$  (Figure 5.8).

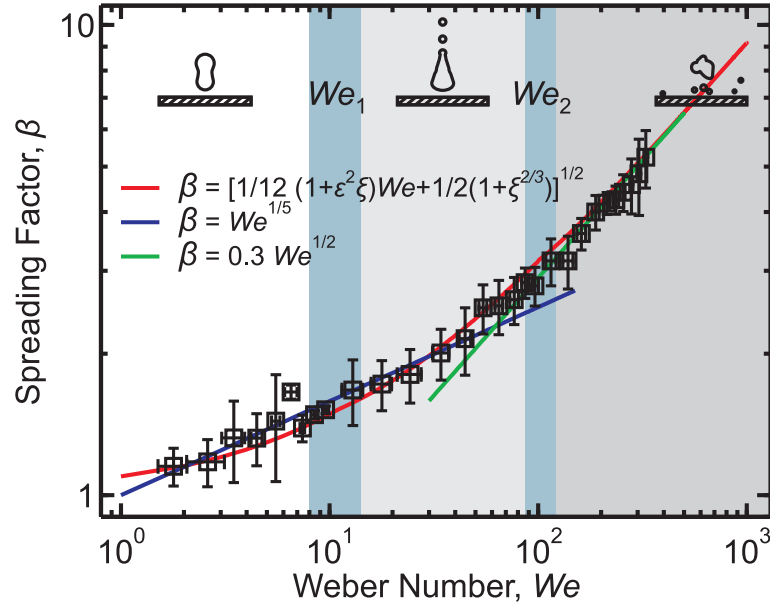


Figure 5.10. Log-log plot of  $\beta$  as a function of  $We$  of the droplet.  $\beta$  increases with the increase of  $We$  all impact regimes. Each square marker represents the mean value of multiple data points and error bars indicate the standard deviations from the mean.

### 5.3.4 Maximum spreading factor

The maximum spreading factor,  $\beta$ , is defined as the ratio of the maximum spreading diameter of the droplet during impact to the initial diameter of the droplet before impact, and can be calculated using the following formula:  $\beta = d_s/d_i$ , where  $d_s$  is the maximum spreading diameter of the droplet during impingement, and  $d_i$  is the initial diameter of the droplet (Figure 5.6). For splashing droplet at  $We \geq We_2$ ,  $d_s$  is measured right before the droplet breaks into many smaller secondary droplets. As previously stated, a free-falling water droplet deforms upon impact, and such deformation becomes more pronounced with the increase of the kinetic energy of the droplet. Since a stronger droplet deformation corresponds to a larger spreading factor, one can expect that  $\beta$  increases with the increase of  $We$ .

As observed experimentally,  $\beta$  increases with the increase of  $We$  in all impact regimes (Figure 5.10). The rate of increase of  $\beta$  in the  $We < We_1$  impact regime is similar to that in the  $We_1 \leq We < We_2$  impact regime, where the maximum spreading factor increases from  $\beta \approx 1.1$  to  $\beta \approx 2.6$  as Weber number increases from

$We \approx 1.7$  to  $We \approx 76.7$ . Empirically, the maximum spreading factor in this impact regimes can be approximated by a scaling of  $\beta \sim We^{1/5}$ . A significant transition occurs right before  $We_2$ , such that  $\beta$  increases at a faster rate in the  $We \geq We_2$  impact regime.

In the  $We \geq We_2$  impact regime, the maximum spreading factor can be approximated by a scaling of  $\beta \sim We^{1/2}$ . Such scaling, is in fact, the generalized scaling law derived from a straightforward energy conservation approach. Using this approach, the scaling of maximum spreading factor is obtained by calculating the radius of the droplet when the initial kinetic energy of the droplet is converted completely into surface energy (Chandra and Avedisian, 1991; Bennett and Poulikakos, 1993). The agreement between this scaling and the experimental data presented here suggests that a straightforward energy conservation approach may adequately predict the droplet spreading behavior upon impact on a non-wetted surface in the medium and high Weber number regime.

As expected, the scaling of  $\beta \sim We^{1/4}$ , as suggested by Clanet et al. (2004), Bartolo et al. (2005), and Biance et al. (2006), fails to capture the droplet spreading behavior in all impact regimes. Note that this scaling law was proposed to counter the straightforward energy conservation approach because of the presence of an internal flow in the droplet during the impact. Such internal flow suggests that the initial kinetic energy is not completely converted into surface energy even when the droplet reaches its maximum spreading diameter, and thus  $\beta$  should be determined by the balance between gravity and surface forces. However, as mentioned by Eggers et al. (2010), these scaling laws are actually similar to each other in such a small range of  $We$ , such that they cannot be reliably discriminated. In the low  $Oh$  and  $Ca$  regime, where the effect of viscous and capillary forces is minimal, the maximum spreading radius should not be dictated by a balance between gravity and surface tension (Eggers et al., 2010).

In the large  $We$  and  $Re$  regimes, two different mechanisms to predict the maximum spreading diameter have been assumed (Eggers et al., 2010). The first assumption is that the effect of viscosity can be neglected such that the maximum spreading

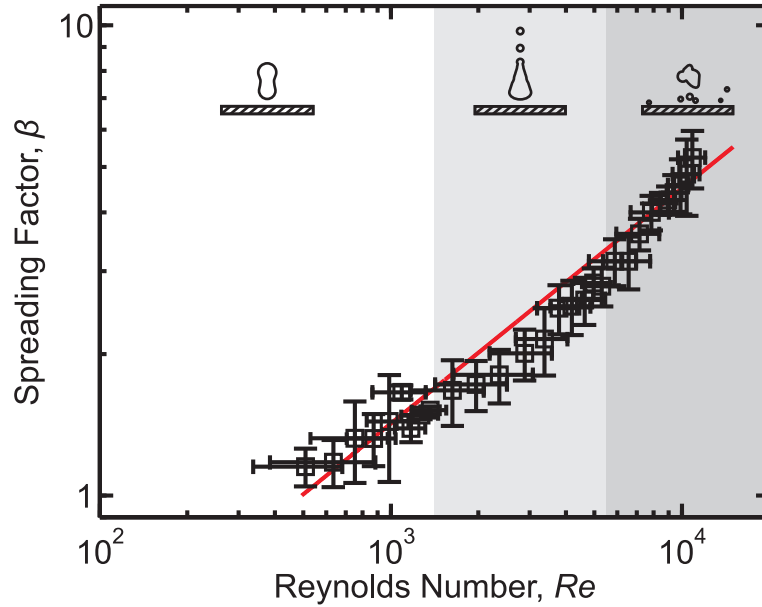


Figure 5.11. Log-log plot of  $\beta$  as a function of  $Re$  of the droplet.  $\beta$  increases with the increase of  $Re$  all impact regimes.

diameter only depends on the balance between kinetic energy and surface tension of the droplet. The second assumption is that the viscous dissipation dominates surface tension and the maximum spreading diameter is determined by the balance between inertia and viscosity. Using the first assumption, the maximum spreading diameter should scale as  $\beta \sim We^{1/2}$ , while using the second assumption, it should scale as  $\beta \sim Re^{1/5}$  (Clanet et al., 2004; Bartolo et al., 2005). It has been demonstrated above that  $\beta \sim We^{1/2}$  in the  $We \geq We_2$  impact regime, confirming the validity of the first assumption.

The second assumption, which is derived from an idea that the spreading behavior is limited the effect of viscosity, may only be satisfied in the high  $Oh$  regime. Since this current study was done in the very low  $Oh$  regime, the obtained experimental data could not be used to confirm the validity of the second assumption. For the sake of argument,  $\beta$  is plotted versus  $Re$  to show if the scaling of  $\beta \sim Re^{1/5}$  is satisfied (Figure 5.11). Although  $\beta$  does increase with the increase of  $Re$ , the scaling of  $\beta \sim Re^{1/5}$  is not satisfied. In fact, empirical approximation of the experimental data shows that the maximum spreading factor scales as  $\beta \sim Re^{1/2}$ . Such poor prediction

of  $\beta$  by the second assumption infers that the loss of kinetic energy of the droplet during impact due to viscous dissipation is indeed minimal. Therefore, the scaling of  $\beta \sim Re^{1/5}$  may not be relevant for use in predicting the droplet spreading behavior on a non-wetted surface in the small viscosity regime.

As stated earlier, many previous studies have been conducted in the past (Chandra and Avedisian, 1991; Pasandideh-Fard et al., 1996; Kim and Chun, 2001; Ukiwe and Kwok, 2004; Vadillo et al., 2009; Li et al., 2010; Eggers et al., 2010; Lee and Lee, 2011) to find a mathematical model that could reliably describes  $\beta$ . These studies show that an accurate model can be made based on the energy conservation approach and by taking the effect of viscous dissipation and surface wettability into account. Based on the energy conservation approach, a balance of energy between phases of drop before, during, and after the impact can be written as follows:

$$KE_1 + SE_1 = KE_2 + SE_2 + W_{12} \quad (5.13a)$$

$$KE_2 + SE_2 - W_{23} = KE_3 + SE_3 \quad (5.13b)$$

where  $KE_1$  and  $SE_1$  are the droplet's kinetic energy and surface energy, respectively, during the free fall phase right before the impact;  $KE_2$  and  $SE_2$  are the droplet's kinetic energy and surface energy, respectively, at the instant of maximum spread during the impact phase;  $KE_3$  and  $SE_3$  are the droplet's kinetic energy and surface energy, respectively, during the rebound phase right after the impact. The loss of energy due to viscous dissipation when the droplet spreads and retracts on the surface during the impact are denoted by  $W_{12}$  and  $W_{23}$  respectively. At the instant of maximum spread, the droplet's kinetic energy can be assumed to be negligible ( $KE_2 = 0$ ) because the velocity of the droplet is basically zero at that exact moment. Equation (5.13a) represents the energy balance between the total of the droplet's energy during the free fall phase right before it impacts the surface and the sum of droplet's energy when it reaches its maximum spreading diameter and the energy consumed to spread the droplet on the surface. Equation (5.13b) represents the energy balance between the sum of the droplet's energy when it reaches its maximum spreading di-

ameter and the energy consumed to retract the droplet on the surface and the total of the droplet's energy during the rebound phase right after it lifts off from the surface. Since it can be assumed that the loss of energy due to viscous dissipation during the spreading and retraction phase is equal,  $W_{12} = W_{23} = W$ , Equation (5.13a) and Equation (5.13b) can be written in a single equation as following:

$$KE_1 + SE_1 = KE_3 + SE_3 + 2W \quad (5.14)$$

where the kinetic energy of the droplet during the free fall and rebound phases is given by

$$KE_1 = \pi \rho d_i^3 v_i^2 / 12 \quad (5.15a)$$

$$KE_3 = \pi \rho d_r^3 v_r^2 / 12 \quad (5.15b)$$

and the surface energy of the droplet during the free fall and rebound phases is given by

$$SE_1 = \pi d_i^2 \sigma \quad (5.16a)$$

$$SE_3 = \pi d_r^2 \sigma \quad (5.16b)$$

Equation (5.14) can be simplified by substituting  $v_r$  and  $d_r$  with  $v_i$  and  $d_i$  using the relation given by the volume ratio  $\xi = (d_r/d_i)^3$  and the coefficient of restitution  $\varepsilon = v_r/v_i$ . Hence, it can be written as:

$$\frac{\pi \rho d_i^3 v_i^2}{12} + \pi d_i^2 \sigma = \frac{\pi \rho \xi d_i^3 \varepsilon^2 v_i^2}{12} + \pi \xi^{2/3} d_i^2 \sigma + 2W \quad (5.17)$$

By substituting Equation (5.15a) and Equation (5.16a) into Equation (5.17),  $W$  can be expressed as:

$$W = \frac{1}{2} [(1 - \varepsilon^2 \xi) KE_1 + (1 - \xi^{2/3}) SE_1] \quad (5.18)$$

where the volume ratio ( $\xi$ ) is described in Equation (5.1) and the coefficient of restitution ( $\varepsilon$ ) is described in Equation (5.12). According to Ukiwe and Kwok (2004), the droplet's surface energy when it reaches its maximum spreading diameter can be

expressed as:

$$SE_2 = \pi\sigma d_s l_s + \frac{\pi}{4}\sigma(d_s - l_s)^2(1 - \cos\theta_s) \quad (5.19)$$

where  $l_s$  and  $\theta_s$  are the thickness and the equilibrium contact angle of the droplet when it reaches its maximum spreading diameter. Experimental data show that the thickness of the droplet when it reaches its maximum diameter decreases rapidly with the increase of Weber number. At a small Weber number,  $We < We_1$ , the droplet's thickness is still comparable to the maximum diameter of the droplet. However, at a moderate Weber number,  $We_1 \leq We < We_2$ , the droplet's thickness becomes an order of magnitude smaller than its maximum diameter. At an even larger Weber number,  $We \geq We_2$ , the droplet's thickness is found to be  $l \ll d_s$ , and can no longer be observed. Hence, as suggested by Pasandideh-Fard et al. (1996), Vadillo et al. (2009), and Lee and Lee (2011), it is reasonable to neglect the first term of Equation (5.19). As mentioned earlier, the static contact angle of the droplet on the superhydrophobic carbon nanotube array is about  $171^\circ$  and the contact angle hysteresis is about  $3^\circ$ , which suggests that the equilibrium contact angle of the droplet during the impact is about  $171^\circ(\pm 3^\circ)$ . Consequently, the last term of Equation (5.19) can be approximated as  $\pi\sigma d_s^2/2$ . The energy balance between phases of the drop before and during the impact can then be written as:

$$\frac{\rho d_i v_i^2}{12\sigma} + 1 = \frac{d_s^2}{2d_i^2} + \frac{1}{24}[(1 - \varepsilon^2\xi)\frac{\pi}{12}\rho d_i^3 v_i^2 + \frac{1}{2}(1 - \xi^{2/3})] \quad (5.20)$$

After simplification,  $\beta$  can be expressed as:

$$\beta = [\frac{1}{12}(1 + \varepsilon^2\xi)We + \frac{1}{2}(1 + \xi^{2/3})]^{1/2} \quad (5.21)$$

where  $\xi$  is described in Equation (5.1) and  $\varepsilon$  is described in Equation (5.12).

## 5.4 Concluding Remarks

In conclusion, this work presents for the first time a complete characterization of water droplet impact behavior on a Cassie state nanostructured superhydrophobic surface. Here, such surface was made of chemically modified carbon nanotube arrays. In addition to its extraordinarily high static contact angle, as well as extremely low contact angle hysteresis and roll-off angle, this surface exhibits a continuous trapped air cushion at the interface between water and the surface. This air film is indeed a signature of an ideal Cassie state superhydrophobic surface.

Three different impact regimes have been experimentally identified while another impact regime is proposed. These regimes are partitioned by three critical Weber numbers, two of which have been experimentally observed. The first impact regime, which was found at  $We < We_1$ , is when the impacting droplet recedes right after it reaches its maximum spreading diameter, and subsequently rebounds off of the surface completely. The second impact regime, which was found at  $We_1 \leq We < We_2$ , is when the rebounding droplet creates a Worthington jet and forms several smaller secondary droplets. The third impact regime, which was found at  $We_2 \leq We < We_3$ , is when the impacting droplet breaks into many smaller secondary droplets once it reaches its maximum spreading diameter, and subsequently the primary droplet rebounds off of the surface. The fourth impact regime, which is proposed to be found at  $We \geq We_3$ , is when the impacting droplet breaks into a myriad of smaller droplets and the primary droplet can no longer be distinguished from the secondary ones. The first and second critical Weber numbers are found at  $We_1 \sim 10^1$  and  $We_2 \sim 10^2$ , respectively, and the third critical Weber number is hypothesized to be found at  $We_3 \sim 10^3$ . Further studies to confirm this hypothesis and to understand the underlying mechanism of droplet segmentation still need to be done.

The volume ratio between the primary and the secondary droplets,  $\xi$ , is found to decrease with the increase of Weber number in all impact regimes other than the first one. In the first impact regime,  $\xi$  is found to be always unity since the droplet remains intact during and subsequent to the impingement. In the second impact regime,  $\xi$

starts to decrease as the rebounded droplet begins to split due to the formation of a Worthington jet. In the third impact regime,  $\xi$  continues to decrease as the droplet breaks into many smaller secondary droplets upon impact. The volume ratio in the second and third impact regimes can be approximated by a scaling of  $\xi \sim We^{-1/8}$  and  $\xi \sim We^{-1}$ , respectively. A more rigorous study needs to be conducted to correlate the number of secondary droplets formed by the splashing phenomenon to the Weber number, and to quantify the volume of each secondary droplet.

The loss of energy due to droplet deformation upon impact is quantified as the coefficient of restitution,  $\varepsilon$ . In the first and second impact regimes, the coefficient of restitution can be approximated by a scaling of  $\varepsilon \sim We^{-1/4}$ . In the third impact regime, the coefficient of restitution can be approximated by a scaling of  $\varepsilon \sim We^{-1/2}$ . Interestingly, the scaling law suggested by Bianche et al. (2006) only agrees to the current experimental data in the third impact regime. This suggests that there are some non-negligible factors responsible for additional loss of energy that have been taken into account in any future studies on the impact behavior of a Leidenfrost drop. Further studies to develop a logical mathematical model based on these experimental data has to be done in the future.

The droplet spreading behavior on a surface upon impact is quantified as the maximum spreading factor,  $\beta$ . In the first and second impact regimes, the maximum spreading factor can be approximated by a scaling of  $\beta \sim We^{1/5}$ . In the third impact regime, the maximum spreading factor can be approximated by a scaling of  $\beta \sim We^{1/2}$ . This scaling of  $\beta \sim We^{1/2}$  is, in fact, the generalized scaling law derived from a simple energy conservation approach and has been originally proposed by Chandra and Avedisian (1991) and Bennett and Poulikakos (1993). Unsurprisingly, the scaling laws of  $\beta \sim We^{1/4}$  and  $\beta \sim Re^{1/5}$ , as suggested by Clanet et al. (2004), Bartolo et al. (2005), and Bianche et al. (2006), do not agree with the obtained experimental data. Therefore, such scaling laws may not be relevant for use in predicting the droplet spreading behavior on a non-wetted surface in a low viscosity regime.

## Chapter 6

# Carbon Nanotube Arrays as Electrodes for Electrochemical Double Layer Capacitor

### 6.1 Introduction

Demand and consumption of global energy is continually increasing across a world whose population will grow to nearly 9 billion people in the next couple of years. It is poised to continue its steady increase in the next several decades. The climate change and the decreasing availability of fossil fuels has hastened the development of satisfying sustainable and renewable energy technologies. Since electrical energy storage systems such as batteries and capacitors are considered the most critical link between the ever increasing renewable energy supply and demand, a lot of work has been done to improve their efficiency and performance. Further, the advancement of micro/nano-electro-mechanical devices for telecommunication and biomedical applications initiates the demand of reliable lightweight electrical energy storage systems with small form factors. In order to fulfil all these requirements, development of new materials with exceptional specific surface area and excellent electrochemical properties has become the focus of much research effort.

Electrical energy can be stored either chemically, e.g. batteries, or physically, e.g., capacitors. Chemically, the electrical energy is converted into chemical energy via Faradaic reduction and oxidation (redox) reactions. Although in principal the

energy conversion from electrical to chemical and vice versa is thermodynamically reversible, practically such conversion often involves some degree of irreversibility due to electrode-electrolyte interphase changes during the charging and discharging processes (Conway, 1999). Therefore, the charge/discharge rates of batteries are very low and their cycle-life is limited to only several thousand cycles. However, depending on the types of batteries, they can have a very high gravimetric energy density of up to 200 Wh/kg (Liu et al., 2010). In contrast to batteries, capacitors physically store electrical energy via non Faradaic electrostatic process. Because of the absence of phase changes due to redox reactions, the charging and discharging processes are highly reversible. Therefore, capacitors in general have an exceptional cyclability, which leads to a very stable behavior over a very long cycle-life and a very high charge/discharge rates. However, the gravimetric energy density of capacitors is typically very low, because it is limited by the accessible surface area of the electrodes.

Great efforts have been made in the last few decades to combine the high energy-storage capability of conventional batteries and the high power-delivery capability of conventional solid state capacitors, resulting in the invention of electrochemical double layer capacitors (EDLCs). EDLCs are electrical energy storage devices that utilize highly reversible electrostatic accumulation of ions of the electrolytes on the surface of the active electrode materials. When an EDLC is charged, cations accumulate on the surface of the negatively polarized electrode creating a capacitor-like electrical double layer separation. Similarly, electric double layer is also formed on the surface of the positively polarized electrode due to the accumulation of anions. When an EDLC is discharged, cations and anions of the electrolytes can be transported back from the surface of the electrodes in a very fast response time (Figure 6.1). Therefore, EDLCs are capable of providing short high-energy bursts that neither batteries nor solid state capacitors can provide efficiently, with a remarkably long cycle-life (Conway, 1999; Simon and Gogotsi, 2008). Such capability has been used to provide high power pulses for a few seconds, for a wide range of applications including electric transportation technology, emergency backup power, consumer electronics such as laptops or cell phones, medical electronics, and aircraft and spacecraft systems such as evacuation

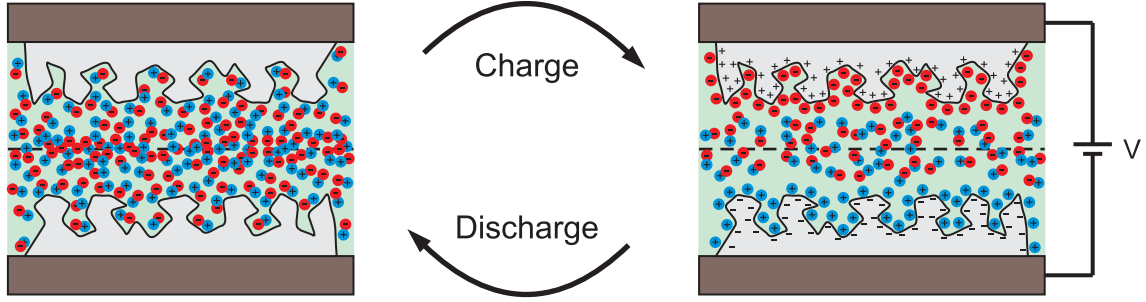


Figure 6.1. Schematic of an electrochemical double layer capacitor.

slides and communication devices (Miller and Simon, 2008; Miller and Burke, 2008).

The gravimetric specific double layer capacitance ( $C_G$ ) of an EDLC is dictated by the dielectric constant of the electrolyte ( $\epsilon_e$ ), the accessible surface area of the electrodes ( $A$ ), and the mass of active electrode materials ( $m$ ) according to the following relation:

$$C_G = \frac{\epsilon_e \epsilon_0 A}{d_{dl} m} \quad (6.1)$$

where  $\epsilon_0$  is the vacuum dielectric constant and  $d_{dl}$  is the electrical double layer separation thickness. Based on Equation 6.1, light weight active electrode materials with high accessible surface area are the key component to achieve a high gravimetric specific capacitance. Among many available materials that can be used as active electrode materials, carbon electrodes are considered the best option due to their excellent conductivity. In addition, carbon is lighter than most elements, and definitely lighter than industrial metal. However, the surface area of bulk carbon electrodes is considered too small to be used effectively as active electrode materials (Figure 6.2.a).

Bulk carbon electrode can be activated to improve their accessible surface area. These activated carbon based materials, known as activated carbon (AC), have been the most widely used active electrode materials in commercially available EDLC (Figure 6.2.b). AC based electrodes are known to have a very high specific surface area, up to 2000 m<sup>2</sup>/g (Simon and Gogotsi, 2008; Lu et al., 2011), due to their tremendous network of micropores (pore size:  $\leq 2$  nm). However, the electrolyte accessibility of micropores dominated network is considerably poor, such that electric double layer cannot be formed on most of the micropores. Thus, AC based EDLC usually exhibits

unsatisfactory capacitance, which is about 10-20% of the theoretical values (Liu et al., 2010).

Carbon active electrode materials can be activated using several known oxidation methods such as liquid-phase or gas-phase oxidations, and plasma treatments. Liquid-phase oxidations are carried out by exposing these materials to strong acids and oxidants, including potassium chlorate ( $\text{KClO}_3$ ), potassium permanganate ( $\text{KMnO}_4$ ), sodium nitrate ( $\text{NaNO}_3$ ), phosphoric acid ( $\text{H}_3\text{PO}_4$ ), nitric acid ( $\text{HNO}_3$ ) and sulfuric acid ( $\text{H}_2\text{SO}_4$ ). It is important to note that, in addition to the highly corrosive nature of these chemicals, the oxidation processes usually involve the generation of toxic and explosive gasses (Marcano et al., 2010). Liquid-phase oxidations are also considered impractical for activating carbon electrode materials, because the capillary forces induced by these liquid chemicals upon drying are very likely to collapse most of the micropores. Therefore, gas-phase oxidations and plasma treatments are more favorable for use in activating carbon electrode materials. Gas-phase oxidations using oxygen ( $\text{O}_2$ ), ozone ( $\text{O}_3$ ) or carbon dioxide ( $\text{CO}_2$ ) gas, as well as water vapor ( $\text{H}_2\text{O}$ ) at an elevated temperature are considered a safer, more convenient, and more practical way compared to their liquid-phase counterparts, especially in large industrial-scale production.

To further improve the performance of EDLC, CNT can be used to replace AC as the active electrode materials. Compared to AC, CNT has a relatively lower specific surface area, since their porous network is dominated by mesopores (pore size: 2-50 nm) and macropores (pore size:  $>50$  nm). However, the presence of mesopores and macropores and the lack of micropores makes the entire surface of CNT easier to access by ions of the electrolyte. Hence, intrinsic capacitance of CNT is typically higher than that of AC (Figure 6.2.c). In addition, the electrical conductivity of CNT, as well as its thermal and mechanical properties, are known to be much superior than those of AC (Jorio et al., 2007). Among diverse types of CNTs, vertically aligned CNT arrays oriented perpendicularly to the current collectors are considered the most suitable active electrode materials for EDLC. Since the physical properties of CNT arrays, such as packing density, number of walls, and length can be varied by

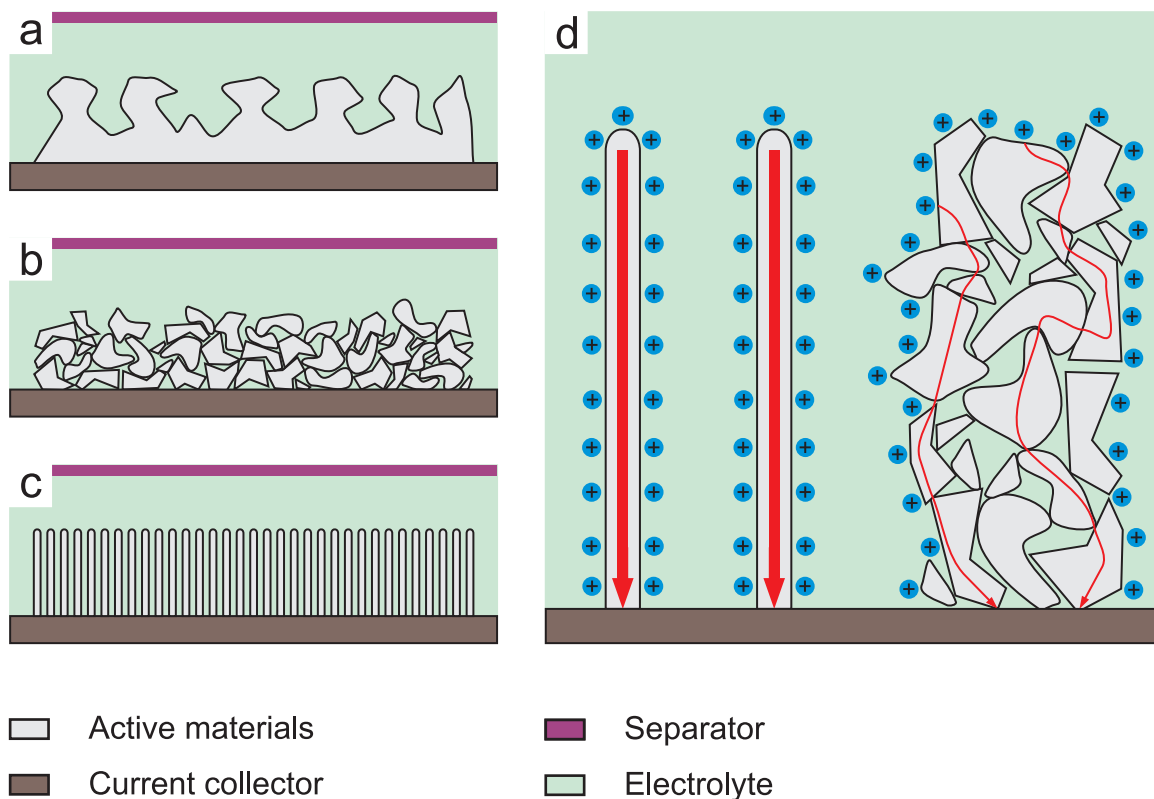


Figure 6.2. Schematic of different types of carbon electrodes for EDLC: (a) bulk carbon, (b) activated carbon, (c) CNT arrays. (d) Comparison between CNT arrays and activated carbon (d).

changing the growth conditions, the porosity of CNT arrays can be tuned such that their porous network is dominated by mesopores whilst maximizing their specific surface area. The volumetric specific surface area of CNT arrays can be extremely high due to their tremendously high aspect ratio of up to 320 millions. Further, the electronic transport along the main axis of CNT arrays is almost perfectly ballistic, which means that the electrons flow directly into the current collector with minimal scattering (Figure 6.2.d). In addition, a low contact resistance between the CNT arrays and the current collector can be maintained, such that the overall IR drop can be lowered to achieve an even higher power density than that of the AC based EDLC.

## 6.2 Materials and Methods

CNT arrays used in this study are grown using thermal CVD technique on catalyst coated silicon substrates. The detail of CVD growth methods can be read in Chapter 2.1.1. These as-grown CNT arrays are then transferred onto 0.1 mm thick titanium foil current collectors (MTI Corporation MF-Ti-Foil-700L-105). To obtain good ohmic contacts between CNT arrays and the current collectors, the top surface of the as-grown CNT arrays is coated with 40 nm platinum-palladium alloy with a ratio of 80:20 prior to the transfer process by sputter coating technique. The coating technique itself is similar to the metal coating technique used prior to SEM imaging. The detailed methods for platinum-palladium sputter coating can be read in Chapter 2.3.1. Subsequently, a thin layer of conductive adhesive (Epoxy Technology EPO-TEK E3081) is manually spread by hand on the top surface of each CNT array. Care has to be taken to ensure the uniformity of the epoxy layer. These CNT arrays are then flipped and placed onto the titanium foil current collectors, then placed in a vacuum oven to cure the adhesive layer. Once the adhesive layer is fully cured, the growth substrates are removed from the CNT arrays using razor blades. Other techniques to obtain a good ohmic contact between CNT arrays and the current collectors are described by Kumar et al. (2006) and Fu et al. (2010). It is also possible to grow VACNTs directly on conducting metal substrates, such as nickel, tungsten, and aluminium foil. However, the fabrication process for such direct growth typically involves either the plasma enhanced CVD (PECVD) or low pressure CVD (LPCVD) method, which is impractical for use in this study (Yoon et al., 2004; Signorelli et al., 2009).

In this study, the gravimetric specific double layer capacitance of multiple sets of CNT arrays with various degrees of oxidation are examined. The degree of oxidation of the CNT arrays is increased by exposure to a longer period of UV/ozone or oxygen plasma treatment and decreased by exposure to vacuum annealing treatment. Both dry oxidation and vacuum annealing treatments are performed subsequent to the CNT arrays transfer process. After the transfer process, the entire CNT array-

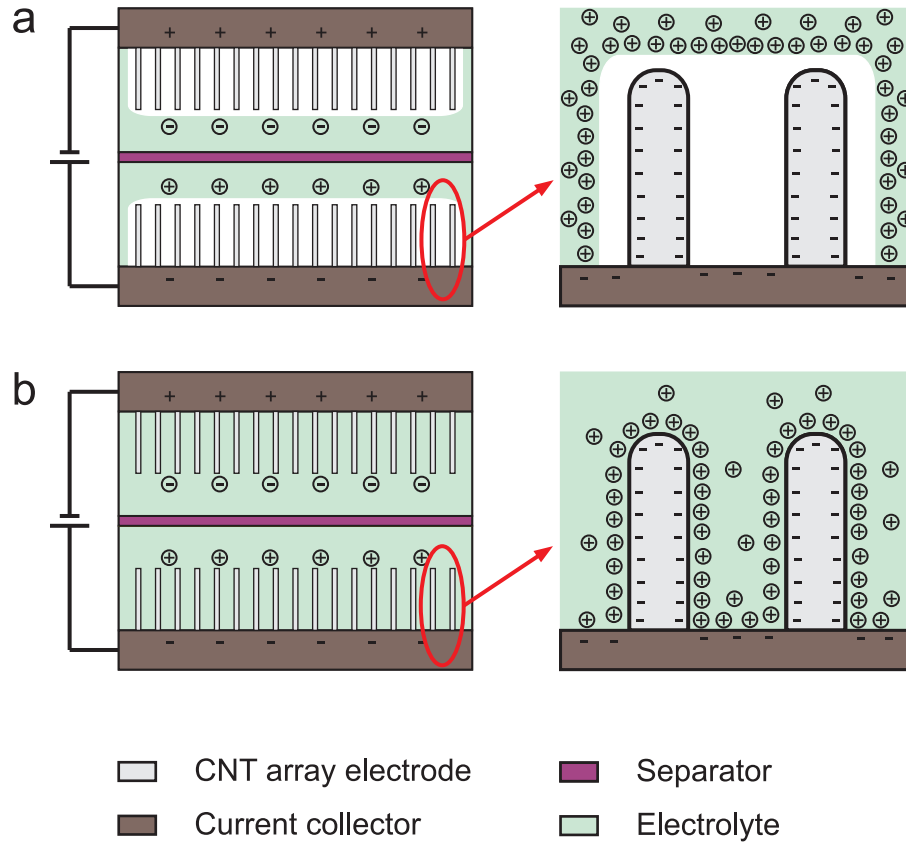


Figure 6.3. Effect of wettability of CNT arrays to the effective surface area of the electrode-electrolyte interface of EDLC when hydrophobic (a) and hydrophilic (b) CNT arrays are used as the electrodes.

titanium current collector assembly is exposed to either dry oxidation or vacuum annealing treatment. The detailed methods for UV/ozone and oxygen plasma treatments can be read in Chapter 2.2.1, and those for vacuum annealing treatment can be read in Chapter 2.2.2. As their degree of oxidation is varied, the wettability of CNT array electrodes is also changed. CNT array electrodes with higher degrees of oxidation are more hydrophilic, while CNT array electrodes with lower degrees of oxidation are more hydrophobic. Hydrophobic CNT arrays are expected to have lower specific capacitance due to their small effective electrolyte-electrode interface area (Figure 6.3). On the other hand, hydrophilic CNT arrays are expected to have higher specific capacitance due to their large effective electrolyte-electrode interface area. Detailed discussions of the relation between degree of oxidation and wettability of CNT arrays can be read in Chapter 3.

Two separate experiments are performed to elucidate the effect of oxidation to the specific capacitance of CNT arrays in both aqueous alkaline and nonaqueous electrolytes. For the aqueous alkaline electrolyte, 6 M potassium hydroxide (KOH) in water is used. For the nonaqueous electrolyte, 1 M tetraethylammonium tetrafluoroborate electrolytes (Et<sub>4</sub>NBF<sub>4</sub>) in propylene carbonate (PC) is used. Prior to the experiment, the entire CNT array electrode-titanium current collector assembly is soaked in the electrolyte for one hour at room temperature. This soaking step is necessary to ensure all available mesopores and macropores on the CNT surface are fully accessed by the electrolyte. This CNT array electrode-titanium current collector assembly is then immediately placed in a split flat test cell (MTI Corporation EQ-STC) and filled with the electrolyte.

According to Equation 6.1, the dielectric constant of the electrolyte is another key component to achieve a high specific capacitance. Since it is assumed that all ions are in the solvated state, the dielectric constant of the electrolyte is dominated by the dielectric constant of the solvent. Typically, protic solvents, such as water, hydrogen cyanide, and formic acid have a very high dielectric constant due to the existence of strongly structured hydrogen bonds. On the other hand, aprotic solvents such as propylene carbonate, acetonitrile and dimethyl formamide typically have a

lower dielectric constant than that of the protic solvents, although it is still higher than that of the unstructured solvents due to the presence of strong dipole-dipole interactions. Water, for instance, has dielectric constant of 80 at 25 °C, while PC has dielectric constant of 64 at the same temperature.

From a capacitance point of view, use of aqueous alkaline usually leads to a higher specific capacitance than in organic electrolytes. However, at high operating potential, discharge of H<sub>2</sub> from the solvent is very likely to happen. Thus, to prevent decomposition due to the electrolysis of water ( $E^0 = 1.23$  V), the operating potential for aqueous electrolytes is limited to 1 V (Simon and Gogotsi, 2008; Miller and Simon, 2008; Stoller et al., 2008). From an energy density and power density perspective, use of nonaqueous solvents is more favored due to the lack of electrochemically active hydrogen atoms, such that a higher operating potential of 2.5-3.5 V is achievable. Among a few available nonaqueous electrolytes that can be reliably used to obtain a high value of specific capacitance, as well as energy density and power density, a mixture of Et<sub>4</sub>NBF<sub>4</sub> in PC is the most common choice. Although Et<sub>4</sub>NBF<sub>4</sub>/PC electrolytes are currently more expensive than their aqueous counterparts, they offer a better stability at a higher operating voltage and at a larger temperature range. Et<sub>4</sub>NBF<sub>4</sub>/PC electrolytes are also considered to be relatively safe due to their low toxicity and volatility nature.

The capacitive behavior of CNT array electrodes with various degrees of oxidation is studied using cyclic voltammetry in a two electrodes configuration. In a two electrodes configuration, CNT arrays serve as both anode and cathode. A separator film is then sandwiched between the anode and cathode to prevent direct electrical contact between them (Figure 6.3.c). However, this separator film has to have enough porosity to allow ions to flow through. In this study, 25  $\mu$ m thick polyethylene films (MTI Corporation EQ-bsf-0025-60) are used as the separator films. The cyclic voltammetry characterization is performed using a potentiostat (Biologic SP-200). Cyclic voltammetry is basically a cyclic measurement of potential-dependent current when the potential is varied linearly across the potential window at a constant scan rate. The potential window for experiments in 6 M KOH electrolyte is limited to 1V,

while for experiments in 1 M Et<sub>4</sub>NBF<sub>4</sub>/PC electrolyte, it is limited to 2.5V to prevent a faradaic reaction with CNT array electrodes and titanium current collectors. The entire cyclic voltammetry characterization is conducted at a scan rate of 100mV/s.

The specific capacitance of CNT array electrodes with various degrees of oxidation is measured using galvanostatic charge-discharge cycles in a two electrodes configuration. The galvanostatic charge-discharge cycles are performed using a potentiostat (Biologic SP-200) at a constant current density, and the response potential is recorded and plotted against time. The specific capacitance measurement is conducted at a constant current density of 5A/g. Note that the current density and specific capacitance are determined and measured based on the mass of CNT array electrodes only. The mass of current collectors, separators, electrolytes, and packaging are not taken into consideration. The cyclic lifetime of CNT based EDLC is also measured using galvanostatic charge-discharge cycles at a constant current density of 5A/g. The performance of CNT based EDLC in terms of their energy density and power density is calculated from the specific capacitance and IR drop obtained by galvanostatic charge-discharge cycles analysis.

## 6.3 Results and Discussion

### 6.3.1 Capacitive behavior of oxidized CNT in KOH

Capacitors, in principle, are free from Faradaic redox reactions. Therefore the plot of current against potential obtained from cyclic voltammetry analysis (called cyclic voltammogram) of ideal capacitors is perfectly rectangular. Unlike ideal capacitors, it is very unlikely for an EDLC to exhibit a pure capacitive behavior that is completely free from Faradaic behavior. However, the Faradaic behavior of a good EDLC is typically minute and not obvious. A bigger problem that always occurs is the presence of a nonzero equivalent series resistance (ESR). ESR can be considered as the total resistance of the EDLC that includes the electrolyte resistance, charge transfer resistance, and contact resistance. The electrolyte resistance depends on the dielec-

tric constant of the electrolyte, while charge transfer resistance is influenced by the compatibility between electrodes and the electrolyte. Contact resistance is the resistance between electrodes and current collectors, and has to be minimized during the fabrication process. Because of the presence of Faradaic processes and the nonzero ESR, the shape of cyclic voltammogram of an EDLC is typically trapezoidal with non-constant current during the linear potential sweep, especially at the beginning and the end of the scan.

The cyclic voltammograms of CNT arrays in 6M KOH in two electrodes configuration show a smooth and symmetrical shape over a potential range of 0-1 V. In general, this behavior can be observed from CNT arrays with low oxygen content. The cyclic voltammograms for CNT arrays with a very low O/C ratio of 3% are featureless (Figure 6.4.a). Such featureless voltammograms indicate the absence of Faradaic reaction during the charge and discharge cycles. A linear increase of response current during the linear potential sweep indicates the nonzero finite ESR of the CNT arrays. Note that the response current recorded from these CNT arrays is extremely low, in the order of  $10^{-5}$  mA. Such low response current can be associated with the extremely low capacitance and tremendously high ESR of these CNT arrays. Since these CNT arrays are actually superhydrophobic, there exists a thin layer of air at the interface between their surface and the electrolyte. Such air layer inhibits electrons transfer from the arrays and blocks charged ions to approach the surface of the CNT arrays from the electrolyte.

Similar behavior is observed for CNT arrays with a slightly higher O/C ratio of 6%. The cyclic voltammograms for these CNT arrays are almost featureless, although a small peak at 0.6 V can be observed (Figure 6.4.b). Compared to those of CNT arrays with an O/C ratio of 3%, these cyclic voltammograms exhibit much higher response currents. A higher response current can be attributed to the presence of higher concentration of oxygenated groups on the surface of these CNT arrays. As discussed in Chapter 3, the presence of polar oxygenated groups on the surface of CNT improves its wettability in highly polar electrolytes. Interestingly, an increase of O/C ratio by 3% is enough to increase the response current four orders of magnitude from

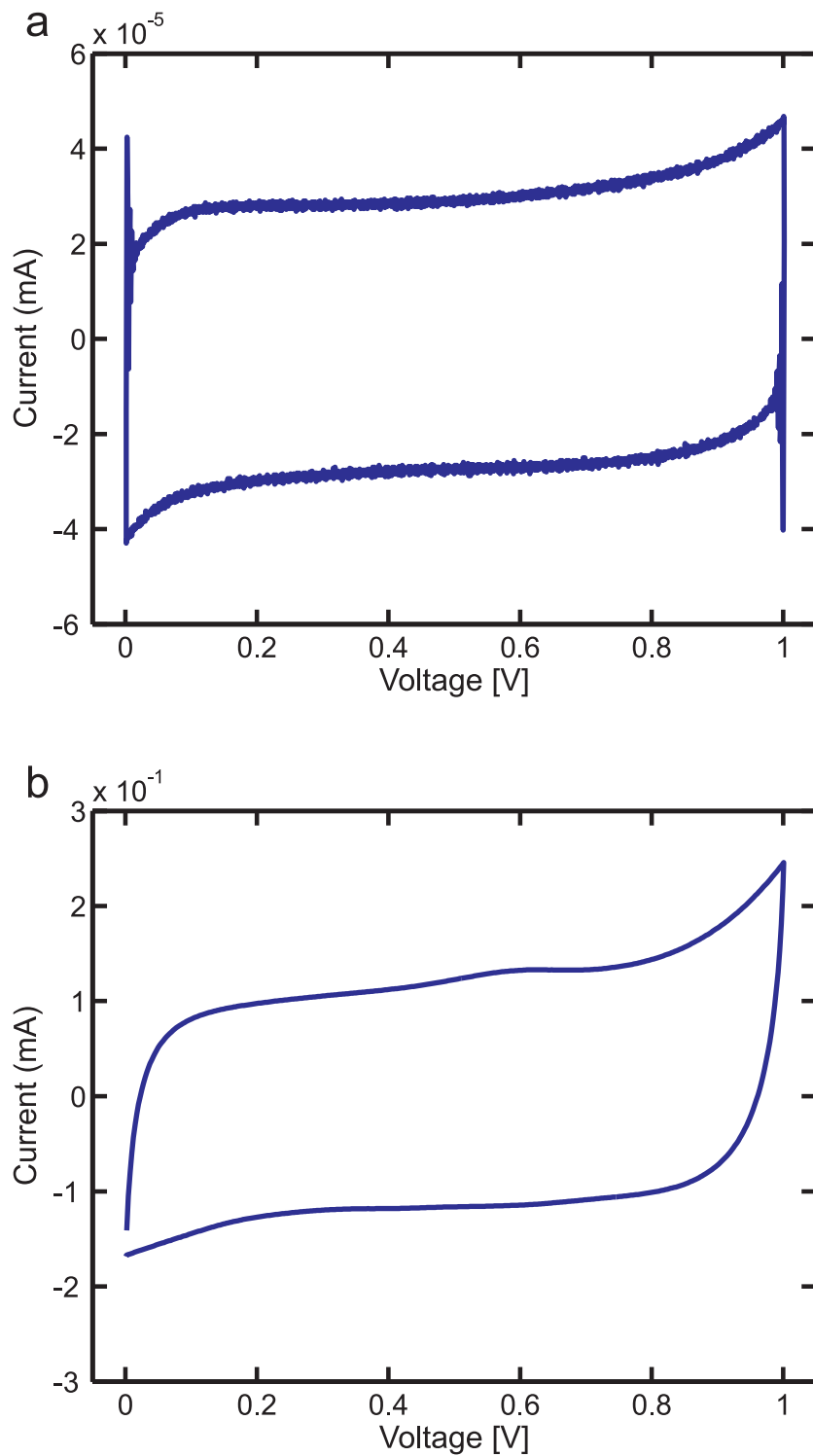


Figure 6.4. Cyclic voltammogram of hydrophobic CNT arrays in 6 M KOH. These CNT arrays have an O/C ratio of 3% (a) and 6% (b).

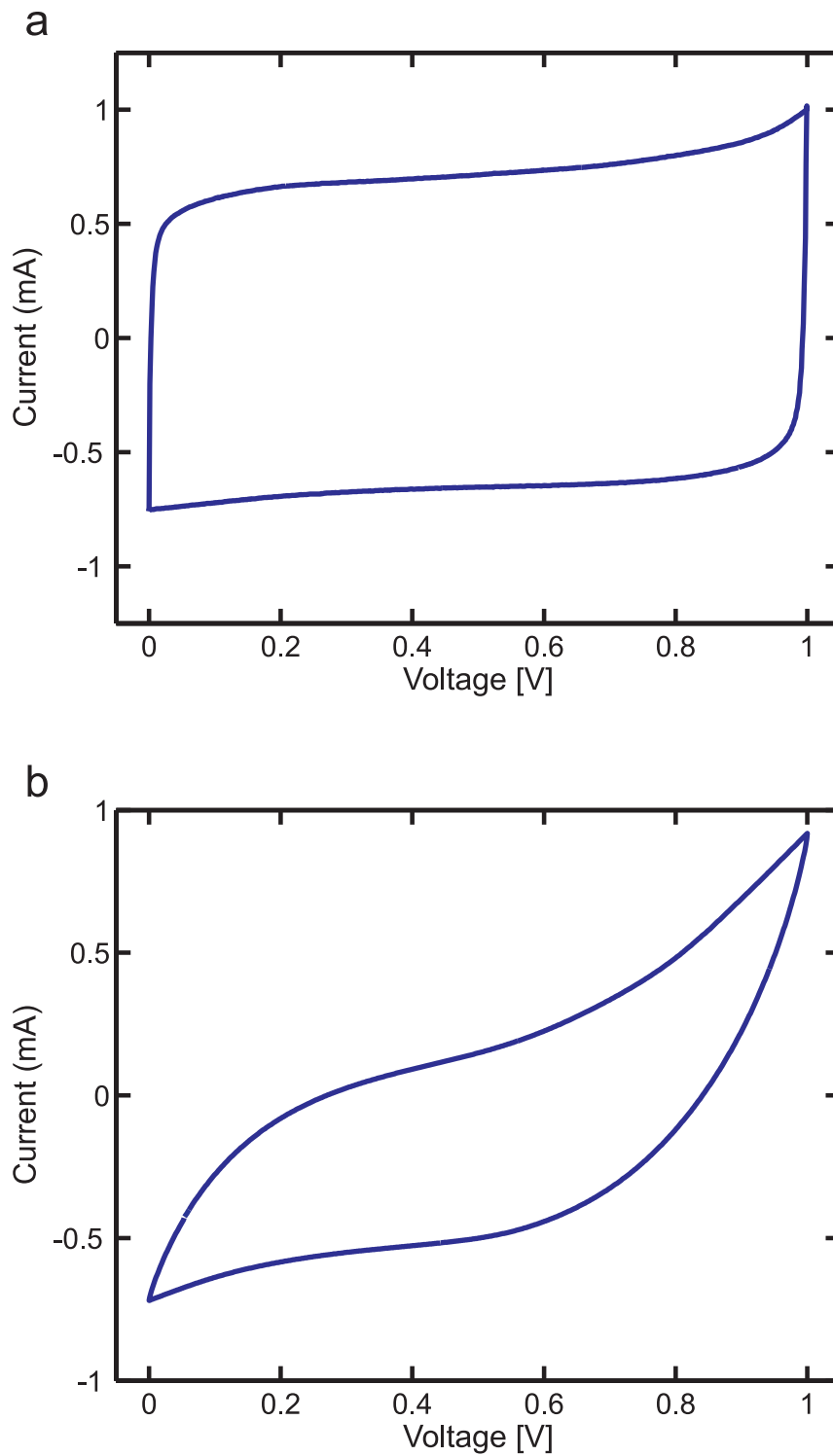


Figure 6.5. Cyclic voltammogram of hydrophilic CNT arrays in KOH. These CNT arrays have an O/C ratio of 12% (a) and 15% (b).

$10^{-5}$  mA to  $10^{-1}$  mA.

Also note that, compared to those of CNT arrays with an O/C ratio of 3%, the cyclic voltammograms of CNT arrays with an O/C ratio of 6% are less symmetric. The response current recorded during charging periods has a steeper slope than that during discharging periods. This suggests that the ESR of these CNT arrays is higher during the charging periods than during the discharging ones. This phenomena is typically caused by the change in electroactive species on the surface of CNT arrays. Such change can also be observed at a potential higher than 0.8 V. A dramatic increase in the response current suggests the occurrence of potential-dependent redox reactions where the relative quantity of electroactive species is dependent on the potential. These electroactive species may be related to the presence of oxygenated groups on the surface of CNT arrays.

The cyclic voltammograms of CNT arrays with a much higher O/C ratio of 13% also exhibit a smooth and almost symmetrical shape over a potential range of 0-1 V. Unlike those of CNT arrays with O/C ratio of 6%, the cyclic voltammograms for these CNT arrays are featureless (Figure 6.5.a). A very sharp transient response when the potential sweep changes signs indicates a rapid charge storage and delivery kinetic of these CNT arrays. A rapid charge storage and delivery kinetic can be attributed to the good wettability of these CNT arrays by the electrolyte. A better wettability also results in the significant increase of the recorded response currents, which are now in the order of 1 mA. Consequently, the capacitance of these CNT arrays is expected to be significantly higher than that of CNT arrays with an O/C ratio of 6%.

A totally different behavior is observed for CNT arrays with an even higher O/C ratio of 21%. The cyclic voltammograms of these CNT arrays are no longer smooth and symmetrical (Figure 6.5.b). In fact, the recorded response current increases almost linearly as the increase of potential with a very steep slope. The large response current hysteresis typically observed between charge and discharge cycles is also diminished. These voltammograms suggest that the double layer capacitance of these CNT arrays is lower than that of CNT arrays with lower O/C ratio. They also imply that the ESR of these CNT arrays is significantly higher than that of

CNT arrays with lower O/C ratio. This behavior may be attributed to the occurrence of potential-dependent redox reactions where the relative quantity of electroactive species is dependent on the potential. As mentioned earlier, these electroactive species may be related to the presence of oxygenated groups on the surface of CNT arrays. Since a higher O/C ratio means a higher concentration of such oxygenated groups, it is expected that the quantity of electroactive species involved during the charging-discharging cycles is also higher.

### **6.3.2 Capacitive behavior of oxidized CNT in Et<sub>4</sub>NBF<sub>4</sub> / PC**

The cyclic voltammograms of CNT arrays with an O/C ratio of 3% in 1M Et<sub>4</sub>NBF<sub>4</sub>/PC in two electrodes configuration show a smooth and symmetrical shape over a potential range of 0-2.5 V. This behavior is similar to that observed from CNT arrays with low oxygen content in 6M KOH. The cyclic voltammograms for these CNT arrays are featureless (Figure 6.6.a). Such featureless voltammograms indicate the absence of Faradaic reaction during the charge and discharge cycles. A slow transient response when the potential sweep changes sign indicates a slow charge storage and delivery kinetic of these highly hydrophobic CNT arrays. Such slow charge storage and delivery kinetic can be attributed to the poor wettability of these CNT arrays by the electrolyte. Although the O/C ratio of both CNT arrays is about the same, the recorded response current in Et<sub>4</sub>NBF<sub>4</sub>/PC electrolyte is much higher than that in KOH electrolyte. The recorded response current in Et<sub>4</sub>NBF<sub>4</sub>/PC electrolyte is about five orders of magnitude higher than that in KOH electrolyte. Such a discrepancy can be attributed to the better compatibility between highly hydrophobic CNT arrays and propylene carbonate. Although propylene carbonate is very polar, with a dipole moment of 4.9 D, the lack of strongly structured hydrogen bonds makes it more compatible with the highly nonpolar CNT arrays. Such compatibility can be seen from the lack of air film at the interface between the bulk surface of CNT arrays and propylene carbonate. Unlike water, propylene carbonate does wet the highly nonpo-

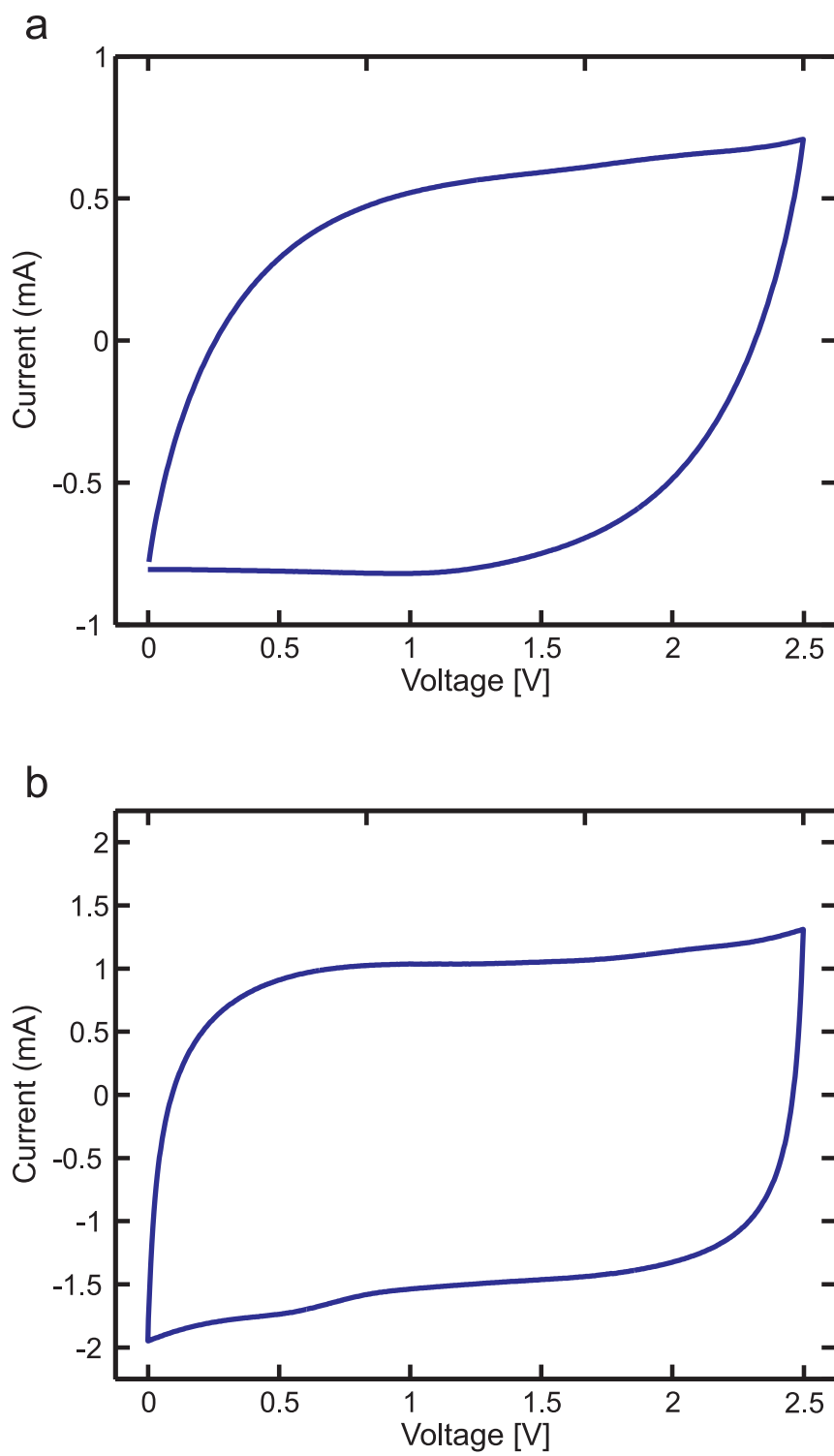


Figure 6.6. Cyclic voltammogram of hydrophobic CNT arrays in Et<sub>4</sub>NBF<sub>4</sub>.

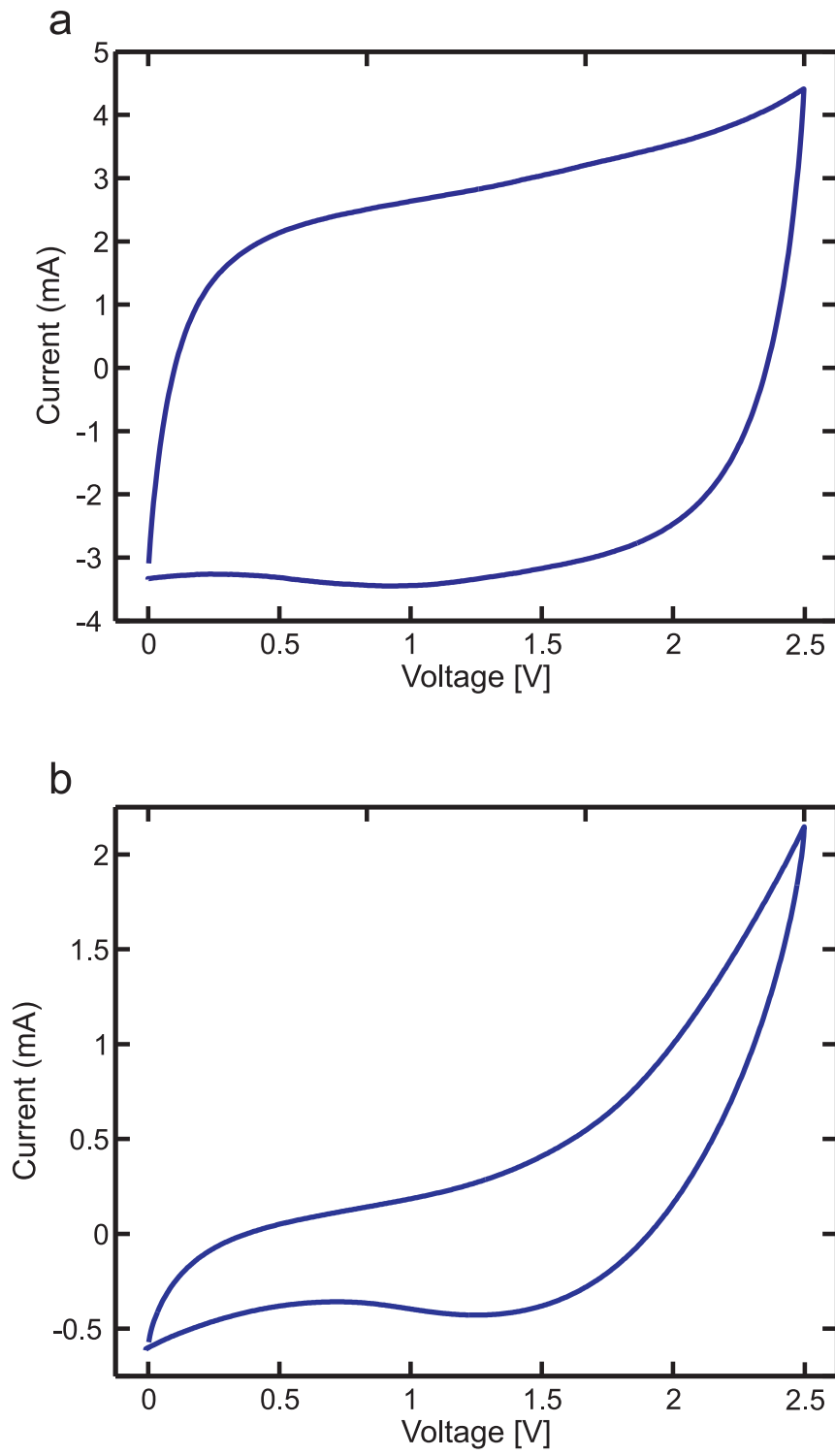


Figure 6.7. Cyclic voltammogram of hydrophilic CNT arrays in Et<sub>4</sub>NBF<sub>4</sub>.

lar CNT arrays, even at room temperature. Although these CNT are not completely wetted by propylene carbonate, the absence of liquid-vapor-solid interface improves the response current by several orders of magnitude.

Similar behavior is observed for CNT arrays with a slightly higher O/C ratio of 6%. The cyclic voltammograms for these CNT arrays are also featureless (Figure 6.6.b). Compared to those of CNT arrays with an O/C ratio of 3%, these cyclic voltammograms exhibit slightly higher response currents. A higher response current can be attributed to the presence of a higher concentration of oxygenated groups on the surface of these CNT arrays. As discussed in Chapter 3, the presence of polar oxygenated groups on the surface of CNT improves its wettability in highly polar electrolytes. A higher response current can also be attributed to the increase of the number of mesopores and macropores of CNT arrays due to the oxidation process. An increase of the number of mesopores and macropores leads to an increase of effective interface surface area between the CNT and the electrolyte. The correlation between oxidation process and the surface area of CNT arrays can be read in Chapter 4. Note that CNT arrays with an O/C ratio of 6% exhibit a sharper transient response when the potential sweep changes sign than the CNT arrays with an O/C ratio of 3%. This sharper transient response indicates a faster charge storage and delivery kinetic, which can be attributed to a better wettability of these CNT arrays by the electrolyte. Also note that, compared to those CNT arrays with an O/C ratio of 3%, the cyclic voltammograms of these CNT arrays are less symmetric. The response current recorded during discharging periods has a steeper slope than that during charging periods. This suggests that the ESR of these CNT arrays is higher during the discharging periods than during the charging ones. This phenomena is typically caused by the discharge of electroactive species from the surface of CNT arrays.

The cyclic voltammograms of CNT arrays with a much higher O/C ratio of 13% also exhibit a smooth and featureless shape over a potential range of 0-2.5 V. Similar to those of CNT arrays with O/C ratio of 6%, the cyclic voltammograms for these CNT arrays are also not perfectly symmetric (Figure 6.7.a). The response current recorded

during charging periods has a steeper slope than that during discharging periods. This suggests that the ESR of these CNT arrays is higher during the charging periods than during the discharging ones. This phenomena is typically caused by significant changes in the quantity of electroactive species on the surface of CNT arrays during the charging period. A very sharp transient response when the potential sweep changes sign indicates a rapid charge storage and delivery kinetic of these CNT arrays. A rapid charge storage and delivery kinetic can be attributed to the good wettability of these CNT arrays by the electrolyte. A better wettability also results in a slight increase of the recorded response currents. An increase of response current with negligible increase of slope implies that the electrochemical characteristic of CNT arrays is dominated by their capacitive behavior (Lufrano and Staiti, 2004; Chen et al., 2002). Consequently, the capacitance of these CNT arrays is expected to be slightly higher than that of CNT arrays with an O/C ratio of 6%.

A totally different behavior is observed for CNT arrays with an even higher O/C ratio of 17%. The cyclic voltammograms of these CNT arrays are no longer smooth and symmetrical (Figure 6.7.b). In fact, the recorded response current increases almost exponentially as the increase of potential with a very steep slope, suggesting the occurrence of potential-dependent redox reactions where the relative quantity of active redox species is dependent on the potential. The large response current hysteresis typically observed between charge and discharge cycles is also diminished. These voltammograms suggest that the double layer capacitance of these CNT arrays is lower than that of CNT arrays with lower O/C ratio. They also imply that the ESR of these CNT arrays is significantly higher than that of CNT arrays with lower O/C ratio. This behavior may be caused by the occurrence of strong potential-dependent redox reactions during charging and discharging cycles. As mentioned earlier, it is very likely that the oxygenated groups adsorbed on the surface of CNT are involved in these Faradaic redox reactions.

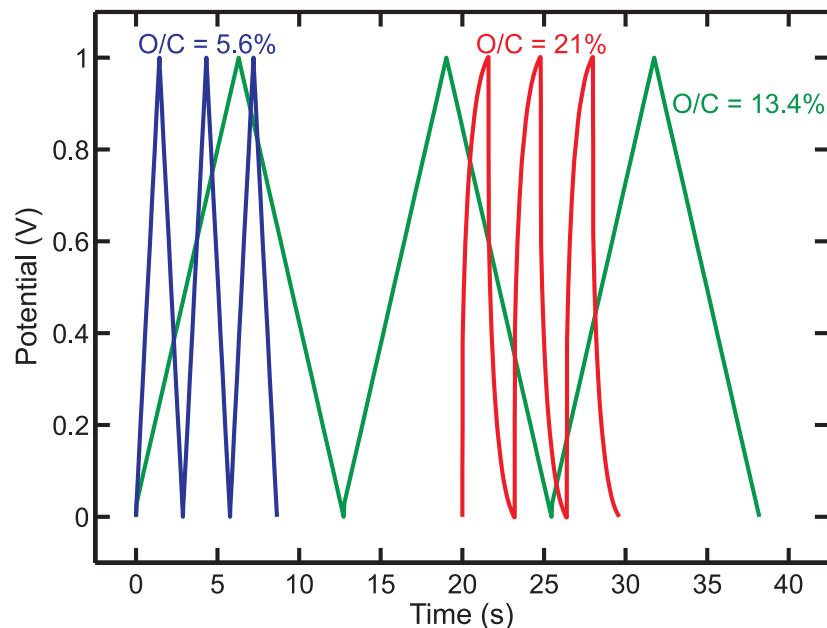


Figure 6.8. Galvanostatic charge discharge cycle of CNT arrays with different oxidation levels in KOH electrolyte.

### 6.3.3 Effect of oxidation on the specific capacitance

Oxidation processes have been known for decades as some of the most credible methods to increase the specific surface area of carbon electrodes. When an oxidation process is performed on carbon electrodes, oxygen atoms attack the defect sites on the surface of the materials, resulting in the removal of impurities and modification of their porous structures. Oxygen is readily physisorbed by carbon structures as molecular oxygen whenever they are exposed to air or any oxygen containing gas. In addition, chemisorptions of oxygen during the oxidation process result in the presence of oxygenated groups on the surface of the materials. AC electrodes are typically made by selective oxidation of carbon rich organic precursors, resulting in a substantial increase of surface area and a better pore size distribution. Further, the presence of oxygenated groups on the surface of AC electrodes have been known to improve their electrochemical characteristics (Simon and Gogotsi, 2008).

Similarly, the oxidation process on CNT arrays should affect their electrochemical characteristics. The effect of oxidation on the specific capacitance of CNT array

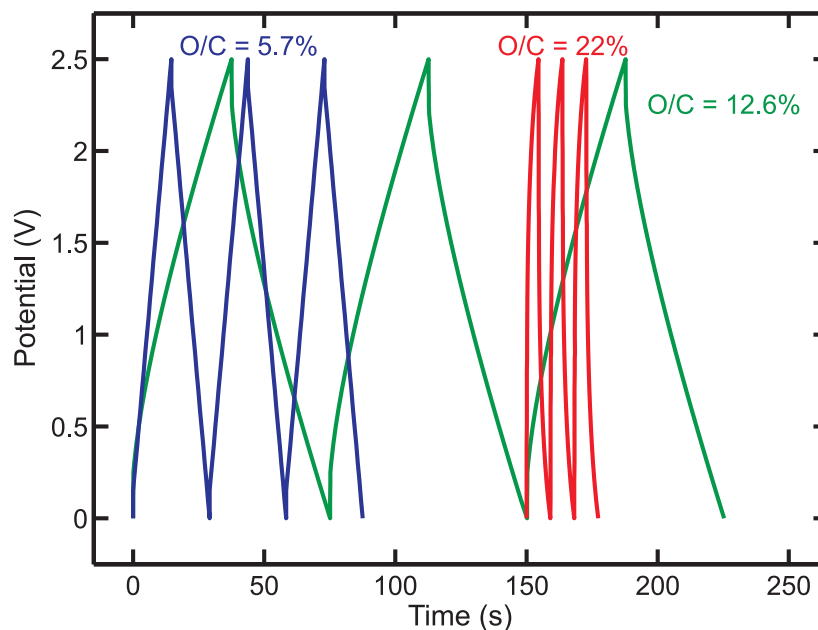


Figure 6.9. Galvanostatic charge discharge cycle of CNT arrays with different oxidation levels in Et<sub>4</sub>NBF<sub>4</sub>/PC electrolyte.

EDLC for both KOH and Et<sub>4</sub>NBF<sub>4</sub>/PC electrolyte can be observed by plotting their specific capacitance against their O/C ratio. As mentioned above, presence of polar oxygenated groups on the surface of CNT arrays should improve their wettability in highly polar electrolytes. On the other hand, presence of such groups has also shown to negatively affect the ESR (Figure 6.5.b and Figure 6.7.b), the self-discharge, and cyclability characteristics, as well as the ion adsorption behavior of the CNT arrays.

Works by Hirsch (2002) and Lee et al. (2010) have shown that the specific capacitance of the CNT arrays can be increased dramatically by the presence of oxygenated groups which increase the number of contact sites with ions of the electrolytes (Lee et al., 2010; Hirsch, 2002; Aria and Gharib, 2011). It has also been known that highly oxidized CNT arrays have higher surface areas and better pore size distributions than the non-oxidized ones. The relation between surface areas and O/C ratio of CNT arrays can be read in Chapter 4. A combination of better wettability and better pore size distributions amplifies the total area of the electric double layer and ultimately enhances the specific capacitance of oxidized CNT arrays.

In this study, the specific capacitance of active electrode materials is measured

using galvanostatic charge/discharge analysis at a constant current density, where the response potential is recorded and plotted against the time. For an ideal capacitor, the shape of potential versus time curve is perfectly triangular, with constant slopes showing a perfect capacitative behavior. Since, in reality, the ESR is always nonzero, the charge/discharge curves of an EDLC are typically curved. An IR drop can be seen obviously from the charge/discharge curves when the ESR is significantly high. It is possible for a CNT array EDLC to have a high ESR. As mentioned earlier, factors that influence ESR of an EDLC include internal resistance of active electrode materials, contact resistance between active electrode materials and current collectors, wettability of active electrode materials by the electrolytes, and conductivity of the electrolyte. Since the internal resistance of CNT arrays is typically very low, such a high ESR may be attributed to a poor wettability by the electrolyte and a poor contact to the current collector.

The shape of potential versus time curves of CNT arrays with low oxidation level in KOH electrolyte is almost perfectly triangular, with constant charging and discharging slopes (Figure 6.8). For CNT arrays with an average O/C ratio of about 5.5%, a full charge and discharge cycle at a current density of 5 A/g can be completed in about three seconds. In addition to their near perfect triangular shape, their galvanostatic curves also exhibit non obvious IR drops, indicating the presence of a non zero but negligible ESR. In fact, their IR drop is measured to be just about tens of millivolts. Similar behavior is also observed from CNT arrays with an average O/C ratio of about 13.5%. Not only are their galvanostatic curves almost perfectly triangular, their IR drop is also measured to be about tens of millivolts. These CNT arrays complete a full charge and discharge cycle at a current density of 5 A/g in about 13 seconds. In contrast, the shape of potential versus time curves of CNT arrays with high oxidation levels in KOH electrolyte is no longer triangular and their charging and discharging slopes are no longer constant. This implies that Faradaic redox reactions are involved during the charging and discharging cycles. For CNT arrays with an average O/C ratio of about 21%, an obvious IR drop can be observed from their galvanostatic curves. In fact, the IR drop of these CNT arrays is measured

to be between 300-400 mV. Undoubtedly, such a large IR drop decreases the performance of these CNT arrays by limiting their effective operating potential to about 60-70% of their original operating potential.

Similar behavior can be observed from CNT arrays in Et<sub>4</sub>NBF<sub>4</sub>/PC electrolyte. The shape of potential versus time curves of CNT arrays with an average O/C ratio of 5.5% is almost perfectly triangular, with constant charging and discharging slopes (Figure 6.9). However the galvanostatic curves of CNT arrays exhibit noticeable IR drops of 100-200 mV, which are about an order of magnitude higher than that in KOH electrolyte. Such high IR drops may be caused to the higher electrolyte resistance of the Et<sub>4</sub>NBF<sub>4</sub>/PC electrolyte. These CNT arrays complete a full charge and discharge cycle at a current density of 5 A/g in about 50 seconds. Surprisingly, the shape of potential versus time curves of CNT arrays with an average O/C ratio of 13% is no longer triangular and their charging and discharging slopes are no longer constant. This implies that Faradaic redox reactions are involved during the charging and discharging cycles even when their oxygen content is still quite low. However, their average IR drop is still considered reasonable. In fact, their average IR drop is measured to be about 250 mV, which is comparable to that of CNT arrays with lower O/C ratio. This IR drop is considered reasonable, although slightly higher than that reported by previous studies (Kumar et al., 2006; Niu et al., 1997; Futaba et al., 2006). Since it takes about 80 seconds for these CNT arrays to complete a full charge and discharge cycle, their capacitance is expected to be higher than that of CNT arrays with lower O/C ratio. Similar non-triangular galvanostatic curves can also be observed from CNT arrays with an average O/C ratio of 22%. Although the shape of potential versus time curves of these CNT arrays are similar to that of CNT arrays with lower O/C ratio, their IR drop is significantly higher. Indeed, the IR drop of these CNT arrays is measured to be between 800-900 mV, which is about 30% of their original operating potential.

Gravimetric specific capacitance can be calculated directly from the galvanostatic

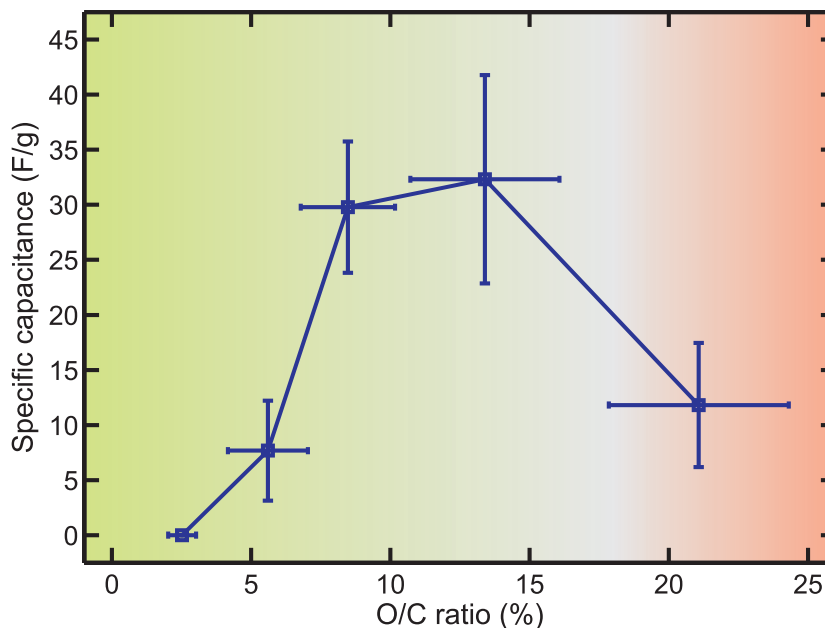


Figure 6.10. Specific capacitance vs oxygen/carbon ratio in KOH.

charge/discharge curves using the following equation:

$$C_G = \frac{I}{(dV/dt)m} \quad (6.2)$$

where the scan rate ( $dV/dt$ ), is measured from the slope of the discharge curves. Electrodes with a steeper slope exhibit a lower specific capacitance, while ones with mild slope exhibit a higher gravimetric capacitance. Since the discharge slope of CNT arrays in KOH electrolyte is much steeper than that in Et4NBF4/PC electrolyte (Figure 6.8 and Figure 6.9), it is expected that the specific capacitance of CNT arrays in KOH electrolyte is lower than that in Et4NBF4/PC electrolyte. Such a difference in discharge slope is apparent even though the potential range for both electrolytes is different. As mentioned earlier, the potential for CNT arrays in KOH electrolyte is swept between 0-1 V, while the potential for CNT arrays in Et4NBF4/PC electrolyte is swept between 0-2.5 V.

In KOH electrolyte, the gravimetric specific capacitance of CNT arrays with an average O/C ratio of 3% is measured to be about 0.003 F/g at a current density of 5 A/g. As expected, the specific capacitance of CNT arrays increases along with the

increase of the O/C ratio of the CNT arrays. In fact, the specific capacitance of CNT arrays increases very quickly at an O/C ratio below 10% (Figure 6.10). Their specific capacitance increases by three orders of magnitude to about 7 F/g, just by doubling the O/C ratio to 6%. As the O/C ratio of the CNT arrays reaches 8.5%, their specific capacitance has improved to almost 30 F/g. However, such a rapid increase of specific capacitance seems to hit a ceiling and start to plateau at an O/C ratio of about 10%. At an O/C ratio of 14%, their specific capacitance reaches its maximum at about 32 F/g.

Interestingly, the specific capacitance of CNT arrays in KOH drops significantly as the O/C ratio goes higher than 15%. At an O/C ratio of about 21%, their specific capacitance is measured to be about 12 F/g. Such a drastic decrease in specific capacitance is very counter intuitive since the wettability of CNT arrays by aqueous solvent with an O/C ratio of 21% is as good as that of CNT arrays with an O/C ratio of 14% (Figure 6.10), as described in Chapter 3.3.3. Further, surface area measurement using BET and Langmuir analysis also indicates an increase of surface area with the increase of O/C ratio. In fact, the surface area of CNT arrays with an O/C ratio of 21% is about 50% higher than that of CNT arrays with an O/C ratio of 15%. Details on the relation between O/C ratio and BET and Langmuir surface area measurement can be read in Chapter 4.3.4.

In Et<sub>4</sub>NBF<sub>4</sub>/PC electrolyte, the gravimetric specific capacitance of CNT arrays with an average O/C ratio of 3% is measured to be about 29 F/g at a current density of 5 A/g. This specific capacitance is significantly higher than that measured in KOH using CNT arrays with the same O/C ratio. Similar to the behavior observed in KOH electrolyte, the specific capacitance of CNT arrays in Et<sub>4</sub>NBF<sub>4</sub>/PC electrolyte increases with the increase of the O/C ratio of the CNT arrays, although the increase rate seems to be linear (Figure 6.10). Their specific capacitance increases to about 48 F/g when the O/C ratio is doubled to 6%. As the O/C ratio of the CNT arrays reaches 8.5%, their specific capacitance improves to almost 62 F/g. And when the O/C ratio of the CNT arrays reaches 12.5%, their specific capacitance reaches its maximum at 83 F/g.

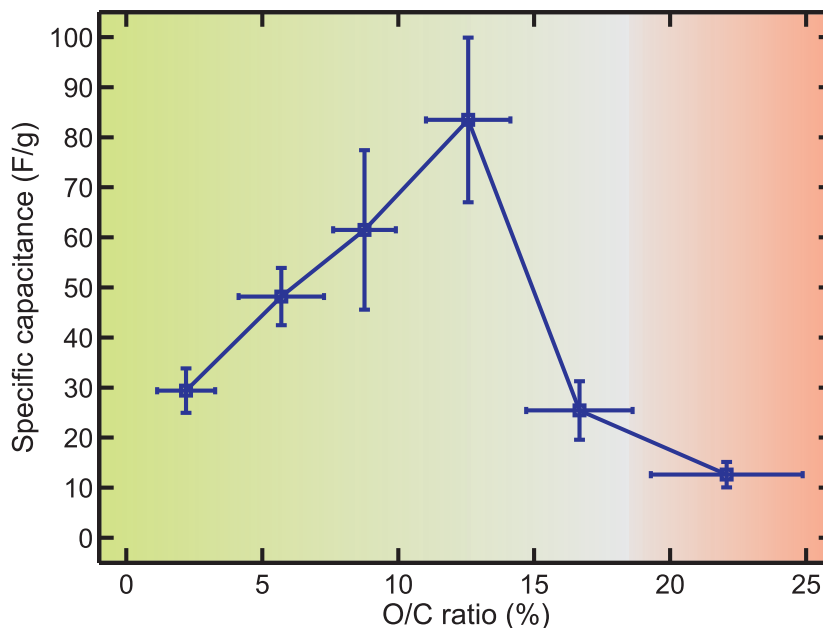
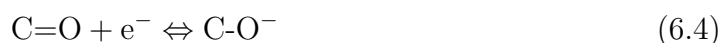


Figure 6.11. Specific capacitance vs oxygen/carbon ratio in Et<sub>4</sub>NBF<sub>4</sub>.

Similar to the behavior observed in KOH electrolyte, the specific capacitance of CNT arrays in Et<sub>4</sub>NBF<sub>4</sub>/PC drops significantly as the O/C ratio goes higher than 15%. At an O/C ratio of about 17%, their specific capacitance is measured to be as low as 25 F/g. Such a decrease in specific capacitance continues at an even higher O/C ratio, such that when the O/C ratio of the CNT arrays reaches 22% their specific capacitance reaches an even lower value of 12 F/g. This finding is indeed surprising since these values are much lower than that of lowly oxidized CNT arrays. Interestingly, this sudden drop in specific capacitance occurs near the threshold of reversible-irreversible oxidation. Detailed discussion on this threshold can be read in Chapter 3 and Chapter 4.

For CNT arrays with a very low O/C ratio, their capacitive behavior is dominated by the non-Faradaic electric double layer behavior. However, a nonzero O/C ratio of these CNT arrays also means that Faradaic redox reactions are also involved during the charging and discharging cycles, although their contribution is limited. As the O/C ratio of the CNT arrays increases due to a prolonged oxidation process, the contribution of Faradaic redox reactions relative to the non-Faradaic electric double

layer to the overall capacitance also increases. Oxygenated groups, whether acidic, basic, neutral, or amphoteric oxides, may act as pseudocapacitive materials attached to the surface of CNT. Oxygenated groups, such as hydroxyl (C-OH) and carbonyl (C=O), are known to be electroactive and may involve in redox reactions of oxygen as follows (Lee et al., 2010; Hsieh and Teng, 2002; Pan et al., 2010; Lee et al., 2012):



CNT arrays with an excessive surface concentration of oxygenated groups due to overoxidation are most likely to exhibit high rates of self-discharge (Pandolfo and Hollenkamp, 2006). During the charging process, dissociation of -OH groups may occur, leading to the formation of -H or -O free radicals. These free radicals may generate molecular H<sub>2</sub>, O<sub>2</sub>, or H<sub>2</sub>O<sub>2</sub>, which are typically involved in self-discharge processes. Moreover, these oxygenated groups are also known to be active catalysts for electrochemical decomposition of electrolytes (Hsieh and Teng, 2002; Pandolfo and Hollenkamp, 2006), resulting in a high leakage current and a high charge transfer resistance. Furthermore, overoxidized CNT arrays are expected to have a lower electrical conductivity than the pristine ones, due to the disappearance of their  $\pi$ -bond network. Detailed discussion about  $\pi$ -bond network of oxidized CNT arrays can be read in Chapter 4.3.1. A combination of low electrical conductivity of overoxidized CNT arrays and a high charge transfer resistance of the electrode-electrolyte interface results in a dramatic increase of ESR. The effect of a high ESR on the capacitive behavior of CNT arrays can be seen obviously from their skewed cyclic voltammogram, where their resistive behavior becomes more dominant than their capacitive behavior (Figure 6.5.b and Figure 6.7.b). All the above mentioned factors contribute to a significant deterioration in capacitance for overoxidized CNT arrays, which is proven by a decrease of specific capacitance of CNT array EDLC by about 20 F/g and 70F/g as the O/C ratio increases by about 10% in KOH and Et<sub>4</sub>NBF<sub>4</sub>/PC electrolytes respectively.

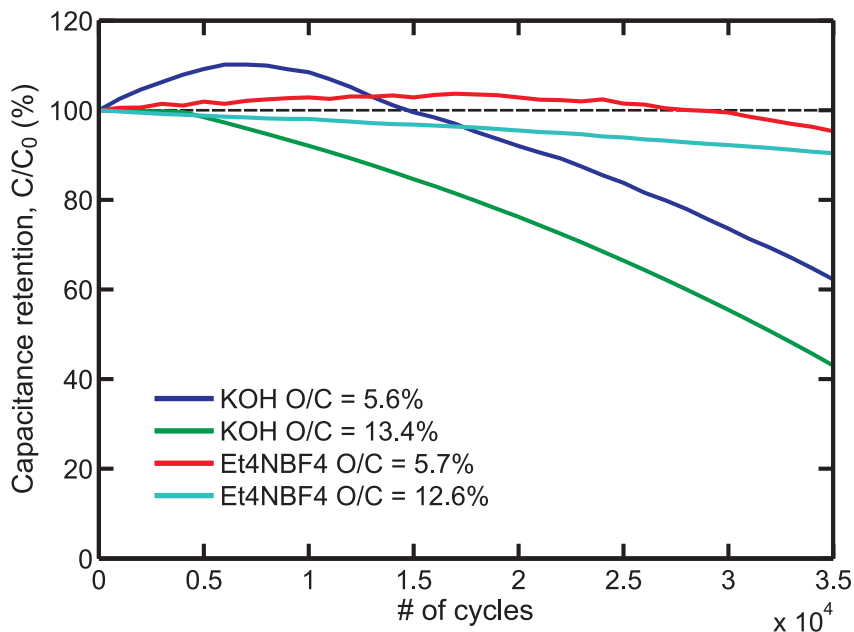


Figure 6.12. Capacitance retention vs number of cycles of CNT arrays with different O/C ratios in both KOH and Et<sub>4</sub>NBF<sub>4</sub>/PC electrolytes.

### 6.3.4 Lifetime and performance

As mentioned earlier, capacitors, including EDLC, in principle have an excellent stability to be used for millions of cycles at a very high charge/discharge rate. Such capability arises from the absence of Faradaic redox reactions that eliminates the electrode-electrolyte interphase changes. Although, in reality, limited Faradaic redox reactions are involved, CNT array EDLC with a very low O/C ratio of less than 5.5% are able to withstand more than 35,000 charge/discharge cycles in Et<sub>4</sub>NBF<sub>4</sub>/PC electrolyte while only losing about 5% of their original capacitance. This cycle lifetime is measured at a current density of 5 A/g (Figure 6.12). Note that there exists a transient condition where the capacitance of these CNT arrays increases for the first tens of thousands of charge/discharge cycles. The capacitance of these CNT arrays starts to decrease once their maximum capacitance is reached, which takes place after they are being cycled for about 15,000 - 20,000 charge/discharge cycles.

A slightly lower capacitance retention capability is exhibited by the optimally oxidized CNT array EDLC with an average O/C ratio of about 12.5%. These CNT arrays

are able to withstand more than 35,000 charge/discharge cycles in Et4NBF4/PC at a current density of 5 A/g, while only losing 10% of their original capacitance (Figure 6.12). Considering the value of their initial capacitance, a decrease of capacitance by 10% after being cycled for more than 35,000 charge/discharge cycles is definitely acceptable. Unlike the CNT arrays with a very low O/C ratio, these CNT arrays do not exhibit a transient condition. Therefore, their initial capacitance is indeed their maximum capacitance. This transient condition is typical for non-wettable electrode materials with a complex porous network and a large number of micropores. Several thousands of charge/discharge cycles are needed for the electrolyte to completely wet the entire surface of the CNT arrays with a very low O/C ratio.

The capacitance retention capability of CNT array EDLC in KOH electrolyte is, in general, worse than that in Et4NBF4/PC electrolyte. Regardless of their O/C ratio, these CNT arrays are not capable of withstanding more than 30,000 charge/discharge cycles without losing more than 20% of their original capacitance (Figure 6.12). In fact, CNT array EDLC with an average O/C ratio of about 5.5% can only withstand 17,000 charge/discharge cycles before losing 20% of their original capacitance. Even worse, CNT array EDLC with an average O/C ratio of about 13.5% can only withstand 18,000 charge/discharge cycles before losing 20% of their original capacitance. Such fast degradation in capacitance is actually expected from these CNT arrays, since the -OH groups from the KOH electrolyte may get chemisorbed by the cathode during the charging periods and may not be completely desorbed during the discharging period. This irreversible chemisorption process increases the concentration of oxygenated groups of the CNT arrays, similar to an oxidation process, such that their O/C ratio increases as they undergo prolonged charge/discharge cycles.

This phenomenon can be actually observed from the increase of specific capacitance of CNT arrays with a very low O/C ratio as the number of cycles increases. Unlike the transient condition observed from the same CNT arrays in Et4NBF4/PC electrolyte, such an increase of specific capacitance is faster. The specific capacitance of CNT arrays with an O/C ratio of about 5.5% in KOH electrolyte reaches its maximum value after being cycled for less than 10,000 charge/discharge cycles. Their

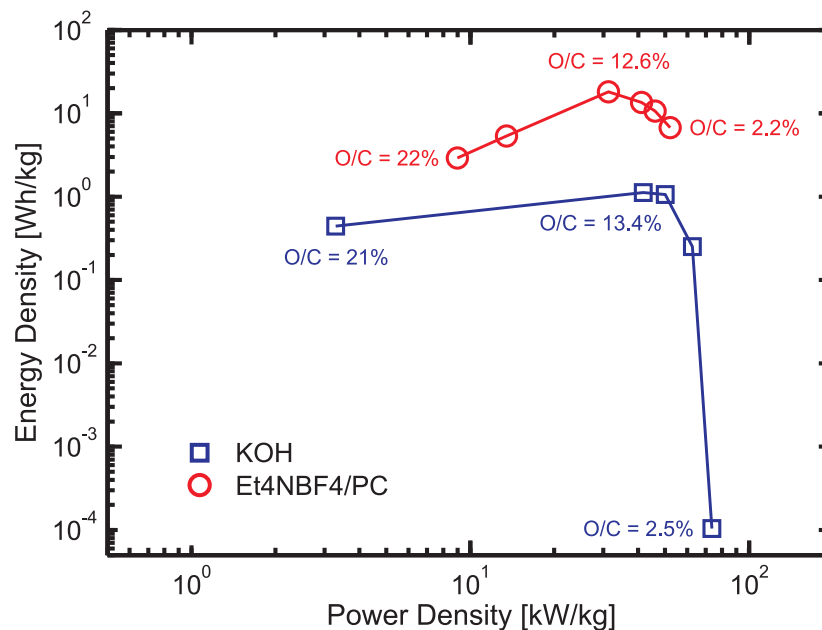


Figure 6.13. Effect of oxidation on the energy density and power density of CNT arrays in KOH and Et4NBF4/PC electrolytes.

specific capacitance quickly decays a few thousands of cycles later in a similar rate as that of optimally oxidized CNT arrays in KOH electrolyte. For the optimally oxidized CNT arrays in KOH electrolyte, their specific capacitance is relatively constant for about 5,000 cycles, after which a decrease in specific capacitance is observed. This finding shows that the oxygenated groups involved in Faradaic redox reactions may negatively affect the cycle lifetime of CNT array EDLC. Although these CNT array EDLC have a poor cyclability, their cycle lifetime is still much longer than that of typical batteries.

The performance of CNT array EDLC can be represented by their gravimetric energy density ( $E_G$ ) and power density ( $P_G$ ). The gravimetric energy density ( $E_G$ ) stored by EDLC depends on the its specific capacitance and is given by the following relation:

$$E_G = \frac{1}{2} C_G \left( \frac{V}{2} \right)^2 \quad (6.5)$$

where  $V$  is the operating potential of EDLC. The gravimetric power density ( $P_G$ ) of EDLC is independent of its specific capacitance. However, it depends on the ESR

and is given by the following relation:

$$P_G = \frac{1}{mR} \left( \frac{V}{2} \right)^2 \quad (6.6)$$

where R is the equivalent series resistance (ESR) measured from the IR drop of EDLC. Therefore, a threefold increase in operating potential achieved using nonaqueous electrolytes will result in an order of magnitude increase in stored energy for the same capacitance value.

Using Equation 6.5 and Equation 6.6, the specific capacitance and ESR of CNT array EDLC can be translated into gravimetric energy density and power density. As the O/C ratio of the CNT arrays increases, their gravimetric energy density increases due to an increase of the specific capacitance. However, at the same time, their gravimetric power density decreases due to an increase of ESR. In Et<sub>4</sub>NBF<sub>4</sub>/PC electrolyte, the energy density is tripled from about 6 Wh/kg to about 18 Wh/kg as the O/C ratio of CNT arrays increases from 2.2% to 12.6%. At the same time, the power density of these CNT arrays decreases from about 52 kW/kg to about 31 kW/kg (figure 6.13). A similar behavior, but in a much more dramatic fashion, is observed when the energy density and power density are measured in KOH electrolyte. The energy density increases by four orders of magnitude from about 0.1 mWh/kg to about 1 Wh/kg as the O/C ratio of CNT arrays increases from 2.5% to 13.4%. Surprisingly, the power density of these CNT arrays is only halved, from about 73 kW/kg to about 41 kW/kg. Note that energy density and power density are measured at a current density of 5 A/g and only the mass of CNT arrays is taken into account.

For the overoxidized CNT arrays, their gravimetric energy density decreases with the increase of their O/C ratio due to a drastic decrease of their specific capacitance. Similarly, their gravimetric power density decreases due to an excessive increase of their ESR. In Et<sub>4</sub>NBF<sub>4</sub>/PC electrolyte, the energy density decreases by an order of magnitude to about 3 Wh/kg as the O/C ratio of CNT arrays increases to 22%. At the same time, the power density of these CNT arrays decreases to about 9 kW/kg (Figure 6.13). A much more dramatic decrease in gravimetric power density is ob-

served when it is measured in KOH electrolyte. Their power density decreases by an order of magnitude to about 3 kW/kg when the O/C ratio of these CNT arrays increases to 21%. For the same decrease of O/C ratio, their energy density is halved to about 0.4 Wh/kg. These results imply that the maximum performance of CNT array EDLC is reached when they are optimally oxidized, and overoxidation always result in a big decrease of performance.

The findings presented above show that CNT array EDLCs offer many advantages compared to other electrical energy storage systems (Figure 6.14). The optimally oxidized CNT array EDLCs in Et<sub>4</sub>NBF<sub>4</sub>/PC have a gravimetric energy density comparable to lead acid batteries and a gravimetric power density comparable to electrolytic capacitors. Clearly, both their gravimetric energy density and power density are higher than those of previously reported electrochemical capacitors (Fernandez et al., 2008; Simon and Burke, 2008; Yoon et al., 2004; Niu et al., 1997; Pandolfo and Hollenkamp, 2006; Du et al., 2005; Shah et al., 2009). However, to better compare this performance to the currently available electrical energy storage systems, the mass of the entire components, including electrolyte, current collectors, separator, and packaging, has to be taken into account in the calculation of gravimetric energy density and power density. Since in this study the electrolyte, current collectors, separator, and packaging are not optimized, their mass cannot be used in the calculation. Using the currently available fabrication techniques commonly used in mass production of battery and EDLC, the overall mass of the complete system, including electrolyte, current collectors, separator, and packaging, is about 10-12 times the mass of the active electrode materials (Fernandez et al., 2008; Simon and Burke, 2008). After dividing by 12, the optimally oxidized CNT array EDLCs in Et<sub>4</sub>NBF<sub>4</sub>/PC electrolyte have a typical gravimetric energy density of 0.1 Wh/kg at a gravimetric power density of 3 kW/kg.

The performance of CNT array EDLC may be further improved by incorporating pseudocapacitive materials onto the CNT. Pseudocapacitive materials, including metal oxides and conducting polymers, have been extensively studied in the past to increase the gravimetric specific capacitance of AC. Ruthenium oxides (RuO<sub>2</sub>),

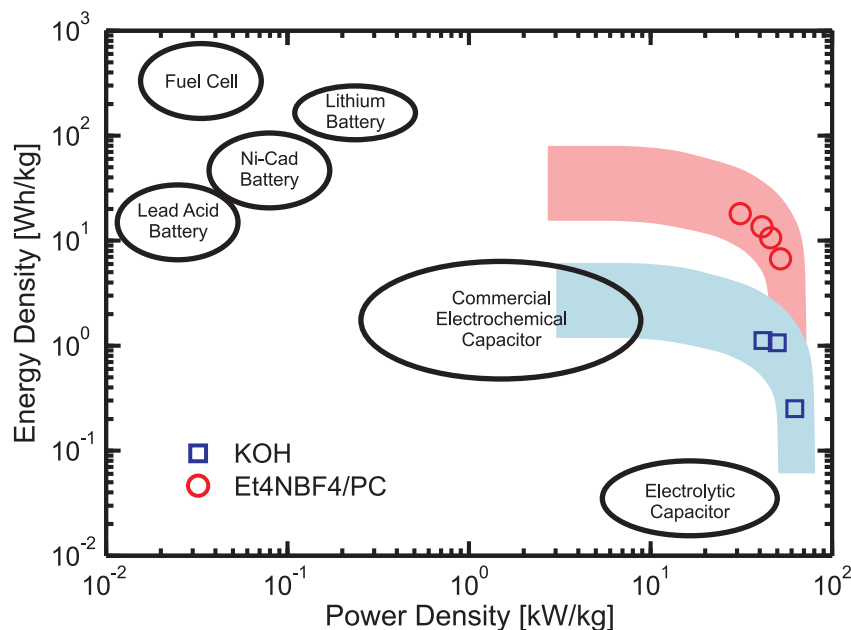


Figure 6.14. Ragone plot of oxidized CNT arrays in KOH and Et<sub>4</sub>NBF<sub>4</sub>/PC electrolytes compared to other electrical energy storage systems.

cobalt oxides (Co<sub>3</sub>O<sub>4</sub>), and manganese oxides (MnO<sub>2</sub>), and titanium dioxide (TiO<sub>2</sub>) are the most common metal oxides to be used along with CNT due to their unique oxidation states that are accessible at relatively low potential and simplicity in fabrication process (Simon and Gogotsi, 2008; Pan et al., 2010). Conducting polymers such as polyaniline (PANI), polypyrrole (PPy), and polythiophene (PT) have been used in many electrochemical applications because of their compatibility with CNT and inherent high specific capacitance (Simon and Gogotsi, 2008; Pan et al., 2010). However, because of the presence of Faradaic redox reactions, both metal oxides and conductive polymers cannot be cycled fast enough and often suffer from lack of stability (Nam et al., 2008; Mi et al., 2007).

Improvement to the performance of CNT array EDLC may also be achieved by incorporating other microporous carbons onto the CNT and using ionic liquid electrolytes. Ionic liquid electrolytes, such as 1-ethyl-3-methylimidazolium bis-(trifluoromethylsulfonyl)-imide (EMIM-Tf<sub>2</sub>N), are non-volatile room-temperature solvent-free electrolytes with large electrochemical window (Lu et al., 2011). A further improvement to the performance of CNT array EDLCs may be achieved by optimizing their physical properties,

especially their packing density. These compacted CNT arrays have a packing density ten times higher than that of common as-grown VACNTs (Futaba et al., 2006).

## 6.4 Concluding Remarks

In conclusion, the findings reported herein show that the electrochemical properties of CNT arrays are influenced by their oxygen adsorbates concentration. By varying the O/C ratio of the CNT arrays, their capacitive behavior can be controlled. The specific capacitance of these CNT arrays increases with the increase of their O/C ratio in both KOH and Et<sub>4</sub>NBF<sub>4</sub>/PC electrolytes. An increase of O/C ratio by about 10% improves their specific capacitance by about 30 F/g and 60 F/g in KOH and Et<sub>4</sub>NBF<sub>4</sub>/PC electrolytes, respectively. This behavior is observed as long as their O/C ratio is kept below 15%. CNT arrays with an O/C ratio higher than 15% exhibit high resistive behavior and low capacitive behavior. These behaviors can be observed from the decrease of specific capacitance of CNT arrays by about 20 F/g and 70F/g as the O/C ratio increases by about 10% in KOH and Et<sub>4</sub>NBF<sub>4</sub>/PC electrolytes, respectively.

Although the gravimetric energy density of CNT arrays EDLCs is relatively higher than that of commercially available EDLC, it is still much lower compared to that of batteries, especially lithium-ion batteries (Lee et al., 2012; Byon et al., 2012). Therefore, it is unlikely for EDLC to substitute batteries as main electrical energy storage devices. However, since EDLC in general have a much better cycle-life and gravimetric power density, they can complement the operation of batteries in hybrid systems (Miller and Simon, 2008). In such systems, an EDLC acts as a buffer to uptake and deliver high power on demand that certainly cannot be handled by batteries. Thus, the battery's energy can be delivered at the capacitor's rate (Conway, 1999).

These EDLC-battery hybrid systems are useful in many modern applications, particularly for small mobile or wireless devices such as mobile phones, wireless sensors, portable computers, and wearable drug delivery systems. These modern devices do not require a lot of energy to be delivered continuously, but instead very short

high-power, low-energy bursts. Using batteries for repeated delivery of high-power bursts will quickly degrade the cycle-life of the batteries. Furthermore, most users do not want to wait for hours to fully charge these devices. Hence, hybridization with EDLC will improve the charging rate of batteries, as well as their cycle-life. EDLC-battery hybrid systems can also be utilized in green transportation and renewable energy applications. Using these systems, as opposed to purely battery-based energy storage systems, the charging/discharging time of mid-sized electric cars may be cut down from several hours to less than an hour. In addition, faster acceleration, higher top speed, and better regenerative braking can all be accommodated by these hybrid systems. EDLC-battery hybrid systems will also allow an efficient production of renewable energy from sun, wind, or ocean tides and currents, by stabilizing the generated power before being stored.

At the moment, the biggest limiting factor in producing CNT array EDLC is their extremely high price. However, CNT arrays are expected to be much cheaper in the near future due to a significant increase in supplies. In addition, since no corrosive liquids need to be used as the electrolytes, cheap lightweight materials such as aluminum, polypropylene, and polyimide can be used for current collectors, separators, and cases, respectively. The small ecological footprint of CNT array EDLC and their lack of toxic materials should be also highlighted. Finally, CNT array EDLC are relatively safe since they do not have reactivity issues associated with lithium, such as thermal runaway.

# Chapter 7

## Summary and Future Works

### 7.1 Summary

As mentioned in Chapter 1.2, the overarching goal of this thesis is to prove the hypothesis that the wettability of CNT arrays can be precisely tuned by controlling the amount of oxygenated groups adsorbed on their surfaces. The secondary goal of this study is to use the CNT arrays in two applications that demonstrate two opposite extremes of wettability of CNT arrays. The findings presented herein show that the goal of this thesis has been achieved. The question whether or not the wettability of CNT arrays can be precisely tuned by controlling the amount of oxygenated groups adsorbed on their surfaces has been answered in Chapter 3. Several specific objectives that have been formulated as guidance to achieve this primary goal have been achieved in Chapter 3 and Chapter 4. Two applications demonstrating the opposite extremes of wettability of CNT arrays are presented in Chapter 6 and Chapter 7. The complete summary of this thesis is described in detail below.

The findings reported herein show that the wetting properties of CNT arrays can be tuned easily and precisely using a combination of UV/ozone and vacuum annealing treatments or oxygen plasma and vacuum annealing treatments. By varying the exposure time of these treatments, the surface concentration of oxygenated functional groups adsorbed on the CNT arrays can be controlled. CNT arrays with very low amounts of oxygenated groups exhibit a superhydrophobic behavior. In addition to their extremely high static contact angle, they cannot be dispersed in DI water, and

their impedance in aqueous electrolytes is extremely high. These arrays have an extreme water repellency capability such that a water droplet will bounce off of their surface upon impact and a thin film of air is formed on their surface as they are immersed in a deep pool of water. In contrast, CNT arrays with a very high surface concentration of oxygenated functional groups exhibit an extreme hydrophilic behavior. In addition to their extremely low static contact angle, they can be dispersed easily in DI water, and their impedance in aqueous electrolytes is tremendously low. Since the bulk structure of the CNT arrays are preserved during the UV/ozone, oxygen plasma, and vacuum annealing treatments, all CNT arrays can be switched repeatedly between superhydrophilic and superhydrophobic, as long as their O/C ratio is kept below 18%.

The effect of oxidation using UV/ozone and oxygen plasma treatments is highly reversible as long as the O/C ratio of the CNT arrays is kept below 18%. At O/C ratios higher than 18%, the effect of oxidation is no longer reversible. This irreversible oxidation is caused by irreversible changes to the CNT atomic structure during the oxidation process. During the oxidation process, CNT arrays undergo three different processes. For CNT arrays with O/C ratios lower than 40%, the oxidation process results in the functionalization of CNT outer walls by oxygenated groups. Although this functionalization process introduces defects, vacancies, and micropores opening, the graphitic structure of the CNT is still largely intact. In this regime, most of the chemisorbed oxygenated groups are in the form of epoxide, hydroxide, or cyclic ether groups. As discussed in Chapter 3, a low concentration of these oxygenated groups can be removed by vacuum annealing treatment, such that the effect of oxidation is reversible for O/C ratios lower than 18%. For O/C ratios between 18% and 40%, the concentration of these oxygenated groups becomes extremely high, such that they form stable pair structures that cannot be easily removed by vacuum annealing treatment.

For CNT arrays with O/C ratios between 40% and 45%, the oxidation process results in the etching of CNT outer walls. This etching process introduces large scale defects and holes that can be seen obviously under TEM at high magnification. Most

of these holes are found to be several layers deep, and in some cases a large portion of the CNT side walls are cut open. Such large scale holes make the inner cavity of CNT accessible from outside. Access to both inner and outer walls of CNT results in a dramatic increase of surface area such that the surface area of the etched CNT is about twice as large as the heavily functionalized, but not etched, CNT. In this O/C ratio range, the densification process of CNT arrays also starts to occur.

For CNT arrays with O/C ratios higher than 45%, the oxidation process results in the exfoliation of the CNT walls and amorphization of the remaining CNT structure. This amorphization process can be implied from the disappearance of the C-C sp<sup>2</sup> peak in the XPS spectra associated with the  $\pi$ -bond network. Such a process results in the disintegration of graphitic structure of the CNT side walls, which can obviously be seen under TEM at high magnification. SADP of the amorphous CNT walls shows an extremely weak line associated with  $\langle 11\bar{2}0 \rangle$  plane and the lack of lines associated with  $\langle 0002 \rangle$  and  $\langle 0004 \rangle$  planes. In this O/C ratio range, densification process of CNT arrays continues to occur, although the etching process takes place at a much higher rate than the densification process. Further increase of O/C ratios will most likely result in the complete decomposition of the CNT walls.

In this thesis, the superhydrophobic CNT arrays have been used for the first time to characterize the water droplet impact behavior on a Cassie state nanostructured superhydrophobic surface. In addition to its extraordinarily high static contact angle, as well as extremely low contact angle hysteresis and roll-off angle, the bulk surface of the superhydrophobic CNT arrays exhibits a continuous cushion of trapped air at the interface between water and the surface. This air film is indeed a signature of an ideal Cassie state superhydrophobic surface.

Three different impact regimes have been experimentally identified, while another impact regime is proposed. These regimes are partitioned by three critical Weber numbers, two of which have been experimentally observed. The first impact regime, which was found at  $We < We_1$ , is when the impacting droplet recedes right after it reaches its maximum spreading diameter, and subsequently rebounds off of the surface completely. The second impact regime, which was found at  $We_1 \leq We < We_2$ , is

when the rebounding droplet creates a Worthington jet and forms several smaller secondary droplets. The third impact regime, which was found at  $We_2 \leq We < We_3$ , is when the impacting droplet breaks into many smaller secondary droplets once it reaches its maximum spreading diameter, and subsequently the primary droplet rebounds off of the surface. The fourth impact regime, which is proposed to be found at  $We \geq We_3$ , is when the impacting droplet breaks into a myriad of smaller droplets and the primary droplet can no longer be distinguished from the secondary ones. The first and second critical Weber numbers are found at  $We_1 \sim 10^1$  and  $We_2 \sim 10^2$ , respectively, and the third critical Weber number is hypothesized to be found at  $We_3 \sim 10^3$ . Further studies to confirm this hypothesis and to understand the underlying mechanism of droplet segmentation still need to be done.

The volume ratio between the primary and the secondary droplets,  $\xi$ , is found to decrease with the increase of Weber number in all impact regimes other than the first one. In the first impact regime,  $\xi$  is found to be always unity since the droplet remains intact during and subsequent to the impingement. In the second impact regime,  $\xi$  starts to decrease as the rebounded droplet begins to split due to the formation of a Worthington jet. In the third impact regime,  $\xi$  continues to decrease as the droplet breaks into many smaller secondary droplets upon impact. The volume ratio in the second and third impact regimes can be approximated by a scaling of  $\xi \sim We^{-1/8}$  and  $\xi \sim We^{-1}$ , respectively. A more rigorous study needs to be conducted to correlate the number of secondary droplets formed by the splashing phenomenon to the Weber number and to quantify the volume of each secondary droplet.

The loss of energy due to droplet deformation upon impact is quantified as the coefficient of restitution,  $\varepsilon$ . In the first and second impact regimes, the coefficient of restitution can be approximated by a scaling of  $\varepsilon \sim We^{-1/4}$ . In the third impact regime, the coefficient of restitution can be approximated by a scaling of  $\varepsilon \sim We^{-1/2}$ . Interestingly, the scaling law suggested by Biance et al. (2006) only agrees to the current experimental data in the third impact regime. This suggests that there are some non-negligible factors responsible for additional loss of energy that have been taken into account in any future studies on the impact behavior of a Leidenfrost drop.

Further studies to develop a logical mathematical model based on these experimental data has to be done in the future.

The droplet spreading behavior on a surface upon impact is quantified as the maximum spreading factor,  $\beta$ . In the first and second impact regimes, the maximum spreading factor can be approximated by a scaling of  $\beta \sim We^{1/5}$ . In the third impact regime, the maximum spreading factor can be approximated by a scaling of  $\beta \sim We^{1/2}$ . This scaling of  $\beta \sim We^{1/2}$  is, in fact, the generalized scaling law derived from a simple energy conservation approach and has been originally proposed by Chandra and Avedisian (1991) and Bennett and Poulikakos (1993). Unsurprisingly, the scaling laws of  $\beta \sim We^{1/4}$  and  $\beta \sim Re^{1/5}$ , as suggested by Clanet et al. (2004), Bartolo et al. (2005), and Biance et al. (2006), do not agree with the obtained experimental data. Therefore, such scaling laws may not be relevant in predicting the droplet spreading behavior on a non-wetted surface in a low viscosity regime.

In this thesis, dry oxidation methods are used for the first time to characterize the influence of oxidation on the capacitive behavior of CNT array EDLCs. The capacitive behavior of CNT array EDLCs can be tailored by varying their oxygen content, represented by their O/C ratio. The specific capacitance of these CNT arrays increases with the increase of their O/C ratio in both KOH and Et4NBF4/PC electrolytes. An increase of O/C ratios by about 10% improves their specific capacitance by about 30 F/g and 60 F/g in KOH and Et4NBF4/PC electrolytes, respectively. This behavior is observed as long as their O/C ratio is kept below 15%. CNT arrays with an O/C ratio higher than 15% exhibit high resistive behavior and low capacitive behavior. These behaviors can be observed from the decrease of specific capacitance of CNT arrays by about 20 F/g and 70F/g as the O/C ratio increases by about 10% in KOH and Et4NBF4/PC electrolytes, respectively. Using Et4NBF4/PC electrolyte, the energy density of optimally oxidized CNT array EDLCs is measured to be about 18 Wh/kg and their power density is measured to about 31 kW/kg. These optimally oxidized CNT arrays are able to withstand more than 35,000 charge/discharge cycles in Et4NBF4/PC at a current density of 5 A/g, while only losing 10% of their original capacitance. Considering the value of their initial capacitance, a decrease of

capacitance by 10% after being cycled for more than 35,000 charge/discharge cycles is definitely acceptable.

## 7.2 Future Works

Although this thesis has answered all questions stated in Chapter 1.2, it also raises many followup questions. Questions regarding the maximum number of oxidation and reduction cycles that CNT arrays can withstand and whether or not this apparent reversible oxidation process introduces defects and holes at the molecular levels are yet to be answered. The detailed oxygen adsorption and desorption mechanisms induced by UV/ozone, oxygen plasma, and vacuum annealing treatments need to be studied further by time dependent in situ characterizations. In addition, the effect of dry chemical modifications in general on other physical properties of CNT, including their mechanical, electrical, thermal, and optical properties, still has to be investigated.

For the superhydrophobic CNT arrays, their performance and durability still need to be characterized fully. Here, the performance of superhydrophobic CNT arrays is judged by the maximum hydrostatic pressure and temperature they can handle before their liquid-vapor-solid interfaces disappear. Their durability is assessed by measuring how long they can maintain their superhydrophobic capability while being completely submerged in water. New research areas and applications that take advantage of these superhydrophobic capability have to be explored. For instance, the use of superhydrophobic CNT arrays as self cleaning surfaces in waste water systems, drag reducing surface on marine vessels, and anti-icing surfaces on heat exchangers should be explored in the future.

Similarly, for the superhydrophilic CNT arrays, their other physical properties, including mechanical, thermal, and electrical properties, still need to be fully characterized. New research areas and applications that take advantage of these superhydrophilic capability have to be explored. For instance, the use of superhydrophilic CNT arrays as electrodes for capacitive deionizer and thermal interface materials for

heat exchangers and thermal distillers should be explored in the future.

# Appendix A

## Effect of Reversible Oxidation on the Energy Gap and Structure of CVD Graphene

### A.1 Introduction

Graphene, a lattice of honeycomb-arranged carbon atoms tightly joined by  $sp^2$  bonds, draws a lot of research interests due to its exceptional properties (Castro Neto et al., 2009; Geim and Novoselov, 2007; Novoselov et al., 2004, 2005, 2006; Zhang et al., 2005; Lee et al., 2008; Frank et al., 2007; Scarpa et al., 2009). Compared to other conductive and semiconductive material, graphene has a superior carrier mobility and lowest resistivity, making it a promising candidate for applications in nanoelectronics (Castro Neto et al., 2009; Geim and Novoselov, 2007; Novoselov et al., 2004, 2005, 2006; Zhang et al., 2005). Nevertheless, the semimetal nature of graphene makes it difficult to control its conductivity by means of a gate electrode (Oostinga et al., 2007). A number of approaches, including the use of electric field (Oostinga et al., 2007), uniaxial strain (Ni et al., 2008; Pereira et al., 2009), as well as nanometer-wide ribbon (Han et al., 2007; Nakada et al., 1996; Ponomarenko et al., 2008), were reported to be successful to open a band gap in graphene. Another possible approach to introduce a band gap opening in graphene is to break its lattice symmetry by introducing foreign atoms and organic dopant molecules (Bostwick et al., 2009; Balog et al., 2010; Sessi et al., 2009; Gierz et al., 2008; Wehling et al., 2008; Luo et al., 2009;

Leconte et al., 2010; Nourbakhsh et al., 2010; Kim et al., 2009; Alzina et al., 2010; Gokus et al., 2009; Childres et al., 2011; Dong et al., 2009; Lu et al., 2008).

Among many known methods to introduce chemical functionalization, the oxidation process has its own virtue for further investigations. The oxidation process of carbon-based structures has been well-studied, and its implementation in large-scale fabrication of microelectronic devices has been well streamlined and engineered. The use of UV/ozone or oxygen plasma treatment to induce oxygen absorption in graphene offers several advantages over well-known wet chemical oxidation methods: both UV/ozone and oxygen plasma treatments do not utilize harsh chemicals, allowing them to be used safely and conveniently. For instance, the well-known Hummer's method (Hummers and Offeman, 1958) and its modified versions (Park and Ruoff, 2009; Li et al., 2008; Sun et al., 2008; Becerril et al., 2008; Marcano et al., 2010) use strong acids and oxidizing agents, and take a significantly long period of time to complete. In addition, the dry oxidation methods allow site-specific oxidation through the use of sacrificial layer masking, making them compatible with current microfabrication processes.

Although many previous studies have reported the successful application of both UV/ozone and oxygen plasma treatments in controlling the electronic properties of graphene, they are so far limited to micromechanical exfoliated graphene on a SiO<sub>2</sub> substrate (Nourbakhsh et al., 2010; Kim et al., 2009; Gokus et al., 2009; Childres et al., 2011; Liu et al., 2013; Zhang et al., 2012). Surprisingly, the use of these treatments on graphene grown epitaxially or by chemical vapor deposition (CVD) method has not been explored. Epitaxial graphene and CVD graphene offer several advantages over exfoliated graphene. The platform area and quality of both epitaxial graphene and CVD graphene are typically several times larger and better than those of exfoliated graphene (Li et al., 2009). Additionally, the shape of epitaxial graphene and CVD graphene can be prepatterned using standard lithography techniques. Furthermore, CVD graphene is known to be transferable onto a flexible substrate with negligible structural damage (Kim et al., 2009; Lee et al., 2011).

Unlike exfoliated graphene on a SiO<sub>2</sub> substrate, epitaxial graphene and CVD

graphene have a strong interaction with their substrates that often complicates the process to tailor the graphene electronic properties. Such strong interaction leads to the formation of replica bands near the Fermi level and renders the graphene metallic (Pletikosi et al., 2009; Murata et al., 2010). Despite this strong graphene-substrate interaction, it is not impossible to introduce an energy gap opening to epitaxial graphene and CVD graphene. In the past, exposure to hot atomic oxygen and hydrogen has been successfully utilized to alter the electronic properties of epitaxial graphene on Ir, Pt, and Ru substrates (Larciprete et al., 2012; Sutter et al., 2010; Vinogradov et al., 2011; Starodub et al., 2010). However, the use of hot atomic oxygen and hydrogen exposure is not very practical since it has to be performed at an elevated temperature under an ultra-high-vacuum condition. A more recent study shows that hydrogen plasma treatment can also be employed to open the energy gap of CVD graphene on nickel by producing  $sp^3$  carbon hybridization (Castellanos-Gomez et al., 2012).

Here we demonstrate for the first time that an energy gap opening of CVD graphene on nickel can also be induced by UV/ozone and oxygen plasma treatments. This finding confirms that both UV/ozone and oxygen plasma treatments have the same capability as hydrogen plasma treatments in converting carbon hybridization of CVD graphene on nickel from  $sp^2$  to  $sp^3$  (Gunes et al., 2011). Similar to the previously reported findings on micromechanical exfoliated graphene on a  $SiO_2$  substrate, the degree of energy gap opening of CVD graphene on nickel is found to be dependent to the oxidation level, where a higher concentration of oxygen adsorbates leads to a larger opening of energy gap. In this work, we also demonstrate for the first time that such opening can be partially recovered by removing the oxygen adsorbates via vacuum annealing treatment. Although such treatment does not completely restore the original electronic properties of CVD graphene, it induces considerable oxygen desorption such that another round of oxidation using UV/ozone and oxygen plasma treatments can be applied to yield a similar energy gap opening. The finding presented herein is important because of the relevance of graphene-metal contact in microelectronic devices.

## A.2 Materials and Methods

All graphene samples used in this study were grown by chemical vapor deposition (CVD) on nickel coated SiO<sub>2</sub>/Si substrates (Graphene Laboratories Inc.) with an average patch size of 3-10  $\mu\text{m}$ . Prior to the experiment, all as-received graphene samples were vacuum annealed in a nitrogen-filled vacuum oven (VWR Signature Vacuum Oven) at a pressure and temperature of 2 torr and 250°C, respectively, for 24 hours to remove any moisture and molecular oxygen adsorbed during storage and handling. Here, these samples are referred as the pristine CVD (CVD-P) graphene. The presence of few-layers graphene after the initial vacuum annealing treatment was confirmed by Raman spectroscopy (Renishaw M1000) obtained with excitation energy of 2.41 eV. These CVD-P samples were then assigned to two different sample sets. One set was subjected to UV/ozone treatment (UVO) and the other set to oxygen plasma treatment (O2P). UVO treatment was performed using a commercial UV/ozone cleaner (Bioforce Nanosciences) at room temperature and pressure for five minutes, while O2P treatment was performed using a commercial remote plasma cleaner (Tepla M4L) under 20 Watts of RF power at a constant oxygen flow rate of 20 SCCM and a chamber pressure of 500 mTorr for five seconds. Here, these samples are referred to as UVO1 graphene and O2P1 graphene, respectively. Vacuum annealing treatment (VA), using the above mentioned parameters, was then applied to these samples, which are denoted as UVO1-VA graphene and O2P1-VA graphene, respectively. Both UVO and O2P treatments, as well as VA treatment were then repeated. Here, these samples are denoted as UVO2 graphene, O2P2 graphene, UVO2-VA graphene, and O2P2-VA graphene, respectively. Subsequently, each sample set was stored in a separate air tight container until microscopy and spectroscopy characterizations were performed.

Atomic-resolution images of graphene were obtained using a scanning tunneling microscope (Digital Instrument Nanoscope IIIa ECSTM) placed directly on the building bedrock foundation to minimize mechanical vibration. These images were acquired in constant height mode using Pt/Ir scanning tips (Veeco, Inc) which has

a typical diameter of 0.25 mm. During the imaging process, a graphene sample was placed on a flat sample stage and clamped from the top with a metal electrode that creates a direct contact with the graphene film. Tunneling I-V and differential conductance characteristics were obtained using the tunneling spectroscopy capability of the same scanning tunneling microscope. Both forward and backward voltage sweeps were performed to minimize the thermal drift during the imaging and measurement. Multiple tunneling I-V spectra were collected from different regions of each graphene sample. Differential conductance characteristic,  $dI/dV$ , was then calculated numerically by taking the first derivative of the tunneling current with respect to the bias voltage. These characteristics were then presented in a two dimensional histogram to show the most probable shape of differential conductance of the sample. A 1D histogram was then extracted from this two dimensional histogram at zero differential conductance,  $dI/dV = 0$ . The energy gap was calculated from the full width at half maximum (FWHM) of this one dimensional histogram. All scanning tunneling microscopy/spectroscopy (STM/STS) imaging and measurements were conducted at room pressure and temperature at a scan rate of 20.3 Hz and a stabilization voltage and current of 100 mV and 65 pA, respectively.

Surface chemistry characterizations were assessed using x-ray photoelectron spectroscopy (Surface Science M-Probe XPS). A monochromatic 1486.6eV Al  $K\alpha$  was used as the x-ray source and was directed at an angle of  $35^\circ$  to the sample surface. The emitted photoelectrons were collected by a hemispherical analyzer positioned at an angle of  $35^\circ$  to the sample surface. The oxygen to carbon atomic ratio (O/C ratio) was calculated from low resolution survey spectra acquired at a binding energy of 1-1000eV with a resolution of 1eV and a spot size of 800  $\mu\text{m}$ . Higher resolution detailed scans were collected on C 1s, O 1s, and Ni 2p regions with a resolution of 0.065eV and a spot size of 100  $\mu\text{m}$ . The C 1s, O 1s, and Ni 2p spectra were acquired at a binding energy of 280-294eV, 526-540eV, and 845-870eV, respectively. Multiple low resolution survey spectra and high resolution C 1s, O 1s, and Ni 2p spectra were collected from different regions of each graphene sample. During the data collection, the sample chamber was maintained at an ultra high vacuum condition with a base

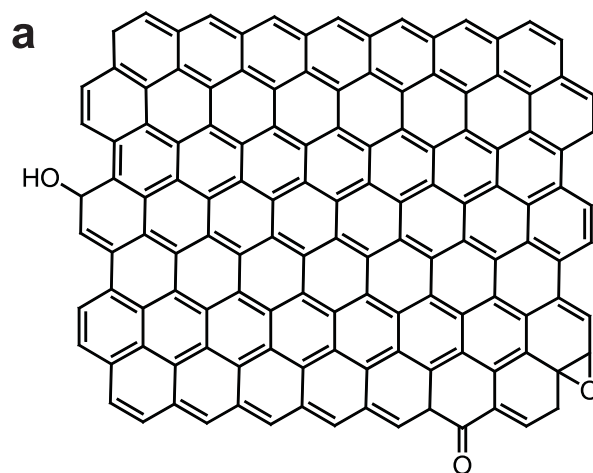
pressure below  $5 \times 10^{-9}$  torr. All photoelectron spectra were obtained using ESCA25 Capture software (Service Physics, V5.01.04) and analyzed using CasaXPS software (Casa Software Ltd, V2.3.15). Deconvolution of the C 1s, O 1s, and Ni 2p high resolution spectra were performed using a Gaussian-Lorentzian peak shape fitting with Shirley baseline correction.

## A.3 Results and Discussion

### A.3.1 Changes in atomic scale morphology probed by scanning tunneling microscopy

The atomically-resolved image of CVD-P graphene samples obtained by scanning tunneling spectroscopy (STM) exhibits a highly-symmetric hexagonal lattice structure with an atomic spacing of about 0.23 nm. Such structure is a typical signature of a pristine graphene layer (Figure A.1) (Liu et al., 2013). The highly-symmetric lattice structure exhibited by CVD-P graphene indicates that it is highly crystalline and has an excellent quality. A faint Moire pattern seen on this image is a common feature of suspended graphene on a nickel surface, and is caused by a mismatch between graphene and nickel lattices (Murata et al., 2010). A similar pattern has also been observed on other metal surfaces (Pletikosi et al., 2009; Vinogradov et al., 2011). No significant variation of Moire pattern across the sample surface suggests that the probed regions have a uniform graphene layer thickness (Castellanos-Gomez et al., 2012).

Similar hexagonal lattice structure can also be seen in the STM image of oxidized graphene, suggesting that its graphitic structure is still practically intact even after being exposed to oxygen plasma treatment for five seconds or to UV/ozone treatment for five minutes. Although a mild distortion to the graphene structure is noticeable, no extended etching front can be observed. This suggests that an intercalation-driven etching process may not be present (Vinogradov et al., 2011; Starodub et al., 2010). Randomly distributed bright spots can be observed in the STM image of the basal



$$E_{\text{gap}} = 0 \text{ eV}$$

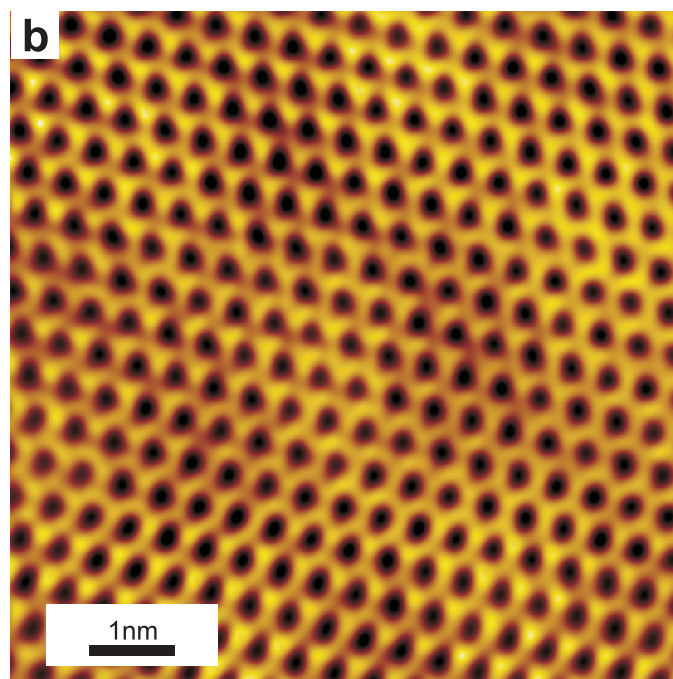
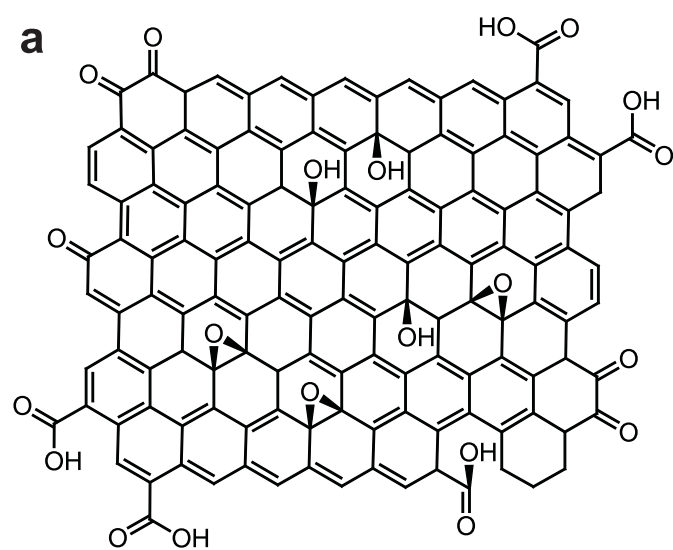


Figure A.1. Schematic (a) and STM image (b) of CVD-P graphene.

plane of UVO1 and O2P1 graphene (Figure A.2). Such bright spots may be attributed to the presence of oxygen adsorbates in the form of epoxide group (Vinogradov et al., 2011; Hossain et al., 2012).

It has been previously reported that the adsorbed oxygen atoms prefer to form epoxide groups on the graphene basal plane due to their stability at room temperature and pressure (Leconte et al., 2010; Vinogradov et al., 2011; Samarakoon and Wang, 2011). Since these bright spots can be found across the sample surface, it suggests that the coverage of oxygen adsorbates introduced by oxygen plasma and UV/ozone treatments is spatially, uniform without any preferential location on the graphene lattice (Hossain et al., 2012). Interestingly, both UVO1 and O2P1 graphene do not exhibit any Moire pattern. The disappearance of the Moire pattern has been previously observed on oxidized graphene on Ir substrate, and is mainly caused by structural transformation in graphene. This transformation is expected because of the change in length of C-C bonds due to the geometrical conversion from the trigonal planar  $sp^2$  carbon hybridization to the tetragonal  $sp^3$  carbon hybridization (Vinogradov et al., 2011; Samarakoon and Wang, 2011; Suggs et al., 2011; Muniz and Maroudas, 2010).

Although epoxide groups are known to be very stable at room temperature and pressure (Leconte et al., 2010; Vinogradov et al., 2011), they can, in principle, be removed at an elevated temperature due to their relatively low binding energy. Thermal reduction treatment, i.e., vacuum annealing, has been demonstrated to be an effective means to remove majority of the chemisorbed oxygen from the graphene basal plane (Vinogradov et al., 2011; Hossain et al., 2012). A highly-symmetric hexagonal lattice structure, similar to that of CVD-P graphene, can be seen in the STM image of the vacuum annealed graphene. Bright spots, which may be attributed to the presence of oxygen adsorbates, can no longer be observed on the basal plane of UVO1-VA and O2P1-VA graphene (Figure A.3). Interestingly, a faint Moire pattern can be observed again on UVO1-VA and O2P1-VA graphene, although it is not as pronounced as that on CVD-P graphene. Such partial recovery of Moire pattern suggests that the distortion to the graphene structure due to the formation of  $sp^3$  bonds has been practically



$$E_{\text{gap}} = 0.11 - 0.15 \text{ eV}$$

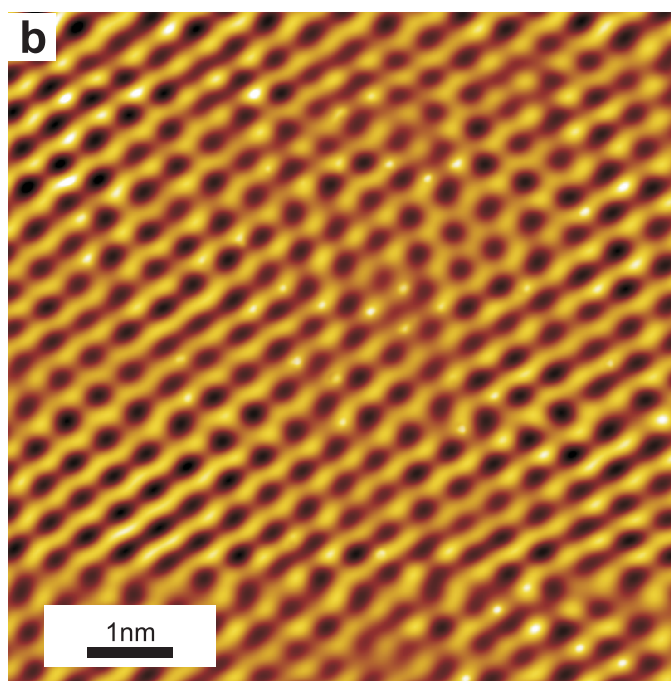


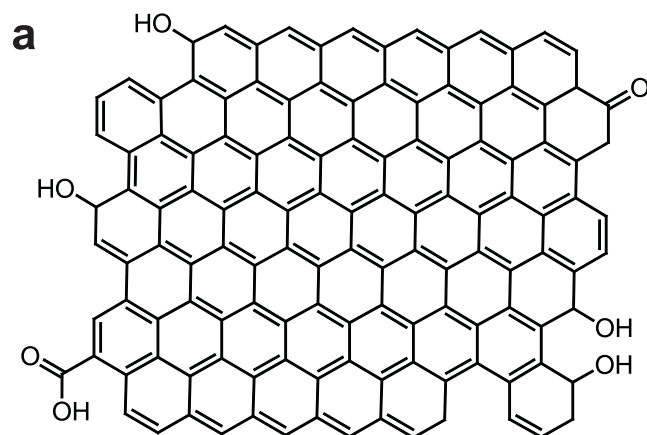
Figure A.2. Schematic (a) and STM image (b) of UVO1 graphene.

eliminated and the sp<sup>2</sup> carbon hybridization has been largely restored (Vinogradov et al., 2011).

### **A.3.2 Evolution of local density of states probed by scanning tunneling spectroscopy**

The effect of oxygen uptake on the electronic characteristic of graphene can be understood by investigating its local electronic density of states (LDOS) before and after the oxidation process. LDOS can be characterized easily using scanning tunneling spectroscopy (STS), because it is proportional to the tunneling differential conductance characteristic ( $dI/dV$ ) and can be obtained by taking the first derivative of the tunneling current with respect to the bias voltage (Yeh et al., 2011). Nevertheless, obtaining  $dI/dV$  spectra that represent the characteristic of the whole sample is not completely straightforward. Since the measured tunneling current depends heavily on the specific configuration of the atoms involved in the tunneling process,  $dI/dV$  fluctuates considerably from one location to another location in one sample and from one sample to another sample. Thus, it is more reliable to deduce the electronic characteristic of the sample by statistically analyzing the obtained  $dI/dV$  spectra (Castellanos-Gomez et al., 2012). Using statistical analysis, the most probable characteristic of each set of sample can be determined (Castellanos-Gomez et al., 2012).

The  $dI/dV$  spectra of CVD-P graphene exhibit a V-like shape with nonzero differential conductance at zero-energy, which implies that its LDOS do not vanish at the Fermi level. Such a characteristic deviates from that of a neutral free-standing pristine graphene where its LDOS is zero at the Fermi level. This finding suggests that CVD-P graphene has a metallic characteristic, which may be caused by a strong hybridization between nickel and carbon bands (Murata et al., 2010). The  $dI/dV$  spectra of the oxidized graphene show a deviation from that of CVD-P graphene around the zero-energy region. Both O2P1 and UVO1 graphene exhibit an accumulation of data points with zero differential conductance around the zero-energy region



$$E_{\text{gap}} = 0.05 - 0.07 \text{ eV}$$

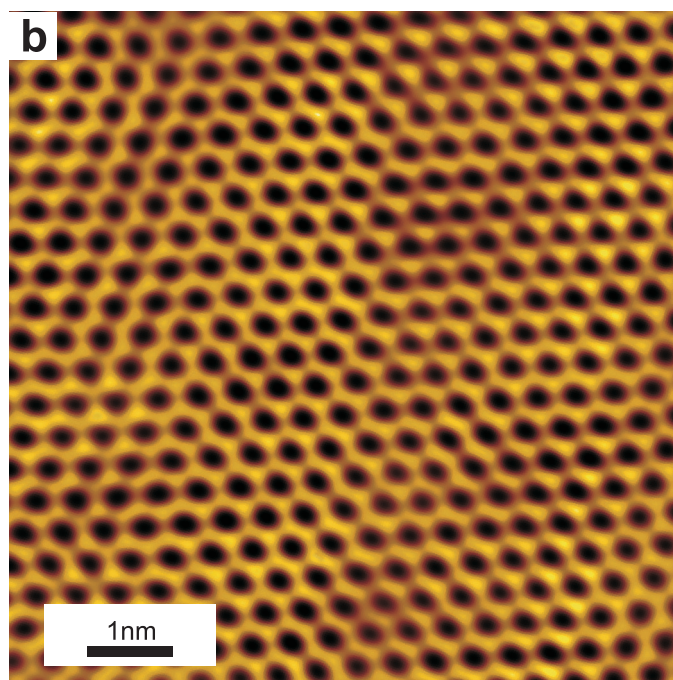


Figure A.3. Schematic (a) and STM image (b) of UVO1-VA graphene.

starts to occur (Figure A.4 and A.5). These zero differential conductance data points are almost normally distributed with a peak close to the zero-energy. Thus, the  $dI/dV$  spectra of O2P1 and UVO1 graphene exhibit a U-like shape with a "flattening" of the differential conductance around the zero-energy region. The occurrence of such flattening indicates an opening of an energy gap in the LDOS, and suggests that the electronic characteristic of O2P1 and UVO1 graphene has been transformed from zero energy gap metallic to semiconducting (Leconte et al., 2010; Nourbakhsh et al., 2010; Castellanos-Gomez et al., 2012; Pandey et al., 2008).

The opening of the energy gap in the LDOS can be partially closed by exposing the oxidized graphene to vacuum annealing (VA) treatment. VA treatment has been successfully used in the past to remove hydrogen and oxygen adsorbates from hydrogenated and oxidized graphene (Zhang et al., 2012; Castellanos-Gomez et al., 2012; Hossain et al., 2012; Elias et al., 2009; Acik et al., 2011, 2010). The  $dI/dV$  spectra of O2P1-VA and UVO1-VA graphene exhibit a V-like shape similar to those of CVD-P graphene (Figure A.4 and A.5). However, unlike those of CVD-P graphene, the  $dI/dV$  spectra of O2P1-VA and UVO1-VA graphene still exhibit an accumulation of data points with zero differential conductance around the zero-energy region, although it is negligible compared to those of O2P1 and UVO1 graphene. In addition, a larger variation in  $dI/dV$  spectra of O2P1-VA and UVO1-VA graphene compared to that of CVD-P graphene, indicates that the spatial fluctuation in LDOS of O2P1-VA and UVO1-VA graphene is considerably larger than that of CVD-P graphene. Hence, it can be deduced that, although VA treatment does reduce the energy gap opening, it does not completely reverse the effect of oxidation. Once a CVD graphene has been exposed to either UVO or O2P treatment, its metallic behavior can no longer be recovered, even after being exposed to VA treatment.

The energy gap in the LDOS can be reopened by reapplying UVO and O2P treatments to these graphene samples. Since the  $dI/dV$  spectra of O2P2 and UVO2 graphene are similar to those of O2P1 and UVO1 graphene, one may expect that the electronic characteristics of these samples are similar. Compared to those of O2P1 and UVO1 graphene, the  $dI/dV$  spectra of O2P2 and UVO2 graphene also

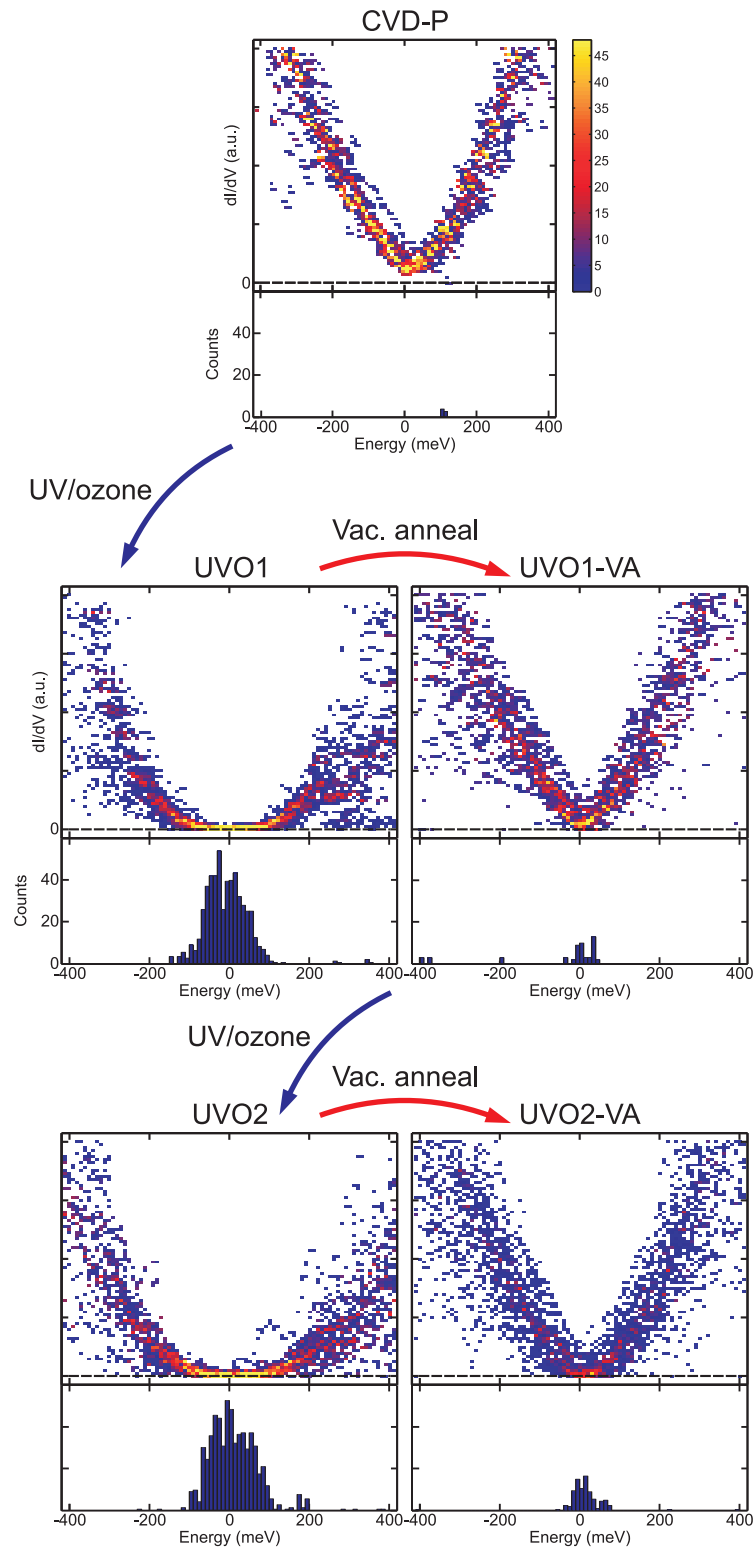


Figure A.4. Evolution of STS spectra of CVD graphene that undergoes UV/ozone and vacuum annealing cycles.

exhibit a U-like shape with a flattening of differential conductance around zero-energy region (Figure A.4 and A.5). The reappearance of such flattening suggests that the energy gap of O2P2 and UVO2 graphene has been once again opened. As expected, reapplication of VA treatment to these graphene samples again closes the energy gap opening, indicated by the disappearance of a flattening of differential conductance around zero-energy region. It is important to note that the  $dI/dV$  spectra of O2P2-VA and UVO2-VA graphene have a considerably larger variation and U-like shape than those of O2P1-VA and UVO1-VA graphene (Figure A.4 and A.5). This suggests that there exist a maximum number of oxidation-reduction cycles that can be applied to the CVD graphene after which its electronic characteristic is no longer tunable.

The opening of energy gap in the LDOS can be extracted from the  $dI/dV$  spectra by plotting the zero differential conductance data points as a one dimensional histogram around the zero-energy region, and calculating the full width at half maximum (FWHM) of this one dimensional histogram (Castellanos-Gomez et al., 2012). After being exposed to UVO and O2P treatments, the energy gap of CVD graphene increases from 0eV for CVD-P graphene to  $0.11(\pm 0.05)$ eV and  $0.13(\pm 0.06)$ eV for UVO1 and O2P1 graphene respectively (Figure A.6.a). Although VA treatment does not completely close the energy gap opening, it does reduce the opening to  $0.05(\pm 0.02)$ eV and  $0.07(\pm 0.03)$ eV for UVO1-VA and O2P1-VA graphene, respectively. A second exposure to UVO and O2P treatments reopens the energy gap to  $0.13(\pm 0.05)$ eV and  $0.15(\pm 0.06)$ eV for UVO2 and O2P2 graphene, respectively. Similarly, a second exposure to VA treatment reduces the energy gap opening to  $0.06(\pm 0.03)$ eV and  $0.03(\pm 0.03)$ eV for UVO2-VA and O2P2-VA graphene, respectively. Note that the value of the energy gap opening after the second cycle is slightly higher than that after the first one. Although the difference between the first and second cycle is not statistically significant, it suggests that the oxidation-reduction cycle using a combination of UVO/O2P and VA treatments may not be completely reversible. An intensive study to determine the maximum number of oxidation-reduction cycles that a CVD graphene can handle is yet to be performed.

It is expected that the opening of energy gap in the LDOS is induced by the

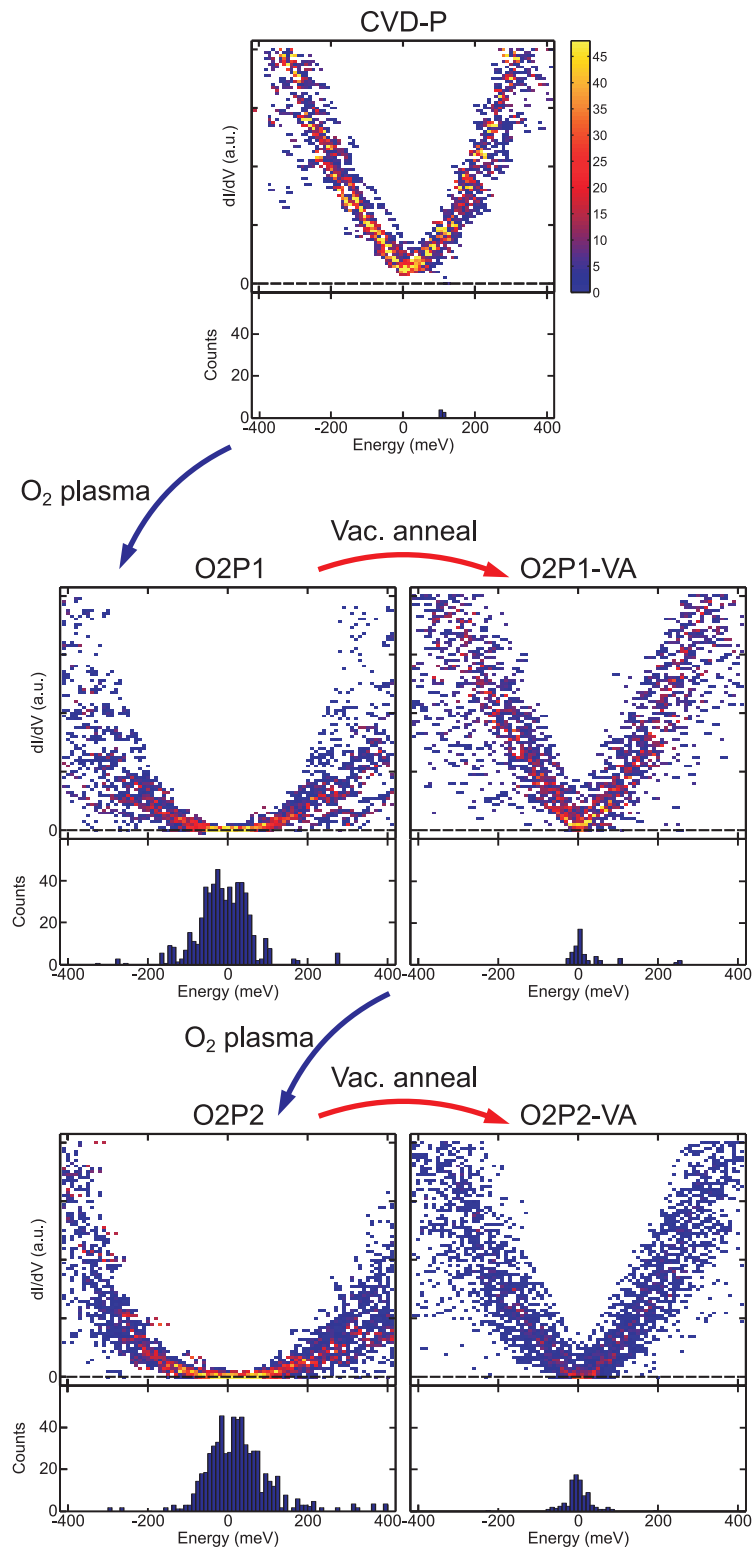


Figure A.5. Evolution of STS spectra of CVD graphene that undergoes oxygen plasma and vacuum annealing cycles.

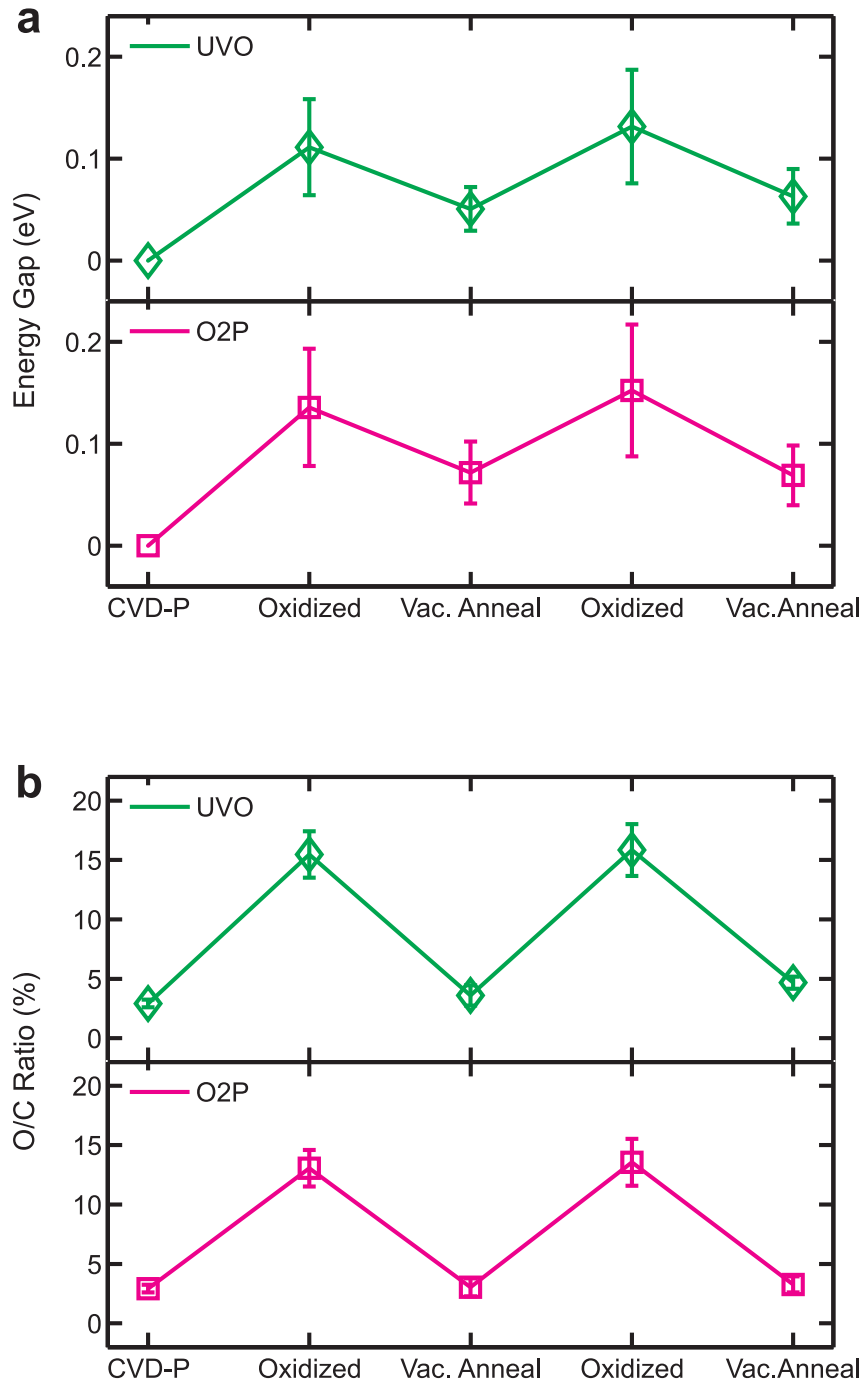


Figure A.6. Energy gap and oxygen/carbon ratio evolution of CVD graphene under induced by dry oxidation and vacuum annealing cycles.

presence of defect sites introduced by oxygen adsorbates. These oxygen adsorbates produce a strong disruption to the  $\pi$ -bond network that facilitates the electron mobility and charge transport across the graphene basal plane (Leconte et al., 2010; Childres et al., 2011; Ito et al., 2008). Since the degree of induced localization depends heavily on the magnitude of such disruption and the spatial distribution of defect sites, an increase of oxygen adsorbate concentration will certainly reduce the electron mobility and lead to an opening in the energy gap (Luo et al., 2009; Leconte et al., 2010; Childres et al., 2011). These defect sites also induce a localization effect, where each of the oxidized sites acts as a strongly repulsive hard wall barrier, and the degree of such localization is dictated by the spatial distribution and the concentration of oxygen adsorbates (Luo et al., 2009). In addition, any alteration to the  $\pi$ -bond network near the defect sites further distorts the electron-phonon couplings and electron-electron interactions (Luo et al., 2009; Manes, 2007).

### **A.3.3 Changes in defects probed by Raman spectroscopy**

Previous studies show that the p-doping level, electron-electron scattering rate, and the total density of state of oxidized graphene are dictated by the defect density associated with surface concentration of oxygen adsorbates (Leconte et al., 2010; Alzina et al., 2010). At a very low concentration, the p-doping level and electron-electron scattering rate increase as the defect density increases Nourbakhsh et al. (2010); Kim et al. (2009); Childres et al. (2011). At a higher concentration of oxygen adsorbates, a continuous decay and smoothing of the van Hove singularities becomes apparent, and a further increase in concentration by a few percent leads into a significant drop of conductance and carrier concentration, which may indicate an Anderson metal-insulator transition (Leconte et al., 2010; Alzina et al., 2010).

The increase of defect site density induced by oxygen adsorbates can be verified by Raman spectroscopy. Three distinct peaks of D band (  $1350\text{cm}^{-1}$ ), G band (  $1585\text{cm}^{-1}$ ), and G' band (  $2695\text{cm}^{-1}$ ) can be seen in the Raman spectra of CVD graphene before and after oxidation (Ferrari et al., 2006; Reina et al., 2009; Dresselhaus et al.,

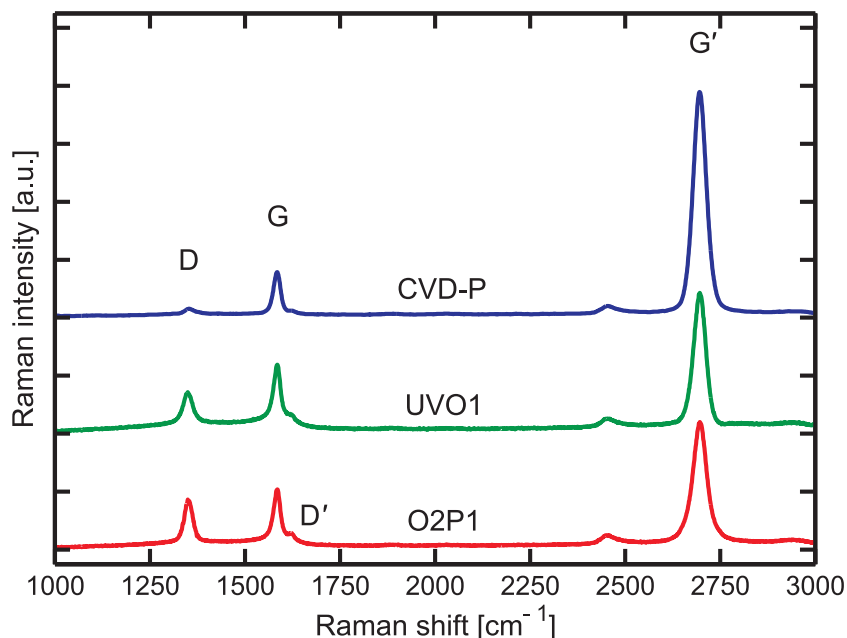


Figure A.7. Raman spectra of CVD graphene before and after dry oxidation and vacuum annealing cycles.

2010; Nourbakhsh et al., 2010; Dresselhaus et al., 2010). The intensity ratio between the non-sp<sup>2</sup> disorder-induced D band and sp<sup>2</sup> symmetry G band,  $I_D/I_G$ , was measured to be 0.19 for the CVD-P graphene. After UVO and O2P treatments, this ratio increases to 0.61 and 0.83 for the UVO1 and O2P1 graphene respectively. In addition, a shoulder D' peak (1620cm<sup>-1</sup>), associated with disorder-induced intravalley resonance Raman scattering, becomes visible in the Raman spectra of UVO1 and O2P1 graphene (Figure A.7) (Nourbakhsh et al., 2010; Samarakoon and Wang, 2011). It has been theorized that the abovementioned disorder-induced Raman scattering is caused by in-phase and out-of-phase stretching of epoxide groups bonded on the graphene basal plane (Samarakoon and Wang, 2011).

### A.3.4 Evolution of surface chemistry probed by X-ray photoelectron spectroscopy

Since the presence of oxygen adsorbates introduces surface defects that ultimately dictate the opening of energy gap in the LDOS, it is imperative to quantify the

concentration of oxygen adsorbates involved during the oxidation-reduction cycle. Here, the concentration of oxygen adsorbates is represented by its oxygen/carbon atomic ratio (O/C ratio). The O/C ratio is calculated from the intensity of the low resolution O 1s and C 1s peaks obtained by x-ray photoelectron spectroscopy (XPS) (Ferrari et al., 2006; Hesse et al., 2005). After being exposed to UVO and O2P treatments, the O/C of CVD graphene increases from 2.92( $\pm$ 0.32)% for CVD-P graphene to 15.45( $\pm$ 1.95)% and 13.06( $\pm$ 1.53)% for UVO1 and O2P1 graphene, respectively (Figure A.6.b). Note that the O/C ratio of CVD-P graphene is not zero, suggesting that a small amount of oxygen is adsorbed at the graphene boundaries during the growth or storage phase and may not be easily removed. After being exposed to VA treatment, the O/C ratio decreases almost to its original value of 3.6( $\pm$ 0.85)% and 3.03( $\pm$ 0.76)% for UVO1-VA and O2P1-VA graphene, respectively. A second exposure to UVO and O2P treatments increases the O/C ratio back to 15.83( $\pm$ 2.18)% and 13.55( $\pm$ 1.96)% for UVO2 and O2P2 graphene, respectively. A second exposure to VA treatment decreases the O/C ratio once again to 4.67( $\pm$ 0.51)% and 3.27( $\pm$ 0.67)% for UVO2-VA and O2P2-VA graphene, respectively. Similar to the value of energy gap opening, the value of O/C ratio after the second cycle is slightly higher than that after the first one.

A direct correlation between the energy gap opening of graphene and the concentration of oxygen adsorbates can be obtained by plotting them against each other (Figure A.8). The correlation between the energy gap of graphene and its O/C ratio is monotonic, regardless of the oxidation method used, which implies that the observed energy gap opening is indeed induced by defects sites introduced by oxygen adsorbates (Luo et al., 2009; Nourbakhsh et al., 2010; Pandey et al., 2008; Ito et al., 2008). As mentioned above, an energy gap of 0.11-0.15eV can be obtained by exposing the CVD graphene to either UVO or O2P treatment, such that they have an O/C ratio of 13-16%. These energy gap values are found to be slightly lower than those predicted by density functional theory (DFT) calculations on free-standing graphene for the same range of O/C ratio (Nourbakhsh et al., 2010; Huang et al., 2012; Guo et al., 2012). However, these energy gap values are found to be an order of magnitude

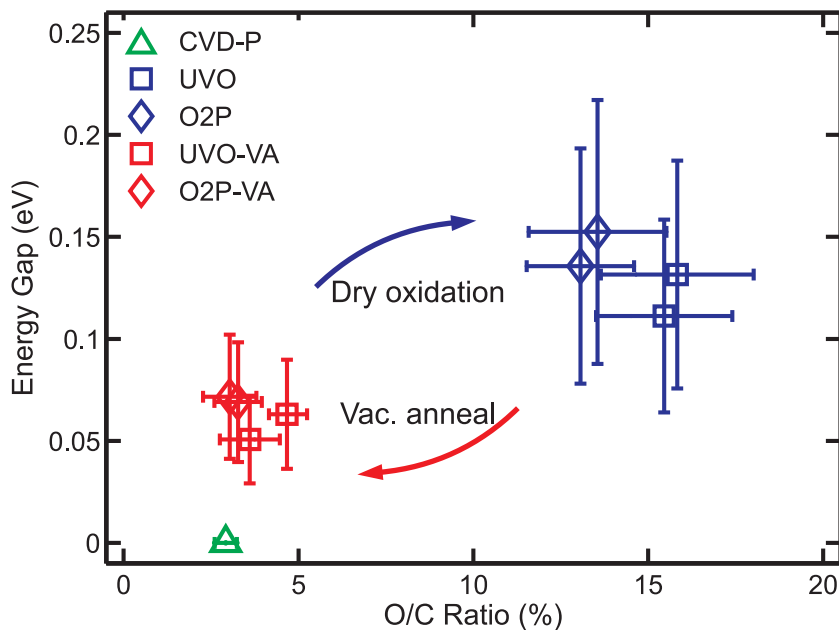


Figure A.8. Energy gap vs oxygen/carbon ratio of CVD graphene induced by dry oxidation and vacuum annealing cycles.

lower than those measured on graphene oxides derived from graphite flakes using wet chemical oxidation method (Guo et al., 2012).

Note that the energy gap of O2P1 and O2P2 graphene is slightly higher than that of UVO1 and UVO2 graphene, respectively, even though their respective O/C ratio is lower. This suggests that the level of disorder in the structural symmetry of graphene is more pronounced due to the physical reaction with the oxygen plasma (Nourbakhsh et al., 2010; Kim et al., 2009). In fact, it has been known that plasma bombardment induces irrecoverable modification to the graphitic structure by converting the carbon hybridization from  $sp^2$  to  $sp^3$ , which further eliminates the  $\pi$ -bond network and alters the electron mobility and charge transport across the basal plane (Elias et al., 2009; Hou et al., 2008).

Deconvolution of the C 1s XPS spectra of CVD graphene samples shows five distinct peaks associated with C-C  $sp^2$  ( $284.5 \pm 0.1$  eV, FWHM 0.9 eV), C-C  $sp^3$  ( $285.5 \pm 0.1$  eV, FWHM 1.3 eV), C-O ( $286.5 \pm 0.1$  eV, FWHM 1.4 eV), C=O ( $287.4 \pm 0.2$  eV, FWHM 1.4 eV), and O-C=O ( $289.1 \pm 0.4$  eV, FWHM 1.7 eV) (Yang et al., 2009; Aria and Gharib, 2011). In addition to an extremely strong C-C  $sp^2$  peak, the C 1s XPS

spectrum of the CVD-P graphene shows a mild C-C sp<sup>3</sup> peak, a very weak C-O peak, and negligible C=O and O-C=O peaks. These C-C sp<sup>3</sup> and C-O peaks may indicate the presence of hydroxyl or other terminal functional groups, such as cyclic ether, at the graphene edges (Figure A.9) (Hossain et al., 2012; Acik et al., 2011, 2010).

The O 1s spectra of CVD graphene samples show three distinct components associated with O-C=O ( $531.5 \pm 0.3$  eV, FWHM 1.4 eV), C=O ( $532.6 \pm 0.3$  eV, FWHM 1.3 eV), and C-O ( $533.5 \pm 0.3$  eV, FWHM 1.4 eV) (Yang et al., 2009). In agreement with its C 1s spectrum, the O 1s XPS spectrum of the CVD-P graphene shows a very strong C-O peak, a weak C=O peak, and a negligible O-C=O peak. The weak C=O peak may indicate the presence of a few carbonyl groups arranged in pairs at the graphene edges (Acik et al., 2011). In addition, it also exhibits an additional O 1s peak ( $535.2 \pm 0.7$  eV, FWHM 1.9 eV), which may be associated with physisorption of molecular oxygen or moisture during storage and handling (Figure A.10) (Biesinger et al., 2009).

Evidence of oxygen uptake by graphene during the UVO or O<sub>2</sub>P treatment can be observed from a considerable increase in the intensity of C-O, C=O, and O-C=O peaks (Figure A.9). Such increases are accompanied by an increase in the intensity of C-C sp<sup>3</sup> peak. In fact, the surface concentration ratio between C-C sp<sup>3</sup> and C-C sp<sup>2</sup> increases from about 10.3% for CVD-P graphene to about 25.3% and 25.7% for UVO1 and O<sub>2</sub>P1 graphene, respectively (Figure A.11.a). Similarly, the surface concentration ratio between total oxygenated groups and C-C sp<sup>2</sup> increases from about 2.7% for CVD-P graphene to about 37.8% and 32.7% for UVO1 and O<sub>2</sub>P1 graphene, respectively (Figure A.11.b). As mentioned earlier, structural transformation due to the formation of sp<sup>3</sup> bonds may lead to the disappearance of Moiré pattern on UVO1 and O<sub>2</sub>P1 graphene (Vinogradov et al., 2011; Samarakoon and Wang, 2011; Suggs et al., 2011; Muniz and Maroudas, 2010). Although O<sub>2</sub>P treatment introduces a lower concentration of oxygenated groups, it induces more C-C sp<sup>3</sup> bonds than UVO treatment. This suggests that some of the sp<sup>3</sup> bonds are formed during the O<sub>2</sub>P treatment by the physical bombardment of plasma (Nourbakhsh et al., 2010; Kim et al., 2009; Elias et al., 2009; Hou et al., 2008). Since this phenomenon is very

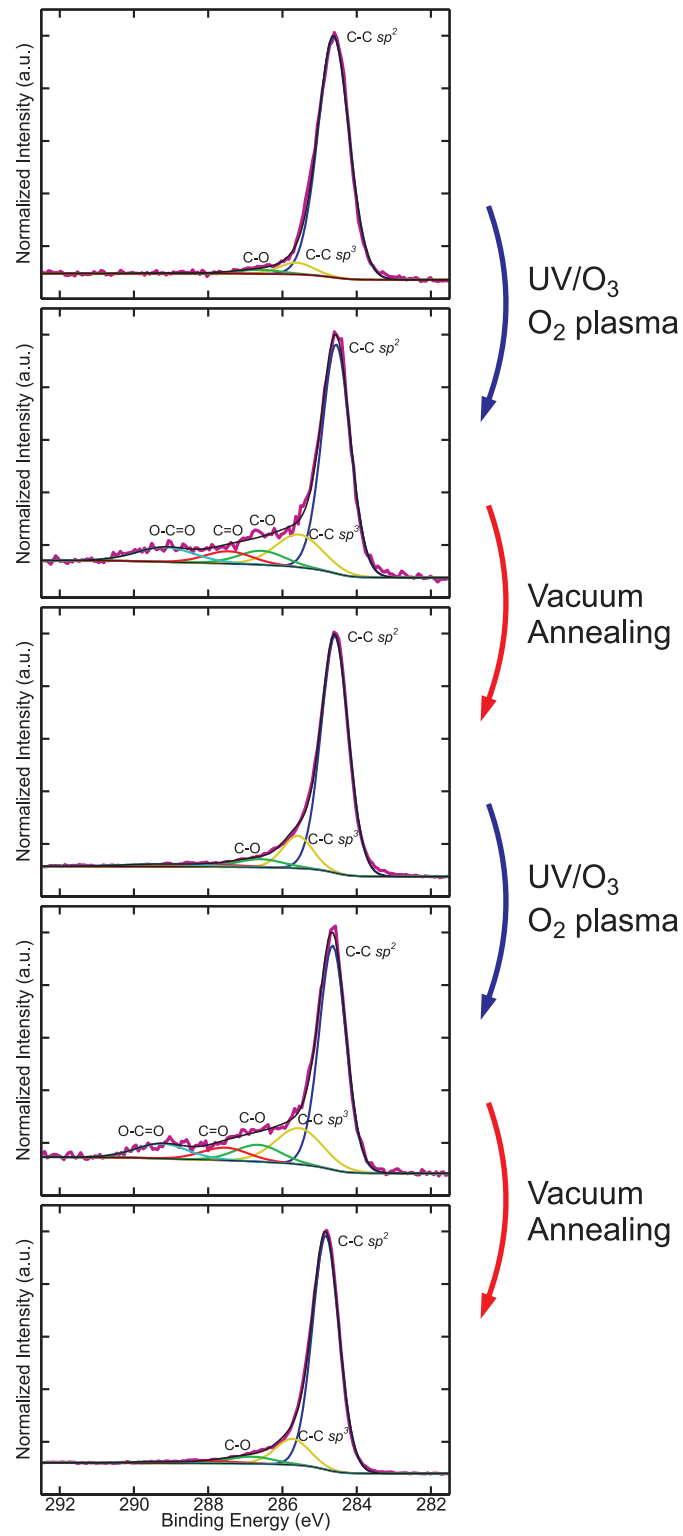


Figure A.9. Evolution of XPS C1s spectra of CVD graphene induced by dry oxidation and vacuum annealing cycles.

unlikely to happen when UVO treatment is used, the increase in concentration of sp<sup>3</sup> bonds can be attributed to that of oxygen adsorbates.

A stronger C-O peak suggests that the concentration of hydroxyl and epoxide groups on the basal plane of UVO1 and O2P1 graphene is significantly higher than that on CVD-P graphene. The apparent increase of intensity of the C=O peak can be associated with an increase of concentration of carbonyl groups on the graphene basal plane or edges. A more pronounced O-C=O peak suggests that both UVO and O2P treatments also induce the formation of carboxyl terminating groups, stabilized by electrostatic repulsive forces among themselves, at the graphene edges (Acik et al., 2011). An epoxide group can be formed when an atomic oxygen radical produced by plasma or ozone is bonded above the middle of a C-C bond (Samarakoon and Wang, 2011). It can also be formed when ozone is adsorbed as ozonide that subsequently lost its molecular oxygen (Suggs et al., 2011). The presence of hydroxyl and carboxyl groups on UVO1 and O2P1 graphene suggests that reactive hydroxyl radicals are involved in the UVO and O2P treatments. These hydroxyl radicals may be generated from moisture in the ambient air or physisorbed water molecules. A reaction between these water molecules and atomic oxygen radicals produced by plasma or ozone gives rise to peroxides, which upon homolysis yields free hydroxyl radicals (Gunes et al., 2011; Acik et al., 2011). In contrast, the presence of hydroxyl and carboxyl groups can be excluded when an oxidation process using hot atomic oxygen at an ultra-high-vacuum is used (Vinogradov et al., 2011).

It has been previously reported that the adsorbed oxygen atoms prefer to form epoxide groups on the graphene basal plane due to their lowest energy configuration (Leconte et al., 2010; Nourbakhsh et al., 2010; Vinogradov et al., 2011; Samarakoon and Wang, 2011). However, the O 1s XPS spectra of the UVO1 and O2P1 graphene show that the ratio between each type of oxygenated groups adsorbed on the graphene basal plane or edges is relatively equal (Figure A.10). When UVO treatment is employed, the relative concentration of each C-O, C=O, and O-C=O group is about the same. Similarly, when O2P treatment is utilized, the O-C=O group is accounted for 36% of the total oxygenated groups, while the rest is split almost equally by C-O and

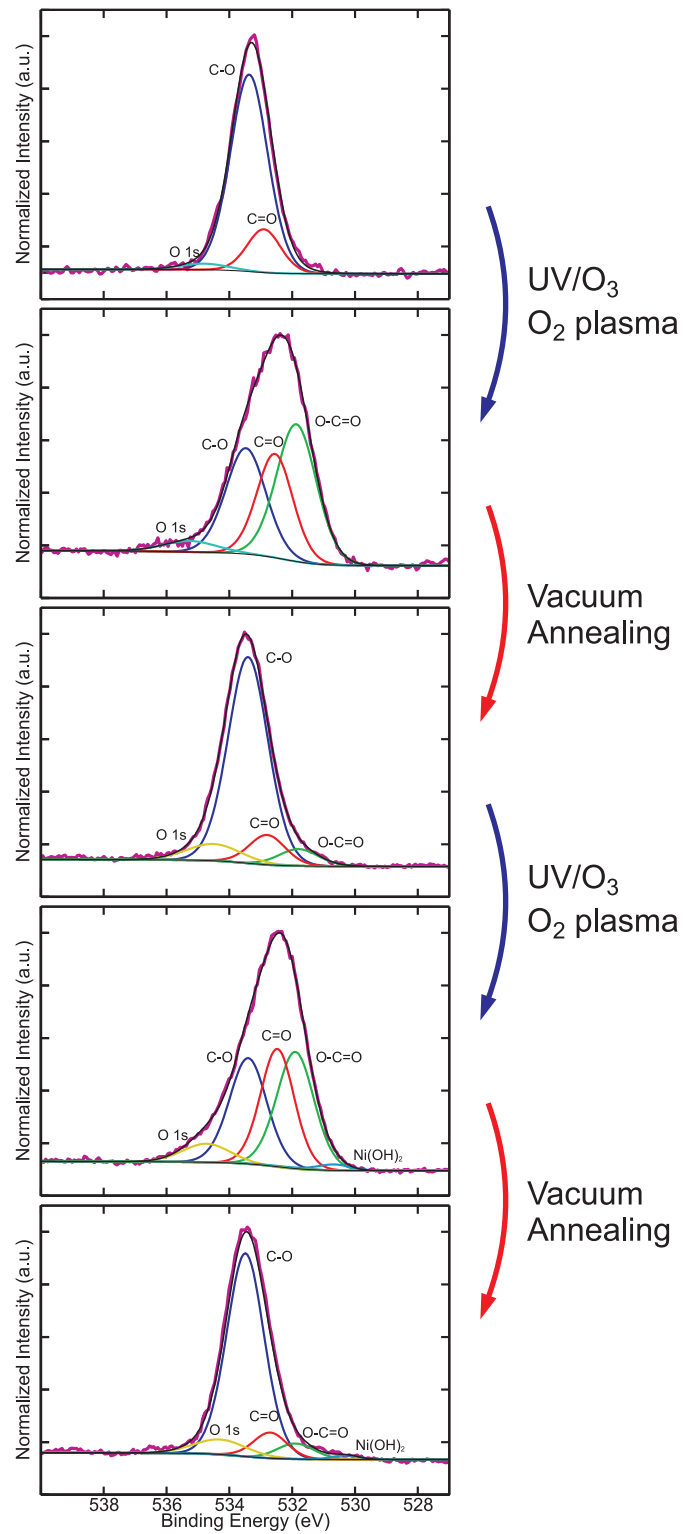


Figure A.10. Evolution of XPS O1s spectra of CVD graphene induced by dry oxidation and vacuum annealing cycles.

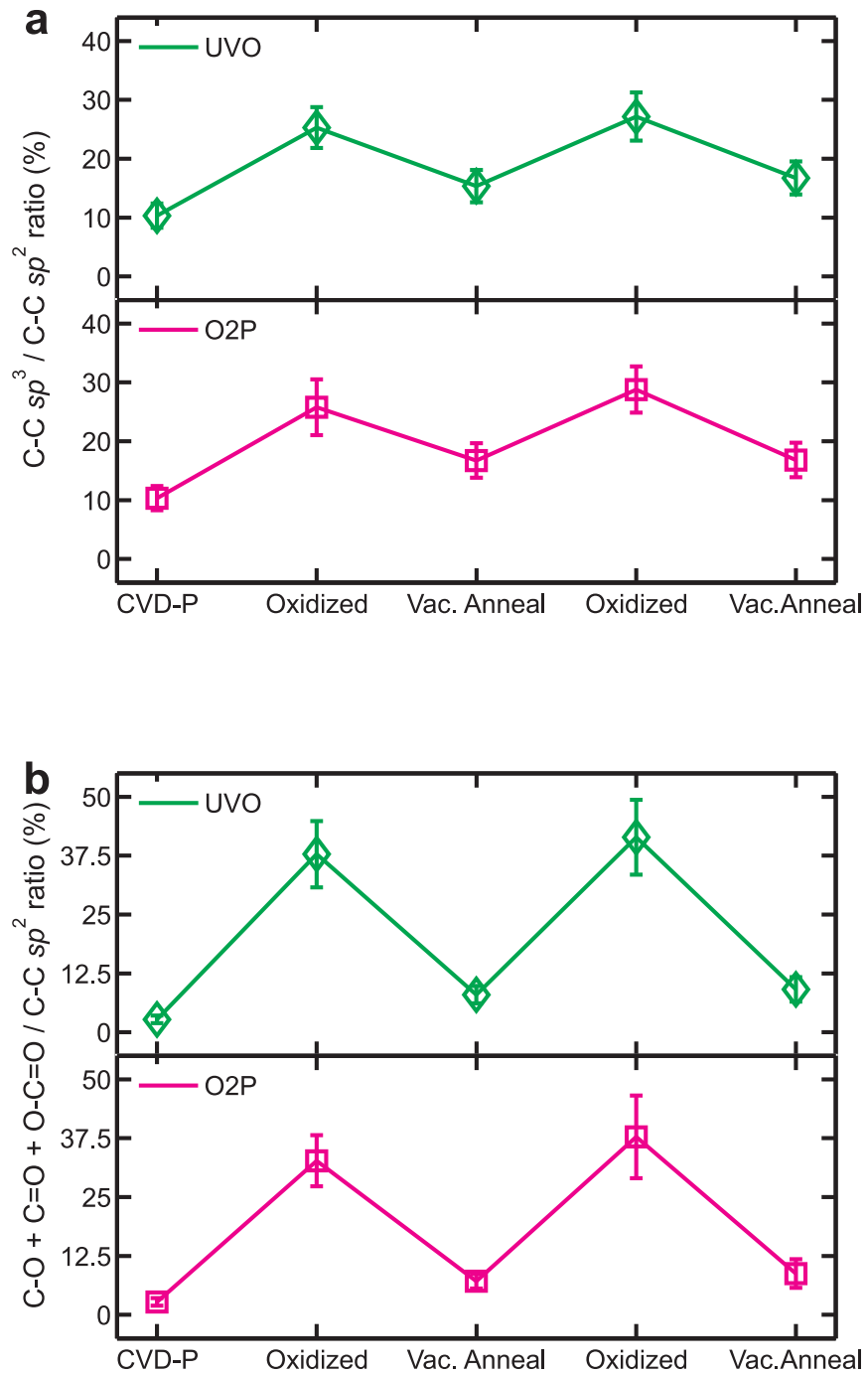


Figure A.11. Evolution of C-C bond concentration of CVD graphene induced by dry oxidation and vacuum annealing cycles.

C=O group (Figure A.12.a, Figure A.12.b, and Figure A.13.a). This suggests that some of the epoxide groups are converted to carbonyl and carboxyl groups during UVO and O2P treatments. It has been known that epoxide groups have the tendency to create pair structures which readily form two neighboring carbonyl groups in a quinone-like configuration (Samarakoon and Wang, 2011; Acik et al., 2011). In addition, the formation of a carbonyl group is often caused by a hydrogen atom migration induced by a weak hydrogen bond between two adjacent hydroxyl groups (Elias et al., 2009). These carbonyl groups are then transformed to carboxyl groups by a rapid reaction between them and hydroxyl radicals (Acik et al., 2011). Since carboxyl groups are relatively stable, a further reaction with atomic oxygen or hydroxyl radical is very unlikely. Note that the relative concentration of carboxyl groups on O2P1 graphene is slightly higher than that on UVO1 graphene, suggesting that O2P treatment generates a higher amount of reactive hydroxyl radicals compared to UVO treatment.

Although epoxide, carbonyl, and carboxyl groups are relatively stable at room temperature and pressure, they can be, in principle, removed at an elevated temperature (Leconte et al., 2010; Vinogradov et al., 2011; Acik et al., 2011). Thermal reduction treatment, i.e., vacuum annealing, has been demonstrated to be an effective means of removing the majority of the chemisorbed oxygen from the graphene basal plane (Vinogradov et al., 2011; Hossain et al., 2012). Previous studies suggest that the effectiveness of VA treatment depends on the temperature and dwell time, as well as the total initial concentration and types of oxygen adsorbates (Acik et al., 2011, 2010). A moderate temperature of 250°C is known to be adequate for initiating the removal of adsorbed hydroxyl, epoxide, carbonyl, and carboxyl groups (Acik et al., 2010). The C 1s XPS spectra of UVO1-VA and O2P1-VA graphene show a significant decrease in concentration of all oxygenated groups, as well as the C-C sp<sup>3</sup> bonds (Figure A.9). In fact, the surface concentration ratio between C-C sp<sup>3</sup> and C-C sp<sup>2</sup>, as well as total oxygenated groups and C-C sp<sup>2</sup>, decreases to about 15-16% and 7-8%, respectively (Figure A.12).

The O 1s XPS spectra of UVO1-VA and O2P1-VA graphene indicate that most

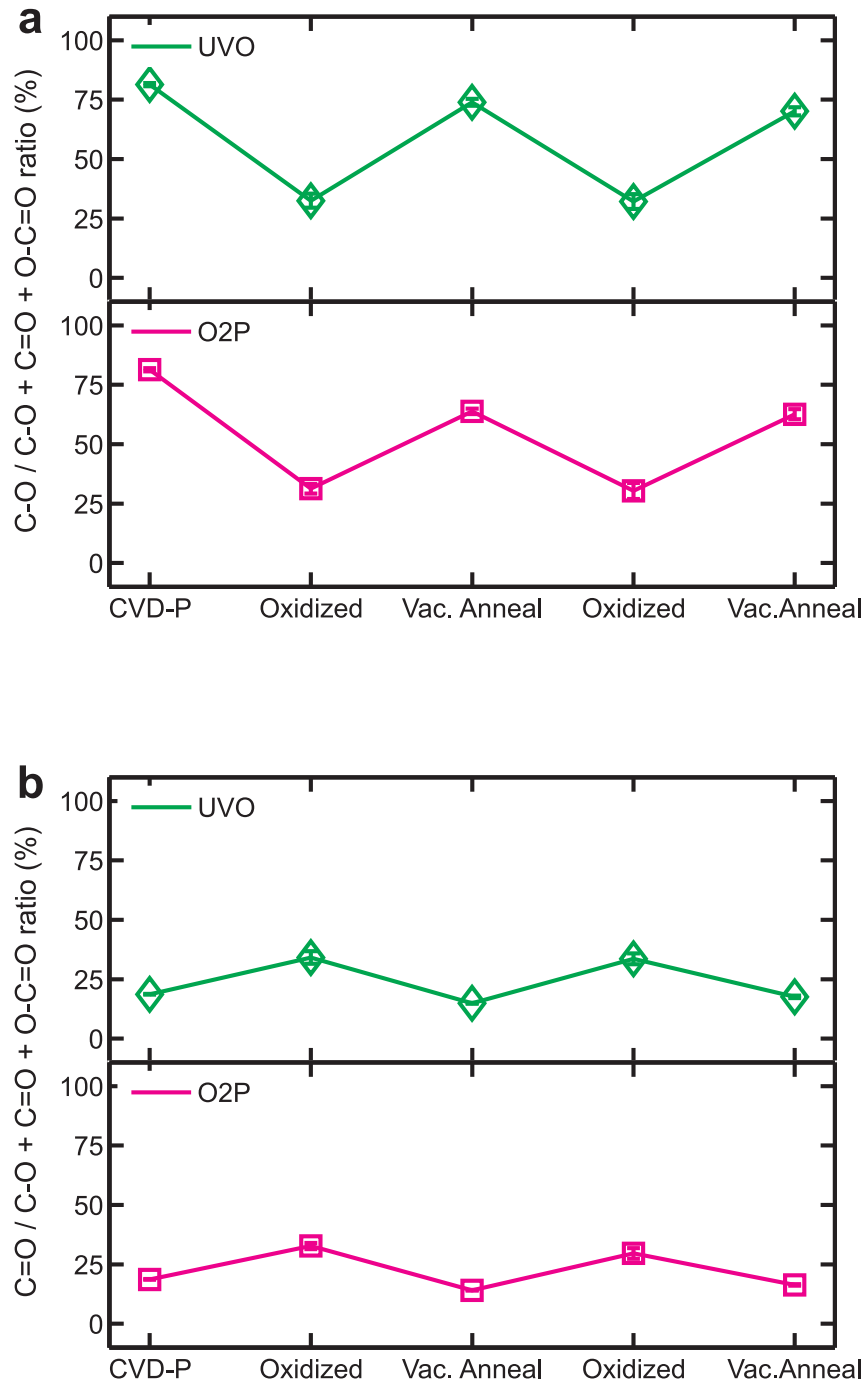


Figure A.12. Evolution of C-O and C=O bonds concentration of CVD graphene induced by dry oxidation and vacuum annealing cycles.

of epoxide and carboxyl groups are removed by VA treatment (Figure A.10), and C-O groups are accounted for about 63-73% of the total remaining oxygenated groups (Figure A.12.a). Nevertheless, it is interesting to note that the relative concentration of O-C=O groups on O2P1-VA graphene is around 22% of the total remaining oxygenated groups, which is about twice than that on UVO1-VA graphene (Figure A.13.a). In addition to differences in the initial concentration of carboxyl groups between both graphene samples, such a discrepancy may also be caused by differences in reproduction rate of carboxyl groups during the VA treatment. Different reproduction rate is possible since O2P1 graphene may have a higher relative concentration of hydroxyl groups compared to UVO1 graphene. The extra hydroxyl radicals produced upon decomposition of hydroxyl groups may have reacted with carbonyl groups to form new carboxyl groups, offsetting the decomposition of carboxyl groups on O2P1-VA graphene.

It has been known that desorption of hydroxyl groups starts at a temperature of 75-100°C, while epoxide groups start to decompose at a slightly higher temperature of 100-125°C (Acik et al., 2011; Bagri et al., 2010). However, most epoxide groups are decomposed at a temperature of 225°C (Acik et al., 2011), leaving behind a small amount of isolated epoxide groups (Bagri et al., 2010; Haubner et al., 2010). Simultaneous desorption of adjacent hydroxyl and epoxide groups are often followed by the formation of in-plane ether groups or out-of-plane carbonyl groups (Acik et al., 2011; Bagri et al., 2010). Since carbonyl groups also start to decompose at a temperature of 200°C (Acik et al., 2011), there is a competition between the formation and decomposition of these groups during the VA treatment at a temperature of 250°C. Such competition is further complicated by the transformation of carboxyl groups to carbonyl groups, which is favorable due to the more stable configuration of carbonyl groups, and the transformation of carbonyl groups to hydroxyl groups during VA treatment (Acik et al., 2011; Bagri et al., 2010). Judging from the relative concentration of C=O groups after VA treatment, which is about 14-15% of the total remaining oxygenated groups (Figure A.12), one can deduce that the decomposition rate of carbonyl groups is higher than their formation rate at this temperature.

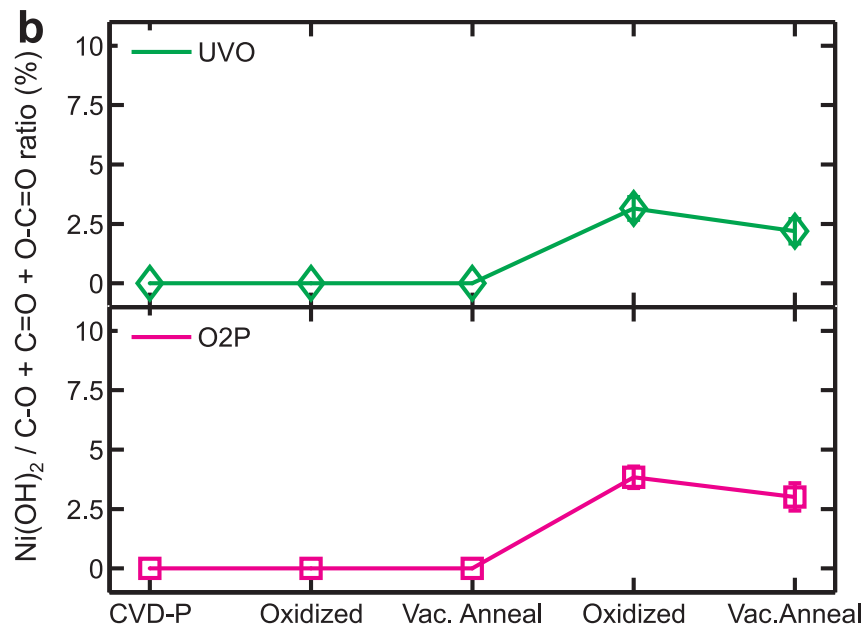
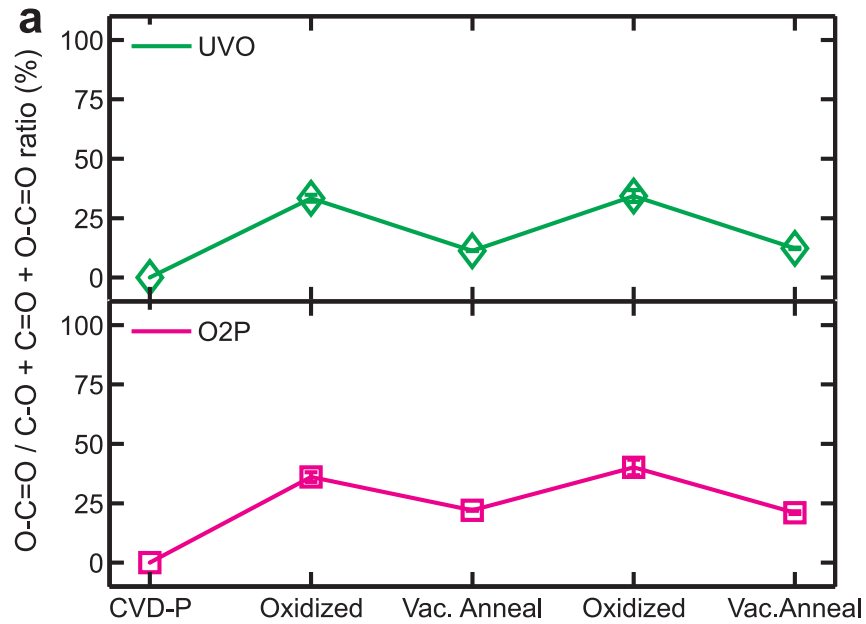


Figure A.13. Evolution of O-C=O bond concentration of CVD graphene induced by dry oxidation and vacuum annealing cycles.

Unlike the removal of hydroxyl and isolated epoxide groups that results in production of H<sub>2</sub>O and O<sub>2</sub>, decomposition of ether groups is typically associated with the production of CO and CO<sub>2</sub> (Acik et al., 2011; Bagri et al., 2010). Since production of CO and CO<sub>2</sub> involves the removal of carbon atom from graphene basal plane and edges, decomposition of ether groups often results in the formation of vacancies and defects (Acik et al., 2011; Li et al., 2006). In contrast, production of H<sub>2</sub>O and O<sub>2</sub> induces minimal defects to the graphene lattice structure (Bagri et al., 2010). Although desorption of carbonyl and carboxyl groups often results in production of CO and CO<sub>2</sub> (Acik et al., 2011), desorption of carbonyl may occasionally produce H<sub>2</sub>O due to their intermediate transformation to hydroxyl groups during VA treatment (Bagri et al., 2010; Haubner et al., 2010). Since the STM images of UVO1-VA and O2P1-VA graphene show the disappearance of bright spots on the graphene basal plane without any apparent vacancies or defects, it can be implied that minimal lattice disorder is introduced during the VA treatment. This suggests that the majority of oxygenated groups adsorbed on the graphene basal plane during UVO and O2P treatments are in the form of hydroxyl groups and isolated epoxide groups. Carbonyl, carboxyl, and perhaps ether groups are more likely to be adsorbed on the graphene edges.

Similar oxygen adsorption processes are observed when these graphene samples are re-exposed to UVO and O2P treatments. An increase in concentration of C-O, C=O, and O-C=O groups, as well as C-C sp<sup>3</sup> bonds, can once again be observed from the C 1s and O 1s XPS spectra of UVO2 and O2P2 graphene (Figure A.9 and Figure A.10). The surface concentration ratio between C-C sp<sup>3</sup> and C-C sp<sup>2</sup>, as well as total oxygenated groups and C-C sp<sup>2</sup>, increases back to about 27-28% and 37-41%, respectively (Figure A.11). Just like after the first treatment, the relative concentration of each C-O, C=O, and O-C=O group is similar to that after the second UVO treatment. However, after the second O2P treatment, the O-C=O group is accounted for 40% of the total oxygenated groups, while the rest is split almost equally by C-O and C=O group (Figure A.12.a, Figure A.12.b, and Figure A.13.a). This noticeable difference in relative concentration of O-C=O groups between UVO2 and

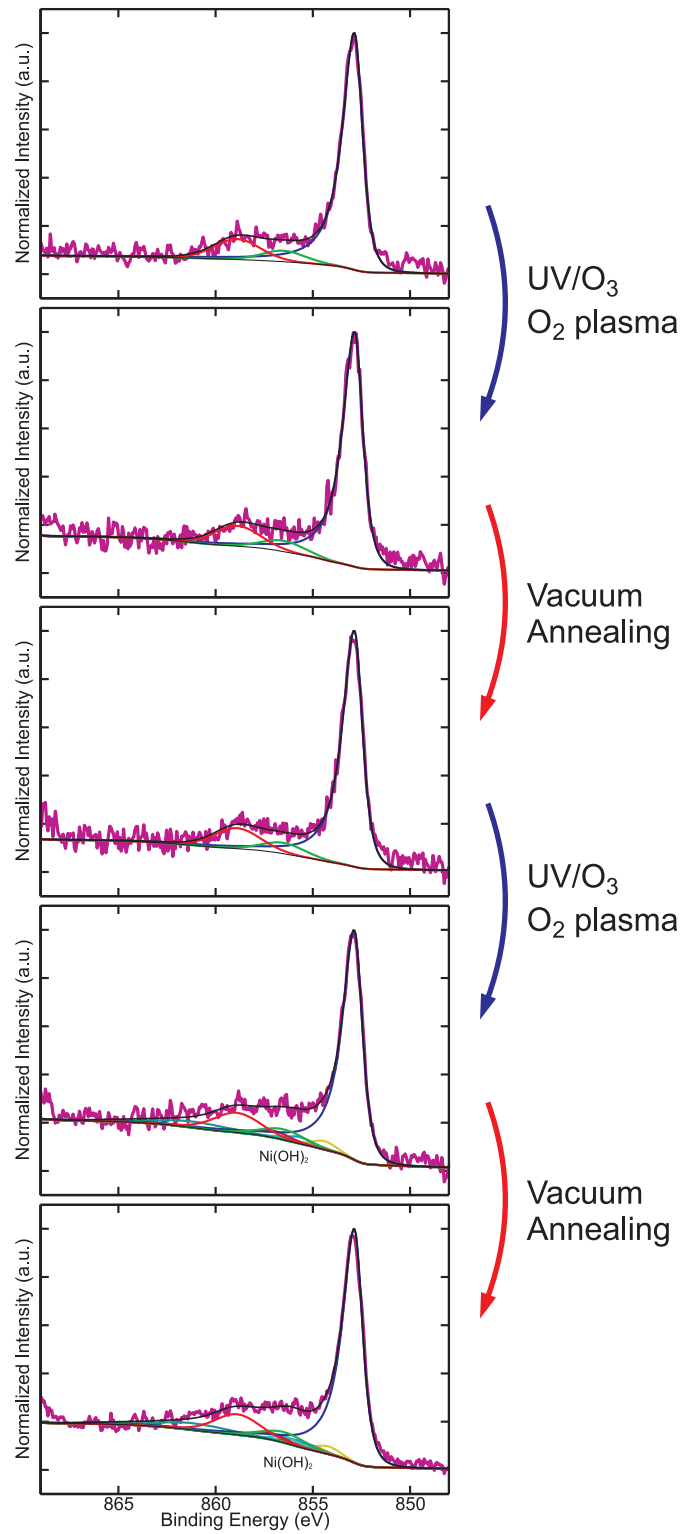


Figure A.14. Evolution of XPS Ni<sub>2</sub>p spectra of CVD graphene induced by dry oxidation and vacuum annealing cycles.

O2P2 graphene highlights the difference in the availability of reactive hydroxyl radicals between UVO and O2P treatments: O2P treatment generates a higher amount of reactive hydroxyl radicals compared to UVO treatment.

As expected, a second exposure to VA treatment cycles back the concentration of all oxygenated groups and C-C sp<sup>3</sup> bonds (Figure A.9). The surface concentration ratio between C-C sp<sup>3</sup> and C-C sp<sup>2</sup>, as well as total oxygenated groups and C-C sp<sup>2</sup>, falls back to about 16-17% and 8-9%, respectively (Figure A.11). Further, the relative concentration of each C-O, C=O, and O-C=O group on UVO2-VA and O2P2-VA graphene is found to be similar to that on UVO1-VA and O2P1-VA graphene (Figure A.12.a, Figure A.12.b, and Figure A.13.a). Note that the concentration of oxygenated groups of UVO2-VA and O2P2-VA graphene is higher than that of UVO1-VA and O2P1-VA graphene, which is higher than that of CVD-P graphene. This indicates that VA treatment does not completely remove the oxygen adsorbates introduced by UVO and O2P treatments. Previous studies show that a complete oxygen removal is difficult to achieve, even at a very high annealing temperature (Acik et al., 2011, 2010; Bagri et al., 2010). However, a complete oxygen removal can be achieved by preventing the formation of stable carbonyl and ether groups during the oxidation process. Hence, an oxidation process using hot atomic oxygen at an ultra-high-vacuum appears to be completely reversible (Vinogradov et al., 2011; Hossain et al., 2012).

It is important to note that the O 1s XPS spectra of UVO1 and O2P1 graphene do not show any peaks associated with Ni-O bonds (Figure A.10). This indicates that the first UVO and O2P treatments do not induce an oxygen uptake by the nickel layer. Deconvolution of the Ni 2p<sub>3/2</sub> XPS spectra of CVD-P graphene shows three distinct peaks that indicate the presence of metallic nickel, with the main Ni metal 2p<sub>3/2</sub> spectral component found at 532.5±0.5 eV (FWHM 1 eV), while the second and third ones can be found at binding energy shifts of +3.65 eV (FWHM 2.6 eV) and +6.05 eV (FWHM 2.8 eV), respectively (Figure A.14) (Biesinger et al., 2009). Similarly, the Ni 2p<sub>3/2</sub> XPS spectra of UVO1 and O2P1 graphene, as well as UVO1-VA and O2P1-VA graphene, show three distinct peaks that indicate the presence

of metallic nickel (Figure A.14). This confirms that the nickel layer is not oxidized and remains in metal form after the first oxidation-reduction cycle. Therefore, it can be implied that the change in the energy gap of CVD graphene observed in the first oxidation-reduction cycle is not induced by the production of nickel oxide or hydroxide during the oxidation process.

However, the nickel layer is no longer in metallic form after the second UVO and O2P treatments. A multiplet associated with Ni(OH)<sub>2</sub> can be seen in the Ni 2p<sub>3/2</sub> XPS spectra of UVO2 and O2P2 graphene (Figure A.14), and is still apparent even after exposure to VA treatment (Figure 6c5). The appearance of such multiplet indicates the appearance of nickel hydroxide layer after the second UVO and O2P treatments, with a relative concentration of 3-4% (Figure A.13.b). Although its relative concentration decreases slightly, this nickel hydroxide layer does not disappear after being exposed to VA treatment. So far, the effect of nickel hydroxide production to the energy gap opening of CVD graphene is still unknown. It is possible that the change in energy gap of CVD graphene observed in the second oxidation-reduction cycle is influenced by the production of nickel oxide or hydroxide during the oxidation process. Nevertheless, an intensive study to determine the effect of nickel oxide or hydroxide to the electronic properties of CVD graphene has to be performed in the future.

## A.4 Concluding Remarks

The work presented herein examines the energy gap and structural evolution of CVD graphene on nickel layer under the influence of dry oxidation and vacuum annealing treatments. Among many available dry oxidation methods, oxygen plasma and UV/ozone treatments are chosen because of their known advantages. These treatments are employed to introduce oxygen adsorbates on CVD graphene. Vacuum annealing treatment is then used to remove the adsorbed oxygen. The topography and electronic properties of CVD graphene are probed using STM/STS. The differential conductance spectra of CVD-P graphene exhibit a nonzero differential con-

ductance at zero-energy, implying its metallic behavior. Exposure to either oxygen plasma or UV/ozone treatment leads to a larger flat region in the two dimensional histogram around the zero-energy where the differential conductance is zero, suggesting an energy gap opening. Such an opening can be reversed, although incompletely, by exposure to vacuum annealing treatment.

The opening in the LDOS of oxidized graphene may be caused by the transformation of carbon hybridization from  $sp^2$  to  $sp^3$  due to the presence of oxygen adsorbates. As probed using XPS, adsorption of oxygen takes place during UV/ozone and oxygen plasma treatments. A noticeable increase in peaks associated with C-O, C=O, and O-C=O bonds suggests that a significant amount of oxygen is adsorbed as hydroxyl, epoxide, carbonyl, and carboxyl groups. Hydroxyl and epoxide groups are mostly adsorbed on the graphene basal plane, while carbonyl and carboxyl groups are adsorbed on the graphene edges. An increase in the peak associated with C-C  $sp^3$  bond implies that the structural transformation of graphene is, indeed, caused by the presence of these oxygenated groups. Subsequent exposure to vacuum annealing treatment decreases the concentration of these oxygen adsorbates. Incomplete closing in the energy gap may be caused by the incomplete removal of oxygen adsorbates.

Oxidation-reduction cycling using a combination of dry oxidation and vacuum annealing treatments seems to be a plausible option to tune the electronic properties, in particular the energy gap, of CVD graphene. The energy gap is positively correlated to the concentration of oxygen adsorbates regardless of oxidation method used. Although the dry oxidation-vacuum annealing cycles are relatively reversible, an oxygen uptake by nickel layer is observed in the second cycle. Nevertheless, the results presented herein show that dry oxidation and vacuum annealing treatments can be indeed used to vary the electronic properties of CVD graphene on nickel.

# Bibliography

- Acik, M., G. Lee, C. Mattevi, M. Chhowalla, K. Cho, and Y. J. Chabal (2010). Unusual infrared-absorption mechanism in thermally reduced graphene oxide. *Nature Materials* 9(10), 840–845.
- Acik, M., G. Lee, C. Mattevi, A. Pirkle, R. M. Wallace, M. Chhowalla, K. Cho, and Y. Chabal (2011). The role of oxygen during thermal reduction of graphene oxide studied by infrared absorption spectroscopy. *The Journal of Physical Chemistry C* 115(40), 19761–19781.
- Alzina, F., H. Tao, J. Moser, Y. Garcia, A. Bachtold, and C. M. Sotomayor-Torres (2010). Probing the electron-phonon coupling in ozone-doped graphene by raman spectroscopy. *Physical Review B* 82(7), 075422.
- Aria, A. I. and M. Gharib (2011). Reversible tuning of the wettability of carbon nanotube arrays: The effect of ultraviolet/ozone and vacuum pyrolysis treatments. *Langmuir* 27(14), 9005–9011.
- Bagri, A., C. Mattevi, M. Acik, Y. Chabal, M. Chhowalla, and V. Shenoy (2010). Structural evolution during the reduction of chemically derived graphene oxide. *Nature chemistry* 2(7), 581–587.
- Balog, R., B. Jorgensen, L. Nilsson, M. Andersen, E. Rienks, M. Bianchi, M. Fanetti, E. Laegsgaard, A. Baraldi, S. Lizzit, Z. Sljivancanin, F. Besenbacher, B. Hammer, T. G. Pedersen, P. Hofmann, and L. Hornekaer (2010). Bandgap opening in graphene induced by patterned hydrogen adsorption. *Nature Materials* 9(4), 315–319.

- Banerjee, S. and S. Wong (2002). Rational sidewall functionalization and purification of single-walled carbon nanotubes by solution-phase ozonolysis. *The journal of physical chemistry B* 106(47), 12144–12151.
- Bartolo, D., C. Josserand, and D. Bonn (2005). Retraction dynamics of aqueous drops upon impact on non-wetting surfaces. *Journal of Fluid Mechanics* 545(-1), 329–338.
- Becerril, H. A., J. Mao, Z. Liu, R. M. Stoltenberg, Z. Bao, and Y. Chen (2008). Evaluation of solution-processed reduced graphene oxide films as transparent conductors. *ACS nano* 2(3), 463–470.
- Bennett, T. and D. Poulikakos (1993). Splat-quench solidification: estimating the maximum spreading of a droplet impacting a solid surface. *Journal of Materials Science* 28(4), 963–970.
- Bhushan, B., Y. C. Jung, and K. Koch (2009). Micro-, nano- and hierarchical structures for superhydrophobicity, self-cleaning and low adhesion. *Philosophical Transactions of The Royal Society A - Mathematical, Physical and Engineering Sciences* 367(1894), 1631–1672.
- Biance, A.-L., F. Chevy, C. Clanet, G. Lagubeau, and D. Quere (2006). On the elasticity of an inertial liquid shock. *Journal of Fluid Mechanics* 554, 47–66.
- Biance, A.-L., C. Clanet, and D. Quere (2003). Leidenfrost drops physics of fluids. *Physics of fluids* 15(6), 1632–1637.
- Bianco, A., K. Kostarelos, and M. Prato (2005). Applications of carbon nanotubes in drug delivery. *Current Opinion in Chemical Biology* 9(6), 674–679.
- Biesinger, M., B. Payne, and A. Gerson (2009). X-ray photoelectron spectroscopic chemical state quantification of mixed nickel metal, oxide and hydroxide systems. *Surface and Interface Analysis* 41(4), 324–332.

- Bostwick, A., J. L. McChesney, K. V. Emtsev, T. Seyller, K. Horn, S. D. Kevan, and E. Rotenberg (2009). Quasiparticle transformation during a metal-insulator transition in graphene. *Physical Review Letters* 103(5), 056404.
- Bronikowski, M. (2006). Cvd growth of carbon nanotube bundle arrays. *Carbon* 44(13), 2822–2832.
- Byon, H. R., B. M. Gallant, S. W. Lee, and Y. Shao-Horn (2012). Role of oxygen functional groups in carbon nanotube/graphene freestanding electrodes for high performance lithium batteries. *Advanced functional materials* 23(8), 1037–1045.
- Castellanos-Gomez, A., M. Wojtaszek, Arramel, N. Tombros, and B. J. van Wees (2012). Reversible hydrogenation and bandgap opening of graphene and graphite surfaces probed by scanning tunneling spectroscopy. *Small* 8(10), 1607–1613.
- Castro Neto, A. H., F. Guinea, N. M. R. Peres, K. S. Novoselov, and A. K. Geim (2009). The electronic properties of graphene. *Reviews of Modern Physics* 81(1), 109–162.
- Chandra, S. and C. Avedisian (1991). On the collision of a droplet with a solid-surface. *Proceedings of the Royal Society A: Mathematical, Physical and Engineering Sciences* 432(1884), 13–41.
- Chang, J. H. and I. W. Hunter (2011). A superhydrophobic to superhydrophilic in situ wettability switch of microstructured polypyrrole surfaces. *Macromolecular Rapid Communications* 32(9-10), 718–723.
- Chen, C., B. Liang, A. Ogino, X. Wang, and M. Nagatsu (2009). Oxygen functionalization of multiwall carbon nanotubes by microwave-excited surface-wave plasma treatment. *The Journal of Physical Chemistry C* 113(18), 7659–7665.
- Chen, C., A. Ogino, X. Wang, and M. Nagatsu (2010). Plasma treatment of multiwall carbon nanotubes for dispersion improvement in water. *Applied physics letters* 96(13), 131504.

- Chen, J. H., W. Z. Li, D. Z. Wang, S. X. Yang, J. G. Wen, and Z. F. Ren (2002). Electrochemical characterization of carbon nanotubes as electrode in electrochemical double-layer capacitors. *Carbon* 40(8), 1193–1197.
- Childres, I., L. A. Jauregui, J. Tian, and Y. P. Chen (2011). Effect of oxygen plasma etching on graphene studied using raman spectroscopy and electronic transport measurements. *New Journal of Physics* 13(2), 025008.
- Cho, S., Y. Hong, and H. Uhm (2007). Hydrophobic coating of carbon nanotubes by ch4 glow plasma at low pressure, and their resulting wettability. *Journal of materials chemistry* 17(3), 232–237.
- Clanet, C., C. Beguin, D. Richard, and D. Quere (2004). Maximal deformation of an impacting drop. *Journal of Fluid Mechanics* 517(-1), 199–208.
- Conway, B. E. (1999). *Electrochemical supercapacitors: scientific fundamentals and technological applications*. New York: Kluwer Academics / Plenum Publisher.
- De Volder, M. F. L., S. H. Tawfick, R. H. Baughman, and A. J. Hart (2013). Carbon nanotubes: Present and future commercial applications. *Science* 339(6119), 535–539.
- Dong, X., D. Fu, W. Fang, Y. Shi, P. Chen, and L.-J. Li (2009). Doping single-layer graphene with aromatic molecules. *Small* 5(12), 1422–1426.
- Dresselhaus, M., A. Jorio, and R. Saito (2010). Characterizing graphene, graphite, and carbon nanotubes by raman spectroscopy. *Annual Review of Condensed Matter Physics* 1(1), 89–108.
- Dresselhaus, M. S., A. Jorio, M. Hofmann, G. Dresselhaus, and R. Saito (2010). Perspectives on carbon nanotubes and graphene raman spectroscopy. *Nano letters* 10(3), 751–758.
- Du, C., J. Yeh, and N. Pan (2005). High power density supercapacitors using locally aligned carbon nanotube electrodes. *Nanotechnology* 16(4), 350.

- Ebert, D. and B. Bhushan (2012). Transparent, superhydrophobic, and wear-resistant coatings on glass and polymer substrates using  $\text{SiO}_2$ ,  $\text{ZnO}$ , and  $\text{ITO}$  nanoparticles. *Langmuir* 28(31), 11391–11399.
- Eggers, J., M. A. Fontelos, C. Josserand, and S. Zaleski (2010). Drop dynamics after impact on a solid wall: Theory and simulations. *Physics of fluids* 22(6), 062101.
- Elias, D. C., R. R. Nair, T. M. G. Mohiuddin, S. V. Morozov, P. Blake, M. P. Halsall, A. C. Ferrari, D. W. Boukhvalov, M. I. Katsnelson, A. K. Geim, and K. S. Novoselov (2009). Control of graphene's properties by reversible hydrogenation: Evidence for graphane. *Science* 323(5914), 610–613.
- Emsley, J. (1980). Very strong hydrogen-bonding. *Chemical Society reviews* 9(1), 91–124.
- Falcon, E., C. Laroche, S. Fauve, and C. Coste (1998). Behavior of one inelastic ball bouncing repeatedly off the ground. *The European physical journal. B* 3(1), 45–57.
- Felten, A., C. Bittencourt, J. J. Pireaux, G. Van Lier, and J. C. Charlier (2005). Radio-frequency plasma functionalization of carbon nanotubes surface  $\text{O}_2$ ,  $\text{NH}_3$ , and  $\text{CF}_4$  treatments. *Journal of applied physics* 98(7), 074308.
- Feng, L., S. Li, Y. Li, H. Li, L. Zhang, J. Zhai, Y. Song, B. Liu, L. Jiang, and D. Zhu (2002). Super-hydrophobic surfaces: From natural to artificial. *Advanced materials* 14(24), 1857–1860.
- Feng, X., L. Feng, M. Jin, J. Zhai, L. Jiang, and D. Zhu (2003). Reversible super-hydrophobicity to super-hydrophilicity transition of aligned  $\text{ZnO}$  nanorod films. *Journal of the American Chemical Society* 126(1), 62–63.
- Fernandez, J., M. Arulepp, J. Leis, F. Stoeckli, and T. Centeno (2008). EDLC performance of carbide-derived carbons in aprotic and acidic electrolytes. *Electrochimica Acta* 53(24), 7111–7116.

- Ferrari, A. C., J. C. Meyer, V. Scardaci, C. Casiraghi, M. Lazzeri, F. Mauri, S. Piscanec, D. Jiang, K. S. Novoselov, S. Roth, and A. K. Geim (2006). Raman spectrum of graphene and graphene layers. *Physical Review Letters* 97(18), 187401.
- Frank, I. W., D. M. Tanenbaum, and P. L. McEuen (2007). Mechanical properties of suspended graphene sheets. *Journal of vacuum science and technology B: Microelectronics and nanometer structures processing, measurement and phenomena* 25(6), 2558–2561.
- Fu, Y., Y. Qin, T. Wang, S. Chen, and J. Liu (2010). Ultrafast transfer of metal-enhanced carbon nanotubes at low temperature for large-scale electronics assembly. *Advanced materials* 22(44), 5039–5042.
- Futaba, D., K. Hata, T. Yamada, T. Hiraoka, Y. Hayamizu, and Y. Kakudate (2006). Shape-engineerable and highly densely packed single-walled carbon nanotubes and their application as super-capacitor electrodes. *Nature Materials* 5(12), 987–994.
- Gao, L. and T. McCarthy (2006a). The "lotus effect" explained: Two reasons why two length scales of topography are important. *Langmuir* 22(7), 2966–2967.
- Gao, L. and T. McCarthy (2006b). A perfectly hydrophobic surface ( $\theta(a)/\theta(r)=180$  degrees/180 degrees). *Journal of the American Chemical Society* 128(28), 9052–9053.
- Gao, L. and T. McCarthy (2007). A commercially available perfectly hydrophobic material ( $\theta(a)/\theta(r)=180$  degrees/180 degrees). *Langmuir* 23(18), 9125–9127.
- Geim, A. and K. Novoselov (2007). The rise of graphene. *Nature Materials* 6(3), 183–191.
- Gierz, I., C. Riedl, U. Starke, C. R. Ast, and K. Kern (2008). Atomic hole doping of graphene. *Nano letters* 8(12), 4603–4607.

- Gokus, T., R. R. Nair, A. Bonetti, M. Bohmler, A. Lombardo, K. S. Novoselov, A. K. Geim, A. C. Ferrari, and A. Hartschuh (2009). Making graphene luminescent by oxygen plasma treatment. *ACS nano* 3(12), 3963–3968.
- Gunes, F., G. H. Han, H.-J. Shin, S. Y. Lee, M. Jin, D. L. Duong, S. J. Chae, E. S. Kim, F. Yao, A. Benayad, J.-Y. Choi, and Y. H. Lee (2011). Uv-light-assisted oxidative sp<sup>3</sup> hybridization of graphene. *NANO: Brief Reports and Reviews* 06(05), 409–418.
- Guo, L., R.-Q. Shao, Y.-L. Zhang, H.-B. Jiang, X.-B. Li, S.-Y. Xie, B.-B. Xu, Q.-D. Chen, J.-F. Song, and H.-B. Sun (2012). Bandgap tailoring and synchronous microdevices patterning of graphene oxides. *The Journal of Physical Chemistry C* 116(5), 3594–3599.
- Han, M. Y., B. Ozyilmaz, Y. B. Zhang, and P. Kim (2007). Energy band-gap engineering of graphene nanoribbons. *Physical Review Letters* 98(20), 206805–206808.
- Haubner, K., J. Murawski, P. Olk, L. M. Eng, C. Ziegler, B. Adolphi, and E. Jaehne (2010). The route to functional graphene oxide. *ChemPhysChem* 11(10), 2131–2139.
- Hesse, R., P. Streubel, and R. Szargan (2005). Improved accuracy of quantitative xps analysis using predetermined spectrometer transmission functions with unifit 2004. *Surface and Interface Analysis* 37(7), 589–607.
- Hirsch, A. (2002). Functionalization of single-walled carbon nanotubes. *Angewandte Chemie International Edition* 41(11), 1853–1859.
- Hong, S. and S. Myung (2007). Nanotube electronics: a flexible approach to mobility. *Nature nanotechnology* 2(4), 207–208.
- Hong, Y. and H. Uhm (2006). Superhydrophobicity of a material made from multi-walled carbon nanotubes. *Applied physics letters* 88(24), 244101.

- Hossain, M. Z., J. E. Johns, K. H. Bevan, H. J. Karmel, Y. T. Liang, S. Yoshimoto, K. Mukai, T. Koitaya, J. Yoshinobu, M. Kawai, A. M. Lear, L. L. Kesmodel, S. L. Tait, and M. C. Hersam (2012). Chemically homogeneous and thermally reversible oxidation of epitaxial graphene. *Nature Chemistry* 4(4), 305–309.
- Hou, Z., B. Cai, H. Liu, and D. Xu (2008). Ar, o<sub>2</sub>, chf<sub>3</sub>, and sf<sub>6</sub> plasma treatments of screen-printed carbon nanotube films for electrode applications. *Carbon* 46(3), 405–413.
- Hsieh, C.-T. and H. Teng (2002). Influence of oxygen treatment on electric double-layer capacitance of activated carbon fabrics. *Carbon* 40(5), 667–674.
- Huang, H. M., Z. B. Li, J. C. She, and W. L. Wang (2012). Oxygen density dependent band gap of reduced graphene oxide. *Journal of applied physics* 111(5), 054317.
- Huang, L., S. Lau, H. Yang, E. Leong, S. Yu, and S. Prawer (2005). Stable superhydrophobic surface via carbon nanotubes coated with a zno thin film. *The Journal of Physical Chemistry B* 109(16), 7746–7748.
- Hummers, W. S. and R. E. Offeman (1958). Preparation of graphitic oxide. *Journal of the American Chemical Society* 80(6), 1339.
- Iijima, S. (1991). Helical microtubules of graphitic carbon. *Nature* 354(6348), 56–58.
- Ito, J., J. Nakamura, and A. Natori (2008). Semiconducting nature of the oxygen-adsorbed graphene sheet. *Journal of applied physics* 103(11).
- Jorio, A., G. Dresselhaus, and M. Dresselhaus (2007). *Carbon Nanotubes: Advanced Topics in the Synthesis, Structure, Properties and Applications*. Berlin: Springer.
- Jung, Y. and B. Bhushan (2008). Dynamic effects of bouncing water droplets on superhydrophobic surfaces. *Langmuir* 24(12), 6262–6269.
- Jung, Y. and B. Bhushan (2009). Dynamic effects induced transition of droplets on biomimetic superhydrophobic surfaces. *Langmuir* 25(16), 9208–9218.

- Kim, D. C., D. Y. Jeon, H. J. Chung, Y. Woo, J. K. Shin, and S. Seo (2009). The structural and electrical evolution of graphene by oxygen plasma-induced disorder. *Nanotechnology* 20(37), 375703.
- Kim, H. and J. Chun (2001). The recoiling of liquid droplets upon collision with solid surfaces. *Physics of fluids* 13(3), 643.
- Kim, K., Y. Zhao, H. Jang, S. Lee, J. Kim, J.-H. Ahn, P. Kim, J.-Y. Choi, and B. Hong (2009). Large-scale pattern growth of graphene films for stretchable transparent electrodes. *Nature* 457(7230), 706–710.
- Kim, U., X. Liu, C. Furtado, G. Chen, R. Saito, and J. Jiang (2005). Infrared-active vibrational modes of single-walled carbon nanotubes. *Physical Review Letters* 95(15), 157402.
- Kim, Y., Y. Ito, K. Tadai, T. Mitani, U. Kim, and H. Kim (2005). Drastic change of electric double layer capacitance by surface functionalization of carbon nanotubes. *Applied physics letters* 87(23), 234106.
- Koch, K. and W. Barthlott (2009). Superhydrophobic and superhydrophilic plant surfaces: an inspiration for biomimetic materials. *Philosophical Transactions of the Royal Society A: Mathematical, Physical and Engineering Sciences* 367(1893), 1487–1509.
- Krupenkin, T., J. Taylor, T. Schneider, and S. Yang (2004). From rolling ball to complete wetting: The dynamic tuning of liquids on nanostructured surfaces. *Langmuir* 20(10), 3824–3827.
- Kumar, A., V. L. Pushparaj, S. Kar, O. Nalamasu, P. M. Ajayan, and R. Baskaran (2006). Contact transfer of aligned carbon nanotube arrays onto conducting substrates. *Applied physics letters* 89(16), 163120.
- Kuznetsova, A., D. Mawhinney, V. Naumenko, J. Yates, J. Liu, and R. Smalley (2000). Enhancement of adsorption inside of single-walled nanotubes: opening the entry ports. *Chemical Physics Letters* 321(3-4), 292–296.

- Lafuma, A. and D. Quere (2003). Superhydrophobic states. *Nature Material* 2(7), 457–460.
- Larciprete, R., S. Ulstrup, P. Lacovig, M. Dalmiglio, M. Bianchi, F. Mazzola, L. Hornekr, F. Orlando, A. Baraldi, P. Hofmann, and S. Lizzit (2012). Oxygen switching of the epitaxial graphenemetal interaction. *ACS nano* 6(11), 9551–9558.
- Lau, K., J. Bico, K. Teo, M. Chhowalla, G. Amaratunga, and W. Milne (2003). Superhydrophobic carbon nanotube forests. *Nano letters* 3(12), 1701–1705.
- Leconte, N., J. Moser, P. Ordejon, H. Tao, A. Lherbier, A. Bachtold, F. Alsina, C. M. Sotomayor Torres, J.-C. Charlier, and S. Roche (2010). Damaging graphene with ozone treatment: A chemically tunable metal - insulator transition. *ACS nano* 4(7), 4033–4038.
- Lee, C., X. Wei, J. W. Kysar, and J. Hone (2008). Measurement of the elastic properties and intrinsic strength of monolayer graphene. *Science* 321(5887), 385–388.
- Lee, J. and S. Lee (2011). Dynamic wetting and spreading characteristics of a liquid droplet impinging on hydrophobic textured surfaces. *Langmuir* 27(11), 6565–6573.
- Lee, S. W., B. M. Gallant, Y. Lee, N. Yoshida, D. Y. Kim, Y. Yamada, S. Noda, A. Yamada, and Y. Shao-Horn (2012). Self-standing positive electrodes of oxidized few-walled carbon nanotubes for light-weight and high-power lithium batteries. *Energy and Environmental Science* 5(1), 5437–5444.
- Lee, S. W., N. Yabuuchi, B. M. Gallant, S. Chen, B.-S. Kim, P. T. Hammond, and Y. Shao-Horn (2010). High-power lithium batteries from functionalized carbon-nanotube electrodes. *Nature Nanotechnology* 5(7), 531–537.
- Lee, W. H., J. Park, S. H. Sim, S. B. Jo, K. S. Kim, B. H. Hong, and K. Cho (2011). Transparent flexible organic transistors based on monolayer graphene electrodes on plastic. *Advanced materials* 23(15), 1752–1756.

- Li, D., M. B. Muller, S. Gilje, R. B. Kaner, and G. G. Wallace (2008). Processable aqueous dispersions of graphene nanosheets. *Nature Nanotechnology* 3(2), 101–105.
- Li, J.-L., K. N. Kudin, M. J. McAllister, R. K. Prudhomme, I. A. Aksay, and R. Car (2006). Oxygen-driven unzipping of graphitic materials. *Physical Review Letters* 96(17), 176101.
- Li, Q., X. F. Zhang, R. F. DePaula, L. X. Zheng, Y. H. Zhao, L. Stan, T. G. Holesinger, P. N. Arendt, D. E. Peterson, and Y. T. Zhu (2006). Sustained growth of ultralong carbon nanotube arrays for fiber spinning. *Advanced materials* 18(23), 3160–3163.
- Li, R., N. Ashgriz, and S. Chandra (2010). Maximum spread of droplet on solid surface: Low reynolds and weber numbers. *Journal of Fluids Engineering* 132(6), 061302–061305.
- Li, X., W. Cai, J. An, S. Kim, J. Nah, D. Yang, R. Piner, A. Velamakanni, I. Jung, E. Tutuc, S. K. Banerjee, L. Colombo, and R. S. Ruoff (2009). Large-area synthesis of high-quality and uniform graphene films on copper foils. *Science* 324(5932), 1312–1314.
- Liu, C., Z. Yu, D. Neff, A. Zhamu, and B. Z. Jang (2010). Graphene-based supercapacitor with an ultrahigh energy density. *Nano letters* 10(12), 4863–4868.
- Liu, W. J., X. A. Tran, X. B. Liu, J. Wei, H. Y. Yu, and X. W. Sun (2013). Characteristics of a single-layer graphene field effect transistor with uv/ozone treatment. *ECS Solid State Letters* 2(1), M1–M4.
- Liu, Y., L. Liu, P. Liu, L. Sheng, and S. Fan (2004). Plasma etching carbon nanotube arrays and the field emission properties. *Diamond and Related Materials* 13(9), 1609–1613.
- Lu, W., R. Hartman, L. Qu, and L. Dai (2011). Nanocomposite electrodes for high-performance supercapacitors. *The Journal of Physical Chemistry Letters* 2(6), 655–660.

- Lu, Y. H., W. Chen, Y. P. Feng, and P. M. He (2008). Tuning the electronic structure of graphene by an organic molecule. *The Journal of Physical Chemistry B* 113(1), 2–5.
- Lufrano, F. and P. Staiti (2004). Conductivity and capacitance properties of a supercapacitor based on nafion electrolyte in a nonaqueous system. *Electrochemical and Solid-State Letters* 7(11), A447–A450.
- Luo, C., H. Zheng, L. Wang, H. Fang, J. Hu, C. Fan, Y. Cao, and J. Wang (2010). Direct three-dimensional imaging of the buried interfaces between water and superhydrophobic surfaces. *Angewandte Chemie International Edition* 49(48), 9145–9148.
- Luo, Z., P. M. Vora, E. H. Mele, A. T. C. Johnson, and J. M. Kikkawa (2009). Photoluminescence and band gap modulation in graphene oxide. *Applied physics letters* 94(11), 111909–111911.
- Manes, J. L. (2007). Symmetry-based approach to electron-phonon interactions in graphene. *Physical Review B* 76(4), 045430.
- Marcano, D. C., D. V. Kosynkin, J. M. Berlin, A. Sinitskii, Z. Sun, A. Slesarev, L. B. Alemany, W. Lu, and J. M. Tour (2010). Improved synthesis of graphene oxide. *ACS nano* 4(8), 4806–4814.
- Mawhinney, D., V. Naumenko, A. Kuznetsova, J. Yates, J. Liu, and R. Smalley (2000). Infrared spectral evidence for the etching of carbon nanotubes: Ozone oxidation at 298 k. *Journal of the American Chemical Society* 122(10), 2383–2384.
- McHale, G., M. I. Newton, and N. J. Shirtcliffe (2010). Immersed superhydrophobic surfaces: Gas exchange, slip and drag reduction properties. *Soft matter* 6(4), 714–719.
- Men, X., Z. Zhang, J. Yang, K. Wang, and W. Jiang (2010). Superhydrophobic/superhydrophilic surfaces from a carbon nanotube based composite coating. *Applied physics A: Materials science and processing* 98(2), 275–280.

- Mi, H., X. Zhang, S. An, X. Ye, and S. Yang (2007). Microwave-assisted synthesis and electrochemical capacitance of polyaniline/multi-wall carbon nanotubes composite. *Electrochemistry communications* 9(12), 2859–2862.
- Miller, J. R. and A. F. Burke (2008). Electrochemical capacitors: Challenges and opportunities for real-world applications. *The Electrochemical Society Interface* 17(1), 53–57.
- Miller, J. R. and P. Simon (2008). Electrochemical capacitors for energy management. *Science* 321(5889), 651–652.
- Muniz, A. R. and D. Maroudas (2010). Hydrogenation effects on the structure and morphology of graphene and single-walled carbon nanotubes. *Journal of applied physics* 108(11), 113532.
- Murata, Y., V. Petrova, B. B. Kappes, A. Ebnonnasir, I. Petrov, Y.-H. Xie, C. V. Ciobanu, and S. Kodambaka (2010). Moir superstructures of graphene on faceted nickel islands. *ACS nano* 4(11), 6509–6514.
- Nagurka, M. and S. G. Huang (2006). A mass-spring-damper model of a bouncing ball. *International journal of engineering education* 22(2), 393–401.
- Nakada, K., M. Fujita, G. Dresselhaus, and M. S. Dresselhaus (1996). Edge state in graphene ribbons: Nanometer size effect and edge shape dependence. *Physical Review B: Condensed matter* 54(24), 1795417961.
- Nam, K.-W., K.-H. Kim, E.-S. Lee, W.-S. Yoon, X.-Q. Yang, and K.-B. Kim (2008). Pseudocapacitive properties of electrochemically prepared nickel oxides on 3-dimensional carbon nanotube film substrates. *Journal of power sources* 182(2), 642–652.
- Naseh, M. V., A. A. Khodadadi, Y. Mortazavi, F. Pourfayaz, O. Alizadeh, and M. Maghrebi (2010). Fast and clean functionalization of carbon nanotubes by dielectric barrier discharge plasma in air compared to acid treatment. *Carbon* 48(5), 1369–1379.

- Ni, Z. H., T. Yu, Y. H. Lu, Y. Y. Wang, Y. P. Feng, and Z. X. Shen (2008). Uniaxial strain on graphene: Raman spectroscopy study and band-gap opening. *ACS nano* 2(11), 2301–2305.
- Niu, C., E. K. Sichel, R. Moch, D. Moy, and H. Tennent (1997). High power electrochemical capacitors based on carbon nanotube electrodes. *Applied physics letters* 70(11), 1480.
- Nourbakhsh, A., M. Cantoro, T. Vosch, G. Pourtois, F. Clemente, M. H. Veen, J. Hofkens, M. M. Heyns, S. D. Gendt, and B. F. Sels (2010). Bandgap opening in oxygen plasma-treated graphene. *Nanotechnology* 21(43), 435203–435211.
- Novoselov, K. S., A. K. Geim, S. V. Morozov, D. Jiang, M. I. Katsnelson, I. V. Grigorieva, S. V. Dubonos, and A. A. Firsov (2005). Two-dimensional gas of massless dirac fermions in graphene. *Nature* 438(7065), 197–200.
- Novoselov, K. S., A. K. Geim, S. V. Morozov, D. Jiang, Y. Zhang, S. V. Dubonos, I. V. Grigorieva, and A. A. Firsov (2004). Electric field effect in atomically thin carbon films. *Science* 306(5696), 666–669.
- Novoselov, K. S., E. McCann, S. V. Morozov, V. I. Fal’ko, M. I. Katsnelson, U. Zeitler, D. Jiang, F. Schedin, and A. K. Geim (2006). Unconventional quantum hall effect and berry’s phase of  $2\pi$  in bilayer graphene. *Nature Physics* 2(3), 177–180.
- Oostinga, J. B., H. B. Heersche, X. Liu, A. F. Morpurgo, and L. M. K. Vanderypen (2007). Gate-induced insulating state in bilayer graphene devices. *Nature Materials* 7(2), 151–157.
- Pan, H., J. Y. Li, and Y. P. Feng (2010). Carbon nanotubes for supercapacitor. *Nanoscale Research Letters* 5(3), 654–668.
- Pandey, D., R. Reifengerger, and R. Piner (2008). Scanning probe microscopy study of exfoliated oxidized graphene sheets. *Surface Science* 602(9), 1607–1613.

- Pandolfo, A. and A. Hollenkamp (2006). Carbon properties and their role in supercapacitors. *Journal of power sources* 157(1), 11–27.
- Park, S. and R. Ruoff (2009). Chemical methods for the production of graphenes. *Nature nanotechnology* 4(4), 217–224.
- Pasandideh-Fard, M., Y. M. Qiao, S. Chandra, and J. Mostaghimi (1996). Capillary effects during droplet impact on a solid surface. *Physics of fluids* 8(3), 650.
- Peng, B., M. Locascio, P. Zapol, S. Li, S. Mielke, G. Schatz, and H. Espinosa (2008). Measurements of near-ultimate strength for multiwalled carbon nanotubes and irradiation-induced crosslinking improvements. *Nature nanotechnology* 3(10), 626–31.
- Peng, Y. and H. Liu (2006). Effects of oxidation by hydrogen peroxide on the structures of multiwalled carbon nanotubes. *Industrial and Engineering Chemistry Research* 45(19), 6483–6488.
- Pereira, V. M., A. H. Castro Neto, and N. M. R. Peres (2009). Tight-binding approach to uniaxial strain in graphene. *Physical Review B* 80(4), 045401.
- Pletikosi, I., M. Kralj, P. Pervan, R. Brako, J. Coraux, A. T. NDiaye, C. Busse, and T. Michely (2009). Dirac cones and minigaps for graphene on ir(111). *Physical Review Letters* 102(5), 056808.
- Ponomarenko, L. A., F. Schedin, M. I. Katsnelson, R. Yang, E. W. W. Hill, K. S. Novoselov, and A. K. Geim (2008). Chaotic dirac billiard in graphene quantum dots. *Science* 320(5874), 356–358.
- Pop, E., D. Mann, Q. Wang, K. Goodson, and H. Dai (2005). Thermal conductance of an individual single-wall carbon nanotube above room temperature. *Nano Letters* 6(1), 96–100.
- Rafiee, J., M. A. Rafiee, Z.-Z. Yu, and N. Koratkar (2010). Superhydrophobic to

- superhydrophilic wetting control in graphene films. *Advanced Materials* 22(19), 2151–2154.
- Range, K. and F. Feuillebois (1998). Influence of surface roughness on liquid drop impact. *Journal of Colloid and Interface Science* 203(1), 16–30.
- Reina, A., X. Jia, J. Ho, D. Nezich, H. Son, V. Bulovic, M. S. Dresselhaus, and J. Kong (2009). Large area, few-layer graphene films on arbitrary substrates by chemical vapor deposition. *Nano letters* 9(1), 30–35.
- Reyssat, M., D. Richard, C. Clanet, and D. Quere (2010). Dynamical superhydrophobicity. *Faraday Discussions* 146, 19–33.
- Richard, D. and D. Quere (2000). Bouncing water drops. *Europhysics Letters (EPL)* 50(6), 769–775.
- Rioboo, R., M. Marengo, and C. Tropea (2002). Time evolution of liquid drop impact onto solid, dry surfaces. *Experiments in fluids* 33(1), 112–124.
- Rioboo, R., C. Tropea, and M. Marengo (2001). Outcomes from a drop impact on solid surfaces atomization and sprays. *Atomization and sprays* 11(2), 155–165.
- Rioboo, R., M. Voue, A. Vaillant, and J. De Coninck (2008). Drop impact on porous superhydrophobic polymer surfaces. *Langmuir* 24(24), 14074–14077.
- Rothstein, J. (2010). Slip on superhydrophobic surfaces. *Annual Review of Fluid Mechanics* 42(1), 89–109.
- Samarakoon, D. K. and X.-Q. Wang (2011). Twist-boat conformation in graphene oxides. *Nanoscale* 3(1), 192–195.
- Sansom, E., D. Rinderknecht, and M. Gharib (2008). Controlled partial embedding of carbon nanotubes within flexible transparent layers. *Nanotechnology* 19(3), 035302.
- Scardino, A. J., H. Zhang, D. J. Cookson, R. N. Lamb, and R. d. Nys (2009). The role of nano-roughness in antifouling. *Biofouling: The Journal of Bioadhesion and Biofilm Research* 25(8), 757–767.

- Scarpa, F., S. Adhikari, and A. S. Phani (2009). Effective elastic mechanical properties of single layer graphene sheets. *Nanotechnology* 20(6), 065709.
- Schiaffino, S. (1997). Molten droplet deposition and solidification at low weber numbers. *Physics of fluids* 9(11), 3172.
- Sessi, P., J. R. Guest, M. Bode, and N. P. Guisinger (2009). Patterning graphene at the nanometer scale via hydrogen desorption. *Nano letters* 9(12), 4343–4347.
- Shah, R., X. Zhang, and S. Talapatra (2009). Electrochemical double layer capacitor electrodes using aligned carbon nanotubes grown directly on metals. *Nanotechnology* 20(39), 395202.
- Sham, M. and J. Kim (2006). Surface functionalities of multi-wall carbon nanotubes after uv/ozone and teta treatments. *Carbon* 44(4), 768–777.
- Shirtcliffe, N. J., G. McHale, M. I. Newton, C. C. Perry, and P. Roach (2005). Porous materials show superhydrophobic to superhydrophilic switching. *Chemical Communications* 0(25), 3135–3137.
- Signorelli, R., D. C. Ku, J. G. Kassakian, and J. E. Schindall (2009). Electrochemical double-layer capacitors using carbon nanotube electrode structures. *Proceedings of the IEEE* 97(11), 1837–1847.
- Simon, P. and A. Burke (2008). Nanostructured carbons: Double-layer capacitance and more. *The Electrochemical Society Interface* 17(1), 38–43.
- Simon, P. and Y. Gogotsi (2008). Materials for electrochemical capacitors. *Nature Materials* 7(11), 845–854.
- Socrates, G. (2001). *Infrared and Raman characteristic group frequencies : tables and charts* (3rd ed. ed.). Chichester: Wiley.
- Stalder, A., G. Kulik, D. Sage, L. Barbieri, and P. Hoffmann (2006). A snake-based approach to accurate determination of both contact points and contact angles.

- Colloids and surfaces A: Physicochemical and engineering aspects* 286(1-3), 92–103.
- Starodub, E., N. C. Bartelt, and K. F. McCarty (2010). Oxidation of graphene on metals. *The Journal of Physical Chemistry C* 114(11), 5134–5140.
- Stoller, M. D., S. Park, Y. Zhu, J. An, and R. S. Ruoff (2008). Graphene-based ultracapacitors. *Nano letters* 8(10), 3498–3502.
- Suggs, K., V. Person, and X.-Q. Wang (2011). Band engineering of oxygen doped single-walled carbon nanotubes. *Nanoscale* 3(6), 2465–2468.
- Sun, X., Z. Liu, K. Welsher, J. T. Robinson, A. Goodwin, S. Zaric, and H. Dai (2008). Nano-graphene oxide for cellular imaging and drug delivery. *Nano Research* 1(3), 203–212.
- Sutter, P., J. T. Sadowski, and E. A. Sutter (2010). Chemistry under cover: Tuning metalgraphene interaction by reactive intercalation. *Journal of the American Chemical Society* 132(23), 8175–8179.
- Tao, Z. and C. Tianhong (2011). Tunable wetting properties of patterned silicon microchannels with varied surface free energy based on layer-by-layer nano self-assembly. *Journal of Micromechanics and Microengineering* 21(4), 045015.
- Tsai, P., S. Pacheco, C. Pirat, L. Lefferts, and D. Lohse (2009). Drop impact upon micro- and nanostructured superhydrophobic surfaces. *Langmuir* 25(20), 12293–12298.
- Ukiwe, C. and D. Y. Kwok (2004). On the maximum spreading diameter of impacting droplets on well-prepared solid surfaces. *Langmuir* 21(2), 666–673.
- Vadillo, D., A. Soucemarianadin, C. Delattre, and D. Roux (2009). Dynamic contact angle effects onto the maximum drop impact spreading on solid surfaces. *Physics of fluids* 21(12), 122002.

- Vinogradov, N. A., K. Schulte, M. L. Ng, A. Mikkelsen, E. Lundgren, N. Martensson, and A. B. Preobrajenski (2011). Impact of atomic oxygen on the structure of graphene formed on ir(111) and pt(111). *The Journal of Physical Chemistry C* 115(19), 9568–9577.
- Wang, L., B. Peng, and Z. Su (2010). Tunable wettability and rewritable wettability gradient from superhydrophilicity to superhydrophobicity. *Langmuir* 26(14), 12203–12208.
- Wang, S. and L. Jiang (2007). Definition of superhydrophobic states. *Advanced materials* 19(21), 3423–3424.
- Wang, X., Q. Li, J. Xie, Z. Jin, J. Wang, Y. Li, K. Jiang, and S. Fan (2009). Fabrication of ultralong and electrically uniform single-walled carbon nanotubes on clean substrates. *Nano Letters* 9(9), 3137–3141.
- Wehling, T. O., K. S. Novoselov, S. V. Morozov, E. E. Vdovin, M. I. Katsnelson, A. K. Geim, and A. I. Lichtenstein (2008). Molecular doping of graphene. *Nano letters* 8(1), 173–177.
- Wei, B. Q., R. Vajtai, and P. Ajayan (2001). Reliability and current carrying capacity of carbon nanotubes. *Applied physics letters* 79(8), 1172.
- Wenzel, R. N. (1936). Resistance of solid surfaces to wetting by water. *Industrial and Engineering Chemistry* 28(8), 988–994.
- Xu, L., R. G. Karunakaran, J. Guo, and S. Yang (2012). Transparent, superhydrophobic surfaces from one-step spin coating of hydrophobic nanoparticles. *ACS Appl. Mater. Interfaces* 4, 1118.
- Xu, T., J. Yang, J. Liu, and Q. Fu (2007). Surface modification of multi-walled carbon nanotubes by o<sub>2</sub> plasma. *Applied Surface Science* 253(22), 8945–8951.
- Yang, D., A. Velamakanni, G. Bozoklu, S. Park, and M. Stoller (2009). Chemical

- analysis of graphene oxide films after heat and chemical treatments by x-ray photoelectron and micro-raman spectroscopy. *Carbon* 47(1), 145–152.
- Yarin, A. (2006). Drop impact dynamics: Splashing, spreading, receding, bouncing. *Annual Review of Fluid Mechanics* 38(1), 159–192.
- Yeh, N. C., M. L. Teague, S. Yeom, B. L. Standley, R. T. P. Wu, D. A. Boyd, and M. W. Bockrath (2011). Strain-induced pseudo-magnetic fields and charging effects on cvd-grown graphene. *Surface Science* 605(1718), 1649–1656.
- Yoon, B.-J., S.-H. Jeong, K.-H. Lee, H. Seok Kim, C. Gyung Park, and J. Hun Han (2004). Electrical properties of electrical double layer capacitors with integrated carbon nanotube electrodes. *Chemical Physics Letters* 388(1-3), 170–174.
- Yu, M. F., O. Lourie, M. J. Dyer, K. Moloni, and T. F. Kelly (2000). Strength and breaking mechanism of multiwalled carbon nanotubes under tensile load. *Science* 287(5453), 637–640.
- Zhang, E. X., A. K. M. Newaz, B. Wang, C. X. Zhang, D. M. Fleetwood, K. I. Bolotin, R. D. Schrimpf, S. T. Pantelides, and M. L. Alles (2012). Ozone-exposure and annealing effects on graphene-on-sio2 transistors. *Applied physics letters* 101(12), 121601.
- Zhang, Y., Y.-W. Tan, H. L. Stormer, and P. Kim (2005). Experimental observation of the quantum hall effect and berry’s phase in graphene. *Nature* 438(7065), 201–204.